THE UNIVERSITY OF CHICAGO

ELECTRONIC STRUCTURE OF MOLECULES AND MATERIALS FROM QUANTUM SIMULATIONS

A DISSERTATION SUBMITTED TO
THE FACULTY OF THE DIVISION OF THE PHYSICAL SCIENCES
IN CANDIDACY FOR THE DEGREE OF
DOCTOR OF PHILOSOPHY

DEPARTMENT OF CHEMISTRY

BY
HE MA

CHICAGO, ILLINOIS
DECEMBER 2020

To my family

TABLE OF CONTENTS

LIST OF FIGURES

LIST OF TABLES

ACKNOWLEDGMENTS

I would like to first thank my PhD advisor Prof. Giulia Galli, who encouraged me to ask big scientific questions since early in my PhD and gave me enormous freedom to choose my research projects. PhD is a difficult journey with many negative results and depressive moments, and I am very grateful that Giulia has been emotionally very supportive during the entire process.

I would like to thank two mentors who played an important role in my PhD: Dr. Hosung Seo and Dr. Marco Govoni. As the first person I worked with after joining the Galli group, Hosung brought me to the field of quantum information science and taught me many things ranging from physics to simulations. Marco has been the mentor for most of my method development projects and gave me a lot of important guidance on the design and implementation of theories and algorithms.

I would like to thank many friends and collaborators in the Galli group. The entire list is way too long to be put here. I am extremely grateful for their friendship and I really enjoyed working in such a warm group.

Besides the Galli group, during my PhD I was very fortunate to have the opportunity to work with several other research groups in different research areas, including Prof. David Awschalom group, Prof. Francois Gygi group, Prof. Vikram Gavini group, and Prof. Norman Yao group. In these collaborations, I had the chance to work with many brilliant people, who taught me many different mindsets and languages and greatly expanded the scope of my PhD study.

Finally, I would like to thank my family, especially my parents. Without their selfless love and emphasis on my education, I cannot be where I am now. I would like to also thank my wife Yanyu for her companion and support during my entire PhD journey.

ABSTRACT

Numerical simulations based on the fundamental laws of quantum mechanics lead to invaluable insights into the microscopic behavior of molecules and materials. In the past decades, quantum mechanical simulations are becoming an increasingly important component for chemical and materials science and industry. In this dissertation, I will present several advancements in the development and application of quantum mechanical methods for first-principles simulations of molecular and condensed systems.

First, I will present a finite-field algorithm for evaluating density response functions based on density functional theory calculations under finite electric fields. The finite-field algorithm enables accurate many-body perturbation theory calculations beyond the random phase approximation. Based on the finite-field approach, we demonstrated GW and Bethe-Salpeter equation calculations of excitation energies of molecules and materials beyond the random phase approximation.

Next, I will present a quantum embedding theory for the study of strongly-correlated electronic states in condensed systems. The quantum embedding theory is capable of constructing a simple, effective model for a selected part of a physical system, where the rest of the system acts as a dielectric screening media that renormalizes the electron-electron interactions in the effective model. We demonstrated quantum simulations of effective models using both classical and quantum computers. This development helps bridge the gap between the systems sizes required to study realistic materials science problems and those that can be tackled with the resources of near-term quantum computers.

In addition to electronic properties, I will present a novel approach to predict certain spin properties (e.g. the hyperfine coupling) for paramagnetic systems using density functional theory calculations on finite-element basis sets. We demonstrated all-electron finite-element DFT calculations of spin properties for both finite and periodic systems. We showed that the results of such calculations can be systematically converged with respect to the basis set size. This development enables robust all-electron calculations of spin properties for paramagnetic

molecules and materials.

Finally, I will present several applications of first-principles methods for the study of spin-defects in semiconductors. Spin-defects in semiconductors are promising physical realizations of quantum bits for quantum information technologies. We present a number of theoretical predictions on various properties of spin-defects that are important for their operation as quantum bits. In particular, we applied density functional theory and many-body perturbation theory to predict the stability and excitation energies of several novel spin-defects in silicon carbide and aluminum nitride; we applied the quantum embedding theory to predict the strongly-correlated excited states of group-4 vacancy centers in diamond; we applied DFT and group theory to construct a microscopic theory for spin-phonon coupling of divacancy defects in silicon carbide; we performed quantum dynamics simulations using the cluster correlation expansion method to predict the coherence time of divacancy spins in the environment of other electron spins and nuclear spins. These studies greatly expanded our understanding of various physical properties of existing spin-defects as well as novel ones, and provided important guidance for the experimental realization and manipulation of these spin-defects as solid-state quantum bits.

CHAPTER 1

INTRODUCTION

The law of quantum mechanics governs all the microscopic processes in nature. The quantum mechanical description of electromagnetic interactions among electrons and nuclei lays the foundation for the human understanding of the world on the molecular level. Thanks to a century of exploration by numerous pioneers, great progress has been made in both theoretical understanding and numerical simulation of molecules and materials using quantum mechanics [146, 191, 133, 237]. Today, quantum mechanical theories and simulations are playing an increasingly important role in the discovery and design of molecules and materials for energy conversion, healthcare, catalysis and quantum technologies.

Many important chemical and materials science problems require an accurate description of electronic states and electronic processes. The first theme of this dissertation is the development of methods and algorithms for electronic structure simulations. The microscopic description of electrons in the electric field of nuclei is given by the many-electron Schrodinger equation. In principle, if the many-electron Schrodinger equation can be solved, one can predict numerous important properties of molecules and materials. Unfortunately, the direct solution of many-electron Schrodinger equation is computationally very demanding as the electronic wavefunction becomes exponentially more complex as the system size increases (the curse of dimensionality). A frequently quoted sentence from P. A. M. Dirac says that *the fundamental laws necessary for the mathematical treatment of a large part of physics and the whole of chemistry are thus completely known, and the difficulty lies only in the fact that application of these laws leads to equations that are too complex to be solved.*

At first sight, the development of electronic structure theory is nothing but finding numerical tricks to tackle the *equations that are too complex to be solved*. This is far from the complete picture. For simulations of realistic systems, one almost always needs to introduce a certain number of approximations to reduce the computational complexity, and many important approximations are based on *physical* insights of the physical and chemical process

instead of bare *numerical* considerations. Furthermore, oftentimes one needs to first cast the many-electron Schrodinger equation into a dramatically different form, based on which one can devise smart approximations that greatly reduce the computational cost without a significant sacrifice of accuracy. Such reformulation requires deep insight into the collective motion of interacting electrons, and is far from obvious if one merely views the electronic structure problem as finding numerical solutions to complex equations.

Two such reformulations are of particular relevance to this work, namely the density functional theory (DFT) [146, 191] and the many-electron perturbation theory (MBPT) [133], summarized in Chapter 2. In the Kohn-Sham formulation of DFT, the many-electron Schrodinger equation is transformed into the Schrodinger equation of non-interacting electrons (Kohn-Sham equations). The past decades witnessed an enormous success of DFT in the prediction of various properties of molecules and materials, especially ground state properties. Despite great effort, DFT is generally considered to be less accurate for predicting excited state properties. MBPT is based on a refomulation of the Schrodinger equation using the language of Green's function, and has been successfully applied to predict excited state properties of molecular and condensed systems, often achieving higher accuracy than DFT. Unfortunately, MBPT is computationally more expensive than DFT, limiting its applicability to large systems. Furthermore, most MBPT calculations are performed with the so-called random-phase approximation (RPA), which limits the accuracy of the description of dielectric screening between electrons. In Chapter 3, we represent a novel approach to compute dielectric screening by performing DFT calculations in finite electric fields, and we apply the finite-field approach to perform efficient MBPT calculations beyond the RPA. In addition to excitation energies, another outstanding challenge for DFT is the description of strongly-correlated electronic states, which are states that cannot be represented by single determinants of one-electron orbitals. In Chapter 4, we describe a quantum embedding theory based on the development in Chapter 3, which is capable of constructing effective models of the strongly-correlated part of a physical system. The effective model can be solved by a

high level of theory such as exact diagonalization, with the rest of the system treated with a lower level of theory such as DFT.

Most electronic structure calculations are performed within two fundamental approximations: nonrelativistic approximation and Born-Oppenheimer approximation. The prediction of certain molecular or materials properties requires going beyond the two fundamental approximations. For instance, certain spin properties of magnetic molecules and materials such as the hyperfine coupling involve magnetic interactions missing in the nonrelativistic Hamiltonian. In Chapter 5, we describe a finite element DFT approach for computing such spin properties of magnetic molecules and materials. Another example is charge transport processes in molecules and materials. Charge transport in many systems involves transitions (hopping) between electronic states that are not eigenstates of the Born-Oppenheimer electronic Hamiltonian. In Appendix B.2, we present an implementation of constrained density functional theory (CDFT) for first-principles calculation of charge transport properties.

The second theme of this dissertation is the first-principles studies of materials for quantum information science (QIS). QIS involves measuring, processing and communicating information by exploiting quantum mechanical phenomena such as superposition and entanglement. QIS represents one of the most ambitious human endeavors in the control and manipulation of quantum mechanical objects on the molecular level, and has the potential to fundamentally revolutionize information technologies. The greatest impact of QIS is likely to be seen first in sensing and metrology, then in communication and simulation, and finally digital computing [332]. Currently, several different types of quantum systems are being explored to act as quantum bits (qubits), the basic units that carry quantum information. Popular realizations include superconducting circuits, trapped ions, semiconductor spin-defects, quantum dots, etc. Each realization has its unique advantages and challenges, and different types of qubits can be coupled to construct hybrid quantum devices with more sophisticated functionalities. In this work, we focus on semiconductor spin-defects, which feature long coherence time and allow for room temperature operation. In Chapter 6 we

present first-principles simulations of spin-defects in diamond, silicon carbide and other host materials. We investigated their ground and excited state electronic structure, as well as their spin properties and quantum coherence dynamics.

The two themes mentioned above are deeply interwoven in several ways. First, the development of novel electronic structure methods and algorithms facilitates the theoretical interpretation of experimental measurements and the computational discovery of novel spin qubits. Second, the simulation of spin-defects provides several challenges for current electronic structure methods and motivates interesting theoretical developments. For instance, the development of the finite-element approach in Chapter 5 is motivated by the study of spin-defects, although it is general and can be applied to other systems as well. Finally, the development of materials for QIS can benefit the electronic structure theory in a more fundamental way. One of the most exciting and challenging areas in QIS is the development of quantum computers, which promise to solve certain tasks exponentially faster than classical computers. The simulation of interacting electrons in molecules and materials is expected to be one of the first areas that will benefit from quantum computation. In Chapter 4, we show proof-of-principle simulations of spin-defects using quantum computers, demonstrating how quantum embedding theory helps quantum computers to tackle complex chemical and materials science problems.

CHAPTER 2

THEORETICAL BACKGROUND

2.1 The electronic structure problem

The microscopic behavior of molecules and materials are governed by interactions among electrons and nuclei. The electronic structure theories focus on the motion of electrons under the influence of nuclei, and are usually formulated within two fundamental approximations: the nonreletivistic approximation and the Born-Oppenheimer approximation. Under the nonreletivistic approximation, electrons and nuclei interacts through Coulomb interaction, and is governed by the well-known Hamiltonian:

$$\mathcal{H} = -\sum_I \frac{1}{2M_I}\nabla_I^2 - \sum_i \frac{1}{2}\nabla_i^2 - \sum_{i,I} \frac{Z_I}{|\boldsymbol{r}_i - \boldsymbol{R}_I|} + \sum_{I<J} \frac{Z_I Z_J}{|\boldsymbol{R}_I - \boldsymbol{R}_J|} + \sum_{i<j} \frac{1}{|\boldsymbol{r}_i - \boldsymbol{r}_j|} \tag{2.1}$$

where the five terms represent nuclear kinetic energy operator, electron kinetic energy operator, electron-nuclei attraction, nuclei-nuclei repulsion and electron-electron repulsion; I, J and i, j index nuclei and electrons, respectively; R and r represent nuclear and electron coordinate; M and Z represent nuclear mass and charge. The nonreletivistic approximation is generally a good approximation for light elements, where the velocity of electrons are much lower than the speed of light. However, the nonreletivistic approximation neglects the magnetic interactions among electrons and nuclear spins, which are important for the determination of certain spin properties of magnetic molecules and materials. In Chapter 5 we will present a formalism to compute spin properties in a perturbative manner starting from nonrelativistic finite-element DFT calculations.

Based on Eq. 2.1, the Born-Oppenheimer approximation is usually applied to separate the degrees of freedom of electrons and nuclei. Under the Born-Oppenheimer approximation,

the electronic motion is governed by the time-independent Schrodinger equation

$$\mathcal{H}_{\text{el}}\Psi_N = E_N\Psi_N \tag{2.2}$$

where E_N and Ψ_N represents the energy and wavefunction of the N^{th} eigenstates of the Born-Oppenheimer electronic Hamiltonian

$$\mathcal{H}_{\text{el}} = -\sum_i \frac{1}{2}\nabla_i^2 - \sum_{i,I} \frac{Z_I}{|\boldsymbol{r}_i - \boldsymbol{R}_I|} + \sum_{i<j} \frac{1}{|\boldsymbol{r}_i - \boldsymbol{r}_j|} + \sum_{I<J} \frac{Z_I Z_J}{|\boldsymbol{R}_I - \boldsymbol{R}_J|} \tag{2.3}$$

Solving Eq. 2.2 is the central task for nonrelativistic electronic structure theory.

The eigenstates Ψ_N are usually called *adiabatic* states. $\mathcal{H}_{\text{el}}$ depends parametrically on nuclear coordinates, and the energy E_N as a function of nuclear coordinates give rise to the N^{th} adiabatic potential energy surface. Within the Born-Oppenheimer approximation, nuclei move on adiabatic potential energy surfaces. However, for the study of certain processes such as charge transfer, it is sometimes desirable to compute the so-called *diabatic* states, which are states that retain the character as nuclei move. Diabatic states are generally *not* eigenstates of the Born-Oppenheimer electronic Hamiltonian and are therefore not directly accessible from common electronic structure calculations. In Section B.2, we describe an implementation of the constrained density functional theory for first-principles calculations of diabatic states and charge transfer rates.

In most electronic structure calculations, Eq. 2.2 is solved using a discrete one-electron basis set. In the second quantized form, the Born-Oppenheimer electronic Hamiltonian reads (neglecting the constant nuclear repulsion term)

$$\mathcal{H}_{\text{el}} = \sum_{ij} t_{ij} a_i^\dagger a_j + \sum_{ijkl} V_{ijkl} a_i^\dagger a_j^\dagger a_l a_k \tag{2.4}$$

where $a^\dagger$ and a are creation and annihilation operators on given single-particle basis state labeled by i, j, k, l; t_{ij} represents the matrix elements of kinetic and electron-nuclei intera-

tions; V_{ijkl} (known as electron repulsion integrals) represents matrix elements of Coulomb interaction between electrons.

As mentioned in Chapter 1, the exact solution of eigenvalues and eigenstates of $\mathcal{H}_{\text{el}}$ grows exponentially as the system size increases, and it is often desirable to reformulate the problem into a form where approximations can be made to facilitate practical calculations. In the following two sections of this chapter, we describe two such reformulations, namely the density functional theory (DFT) and many-body perturbation theory (MBPT). Both DFT and MBPT have been applied to predict various ground and excited state properties of molecules and materials, and is particularly successful for systems where the electron correlations are weak. For systems exhibiting strongly-correlated electrons, accurate calculations become very challenging for DFT and MBPT, In Chapter 4 we describe a quantum embedding theory to construct effective Hamiltonians similar in form to Eq. 2.4, but acts only on the strongly-correlated part of the system. The effective Hamiltonian can then be solved with quantum chemistry methods such as full configuration interaction, or more ambitiously, with quantum computation.

2.2 Density functional theory

DFT is one of the most successful electronic structure theories so far. The seminal work by Hohenberg and Kohn demonstrates [146] that all the ground and excited state properties of a system of interacting electrons are completely determined by its ground state electron density, and that the ground state electron density can be obtained by minimizing the total energy functional:

$$E[n] = \int V_{\text{ext}}(\boldsymbol{r}) n(\boldsymbol{r}) \mathrm{d}\boldsymbol{r} + F[n] \tag{2.5}$$

where F is a universal functional of electron density n. Most DFT calculations performed today are based on the Kohn-Sham scheme [191], which casts the solution of Eq. into the

solution of the Kohn-Sham equation

$$H^{\mathrm{KS}}\psi_i = \varepsilon_i \psi_i \tag{2.6}$$

The Kohn-Sham equation is a Schrodinger equation of independent electrons governed by the Kohn-Sham Hamiltonian H^{KS}

$$H^{\mathrm{KS}} = T + V_{\mathrm{ion}} + V_H + V_{\mathrm{xc}} \tag{2.7}$$

where T denote kinetic energy operator and V_{ion}, V_H and V_{xc} denote ionic, Hartree and exchange-correlation potential, respectively. The exchange-correlation potential V_{xc} is defined as the functional derivative of the so-called exchange-correlation functional E_{xc} with respect to electron density n

$$V_{\mathrm{xc}} = \frac{\delta E_{\mathrm{xc}}[n]}{\delta n} \tag{2.8}$$

The exact form of exchange-correlation functional E_{xc} is unknown, and approximate forms are required to perform practical DFT calculations. The development of exchange-correlation functional is one of the central topics for DFT research. In the past decades, more than 200 approximate forms of E_{xc} has been proposed, which can be roughly classified using the Jacob's ladder for DFT. The first rung of Jacob's ladder denotes the local density approximation (LDA), where E_{xc} is a functional of electron density only. Higher rungs of Jacob's ladder corresponds to more sophisticated functionals where E_{xc} depends also on derivatives of electron density and contains nonlocal terms from wavefunction theory.

It is often stated that DFT is a mean-field theory, and this thesis also mentioned this statement in several places. Here, I hope to emphasize that this statement needs to be interpreted with caution. The Kohn-Sham formulation of DFT solves the Kohn-Sham equation that describes the Kohn-Sham reference system of noninteracting electrons, and yields the

exact energy and electron density of the system if the exact exchange-correlation functional is used. The Kohn-Sham reference system (hence the Kohn-Sham orbitals and Kohn-Sham eigenvalues) does not have direct physical meaning. In practical calculations, one often associates Kohn-Sham eigenvalues and their differences to various excitation energies of the physical system, which in many cases lead to reasonable predictions and provide valuable insights to the physical system. However, such association is not theoretically rigorous, and by using such association one is attaching physical meaning to the mean-field solutions of the Kohn-Sham reference system. Therefore, in some sense it would be more accurate to say that DFT is often *used* as a mean-field theory, as one assumes that the excitation energies and wavefunction of Kohn-Sham systems are reasonable approximations to those of real systems.

2.3 Many-body perturbation theory

MBPT is a mathematical reformulation of the Schrodinger equation of interacting electrons using Green's functions. The seminal paper by Hedin [133] presents a set of equations that connects five important fundamental quantities of a physical system including the one-electron Green's function G, self-energy Σ, screened Coulomb interaction W, irreducible polarizability P and vertex function Γ

$$\Sigma(1,2) = iG(1,\bar{4})W(1^+,\bar{3})\Gamma(\bar{4},2;\bar{3}), \tag{2.9}$$

$$W(1,2) = v_{\mathrm{c}}(1,2) + v_{\mathrm{c}}(1,\bar{3})P(\bar{3},\bar{4})W(\bar{4},2), \tag{2.10}$$

$$P(1,2) = -iG(1,\bar{3})G(\bar{4},1)\Gamma(\bar{3},\bar{4},2), \tag{2.11}$$

$$\Gamma(1,2;3) = \delta(1,2)\delta(1,3) + \frac{\delta\Sigma(1,2)}{\delta G(\bar{4},\bar{5})}G(\bar{4},\bar{6})G(\bar{7},\bar{5})\Gamma(\bar{6},\bar{7},3), \tag{2.12}$$

$$G(1,2) = G^0(1,2) + G^0(1,\bar{3})\Sigma(\bar{3},\bar{4})G(\bar{4},2). \tag{2.13}$$

where G_0 denotes the one-electron Green's function of independent electrons; v_c denotes the (bare) Coulomb interaction; indices 1, 2, ... are shorthand notations for space-time points $(\boldsymbol{r}_1, t_1)$, $(\boldsymbol{r}_2, t_2)$, ...; indices with bars are integrated over.

Exact solution of Hedin's equation yield the exact one-electron Green's function, which encodes the excitation energies of charge excitations (electron addition or removal) of the physical system. Unfortunately, in practical calculations it is difficult to solve the entire set of Hedin's equations in a self-consistent manner. In the famous GW approximation, the vertex function Γ is assumed to be a delta function (random phase approximation, RPA), and the self-energy is approximated as

$$\Sigma(1,2) = iG(1,2)W(1^+,2) \tag{2.14}$$

GW calculations have been successfully applied to predict bandgaps of semiconductors. Most practical GW calculations are performed in a perturbative manner (G_0W_0) on top of a mean-field description of the system. If Kohn-Sham eigenvalues and orbitals from DFT calculations are used as the starting point for a G_0W_0 calculation, the charged excitation energies (quasiparticle energies $\varepsilon^{\mathrm{QP}}$) of a system can be computed by adding perturbative corrections to the Kohn-Sham eigenvalues ε

$$\varepsilon_i^{\mathrm{QP}} = \varepsilon_i + \langle \Sigma(\varepsilon_i^{\mathrm{QP}}) - V_{\mathrm{xc}} \rangle \tag{2.15}$$

The RPA assumed in most GW calculations equates the irreducible polarizability P to that of independent electrons, which is the density response function of the Kohn-Sham system (commonly denoted as χ_0) if a DFT starting point is used. This neglects the exchange-correlation effects in the description of dielectric screening. Section 3.1 presents a finite-field algorithm for evaluating density response functions and dielectric screening effects beyond the RPA.

In addition to charged excitations, MBPT can also predict neutral excitation energies

through the solution of the Bethe-Salpeter equation (BSE) for two-electron Green's functions. Section 3.2 presents the application of the finite-field algorithm to the solution of BSE.

CHAPTER 3

FINITE FIELD ALGORITHM FOR MANY-BODY PERTURBATION THEORY

As briefly summarized in the previous chapter, many-body perturbation theory (MBPT) is a Green's function theory for electronic excitations of condensed and molecular systems. The two most common types of MBPT calculations are the GW calculation and Bethe-Salpeter equation (BSE) calculation, which are capable of predicting charged excitation energies and neutral excitation energies of the physical system, respectively. MBPT calculations require a microscopic description of the dielectric screening effect, which is characterized by density response functions. As mentioned earlier, most MBPT calculations assume the random phase approximation (RPA) when evaluating density response functions, which neglects exchange-correlation effects in the dielectric screening. In Section 3.1 we describe a finite-field algorithm for evaluating density response functions and performing GW calculations beyond the RPA. In Section 3.2 we present the application of the finite-field algorithm in BSE calculations.

3.1 Finite field calculation of response functions

Adapted with permission from H. Ma, M. Govoni, F. Gygi, and G. Galli. Journal of Chemical Theory and Computations. 15 (1), 154 (2019). https://doi.org/10.1021/acs.jctc.8b00864.

We describe a finite-field approach to compute density response functions, which allows for efficient G_0W_0 and $G_0W_0\Gamma_0$ calculations beyond the random phase approximation. The method is easily applicable to density functional calculations performed with hybrid functionals. We present results for the electronic properties of molecules and solids and we discuss a general scheme to overcome slow convergence of quasiparticle energies obtained from $G_0W_0\Gamma_0$ calculations, as a function of the basis set used to represent the dielectric matrix.

3.1.1 Introduction

Accurate, first principles predictions of the electronic structure of molecules and materials are important goals in chemistry, condensed matter physics and materials science [271]. In the past three decades, density functional theory (DFT) [146, 191] has been successfully adopted to predict numerous properties of molecules and materials [28]. In principle, any ground or excited state properties can be formulated as functionals of the ground state charge density. In practical calculations, the ground state charge density is determined by solving the Kohn-Sham (KS) equations with approximate exchange-correlation functionals, and many important excited state properties are not directly accessible from the solution of the KS equations. The time-dependent formulation of DFT (TDDFT) [314] in the frequency domain [49] provides a computationally tractable method to compute excitation energies and absorption spectra. However, using the common adiabatic approximation to the exchange-correlation functional, TDDFT is often not sufficiently accurate to describe certain types of excited states such as Rydberg and charge transfer states [51], especially when semilocal

functionals are used.

A promising approach to predict excited state properties of molecules and materials is many-body perturbation theory (MBPT) [133, 157, 237]. Within MBPT, the GW approximation can be used to compute quasiparticle energies that correspond to photoemission and inverse photoemission measurements; furthermore, by solving the Bethe-Salpeter equation (BSE), one can obtain neutral excitation energies corresponding to optical spectra. For many years since the first applications of MBPT [157], its use has been hindered by its high computational cost. In the last decade, several advances have been proposed to improve the efficiency of MBPT calculations [376, 258, 214], which are now applicable to simulations of relatively large and complex systems, including nanostructures and heterogeneous interfaces [291, 285, 211]. In particular, GW and BSE calculations can be performed using a low rank representation of density response functions [260, 286, 117, 118], whose spectral decomposition is obtained through iterative diagonalization using density functional perturbation theory (DFPT) [22, 21]. This method does not require the explicit calculation of empty electronic states and avoids the inversion or storage of large dielectric matrices. The resulting implementation in the WEST code has been successfully applied to investigate numerous systems including defects in semiconductors [334, 335], nanoparticles[322], aqueous solutions[93, 285, 95], and solid/liquid interfaces[117, 104] .

In this work, we developed a finite-field (FF) approach to evaluate density response functions entering the definition of the screened Coulomb interaction W. The FF approach can be used as an alternative to DFPT, and presents the additional advantage of being applicable, in a straightforward manner, to both semilocal and hybrid functionals. In addition, FF calculations allow for the direct evaluation of density response functions beyond the random phase approximation (RPA).

Here we first benchmark the accuracy of the FF approach for the calculation of several density response functions, from which one can obtain the exchange correlation kernel (f_{xc}), defined as the functional derivative of the exchange-correlation potential with respect to the

charge density. Then we discuss G_0W_0 calculations for various molecules and solids, carried out with either semilocal or hybrid functionals, and by adopting different approximations to include vertex corrections in the self-energy. In the last two decades a variety of methods [350, 89, 323, 233, 48, 371, 249, 340, 338, 311, 121, 56, 202, 203, 226] has been proposed to carry out vertex-corrected GW calculations, with different approximations to the vertex function Γ and including various levels of self-consistency between G, W and Γ. Here we focus on two formulations that are computationally tractable also for relatively large systems, denoted as $G_0W_0^{f_{\rm xc}}$ and $G_0W_0\Gamma_0$. In $G_0W_0^{f_{\rm xc}}$, $f_{\rm xc}$ is included in the evaluation of the screened Coulomb interaction W; in $G_0W_0\Gamma_0$, $f_{\rm xc}$ is included in the calculation of both W and the self-energy Σ through the definition of a local vertex function. Most previous $G_0W_0^{f_{\rm xc}}$ and $G_0W_0\Gamma_0$ calculations were restricted to the use of the LDA functional [350, 89, 371, 249], for which an analytical expression of $f_{\rm xc}$ is available. Paier *et al.* [275] reported $GW_0^{f_{\rm xc}}$ results for solids obtained with the HSE03 range-separated hybrid functional [141], and the exact exchange part of $f_{\rm xc}$ is defined using the nanoquanta kernel [300, 234, 353, 48]. In this work semilocal and hybrid functionals are treated on equal footing, and we present calculations using LDA [281], PBE [279] and PBE0 [280] functionals, as well as a dielectric-dependent hybrid (DDH) functional for solids [346].

A recent study of Thygesen and co-workers [325] reported basis set convergence issues when performing $G_0W_0\Gamma_0$@LDA calculations, which could be overcome by applying a proper renormalization to the short-range component of $f_{\rm xc}$ [268, 269, 277]. In our work we generalized the renormalization scheme of Thygesen *et al.* to functionals other than LDA, and we show that the convergence of $G_0W_0\Gamma_0$ quasiparticle energies is significantly improved using the renormalized $f_{\rm xc}$.

The rest of the paper is organized as follows. In Section 2 we describe the finite-field approach and benchmark its accuracy. In Section 3 we describe the formalism used to perform GW calculations beyond the RPA, including a renormalization scheme for $f_{\rm xc}$, and we compare the quasiparticle energies obtained from different GW approximations (RPA or

vertex-corrected) for molecules in the GW100 test set [378] and for several solids. Finally, we summarize our results in Section 4.

3.1.2 The finite-field approach

We first describe the FF approach for iterative diagonalization of density response functions and we then discuss its robustness and accuracy.

Formalism

Our G_0W_0 calculations are based on DFT single-particle energies and wavefunctions, obtained by solving the Kohn-Sham (KS) equations:

$$H_{\rm KS}\psi_m(\boldsymbol{r}) = \varepsilon_m\psi_m(\boldsymbol{r}), \tag{3.1}$$

where the KS Hamiltonian $H_{\rm KS} = T + V_{\rm SCF} = T + V_{\rm ion} + V_{\rm H} + V_{\rm xc}$. T is the kinetic energy operator; $V_{\rm SCF}$ is the KS potential that includes the ionic $V_{\rm ion}$, the Hartree $V_{\rm H}$ and the exchange-correlation potential $V_{\rm xc}$. The charge density is given by $n(\boldsymbol{r}) = \sum_m^{\rm occ.} |\psi_m(\boldsymbol{r})|^2$. For simplicity we omitted the spin index.

We consider the density response function (polarizability) of the KS system $\chi_0(\boldsymbol{r}, \boldsymbol{r'})$ and that of the physical system $\chi(\boldsymbol{r}, \boldsymbol{r'})$; the latter is denoted as $\chi_{\rm RPA}(\boldsymbol{r}, \boldsymbol{r'})$ when the random phase approximation (RPA) is used. The variation of the charge density due to either a variation of the KS potential $\delta V_{\rm SCF}$ or the external potential $\delta V_{\rm ext}$ is given by:

$$\delta n(\boldsymbol{r}) = \int K(\boldsymbol{r}, \boldsymbol{r'})\delta V(\boldsymbol{r'})d\boldsymbol{r'}, \tag{3.2}$$

where $K = \chi_0(\boldsymbol{r}, \boldsymbol{r'})$ if $\delta V(\boldsymbol{r'}) = \delta V_{\rm SCF}(\boldsymbol{r'})$ and $K = \chi(\boldsymbol{r}, \boldsymbol{r'})$ if $\delta V(\boldsymbol{r'}) = \delta V_{\rm ext}(\boldsymbol{r'})$. The density response functions of the KS and physical system are related by a Dyson-like equa-

tion:

$$\chi(\boldsymbol{r},\boldsymbol{r'}) = \chi_0(\boldsymbol{r},\boldsymbol{r'}) + \int d\boldsymbol{r''} \int d\boldsymbol{r'''} \chi_0(\boldsymbol{r},\boldsymbol{r''}) \left[v_{\mathrm{c}}(\boldsymbol{r''},\boldsymbol{r'''}) + f_{\mathrm{xc}}(\boldsymbol{r''},\boldsymbol{r'''}) \right] \chi(\boldsymbol{r'''},\boldsymbol{r'}) \quad (3.3)$$

where $v_{\mathrm{c}}(\boldsymbol{r},\boldsymbol{r'}) = \frac{1}{|\boldsymbol{r}-\boldsymbol{r'}|}$ is the Coulomb kernel and $f_{\mathrm{xc}}(\boldsymbol{r},\boldsymbol{r'}) = \frac{\delta V_{\mathrm{xc}}(\boldsymbol{r})}{\delta n(\boldsymbol{r'})}$ is the exchange-correlation kernel.

Within the RPA, f_{xc} is neglected and $\chi(\boldsymbol{r},\boldsymbol{r'})$ is approximated by:

$$\chi_{\mathrm{RPA}}(\boldsymbol{r},\boldsymbol{r'}) = \chi_0(\boldsymbol{r},\boldsymbol{r'}) + \int d\boldsymbol{r''} \int d\boldsymbol{r'''} \chi_0(\boldsymbol{r},\boldsymbol{r''}) v_{\mathrm{c}}(\boldsymbol{r''},\boldsymbol{r'''}) \chi(\boldsymbol{r'''},\boldsymbol{r'}). \quad (3.4)$$

In the plane-wave representation (for simplicity we only focus on the Γ point of the Brillouin zone), $v_{\mathrm{c}}(\boldsymbol{G},\boldsymbol{G'}) = \frac{4\pi\delta(\boldsymbol{G},\boldsymbol{G'})}{|\boldsymbol{G}|^2}$ (abbreviated as $v_{\mathrm{c}}(\boldsymbol{G}) = \frac{4\pi}{|\boldsymbol{G}|^2}$). We use $K(\boldsymbol{G},\boldsymbol{G'})$ to denote a general response function ($K \in \{\chi_0, \chi_{\mathrm{RPA}}, \chi\}$), and define the dimensionless response function $\tilde{K}(\boldsymbol{G},\boldsymbol{G'})$ ($\tilde{K} \in \{\tilde{\chi}_0, \tilde{\chi}_{\mathrm{RPA}}, \tilde{\chi}\}$) by symmetrizing $K(\boldsymbol{G},\boldsymbol{G'})$ with respect to v_{c}:

$$\tilde{K}(\boldsymbol{G},\boldsymbol{G'}) = v_{\mathrm{c}}^{\frac{1}{2}}(\boldsymbol{G}) K(\boldsymbol{G},\boldsymbol{G'}) v_{\mathrm{c}}^{\frac{1}{2}}(\boldsymbol{G'}). \quad (3.5)$$

The dimensionless response functions $\tilde{\chi}_{\mathrm{RPA}}$ and $\tilde{\chi}_0$ (see Eq. 3.4) have the same eigenvectors, and their eigenvalues are related by:

$$\lambda_i^{\mathrm{RPA}} = \frac{\lambda_i^0}{1-\lambda_i^0} \quad (3.6)$$

where λ_i^{RPA} and λ_i^0 are eigenvalues of $\tilde{\chi}_{\mathrm{RPA}}$ and $\tilde{\chi}_0$, respectively. In general the eiegenvalues and eigenvectors of $\tilde{\chi}_{\mathrm{RPA}}$ are different from those of $\tilde{\chi}$ due to the presence of f_{xc} in Eq. 3.3.

In our GW calculations we use a low rank decomposition of $\tilde{K}$:

$$\tilde{K} = \sum_i^{N_{\mathrm{PDEP}}} \lambda_i \left|\xi_i\right\rangle \left\langle\xi_i\right| \quad (3.7)$$

where λ and $|\xi\rangle$ denote eigenvalue and eigenvectors of $\tilde{K}$, respectively. The set of ξ constitute

a projective dielectric eigenpotential (PDEP) basis [260, 286, 117], and the accuracy of the low rank decomposition is controlled by N_{PDEP}, the size of the basis. In the limit of $N_{\mathrm{PDEP}} = N_{\mathrm{PW}}$ (the number of plane waves), the PDEP basis and the plane wave basis are related by a unitary transformation. In practical calculations it was shown that [260, 286] one only need $N_{\mathrm{PDEP}} \ll N_{\mathrm{PW}}$ to converge the computed quasiparticle energies. To obtain the PDEP basis, an iterative diagonalization is performed for $\tilde{K}$, e.g. with the Davidson algorithm [66]. The iterative diagonalization requires evaluating the action of $\tilde{K}$ on an arbitrary trial function ξ:

$$\begin{aligned}(\tilde{K}\xi)(\boldsymbol{G}) &= \sum_{\boldsymbol{G'}} v_c^{\frac{1}{2}}(\boldsymbol{G}) K(\boldsymbol{G}, \boldsymbol{G'}) v_c^{\frac{1}{2}}(\boldsymbol{G'}) \xi(\boldsymbol{G'}) \\ &= v_c^{\frac{1}{2}}(\boldsymbol{G}) \mathcal{FT} \left\{ \int K(\boldsymbol{r}, \boldsymbol{r'}) \left(\mathcal{FT}^{-1} \left[v_c^{\frac{1}{2}}(\boldsymbol{G'}) \xi(\boldsymbol{G'}) \right] \right) (\boldsymbol{r'}) d\boldsymbol{r'} \right\} (\boldsymbol{G})\end{aligned} \tag{3.8}$$

where $\mathcal{FT}$ and $\mathcal{FT}^{-1}$ denote forward and inverse Fourier transforms respectively. By using Eq. 3.8 we cast the evaluation of $\tilde{K}\xi$ to an integral in real space.

Defining a perturbation $\delta V(\boldsymbol{G'}) = v_c^{\frac{1}{2}}(\boldsymbol{G'}) \xi(\boldsymbol{G'})$, the calculation of the real space integral in Eq. 3.8 is equivalent to solving for the variation of the charge density δn due to δV:

$$\int K(\boldsymbol{r}, \boldsymbol{r'}) \left(\mathcal{FT}^{-1} \left[v_c^{\frac{1}{2}}(\boldsymbol{G'}) \xi(\boldsymbol{G'}) \right] \right) (\boldsymbol{r'}) d\boldsymbol{r'} = \int K(\boldsymbol{r}, \boldsymbol{r'}) \delta V(\boldsymbol{r'}) d\boldsymbol{r'} \equiv \delta n(\boldsymbol{r}). \tag{3.9}$$

In previous works $\delta n(\boldsymbol{r})$ was obtained using DFPT for the case of $K = \chi_0$ [117]. In this work we solve Eq. 3.9 by a finite-field approach. In particular, we perform two SCF calculations under the action of the potentials $\pm\delta V$:

$$(H_{\mathrm{KS}} \pm \delta V) \psi_m^{\pm}(\boldsymbol{r}) = \varepsilon_m^{\pm} \psi_m^{\pm}(\boldsymbol{r}), \tag{3.10}$$

and $\delta n(\boldsymbol{r})$ is computed through a finite difference:

$$\delta n(\boldsymbol{r}) = \frac{1}{2}\left[\sum_{m}^{\text{occ.}} \left|\psi_m^+(\boldsymbol{r})\right|^2 - \sum_{m}^{\text{occ.}} \left|\psi_m^-(\boldsymbol{r})\right|^2\right] \tag{3.11}$$

In Eq. 3.11 we use a central difference instead of forward/backward difference to increase the numerical accuracy of the computed $\delta n(\boldsymbol{r})$.

If in the SCF procedure adopted in Eq. 3.10 all potential terms in the KS Hamiltonian are computed self-consistently, then the solution of Eq. 3.11 yields $K = \chi$ (see Eq. 3.9). If V_{xc} is evaluated for the initial charge density (i.e. $V_{\text{xc}} = V_{\text{xc}}[n_0]$) and kept fixed during the SCF iterations, then the solution of Eq. 3.11 yields $K = \chi_{\text{RPA}}$. If both V_{xc} and V_{H} are kept fixed, the solution of Eq. 3.11 yields $K = \chi_0$.

Unlike DFPT, the finite-field approach adopted here allows for the straightforward calculation of response functions beyond the RPA (i.e. for the calculation of χ instead of χ_0 or χ_{RPA}), and it can be readily applied to hybrid functionals for which analytical expressions of f_{xc} are not available. We note that finite-field calculations with hybrid functionals can easily benefit from any methodological development that reduces the computational complexity of evaluating exact exchange potentials [125, 127, 68].

Once the PDEP basis is obtained by iterative diagonalization of $\tilde{\chi}_0$, the projection of $\tilde{\chi}$ on the PDEP basis can also be performed using the finite-field approach. Then the symmetrized exchange-correlation kernel $\tilde{f}_{\text{xc}} = v_{\text{c}}^{-\frac{1}{2}} f_{\text{xc}} v_{\text{c}}^{-\frac{1}{2}}$ can be computed by inverting the Dyson-like equation (Eq. 3.3):

$$\tilde{f}_{\text{xc}} = \tilde{\chi}_0^{-1} - \tilde{\chi}^{-1} - 1. \tag{3.12}$$

On the right hand side of Eq. 3.12 all matrices are $N_{\text{PDEP}} \times N_{\text{PDEP}}$ and therefore the resulting $\tilde{f}_{\text{xc}}$ is also defined on the PDEP basis.

When using orbital-dependent functionals such as meta-GGA and hybrid functionals, the $\tilde{f}_{\text{xc}}$ computed from Eq. 3.12 should be interpreted with caution. In this case, DFT calculations for $H_{\text{KS}} \pm \delta V$ can be performed using either the optimized effective potential

(OEP) or the generalized Kohn-Sham (GKS) scheme. In the OEP scheme, v_{xc} is local in space and $f_{\mathrm{xc}}(\boldsymbol{r}, \boldsymbol{r'}) = \frac{\delta V_{\mathrm{xc}}(\boldsymbol{r})}{\delta n(\boldsymbol{r'})}$ depends on $\boldsymbol{r}$ and $\boldsymbol{r'}$, as in the case of semilocal functionals. In the GKS scheme, V_{xc} is non-local and $f_{\mathrm{xc}}(\boldsymbol{r}, \boldsymbol{r'}; \boldsymbol{r''}) = \frac{\delta V_{\mathrm{xc}}(\boldsymbol{r}, \boldsymbol{r'})}{\delta n(\boldsymbol{r''})}$ depends on three position vectors. We expect δn to be almost independent of the chosen scheme, whether GKS or OEP, since both methods yield the same result within first order in the charge density [200]. We conducted hybrid functional calculations within the GKS scheme, assuming that for every GKS calculation an OEP can be defined yielding the same charge density; with this assumption the f_{xc} from Eq. 3.12 is well defined within the OEP formalism.

Implementation and Verification

We implemented the finite-field algorithm described above by coupling the WEST [117] and Qbox [124] codes in client-server mode, using the workflow summarized in Fig. 3.1. In particular, in our implementation the WEST code performs an iterative diagonalization of $\tilde{K}$ by outsourcing the evaluation of the action of $\tilde{K}$ on an arbitrary function to Qbox, which performs DFT calculations in finite field. The two codes communicate through the filesystem.

To verify the correctness of our implementation, we computed $\tilde{\chi}_0$, $\tilde{\chi}^{\mathrm{RPA}}$, $\tilde{\chi}$ for selected molecules in the GW100 set and we compared the results to those obtained with DFPT. Section 3.1.4 summarizes the parameters used including plane wave cutoff E_{cut}, N_{PDEP} and size of the simulation cell. In finite-field calculations we optimized the ground state wavefunction using a preconditioned steepest descent algorithm with Anderson acceleration[7]. The magnitude of δV was chosen to insure that calculations were performed within the linear response regime (see Section 3.1.4). All calculations presented in this section were performed with the PBE functional unless otherwise specified.

Fig. 3.2a shows the eigenvalues of $\tilde{\chi}_{\mathrm{RPA}}$ for a few molecules obtained with three approaches: iterative diagonalization of $\tilde{\chi}_{\mathrm{RPA}}$ with the finite-field approach; iterative diagonalization of $\tilde{\chi}_0$ with either the finite-field approach or with DFPT, followed by a transformation

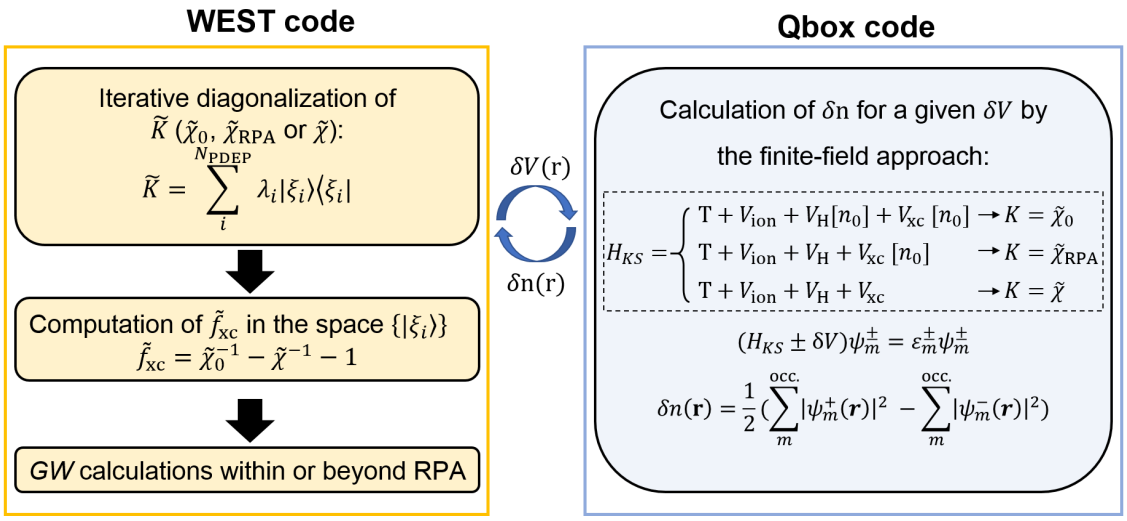

Figure 3.1: Workflow of finite-field calculations. The WEST code performs an iterative diagonalization of $\tilde{K}$ ($\tilde{\chi}_0$, $\tilde{\chi}_{\mathrm{RPA}}$, $\tilde{\chi}$). In GW calculations beyond the RPA, $\tilde{f}_{\mathrm{xc}}$ is computed from Eq. 3.12, which requires computing the spectral decomposition of $\tilde{\chi}_0$ and evaluating $\tilde{\chi}$ in the space of $\tilde{\chi}_0$ eigenvectors. Finite-field calculations are carried out by the Qbox code. If the Hartree (V_{H}) and exchange correlation potential (V_{xc}) are updated self-consistently when solving Eq. 3.10, one obtains $K = \chi$; if V_{xc} is evaluated at the initial charge density n_0 and kept fixed during the SCF procedure, one obtains $K = \chi_{\mathrm{RPA}}$; if both V_{xc} and V_{H} are evaluated for n_0 and kept fixed, one obtains $K = \chi_0$. The communications of δn and δV between WEST and Qbox is carried through the filesystem.

of eigenvalues as in Eq. 3.6. The three approaches yield almost identical eigenvalues.

The eigenvectors of the response functions are shown in Fig. 3.2b, where we report elements of the matrices defined by the overlap between finite-field and DFPT eigenvectors. The inner product matrices are block-diagonal, with blocks corresponding to the presence of degenerate eigenvalues. The agreement between eigenvalues and eigenvectors shown in Fig. 3.2 verifies the accuracy and robustness of finite-field calculations.

Fig. 3.3 shows the eigendecomposition of $\tilde{\chi}$ compared to that of $\tilde{\chi}_{\mathrm{RPA}}$.

As indicated by Fig. 3.3a, including f_{xc} in the evaluation of χ results in a stronger screening. The eigenvalues of $\tilde{\chi}$ are systematically more negative than those of $\tilde{\chi}_{\mathrm{RPA}}$, though they asymptotically converge to zero in the same manner. While the eigenvalues are different, the eigenvectors (eigenspaces in the case of degenerate eigenvalues) are almost identical, as indicated by the block-diagonal form of the eigenvector overlap matrices (see Fig. 3.3b).

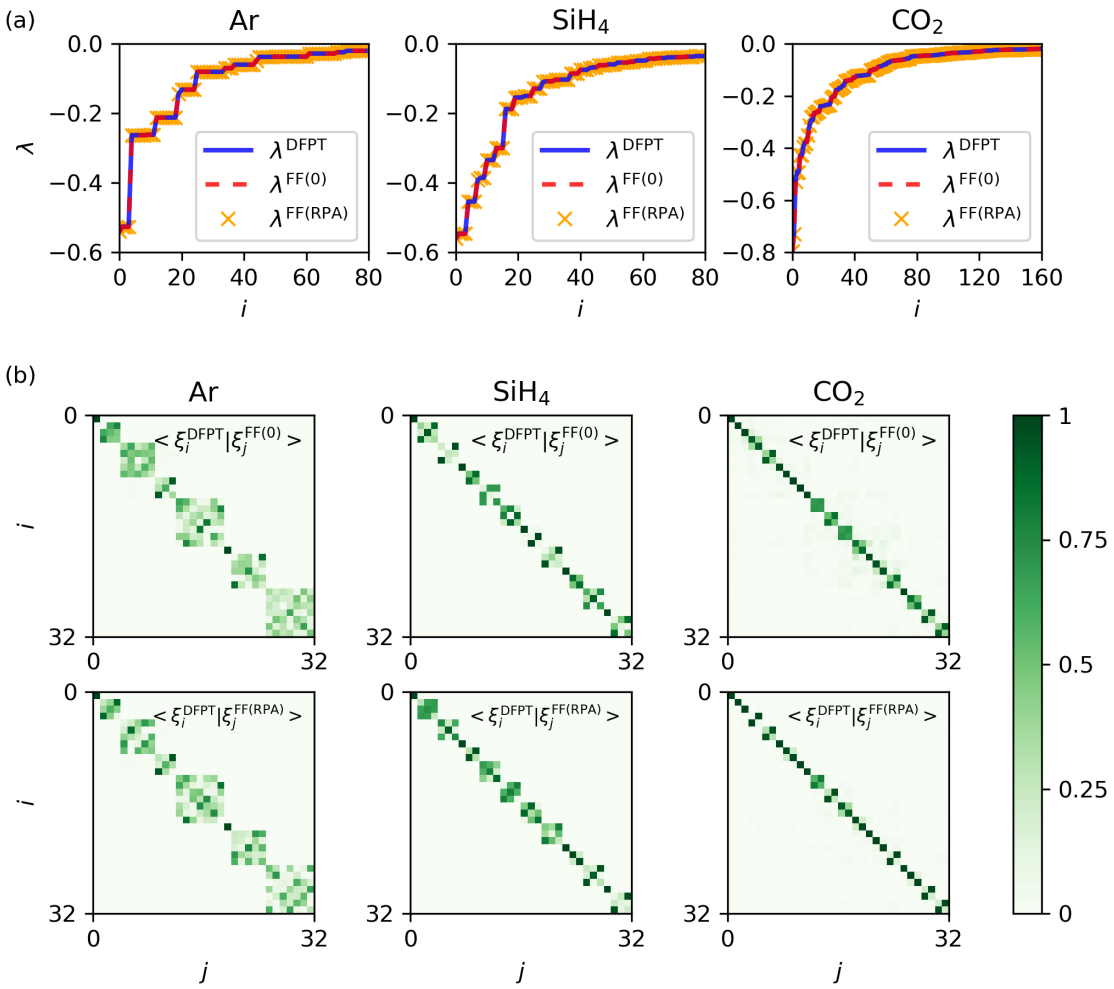

Figure 3.2: Comparison of the eigenvalues(a) and eigenfunctions(b) of $\tilde{\chi}_{\mathrm{RPA}}$ obtained from density functional perturbation theory (DFPT) and finite-field (FF) calculations. Three approaches are used: diagonalization of $\tilde{\chi}_0$ by DFPT, diagonalization of $\tilde{\chi}_0$ by FF (denoted by FF(0)) and diagonalization of $\tilde{\chi}_{\mathrm{RPA}}$ by FF (denoted by FF(RPA)). In the case of DFPT and FF(0), Eq. 3.6 was used to obtain the eigenvalues of $\tilde{\chi}_{\mathrm{RPA}}$ from those of $\tilde{\chi}_0$. In (b) we show the first 32×32 elements of the $\langle \xi^{\mathrm{DFPT}} | \xi^{\mathrm{FF(0)}} \rangle$ and $\langle \xi^{\mathrm{DFPT}} | \xi^{\mathrm{FF(RPA)}} \rangle$ matrices (see Eq. 3.7).

Finally, $\tilde{f}_{\mathrm{xc}}$ can be computed from $\tilde{\chi}$ and $\tilde{\chi}_0$ according to Eq. 3.12. Due to the similarity of the eigenvectors of $\tilde{\chi}$ and $\tilde{\chi}_{\mathrm{RPA}}$ (identical to that of $\tilde{\chi}_0$), the $\tilde{f}_{\mathrm{xc}}$ matrix is almost diagonal. In Section 3.1.4 we show the $\tilde{f}_{\mathrm{xc}}$ matrix in the PDEP basis for a few systems. To verify the accuracy of $\tilde{f}_{\mathrm{xc}}$ obtained by the finite-field approach, we performed calculations with the LDA functional, for which f_{xc} can be computed analytically. In Fig. 3.4 we present for a number of systems the average relative difference of the diagonal terms of the $\tilde{f}_{\mathrm{xc}}$ matrices

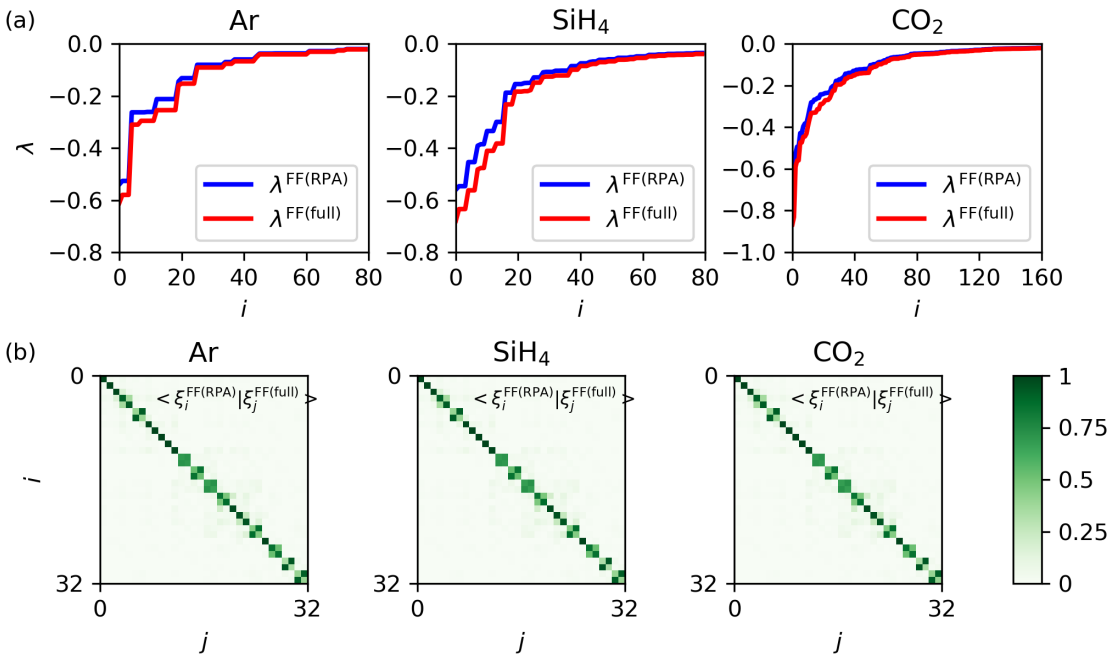

Figure 3.3: Comparison of eigenvalues(a) and eigenfunctions(b) of $\tilde{\chi}$ and $\tilde{\chi}_{\mathrm{RPA}}$ obtained from finite-field calculations. In (b), the first 32×32 elements of the $\langle \xi^{\mathrm{RPA}} | \xi^{\mathrm{full}} \rangle$ matrices are presented.

obtained analytically and through finite-field (FF) calculations. We define Δf_{xc} as

$$\Delta f_{\mathrm{xc}} = \frac{1}{N_{\mathrm{PDEP}}} \sum_{i}^{N_{\mathrm{PDEP}}} \frac{\left| \langle \xi_i | \tilde{f}_{\mathrm{xc}}^{\mathrm{FF}} | \xi_i \rangle - \langle \xi_i | \tilde{f}_{\mathrm{xc}}^{\mathrm{analytical}} | \xi_i \rangle \right|}{\left| \langle \xi_i | \tilde{f}_{\mathrm{xc}}^{\mathrm{analytical}} | \xi_i \rangle \right|}. \tag{3.13}$$

As shown in Fig. 3.4, Δf_{xc} is smaller than a few percent for all systems studied here. To further quantify the effect of the small difference found for the $\tilde{f}_{\mathrm{xc}}$ matrices on GW quasiparticle energies, we performed $G_0W_0^{f_{\mathrm{xc}}}$@LDA calculations for all the systems shown in Fig. 3.4, using the analytical f_{xc} and f_{xc} computed from finite-field calculations. The two approaches yielded almost identical quasiparticle energies, with mean absolute deviations of 0.04 and 0.004 eV for HOMO and LUMO levels, respectively.

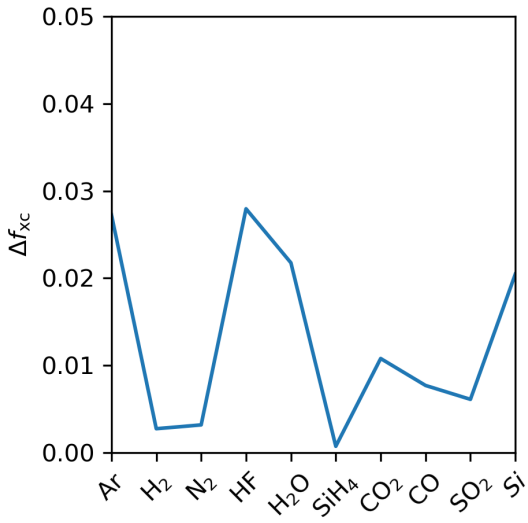

Figure 3.4: Average relative differences Δf_{xc} (see Eq. 3.13) between diagonal elements of the $\tilde{f}_{\mathrm{xc}}$ matrices computed analytically and numerically with the finite-field approach. Calculations were performed with the LDA functional.

3.1.3 GW calculations

Formalism

In this section we discuss GW calculations within and beyond the RPA, utilizing f_{xc} computed with the finite-field approach. In the following equations we use 1, 2, ... as shorthand notations for $(\boldsymbol{r}_1, t_1)$, $(\boldsymbol{r}_2, t_2)$, ... Indices with bars are integrated over. When no indices are shown, the equation is a matrix equation in reciprocal space or in the PDEP basis. The following discussion focuses on finite systems; for periodic systems a special treatment of the long-range limit of χ is required and relevant formulae are presented in Section 3.1.4.

Based on a KS reference system, the Hedin equations [133] relate the exchange-correlation self-energy Σ_{xc} (abbreviated as Σ), Green's function G, the screened Coulomb interaction W, the vertex Γ and the irreducible polarizability P:

$$\Sigma(1,2) = iG(1,\bar{4})W(1^+,\bar{3})\Gamma(\bar{4},2;\bar{3}), \tag{3.14}$$

$$W(1,2) = v_{\rm c}(1,2) + v_{\rm c}(1,\bar{3})P(\bar{3},\bar{4})W(\bar{4},2), \tag{3.15}$$

$$P(1,2) = -iG(1,\bar{3})G(\bar{4},1)\Gamma(\bar{3},\bar{4},2), \tag{3.16}$$

$$\Gamma(1,2;3) = \delta(1,2)\delta(1,3) + \frac{\delta\Sigma(1,2)}{\delta G(\bar{4},\bar{5})}G(\bar{4},\bar{6})G(\bar{7},\bar{5})\Gamma(\bar{6},\bar{7},3), \tag{3.17}$$

$$G(1,2) = G^0(1,2) + G^0(1,\bar{3})\Sigma(\bar{3},\bar{4})G(\bar{4},2). \tag{3.18}$$

We consider three different G_0W_0 approximations: the first is the common G_0W_0 formulation within the RPA, here denoted as $G_0W_0^{\rm RPA}$, where $\Gamma(1,2;3) = \delta(1,2)\delta(1,3)$ and Σ is given by:

$$\Sigma(1,2) = iG(1,2)W_{\rm RPA}(1^+,2), \tag{3.19}$$

where

$$W_{\rm RPA}(1,2) = v_{\rm c}(1,2) + v_{\rm c}(1,\bar{3})\chi_{\rm RPA}(\bar{3},\bar{4})v_{\rm c}(\bar{4},2), \tag{3.20}$$

and

$$\chi_{\rm RPA} = (1 - \chi_0 v_{\rm c})^{-1}\chi_0. \tag{3.21}$$

The second approximation, denoted as $G_0W_0^{f_{\rm xc}}$, includes $f_{\rm xc}$ in the definition of W. Specifically, χ is computed from χ_0 and $f_{\rm xc}$ with Eq. 3.3:

$$\chi = (1 - \chi_0(v_c + f_{\rm xc}))^{-1}\chi_0, \tag{3.22}$$

and is used to construct the screened Coulomb interaction beyond the RPA:

$$W_{f_{\rm xc}} = v_{\rm c}(1,2) + v_{\rm c}(1,\bar{3})\chi(\bar{3},\bar{4})v_{\rm c}(\bar{4},2). \tag{3.23}$$

The third approximation, denoted as $G_0W_0\Gamma_0$, includes $f_{\rm xc}$ in both W and Σ. In particular, an initial guess for Σ is constructed from $V_{\rm xc}$:

$$\Sigma_0(1,2) = \delta(1,2)V_{\rm xc}(1) \tag{3.24}$$

from which one can obtain a zeroth order vertex function by iterating Hedin's equations once [350]:

$$\Gamma_0(1,2;3) = \delta(1,2)(1 - f_{\rm xc}\chi_0)^{-1}(1,3). \tag{3.25}$$

Then the self-energy Σ is constructed using G, $W_{f_{\rm xc}}$ and Γ_0:

$$\begin{aligned}\Sigma(1,2) &= iG(1,\bar{4})W_{f_{\rm xc}}(1^+,\bar{3})\Gamma_0(\bar{4},2;\bar{3}) \\ &= iG(1,2)W_\Gamma(1^+,\bar{3})\end{aligned} \tag{3.26}$$

where we defined an effective screened Coulomb interaction

$$W_\Gamma = v_{\rm c}(1,2) + v_{\rm c}(1,\bar{3})\chi_\Gamma(\bar{3},\bar{4})v_{\rm c}(\bar{4},2), \tag{3.27}$$

$$\chi_\Gamma = [v_{\rm c} - v_{\rm c}\chi_0(v_{\rm c} + f_{\rm xc})]^{-1} - v_{\rm c}^{-1}. \tag{3.28}$$

The symmetrized forms of the three different density response functions (reducible polarizabilities) defined in Eq. 3.21, 3.22, 3.28 are:

$$\tilde{\chi}_{\rm RPA} = [1 - \tilde{\chi}_0]^{-1}\tilde{\chi}_0 \tag{3.29}$$

$$\tilde{\chi} = [1 - \tilde{\chi}_0(1 + \tilde{f}_{\rm xc})]^{-1}\tilde{\chi}_0 \tag{3.30}$$

$$\tilde{\chi}_\Gamma = [1 - \tilde{\chi}_0(1 + \tilde{f}_{\rm xc})]^{-1} - 1 \tag{3.31}$$

Eqs. 3.29-3.31 have been implemented in the WEST code [117].

We note that finite-field calculations yield $\tilde{f}_{\rm xc}$ matrices at zero frequency. Hence the results presented here correspond to calculations performed within the adiabatic approximation, as they neglect the frequency dependence of $\tilde{f}_{\rm xc}$. An interesting future direction would be to compute frequency-dependent $\tilde{f}_{\rm xc}$ by performing finite-field calculations using

real-time time-dependent DFT (RT-TDDFT).

When using the $G_0W_0\Gamma_0$ formalism, the convergence of quasiparticle energies with respect to N_{PDEP} turned out to be extremely challenging. As discussed in Ref.325 the convergence problem originates from the incorrect short-range behavior of $\tilde{f}_{\mathrm{xc}}$. In Section 3.2 below we describe a renormalization scheme of $\tilde{f}_{\mathrm{xc}}$ that improves the convergence of $G_0W_0\Gamma_0$ results.

Renormalization of f_{xc}

Thygesen and co-workers [325] showed that $G_0W_0\Gamma_0$@LDA calculations with f_{xc} computed at the LDA level exhibit poor convergence with respect to the number of unoccupied states and plane wave cutoff. We observed related convergence problems of $G_0W_0\Gamma_0$ quasiparticle energies as a function of N_{PDEP}, the size of the basis set used here to represent response functions (see Section 3.1.4). In this section we describe a generalization of the f_{xc} renormalization scheme proposed by Thygesen and co-workers [268, 269, 277] to overcome convergence issues.

The approach of Ref.325 is based on the properties of the homogeneous electron gas (HEG). For an HEG with density n, $f_{\mathrm{xc}}^{\mathrm{HEG}}[n](\boldsymbol{r},\boldsymbol{r'})$ depends only on $(\boldsymbol{r}-\boldsymbol{r'})$ due to translational invariance, and therefore $f_{\mathrm{xc}}^{\mathrm{HEG}}[n]_{\boldsymbol{GG'}}(\boldsymbol{q})$ is diagonal in reciprocal space. We denote the diagonal elements of $f_{\mathrm{xc}}^{\mathrm{HEG}}[n]_{\boldsymbol{GG'}}(\boldsymbol{q})$ as $f_{\mathrm{xc}}^{\mathrm{HEG}}[n](\boldsymbol{k})$ where $\boldsymbol{k}=\boldsymbol{q}+\boldsymbol{G}$. When using the LDA functional, the exchange kernel f_x exactly cancels the Coulomb interaction v_c at wavevector $k=2k_F$ (the correlation kernel f_c is small compared to f_{x} for $k\geq 2k_F$), where k_F is the Fermi wavevector. For $k\geq 2k_F$, $f_{\mathrm{xc}}^{\text{HEG-LDA}}$ shows an incorrect asymptotic behavior, leading to an unphysical correlation hole [268, 269]. Hence Thygesen and co-workers introduced a renormalized LDA kernel $f_{\mathrm{xc}}^{\text{HEG-rLDA}}(k)$ by setting $f_{\mathrm{xc}}^{\text{HEG-rLDA}}(k)=f_{\mathrm{xc}}^{\text{HEG-LDA}}(k)$ for $k\leq 2k_F$ and $f_{\mathrm{xc}}^{\text{HEG-rLDA}}(k)=-v_c(k)$ for $k>2k_F$. They demonstrated that the renormalized f_{xc} improves the description of the short-range correlation hole as well as the correlation energy, and when applied to GW calculations substantially accelerates the basis set convergence of $G_0W_0\Gamma_0$ quasiparticle energies.

While within LDA $f_{\rm xc}$ can be computed analytically and $v_c + f_{\rm x} = 0$ at exactly $k = 2k_F$, for a general functional it is not known *a priori* at which k this condition is satisfied. In addition, for inhomogenous systems such as molecules and solids the $f_{\rm xc}$ matrix is not diagonal in reciprocal space. The authors of Ref 325 used a wavevector symmetrization approach to evaluate $f_{\rm xc}^{\text{HEG-rLDA}}$ for inhomogenous systems, which is not easily generalizable to the formalism adopted in this work, where $f_{\rm xc}$ is represented in the PDEP basis.

To overcome these difficulties, here we first diagonalize the $\tilde{f}_{\rm xc}$ matrix in the PDEP basis:

$$\tilde{f}_{\rm xc} = \sum_{i}^{N_{\rm PDEP}} f_i \left|\zeta_i\right\rangle \left\langle\zeta_i\right|, \tag{3.32}$$

where f and ζ are eigenvalues and eigenvectors of $\tilde{f}_{\rm xc}$. Then we define a renormalized $\tilde{f}_{\rm xc}$ as:

$$\tilde{f}_{\rm xc}^{r} = \sum_{i}^{N_{\rm PDEP}} \max(f_i, -1) \left|\zeta_i\right\rangle \left\langle\zeta_i\right|. \tag{3.33}$$

Note that for $\tilde{f}_{\rm xc} = -1$, $f_{\rm xc} = -v_c$, therefore $f_{\rm xc}^{r}$ is strictly greater or equal to $-v_c$. When applied to the HEG, the $f_{\rm xc}^{r}$@LDA is equivalent to $f_{\rm xc}^{\text{HEG-rLDA}}$ in the limit $N_{\rm PDEP} \to \infty$, where the PDEP and plane-wave basis are related by a unitary transformation. Thus, Eq. 3.33 represents a generalization of the scheme of Thygesen *et al.* to any functional and to inhomogeneous electron gases. When using $f_{\rm xc}^{r}$, we observed a faster basis set convergence of $G_0W_0\Gamma_0$ results than $G_0W_0^{\rm RPA}$ results, consistent with Ref. 325. In Section 3.1.4 we discuss in detail the effect of the $f_{\rm xc}$ renormalization on the description of the density response functions χ and χ_Γ, and we rationalize why the renormalization improves the convergence of $G_0W_0\Gamma_0$ results. Here we only mention that the response function $\tilde{\chi}_\Gamma$ may possess positive eigenvalues for large PDEP indices. When the renormalized $f_{\rm xc}$ is used, the eigenvalues of $\tilde{\chi}_\Gamma$ are guaranteed to be nonpositive and they decay rapidly toward zero as the PDEP index increase, which explains the improved convergence of $G_0W_0\Gamma_0$ quasiparticle energies.

All $G_0W_0\Gamma_0$ results shown in Section 3.3 were obtained with renormalized $f_{\rm xc}$ matrices,

while $G_0W_0^{f_{\rm xc}}$ calculations were performed without renormalizing $f_{\rm xc}$, since we found that the renormalization had a negligible effect on $G_0W_0^{f_{\rm xc}}$ quasiparticle energies (see Section 3.1.4).

Results

In this section we report *GW* quasiparticle energies for molecules in the GW100 set [378] and for several solids. Calculations are performed at $G_0W_0^{\rm RPA}$, $G_0W_0^{f_{\rm xc}}$ and $G_0W_0\Gamma_0$ levels of theory and with semilocal and hybrid functionals. Computational parameters including $E_{\rm cut}$ and $N_{\rm PDEP}$ for all calculations are summarized in Section 3.1.4. A discussion of the convergence of $G_0W_0^{\rm RPA}$ quasiparticle energies with respect to these parameters can be found in Ref.118.

We computed the vertical ionization potential (VIP), vertical electron affinity (VEA) and fundamental gaps for molecules with LDA, PBE and PBE0 functionals. VIP and VEA are defined as VIP $= \varepsilon^{\rm vac} - \varepsilon^{\rm HOMO}$ and VEA $= \varepsilon^{\rm vac} - \varepsilon^{\rm LUMO}$ respectively, where $\varepsilon^{\rm vac}$ is the vacuum level estimated with the Makov-Payne method [227]; $\varepsilon^{\rm HOMO}$ and $\varepsilon^{\rm LUMO}$ are HOMO and LUMO *GW* quasiparticle energies, respectively. The results are summarized in Fig. 3.5, where VIP and VEA computed at $G_0W_0^{f_{\rm xc}}$ and $G_0W_0\Gamma_0$ levels are compared to results obtained at the $G_0W_0^{\rm RPA}$ level.

Compared to $G_0W_0^{\rm RPA}$ results, the VIP computed at the $G_0W_0^{f_{\rm xc}}$ and $G_0W_0\Gamma_0$ level are systematically lower, the VEA computed at the $G_0W_0^{f_{\rm xc}}/G_0W_0\Gamma_0$ level are systematically higher/lower. The deviation of $G_0W_0\Gamma_0$ from $G_0W_0^{\rm RPA}$ results is more than twice as large as that of $G_0W_0^{f_{\rm xc}}$ results.

In Fig. 3.6 we compare *GW* results with experiments and quantum chemistry CCSD(T) results [195]. The corresponding MD and mean absolute deviations (MAD) are summarized in Table 3.1. At the $G_0W_0^{\rm RPA}$@PBE level, the MAD for the computed VIP values compared to CCSD(T) and experimental results are 0.50 and 0.55 eV respectively, and the MAD for the computed VEA compared to experiments is 0.46 eV. These MAD values (0.50/0.55/0.46

eV) are comparable to previous benchmark studies on the GW100 set using the FHI-aims (0.41/0.46/0.45 eV) [378], VASP (0.44/0.49/0.42 eV) [226] and WEST codes (0.42/0.46/0.42 eV) [118], although in this work we did not extrapolate our results with respect to the basis set due to the high computational cost.

Table 3.1: Mean deviation and mean absolute deviation (in brackets) for *GW* results compared to experimental results and CCSD(T) calculations. We report vertical ionization potentials (VIP), vertical electron affinities (VEA) and the fundamental electronic gaps. All values are given in eV.

	CCSD(T) VIP	Exp. VIP	Exp. VEA	Exp. Gap
$G_0W_0^{\mathrm{RPA}}$@LDA	-0.23 (0.34)	-0.19 (0.43)	0.04 (0.45)	0.21 (0.56)
$G_0W_0^{\mathrm{fxc}}$@LDA	-0.39 (0.48)	-0.35 (0.53)	0.21 (0.51)	0.50 (0.69)
$G_0W_0\Gamma_0$@LDA	-0.58 (0.62)	-0.54 (0.63)	-0.49 (0.59)	0.04 (0.53)
$G_0W_0^{\mathrm{RPA}}$@PBE	-0.43 (0.50)	-0.39 (0.55)	-0.09 (0.46)	0.28 (0.57)
$G_0W_0^{\mathrm{fxc}}$@PBE	-0.56 (0.62)	-0.52 (0.65)	0.08 (0.49)	0.56 (0.75)
$G_0W_0\Gamma_0$@PBE	-0.99 (1.01)	-0.95 (0.98)	-0.77 (0.84)	0.15 (0.58)
$G_0W_0^{\mathrm{RPA}}$@PBE0	-0.05 (0.20)	-0.01 (0.34)	-0.26 (0.41)	-0.26 (0.47)
$G_0W_0^{\mathrm{fxc}}$@PBE0	-0.29 (0.39)	-0.25 (0.48)	0.04 (0.43)	0.26 (0.52)
$G_0W_0\Gamma_0$@PBE0	-0.45 (0.49)	-0.41 (0.54)	-1.10 (1.11)	-0.68 (0.75)

Finally we report $G_0W_0^{\mathrm{RPA}}$, $G_0W_0^{f_{\mathrm{xc}}}$ and $G_0W_0\Gamma_0$ results for several solids: Si, SiC (4H), C (diamond), AlN, WO_3 (monoclinic), Si_3N_4 (amorphous). We performed calculations starting with LDA and PBE functionals for all solids, and for Si we also performed calculations with a dielectric-dependent hybrid (DDH) functional [346]. All solids are represented by supercells with 64-96 atoms (see Section 3.1.4) and only the Γ-point is used to sample the Brillioun zone. In Table 3.2 we present the band gaps computed with different *GW* approximations and functionals. Note that the supercells used here do not yield fully converged results as a function of supercell size (or k-point sampling); however the comparisons between different *GW* calculations are sound and represent the main result of this section.

Overall, band gaps obtained with different *GW* approximations are rather similar, with differences much smaller than those observed for molecules. To further investigate the positions of the band edges obtained from different *GW* approximations, we plotted in

Table 3.2: Band gaps (eV) for solids computed by different GW approximations and exchange-correlation (XC) functionals. All calculations are performed at the Γ-point of supercells with 64-96 atoms (see Section 3.1.4 for details).

System	XC	DFT	$G_0W_0^{\mathrm{RPA}}$	$G_0W_0^{f_{\mathrm{xc}}}$	$G_0W_0\Gamma_0$
Si	LDA	0.55	1.35	1.32	1.26
	PBE	0.73	1.39	1.36	1.31
	DDH	1.19	1.57	1.48	1.51
C	LDA	4.28	5.99	5.92	5.88
	PBE	4.46	6.05	5.97	5.93
SiC (4H)	LDA	2.03	3.27	3.16	3.24
	PBE	2.21	3.28	3.15	3.25
AlN	LDA	3.85	5.67	5.51	5.89
	PBE	4.04	5.67	5.48	5.83
WO_3 (monoclinic)	LDA	1.68	3.10	2.69	3.26
	PBE	1.78	2.97	2.52	3.13
Si_3N_4 (amorphous)	LDA	3.04	4.84	4.65	4.83
	PBE	3.19	4.87	4.64	4.84

Fig. 3.7 the GW quasiparticle corrections to VBM and CBM, defined as $\Delta_{\mathrm{VBM/CBM}} = \varepsilon^{\mathrm{GW}}_{\mathrm{VBM/CBM}} - \varepsilon^{\mathrm{DFT}}_{\mathrm{VBM/CBM}}$ where $\varepsilon^{\mathrm{GW}}_{\mathrm{VBM/CBM}}$ and $\varepsilon^{\mathrm{DFT}}_{\mathrm{VBM/CBM}}$ are the GW quasiparticle energy and the Kohn-Sham eigenvalue corresponding to the VBM/CBM, respectively.

Compared to $G_0W_0^{\mathrm{RPA}}$, VBM and CBM computed at the $G_0W_0^{f_{\mathrm{xc}}}$ level are slightly lower, while VBM and CBM computed at the $G_0W_0\Gamma_0$ level are significantly higher. The difference between band edge energies computed by different GW approximations is larger with the DDH functional, compared to that of semilocal functionals. Overall the trends observed for solids are consistent with those found for molecules.

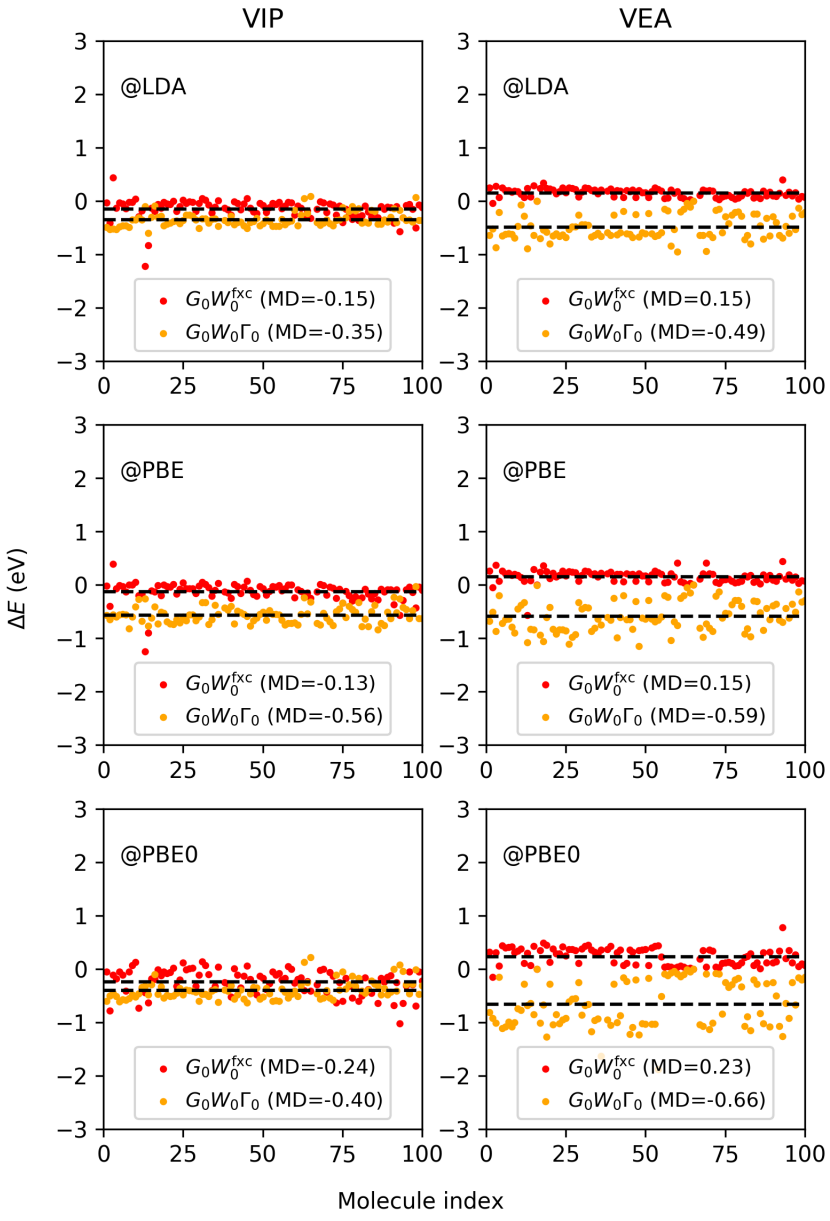

Figure 3.5: Difference (ΔE) between vertical ionization potential (VIP) and vertical electron affinity (VEA) of molecules in the GW100 set computed at the $G_0W_0^{f_{\mathrm{xc}}}/G_0W_0\Gamma_0$ level and corresponding $G_0W_0^{\mathrm{RPA}}$ results. Mean deviations (MD) in eV are shown in brackets and represented with black dashed lines. Results are presented for three different functionals (LDA, PBE and PBE0) in the top, middle and bottom panel, respectively.

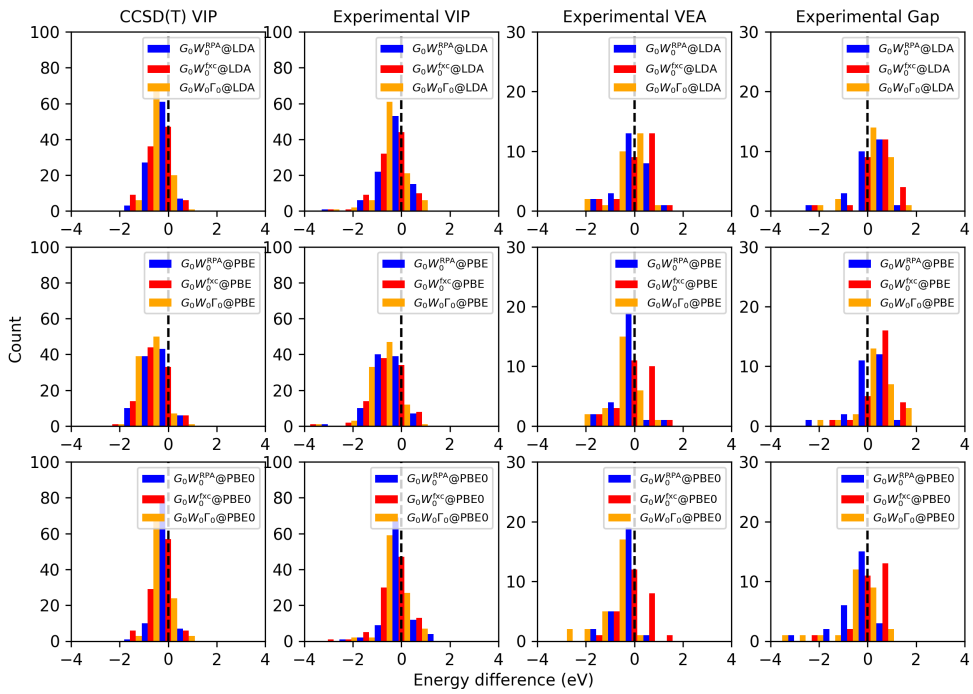

Figure 3.6: Vertical ionization potential (VIP), vertical electron affinity (VEA) and electronic gap of molecules in the GW100 set computed at $G_0W_0^{\mathrm{RPA}}$, $G_0W_0^{f_{\mathrm{xc}}}$ and $G_0W_0\Gamma_0$ levels of theory, compared to experimental and CCSD(T) results (black dashed lines).

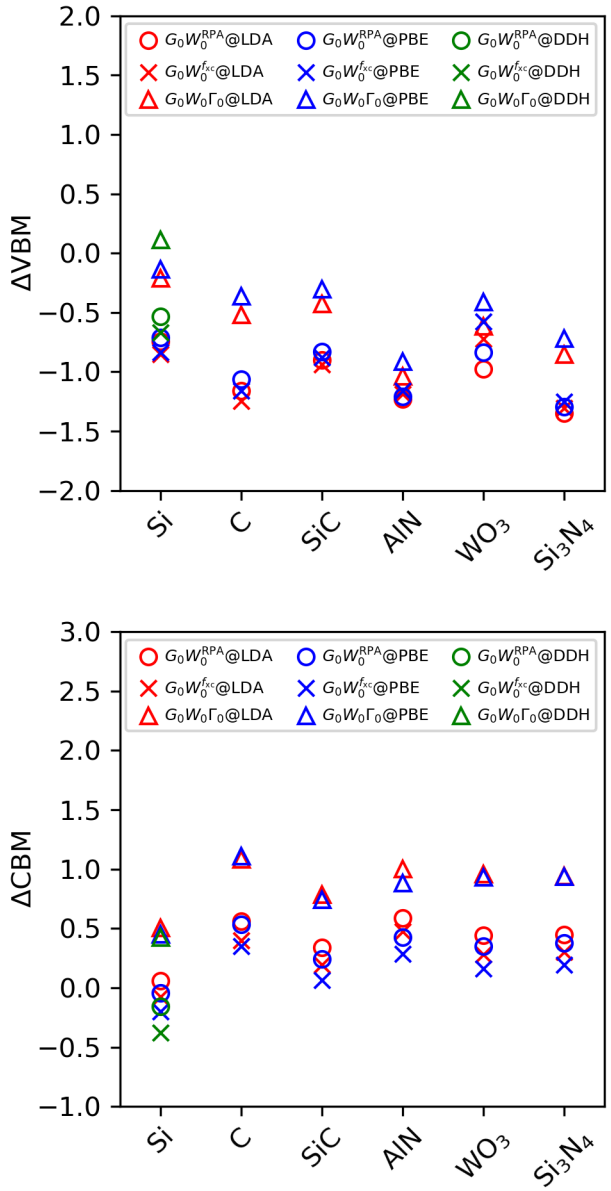

Figure 3.7: *GW* quasiparticle corrections to the valance band maximum (VBM) and the conduction band minimum (CBM). Circles, squares and triangles are $G_0W_0^{\mathrm{RPA}}$, $G_0W_0^{f_{\mathrm{xc}}}$ and $G_0W_0\Gamma_0$ results respectively; red, blue, green markers correspond to calculations with LDA, PBE and DDH functionals.

3.1.4 Technical details

Computational setup of DFT and *GW* calculations

In this section we describe the computational setup of DFT and *GW* calculations presented in our paper. The energy cutoff (E_{cut}), number of eigenpotentials for the spectral decomposition of the response functions (N_{PDEP}) and the cell size for all systems studied in our work are summarized in Table 3.3 and 3.4. All calculations are performed with norm-conserving pseudopotentials of the SG15 library [324].

The values of E_{cut} are chosen such that the HOMO's for molecules and the VBM's for solids are converged within 0.01 eV at the DFT(PBE) level. To minimize spurious interactions between periodic images, cubic cells with edge of 25Å are used for molecules; for solids, we used PBE lattice constants. For molecules, $N_{\text{PDEP}} = 10N_v$ where N_v is the number of valence electrons [118]; $N_{\text{PDEP}} = 2048$ for solids.

Table 3.3: The parameters E_{cut} and N_{PDEP} for molecules. Molecules are simulated in cubic cells with edge of 25Å.

Index	Formula	CAS Number	Ecut (Ry)	N_{PDEP}
1	C_8H_{10}	100-41-4	60	420
2	O_3	10028-15-6	70	180
3	BN	10043-11-5	55	80
4	C_4H_{10}	106-97-8	50	260
5	C_7H_8	108-88-3	55	360
6	C_6H_6O	108-95-2	60	360
7	C_5H_5N	110-86-1	60	300
8	C_4	12184-80-4	60	160
9	P_2	12185-09-0	35	100
10	Ag_2	12187-06-3	45	380
11	Cu_2	12190-70-4	80	380
12	CO_2	124-38-9	60	160
13	BeO	1304-56-9	55	100
14	MgO	1309-48-4	50	160
15	BH_3	13283-31-3	45	60
16	H_2	1333-74-0	50	20
17	BF	13768-60-0	60	100
18	Li_2	14452-59-6	50	60

Continued on next page

Table 3.3: Continued.

Index	Formula	CAS Number	Ecut (Ry)	N_{PDEP}
19	Si_5H_{12}	14868-53-2	45	320
20	Si_2H_6	1590-87-0	40	140
21	COSe	1603-84-5	65	160
22	GaCl	17108-85-9	60	200
23	PN	17739-47-8	60	100
24	B_2H_6	19287-45-7	50	120
25	As_2	23878-46-8	30	100
26	Na_2	25681-79-2	40	180
27	K_2	25681-80-5	30	180
28	Rb_2	25681-81-6	30	180
29	N_2H_4	302-01-2	45	140
30	C_6F_6	392-56-3	60	660
31	Na_4	39297-86-4	45	360
32	Na_6	39297-88-6	40	540
33	COS	463-58-1	65	160
34	H_2CO	50-00-0	65	120
35	CI_4	507-25-5	55	720
36	C_5H_6	542-92-7	60	260
37	CuCN	544-92-3	75	280
38	CBr_4	558-13-4	55	320
39	CCl_4	56-23-5	55	320
40	CH_4N_2O	57-13-6	55	240
41	C_2H_3Br	593-60-2	60	180
42	C_2H_3I	593-66-8	45	280
43	$(C_2H_5)_2O$	60-29-7	55	320
44	$C_6H_5NH_2$	62-53-3	55	360
45	C_8H_8	629-20-9	55	400
46	CO	630-08-0	65	100
47	CH_3CH_2OH	64-17-5	55	200
48	HCOOH	64-18-6	70	180
49	$C_5H_6N_2O_2$	65-71-4	65	480
50	$C_4H_4N_2O_2$	66-22-8	65	420
51	CH_3OH	67-56-1	55	140
52	$C_4H_5N_3O$	71-30-7	65	420
53	C_6H_6	71-43-2	60	300
54	$C_5H_5N_5$	73-24-5	65	500
55	$C_5H_5N_5O$	73-40-5	65	560
56	CH_4	74-82-8	45	80
57	C_2H_6	74-84-0	50	140
58	C_2H_4	74-85-1	55	120
59	C_2H_2	74-86-2	55	100

Continued on next page

Table 3.3: Continued.

Index	Formula	CAS Number	Ecut (Ry)	N_{PDEP}
60	HCN	74-90-8	65	100
61	C_3H_8	74-98-6	50	200
62	Kr	7439-90-9	30	80
63	Ne	7440-01-9	45	80
64	Ar	7440-37-1	30	80
65	He	7440-59-7	70	20
66	Xe	7440-63-3	45	180
67	SO_2	7446-09-5	65	180
68	C_2H_3Cl	75-01-4	60	180
69	C_2H_3F	75-02-5	60	180
70	CH_3CHO	75-07-0	65	180
71	CS_2	75-15-0	60	160
72	C_3H_6	75-19-4	50	180
73	CF_4	75-73-0	65	320
74	I_2	7553-56-2	30	340
75	LiH	7580-67-8	55	40
76	HCl	7647-01-0	30	80
77	NaCl	7647-14-5	40	160
78	HF	7664-39-3	65	80
79	NH_3	7664-41-7	45	80
80	KH	7693-26-7	30	100
81	H_2O_2	7722-84-1	70	140
82	Br_2	7726-95-6	30	140
83	N_2	7727-37-9	70	100
84	H_2O	7732-18-5	50	80
85	BrK	7758-02-3	30	160
86	F_2	7782-41-4	65	140
87	Cl_2	7782-50-5	40	140
88	GeH_4	7782-65-2	45	180
89	HN_3	7782-79-8	65	160
90	SH_2	7783-06-4	30	80
91	MgF_2	7783-40-6	65	240
92	SF_4	7783-60-0	60	340
93	TiF_4	7783-63-3	70	400
94	AlF_3	7784-18-1	70	320
95	AlI_3	7784-23-8	40	620
96	AsH_3	7784-42-1	40	80
97	$MgCl_2$	7786-30-3	40	240
98	LiF	7789-24-4	65	100
99	PH_3	7803-51-2	40	80
100	SiH_4	7803-62-5	45	80

Table 3.4: The parameter E_{cut}, N_{atom} (number of atoms), cell type and lattice constants for solids. N_{atom} and cell types are reported for the supercells used in actual calculations. Lattice constants are reported for the unit cells used to construct supercells. $N_{\text{PDEP}} = 2048$ is used.

System	E_{cut} (Ry)	N_{atom}	Cell type	Lattice constants (Å)
AlN	60	96	orthorhombic	a = 3.13, c = 5.02
C	60	64	cubic	a = 3.57
Si	30	64	cubic	a = 5.48
Si_3N_4	60	56	cubic	a = 8.35
4H-SiC	45	96	orthorhombic	a = 3.10, c = 5.07
WO_3	55	32	monoclinic	a = 7.31, b = 7.54, c = 7.69, $\beta = 90.88°$

Convergence of finite-field calculations

In finite-field calculations, the response $\delta n = \delta n(a, N_{\text{SCF}}; K)$ to an applied potential δV depends on the amplitude of δV (we denote with a the scaled amplitude, see below), the number of SCF cycles N_{SCF}, and the type of response function K: χ_0, χ_{RPA}, χ. In this section we investigate the dependence of δn on a and N_{SCF}. All calculations were carried out with the PBE functional and the wavefunction was optimized with a preconditioned steepest descent algorithm with Anderson acceleration.

Amplitude of the applied potential δV

We define the amplitude of a given δV as $\text{amp}(\delta V) = \max_{\boldsymbol{r}} |\delta V(\boldsymbol{r})|$ and we compute $\delta n(a)$ as:

$$\delta n(a) = \frac{\text{amp}(\delta V)}{a} \int K(\boldsymbol{r}, \boldsymbol{r}') \left\{ \frac{a}{\text{amp}(\delta V)} \delta V(\boldsymbol{r}') \right\} d\boldsymbol{r}', \tag{3.34}$$

where the integration is performed by the finite-field approach. In principle, for any a chosen within the linear response regime, one should get identical results for $\delta n(a)$. In practice, a value of a that is too small gives rise to large numerical errors.

To determine the optimal range for a, we computed $\delta n(a)$ for $\delta V = v_c^{\frac{1}{2}} \xi_1$, where ξ_1 is the first eigenvector of K, for a number of systems, and we varied a between 10^{-5} to 10^{-2} Hartree. All calculations were performed with 10 self-consistent cycles. In Fig 3.8 we plot the relative difference of δn computed with different amplitudes for two molecules (Ar, SiH_4) and for bulk Si.

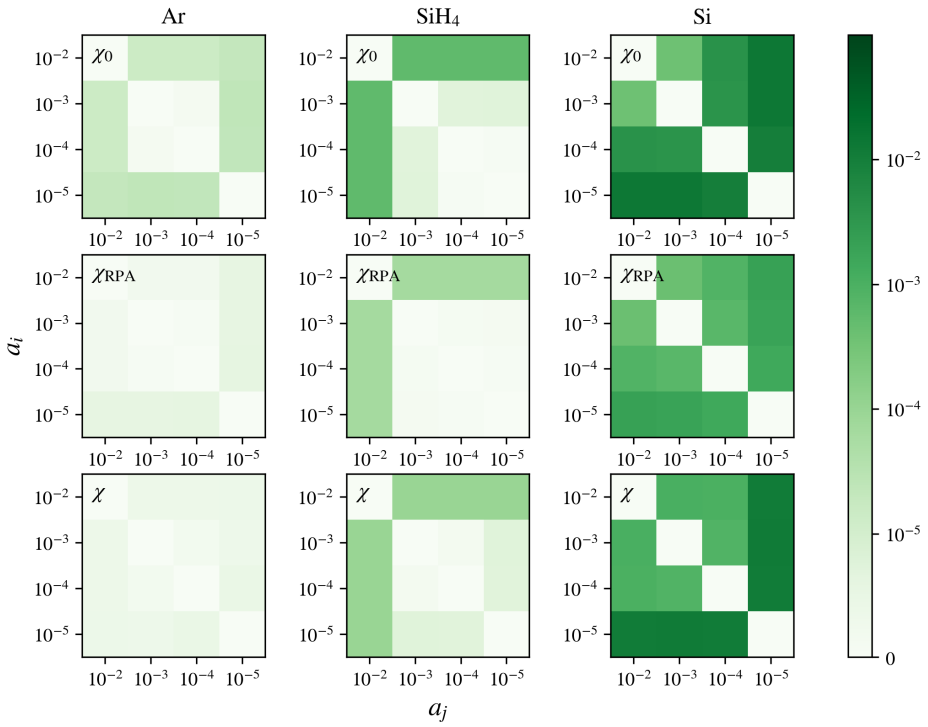

Figure 3.8: Relative difference $\Delta_{ij} = \frac{|\delta n(a_i) - \delta n(a_j)|}{|\delta n(a_j)|}$, where $|...|$ is the 2-norm of δn's (see Eq. 3.34) defined on a real space grid.

We found that for all choices of $K = \chi_0, \chi^{\mathrm{RPA}}, \chi$, the relative differences of δn's are smaller than 10^{-2} for amplitudes between 10^{-2} and 10^{-4} Hartree.

Number of SCF cycles

For a given response function K, we tested the convergence of δn as a function of N_{SCF}. In Fig. 3.9 we show the convergence of δn with respect to N_{SCF} for Ar, SiH_4 and bulk Si.

We see that for all choices of $K = \chi_0, \chi^{\mathrm{RPA}}, \chi$, δn converges within 0.02 with $N_{\mathrm{SCF}} = 10$. The convergence of χ^{RPA} and χ requires a slightly smaller number of SCF cycles compared to that of χ_0. The same trend was observed for other molecules and solids considered in this work.

Comparison of finite-field approach and density functional perturbation theory

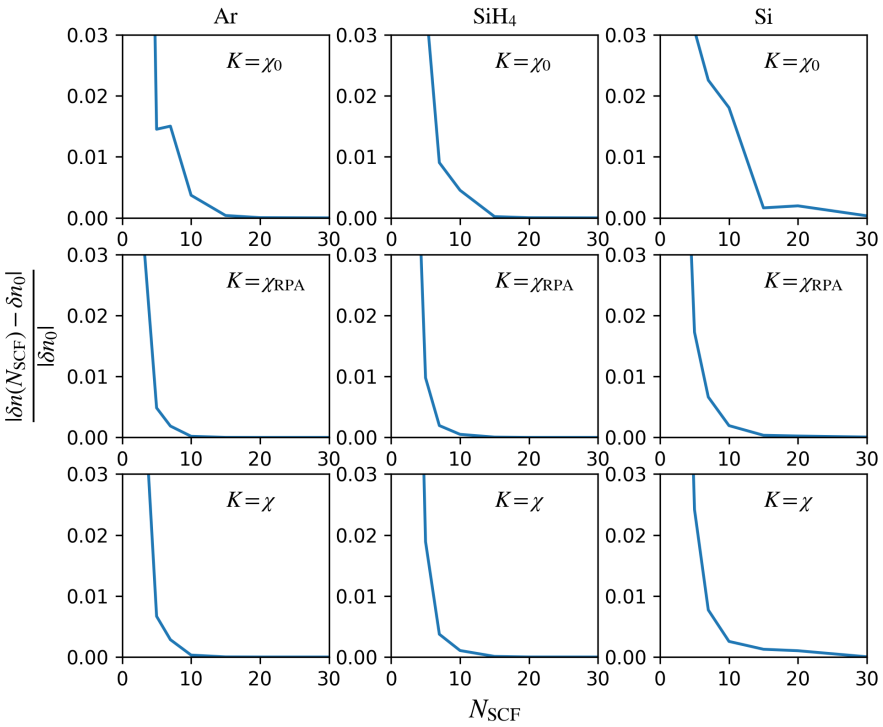

Figure 3.9: Relative difference between $\delta n(N_{\mathrm{SCF}})$ and the converged result δn_0. δn_0 is computed with $N_{\mathrm{SCF}} = 50$. See Eq. 3.34 for the definition of δn.

Based on the results of the two previous subsections, we carried out all the calculations shown in the previous sections with $a = 10^{-3}$ Hartree and $N_{\mathrm{SCF}} = 10$. Here we show that this choice of a and N_{SCF} gives accurate spectral decomposition of response functions for G_0W_0 calculations.

We carried out $G_0W_0^{\mathrm{RPA}}$ calculations for the GW100 test set, with the spectral decomposition of χ_0 computed by either the finite-field (FF) approach with a and N as specified above or by density functional perturbation theory (DFPT). All parameters (N_{PDEP}, etc.) for $G_0W_0^{\mathrm{RPA}}$ calculations are the same as those given in Section 3.1.4. In Fig 3.10 we compare the VIP and VEA obtained with FF and DFPT.

Calculations based on χ_0 computed with FF and DFPT yield almost identical VIP and VEA. The mean absolute deviation for VIP (VEA) between the two sets of calculations is 0.005 (0.005) eV.

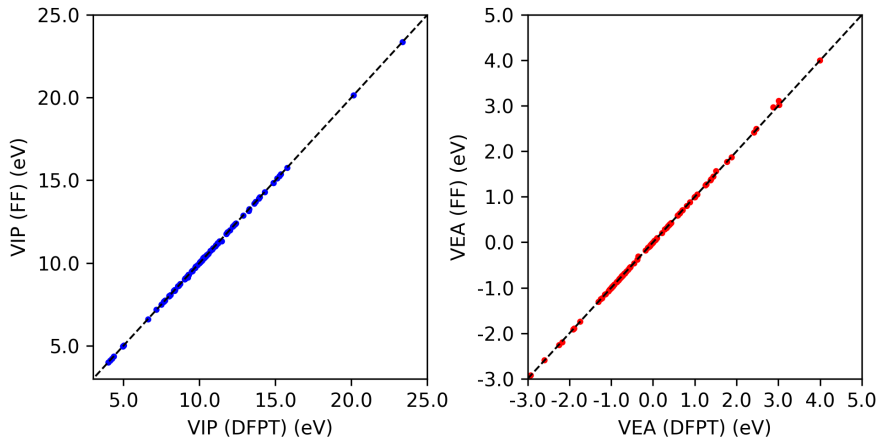

Figure 3.10: Comparison of VIP and VEA for the GW100 set obtained at the $G_0W_0^{\mathrm{RPA}}$@PBE level, with χ_0 computed with either the finite-field (FF) approach or DFPT. Diagonal dash lines are DFPT results, dots are FF results.

Exchange-correlation kernel in the PDEP basis

Fig. 3.11 presents the symmetrized exchange-correlation kernel $\tilde{f}_{\mathrm{xc}}$ matrix in the PDEP basis for Ar, SiH_4 and CO_2 molecule.

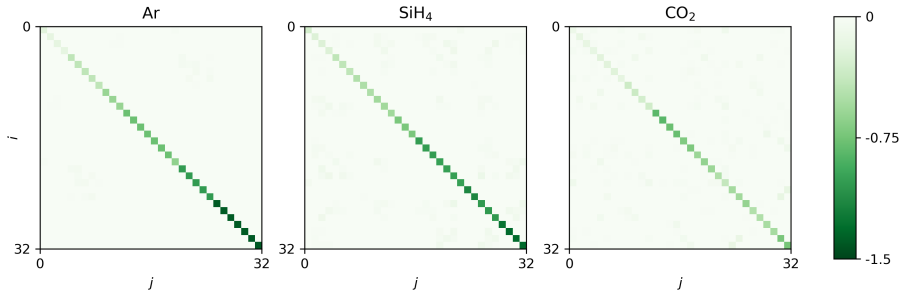

Figure 3.11: First 32×32 matrix elements of the exchange-correlation kernel in PDEP basis (the space of $\tilde{\chi}_0$ eigenvectors) for Ar, SiH_4 and CO_2 molecule.

As shown in Fig. 3.11, the $\tilde{f}_{\mathrm{xc}}$ matrix is almost diagonal in the PDEP basis due to the similarity of $\tilde{\chi}_0$ and $\tilde{\chi}$ eigenvectors.

GW calculations beyond the random phase approximation for periodic systems

In this section we derive the expression of response functions for periodic systems. For periodic systems, we partition $\tilde{\chi}$, $\tilde{\chi}_0$ and $\tilde{f}_{xc}$ in G space into different components: the head ($\boldsymbol{G} = \boldsymbol{G'} = 0$), wing ($\boldsymbol{G} = 0, \boldsymbol{G'} \neq 0$ or $\boldsymbol{G'} = 0, \boldsymbol{G} \neq 0$) and body ($\boldsymbol{G} \neq 0$ and $\boldsymbol{G'} \neq 0$). We write $\tilde{\chi}_0$ and $\tilde{f}_{\mathrm{xc}}$ as:

$$\tilde{\chi}_0 = \begin{bmatrix} h & W^\dagger \\ W & B \end{bmatrix} \tag{3.35}$$

$$\tilde{f}_{\mathrm{xc}} = \begin{bmatrix} -\alpha & 0 \\ 0 & F \end{bmatrix} \tag{3.36}$$

where h, W and B are head, wing and body of $\tilde{\chi}_0$. F and $-\alpha$ are body and head of $\tilde{f}_{\mathrm{xc}}$. In the GW formalism adopted in this work, B and F are approximated by their low-rank decomposition, and they correspond to the $\tilde{\chi}_0$ and $\tilde{f}_{\mathrm{xc}}$ discussed previously.

Inserting Eq. 3.35, 3.36 into Eq. 3.29, 3.30, 3.31 and solving for the head and body of $\tilde{\chi}$, one obtains:

$$\tilde{\chi}^{\mathrm{head}} = \begin{cases} \frac{1}{k} - 1 & G_0 W_0^{\mathrm{RPA}} \\ \frac{1-k}{k(1-\alpha)} & G_0 W_0^{f_{\mathrm{xc}}} \\ \frac{1}{k} - 1 & G_0 W_0 \Gamma_0 \end{cases} \tag{3.37}$$

$$\tilde{\chi}^{\mathrm{body}} = \begin{cases} MB + \frac{1}{k} MWW^\dagger M & G_0 W_0^{\mathrm{RPA}} \\ MB + \frac{1-\alpha}{k} MWW^\dagger [I + (I+F)MB] & G_0 W_0^{f_{\mathrm{xc}}} \\ M + \frac{1-\alpha}{k} MWW^\dagger (I+F)M - I & G_0 W_0 \Gamma_0 \end{cases} \tag{3.38}$$

where I is the $N_{\mathrm{PDEP}} \times N_{\mathrm{PDEP}}$ identity matrix, and

$$k = \begin{cases} 1 - h - W^{\dagger} M W & G_0 W_0^{\mathrm{RPA}} \\ 1 - (1-\alpha)h - (1-\alpha) W^{\dagger}(I+F) M W & G_0 W_0^{f_{\mathrm{xc}}}, G_0 W_0 \Gamma_0 \end{cases} \tag{3.39}$$

$$M = \begin{cases} (I - B)^{-1} & G_0 W_0^{\mathrm{RPA}} \\ [I - B(I+F)]^{-1} & G_0 W_0^{f_{\mathrm{xc}}}, G_0 W_0 \Gamma_0 \end{cases} \tag{3.40}$$

Finally, the screened Coulomb interaction is computed from Eq. 21, 22, 23 of Ref.117 using the head and body of $\tilde{\chi}$, as derived above.

In the calculation for solids presented in the previous sections we neglected the head of $\tilde{f}_{\mathrm{xc}}$ by setting $\alpha = 0$. In selected cases, we included the head by computing α from the high-frequency dielectric constant of the material, as suggested in Ref.41, and we found that the effect of the head on the computed quasiparticle energies was negligible. In Fig. 3.12 we present the quasiparticle energies of Si computed with $\alpha = 0$ and $\alpha = 0.016$ (note that $\alpha = 0.016$ here corresponds to $\alpha = 0.2$ in Ref.41 due to a difference of 4π in the normalization factors used here and in Ref.41). We see from Fig. 3.12 that $\alpha = 0$ and $\alpha = 0.016$ lead to very similar quasiparticle energies for both $G_0 W_0^{f_{\mathrm{xc}}}$ and $G_0 W_0 \Gamma_0$ calculations.

Renormalization of the exchange-correlation kernel

To illustrate the effect of renormalization on GW calculations, in Fig. 3.13 we present the $\tilde{\chi}_0$, $\tilde{f}_{\mathrm{xc}}$, $[1 - \tilde{\chi}_0(1 + \tilde{f}_{\mathrm{xc}})]^{-1}$, $\tilde{\chi}_{\mathrm{RPA}}$, $\tilde{\chi}$ and $\tilde{\chi}_{\Gamma}$ matrices in the PDEP basis for the SiH_4 molecule. Calculations were performed with the PBE functional. Since $\tilde{\chi}_0$ is by definition diagonal in the PDEP basis and $\tilde{f}_{\mathrm{xc}}$ is nearly diagonal (see Fig. 3.11), in Fig. 3.13 only the diagonal elements of matrices are shown, and in the following discussion when we refer to these matrices we consider only their diagonal elements, which correspond approximately to their eigenvalues.

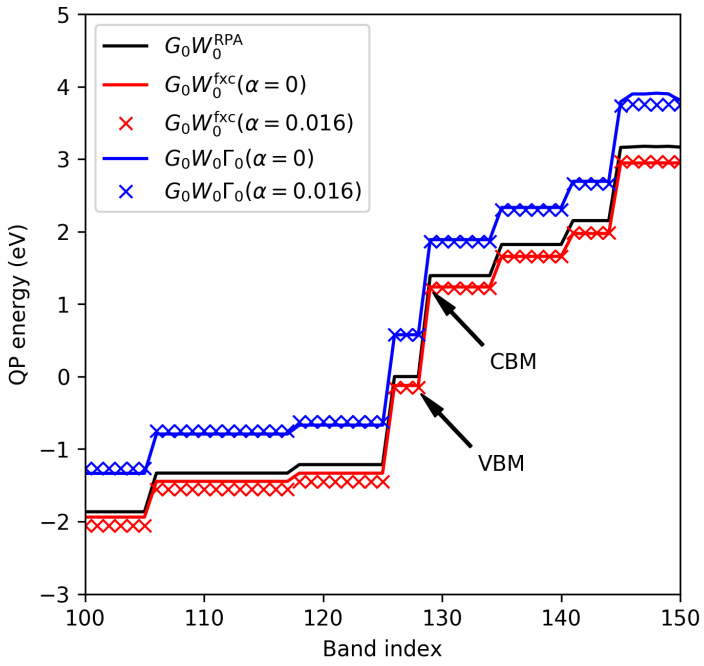

Figure 3.12: Quasiparticle energies of Si (64-atom supercell, PBE functional) computed with and without the head of $\tilde{f}_{\mathrm{xc}}$. VBM obtained at $G_0W_0^{\mathrm{RPA}}$ level is set as the zero of energy.

According to Fig. 3.13, as the PDEP index increases, $\tilde{\chi}_0$ asymptotically decays to zero while the magnitude of $\tilde{f}_{\mathrm{xc}}$ keeps increasing, leading to the slow decaying tail of the $[1-\tilde{\chi}_0(1+\tilde{f}_{\mathrm{xc}})]^{-1}$ matrix. In the case of $\tilde{\chi}$, the slow decaying tail of $[1-\tilde{\chi}_0(1+\tilde{f}_{\mathrm{xc}})]^{-1}$ is suppressed by being multiplied by $\tilde{\chi}_0$ (see Eq. 3.30), leading to similar tails for $\tilde{\chi}$ and $\tilde{\chi}_{\mathrm{RPA}}$; on the other hand, $\tilde{\chi}_\Gamma$ shows the same slow decay as $[1-\tilde{\chi}_0(1+\tilde{f}_{\mathrm{xc}})]^{-1}$ (see Eq. 3.31). Note that for large PDEP indices $\tilde{\chi}_\Gamma$ can be positive as $\tilde{f}_{\mathrm{xc}}$ decreases below -1. An effective response function ($\tilde{\chi}_\Gamma$) with positive eigenvalues may be unphysical. On the contrary, $\tilde{\chi}_{\mathrm{RPA}}$ and $\tilde{\chi}$ are always negative.

By renormalizing $\tilde{f}_{\mathrm{xc}}$ (see Fig. 3.14) we exclude the short-range components of f_{xc} that are smaller than $-v_c$ (i.e. eigenvalues of $\tilde{f}_{\mathrm{xc}}$ smaller than -1), and therefore we enforce the negativity of $\tilde{\chi}_\Gamma$ and ensure its fast convergence toward zero.

To illustrate the effect of the f_{xc} renormalization on GW quasiparticle energies, in Fig.

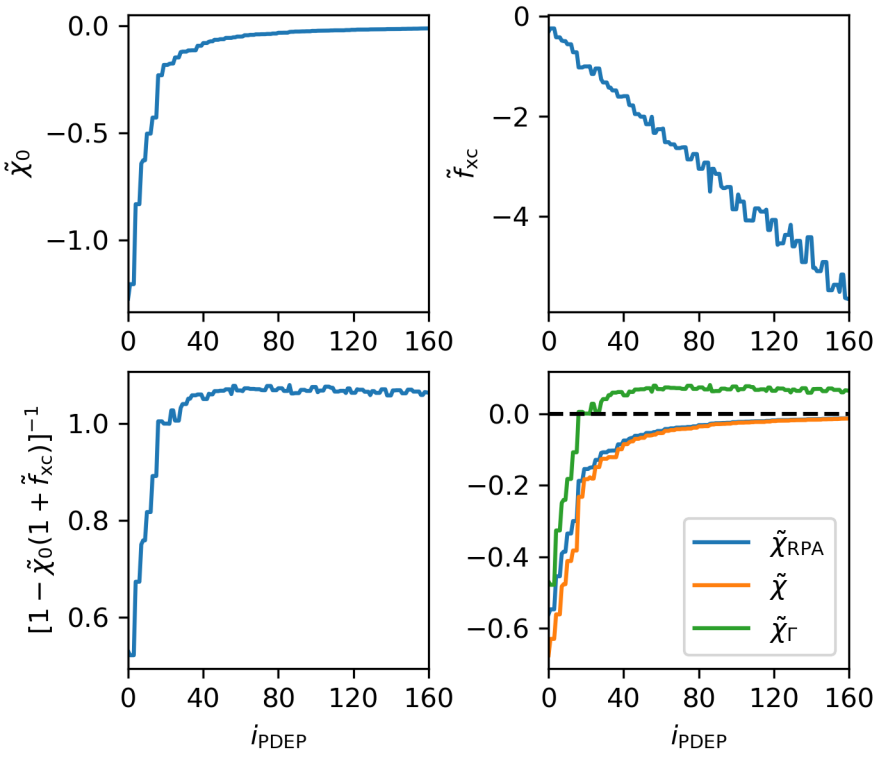

Figure 3.13: Diagonal elements of $\tilde{\chi}_0$, $\tilde{f}_{\text{xc}}$, $[1-\tilde{\chi}_0(1+\tilde{f}_{\text{xc}})]^{-1}$, $\tilde{\chi}_{\text{RPA}}$, $\tilde{\chi}$ and $\tilde{\chi}_\Gamma$ for the SiH_4 molecule.

3.15 we present the electronic gap of Si and SiH_4 computed at $G_0W_0^{f_{\text{xc}}}$ and $G_0W_0\Gamma_0$ levels of theory as a function of N_{PDEP}, using either un-renormalized or renormalized f_{xc}. $G_0W_0^{f_{\text{xc}}}$ results are barely affected by the renormalization, which primarily acts on the tail of $\tilde{f}_{\text{xc}}$, which is suppressed by being multiplied by $\tilde{\chi}_0$ when computing $\tilde{\chi}$. On the other hand, the convergence of $G_0W_0\Gamma_0$ results is significantly improved with renormalized $\tilde{f}_{\text{xc}}$.

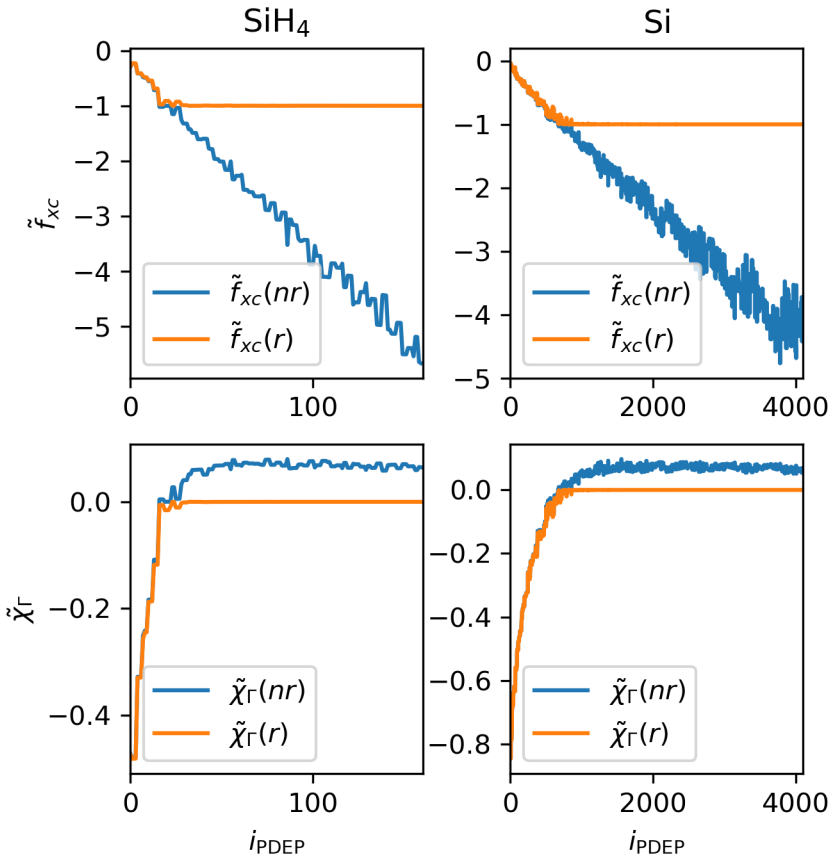

Figure 3.14: Diagonal elements of un-renormalized (nr) and renormalized (r) $\tilde{f}_{\mathrm{xc}}$ matrices and resulting $\tilde{\chi}_\Gamma$ matrices for the SiH_4 molecule and bulk Si.

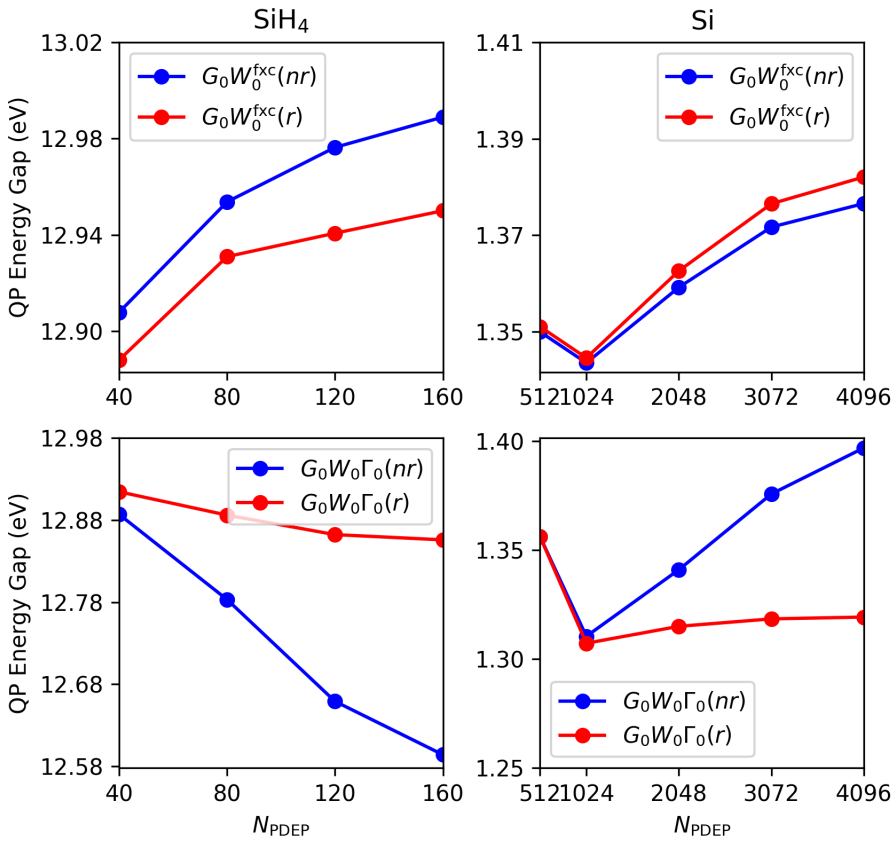

Figure 3.15: Convergence of GW quasiparticle gaps of SiH_4 and Si as a function of N_{PDEP}, using either un-renormalized (nr) or renormalized (r) $\tilde{f}_{\mathrm{xc}}$ matrices.

3.1.5 Conclusions

In summary, we developed a finite-field approach to compute density response functions (χ_0, χ_{RPA} and χ) for molecules and materials. The approach is non-perturbative and can be used in a straightforward manner with both semilocal and orbital-dependent functionals. Using this approach, we computed the exchange-correlation kernel f_{xc} and performed GW calculations using dielectric responses evaluated beyond the RPA.

We evaluated quasiparticle energies for molecules and solids and compared results obtained within and beyond the RPA, and using DFT calculations with semilocal and hybrid functionals as input. We found that the effect of vertex corrections on quasiparticle energies is more notable when using input wavefunctions and single-particle energies from hybrid functionals calculations. For the small molecules in the GW100 set, $G_0W_0^{f_{\mathrm{xc}}}$ calculations yielded lower VIP and higher VEA compared to $G_0W_0^{\mathrm{RPA}}$ results; $G_0W_0\Gamma_0$ calculations yielded lower VIP and VEA compared to $G_0W_0^{\mathrm{RPA}}$ results. In the case of solids, the energy of the VBM and CBM shifts in the same direction, relative to RPA results, when vertex corrections are included, and overall the band gaps were found to be rather insensitive to the choice of the GW approximation.

In addition, we reported a scheme to renormalize f_{xc}, which is built on previous work [325] using the LDA functional. The scheme is general and applicable to any exchange-correlation functional and to inhomogeneous systems including molecules and solids. Using the renormalized $\tilde{f}_{\mathrm{xc}}$, the basis set convergence of $G_0W_0\Gamma_0$ results was significantly improved.

Overall, the method introduced in our work represents a substantial progress towards efficient computations of dielectric screening and large-scale G_0W_0 calculations for molecules and materials beyond the random phase approximation.

3.2 Bethe-Salpeter equation

We present a method to compute optical spectra and exciton binding energies of molecules and solids based on the solution of the Bethe-Salpeter equation (BSE) and the calculation of the screened Coulomb interaction in finite field. The method does not require the explicit evaluation of dielectric matrices nor of virtual electronic states, and can be easily applied without resorting to the random phase approximation. In addition, it utilizes localized orbitals obtained from Bloch states using bisection techniques, thus greatly reducing the complexity of the calculation and enabling the efficient use of hybrid functionals to obtain single particle wavefunctions. We report exciton binding energies of several molecules and absorption spectra of condensed systems of unprecedented size, including water and ice samples with hundreds of atoms.

3.2.1 Introduction

The ability to simulate optical properties of materials from first principles is key to building predictive strategies for the design of new materials and molecules, as well as to interpreting increasingly complex experimental results [52, 283, 287]. The last three decades have witnessed a tremendous success of many-body perturbation theory (MBPT) [271, 237] in the description of the interaction of molecules and condensed matter with light. MBPT, a Green's function method, can be used to accurately compute various excitation properties, based on single particle energies and orbitals obtained, e.g. within density functional theory (DFT) [146, 191]. In particular, by solving the Dyson equation [88] within the GW approximation [133] and the Bethe-Salpeter equation (BSE) [271, 317], one can accurately predict the energy of charged and neutral excitations [271], excitonic and charge transfer

states [32, 304], and optical absorption spectra [130, 357, 309, 33, 291]. However, the solution of the BSE is computationally demanding, more so, for example, than the use of time-dependent density functional theory (TD-DFT) with semi-local or hybrid exchange-correlation (xc) functionals [314, 235, 386]. Therefore, TD-DFT is still widely used to compute absorption spectra, albeit often yielding less accurate results than the BSE.

The unfavorable cost of conventional approaches [5, 310, 29, 232, 238, 50] to solve the BSE is mainly due to the evaluation of explicit summations over virtual states and to the need of evaluating and inverting large dielectric matrices. In particular, the straightforward diagonalization of the two-body exciton Hamiltonian in the basis of electron-hole pairs requires a workload of order $O(N^6)$, where N is the number of electrons in the system [5, 309]. A formulation of the BSE without empty states that sidesteps the diagonalization of the two-body exciton Hamiltonian, and does not require the inversion of dielectric matrices was recently proposed [304, 305, 291], and shown to accurately yield absorption spectra over a wide range of frequencies using the Liouville-Lanczos algorithm [386, 303]. A distinctive feature of this formalism based on density matrix perturbation theory (DMPT) is the utilization of projective dielectric eigenpotentials (PDEP) [400, 399] to compute screened exchange integrals. Despite the advantages of the DMPT formulation and its more favourable $O(N^4)$ scaling, drawbacks remain, including the need to extrapolate the results as a function of the number of dielectric eigenpotentials and, most importantly, the difficulty to use DFT calculations with hybrid density functionals [280, 45, 346] as a starting point for the BSE solution.

In this Letter, we present a novel method to solve the BSE by performing calculations in finite electric fields. The two key features of the method are: (i) the direct evaluation of the screened Coulomb interaction in finite field (FF), thus eliminating the need to compute dielectric matrices altogether; (ii) the use of a compact, localized representation [125] of the ground state Kohn-Sham (KS) wavefunctions, leading to a great reduction of the cost to evaluate screened exchange integrals. We show that these features lead to a major im-

provement in the efficiency of the BSE solution and, importantly, to the straightforward use of the results of hybrid functionals as a starting point for GW and BSE calculations. The FF-BSE can be used to compute not only the properties of single molecules or solids, but its solution may be easily coupled to first principles molecular dynamics (FPMD) simulations to obtain, e.g. optical spectra over multiple snapshots extracted from trajectories at finite temperature and pressure, as we show below. We report examples for the optical spectra of liquid water and ice as obtained by averaging over multiple trajectories, for systems with up to 2,048 electrons. In addition, we present the results of calculations using ground state wavefunctions computed with hybrid functionals [346].

3.2.2 Method

Absorption spectra of solids and molecules can be obtained by computing the imaginary part of the macroscopic dielectric function $\mathrm{Im}\epsilon^M_{ij} = 4\pi Im\frac{\partial P_i}{\partial E_j}$, where $\mathbf{E}$ is the macroscopic electric field, and $\mathbf{P} = -\frac{1}{\Omega}\mathrm{Tr}\left\{\hat{\mathbf{r}}\hat{\rho}\right\}$ the macroscopic polarization, $\hat{\mathbf{r}}$ is the position operator, and $\hat{\rho}$ the density matrix. We obtain $\frac{\partial P_i}{\partial E_j}$ from the solution of the Liouville equation for the density matrix.[386] For a system described by a mean-field Hamiltonian $\hat{H}(\hat{\rho})$ subject to a monochromatic electrostatic potential $\phi(\omega) = -\mathbf{E}(\omega)\cdot\mathbf{r}$, the time evolution of the density matrix is given by the Liouville equation $\omega\hat{\rho} = [\hat{H}(\hat{\rho}) - \hat{\phi}, \hat{\rho}]$. Upon linearization, we obtain the first order variation of the density matrix as the solution of the following non-homogeneous linear system:

$$(\omega - \mathcal{L})\Delta\hat{\rho} = -[\hat{\phi}, \hat{\rho}^o]\,, \tag{3.41}$$

where $\hat{\rho}^o$ is the unperturbed density matrix. The Liouville superoperator $\mathcal{L}$ acting on $\Delta\hat{\rho}$ is defined as

$$\mathcal{L}\Delta\hat{\rho} = [\hat{H}^o, \Delta\hat{\rho}] + [\Delta\hat{V}_{\mathrm{H}}, \hat{\rho}^o] + [\Delta\hat{\Sigma}, \hat{\rho}^o]\,, \tag{3.42}$$

where $\hat{H}^o$ is the unperturbed Hamiltonian, and $\Delta\hat{V}_H$ and $\Delta\hat{\Sigma}$ are the first-order variation of the Hartree and the exchange-correlation (xc) self-energy induced by $\Delta\hat{\rho}$, respectively. The change in polarization induced by $\mathbf{E}$, entering the definition of the absorption spectrum, can hence be expressed as $\frac{\partial P_i}{\partial E_j} = -\frac{1}{\Omega}\mathrm{Tr}\left\{\hat{r}_i \frac{\partial \Delta\hat{\rho}}{\partial E_j}\right\}$. As previously noted [304], the homogeneous linear system corresponding to Eq. 3.41 is a secular equation with neutral excitation energies as eigenvalues; these energies are equivalent to those obtained by solving the BSE with static screening if an effective Hamiltonian and the COHSEX self-energy [133, 237] are utilized for $\hat{H}^o$ and $\Delta\hat{\Sigma}$, respectively. However, unlike BSE solvers based on the diagonalization of the two-particle electron-hole Hamiltonian[271], Eq. 3.41 can be solved without defining a transition space, and hence a direct product of occupied and unoccupied active subspaces. In order to avoid such definition and the need to compute virtual electronic orbitals, we introduce the auxiliary functions $|a_v^j\rangle = \hat{P}_c \frac{\partial \Delta\hat{\rho}}{\partial E_j} |\varphi_v\rangle$, where φ_v is the v-th occupied state of the unperturbed Hamiltonian (with energy ε_v); $\hat{P}_c = 1 - \sum_{v=1}^{N_{\mathrm{occ}}} |\varphi_v\rangle \langle\varphi_v|$ is the projector onto the unoccupied manifold [21], and N_{occ} is the number of occupied states. It has been shown that an Hermitian solution of Eq. 3.41 can be written as $\frac{\partial \Delta\hat{\rho}}{\partial E_j} = \sum_{v=1}^{N_{\mathrm{occ}}} \left(|\varphi_v\rangle \langle a_v^j| + |a_v^j\rangle \langle\varphi_v| \right)$, and the functions a_v^j are obtained from the solution of the following non-homogeneous linear systems:

$$\sum_{v'=1}^{N_{\mathrm{occ}}} \left(\omega\delta_{vv'} - D_{vv'} - K^{1e}_{vv'} + K^{1d}_{vv'} \right) |a_{v'}^j\rangle = \hat{P}_c \hat{r}_j |\varphi_v\rangle \ , \tag{3.43}$$

where the three terms on the RHS of Eq. 3.42 are:

$$D_{vv'} |a_{v'}^j\rangle = \hat{P}_c \left(\hat{H}^o - \varepsilon_v \right) \delta_{vv'} |a_{v'}^j\rangle \ , \tag{3.44}$$

$$K^{1e}_{vv'} |a_{v'}^j\rangle = 2\hat{P}_c \left(\int d\mathbf{r'} v_c(\mathbf{r}, \mathbf{r'}) \varphi^*_{v'}(\mathbf{r'}) a^j_{v'}(\mathbf{r'}) \right) \varphi_v(\mathbf{r}) \, , \tag{3.45}$$

$$K^{1d}_{vv'} |a_{v'}^j\rangle = \hat{P}_c \tau_{vv'}(\mathbf{r}) a^j_{v'}(\mathbf{r}) \, . \tag{3.46}$$

and we have defined the screened integrals $\tau_{vv'}(\mathbf{r}) = \int W(\mathbf{r}, \mathbf{r'}) \varphi_v(\mathbf{r'}) \varphi^*_{v'}(\mathbf{r'}) d\mathbf{r'}$, where W and v_c are the screened and bare Coulomb interactions, respectively. Eq. 3.43 can be solved

for multiple frequencies using the Lanczos algorithm. The evaluation of the integrals $\tau_{vv'}$ represents the most expensive part of the calculation because it entails a computation of the dielectric matrix. Recently, Eq. 3.43-3.46 were solved using Kohn-Sham (KS) states as input, using DFT calculations with semi-local functionals, and a spectral representation of the dielectric matrix via its eigenvectors, called projective dielectric eigenpotentials (PDEP).[305, 293, 292]

Here we introduce a new approach with two key features: (i) the screened integrals are directly computed from finite field calculations avoiding any explicit evaluation of the dielectric matrix; in addition, (ii) the total number of required integrals, in principle equal to $N_{\rm occ}^2$, is reduced to a much smaller number that scales linearly with the system size, by using a compact, localized representation of single particle wavefunctions. The very same representation is adopted to increase the efficiency of hybrid-DFT calculations[125], leading to a formulation of BSE which requires the very same workload when using local or hybrid-DFT starting points. We now illustrate steps (i) and (ii) in detail.

Using the definition of the screened Coulomb interaction in terms of the density-density response function, $W = v_c + v_c\chi v_c$, we express the screened integrals as $\tau_{vv'} = \tau^u_{vv'} + v_c\chi\tau^u_{vv'}$, where $\tau^u_{vv'}(\mathbf{r}) = \int v_c(\mathbf{r},\mathbf{r'})\varphi_v(\mathbf{r'})\varphi^*_{v'}(\mathbf{r'})d\mathbf{r'}$ are obtained by multiplying orbitals in real space and then applying the bare Coulomb potential v_c in reciprocal space. For each $\tau^u_{vv'}$ we determined two densities ($\rho^{\pm}_{vv'}$) by solving self-consistently the uncoupled-perturbed KS equations with Hamiltonian ($\hat{H}^o \pm \tau^u_{vv'}$). The screened exchange integrals are then obtained as:

$$\tau_{vv'}(\mathbf{r}) = \tau^u_{vv'}(\mathbf{r}) + \int v_c(\mathbf{r},\mathbf{r'})\frac{\rho^+_{vv'}(\mathbf{r'}) - \rho^-_{vv'}(\mathbf{r'})}{2}d\mathbf{r'}\,, \tag{3.47}$$

where a central finite difference formula was used to compute the linear variation of the density, i.e. $\chi\tau^u_{vv'}$. The algorithm described above was implemented by coupling the WEST [117] and Qbox [124] codes, operating in client-server mode, thus enabling massive parallel calculations by assigning independent finite field calculations to different Qbox instances, which may be started at any point during, e.g. a first principle MD simulation.

Next we reduced the number of integrals to compute, in principle equal to $N_{\rm occ}^2$, by localizing single particle wavefunctions in appropriate regions of real space and neglecting those orbital pairs that do not overlap. To do so we used the recursive bisection technique[125], whereby orbitals are truncated in subdomains of variable size while controlling the 2-norm error caused by the truncation procedure. This technique was previously used to improve the efficiency of calculations of exact exchange integrals and is here applied to *screened* exchange integrals. When using orbital bisection, a unitary transformation U: $|\tilde{\varphi}_m\rangle = \sum_v U_{mv}|\varphi_v\rangle$ of the occupied KS states is evaluated, and used to transform the matrix $\tilde{\tau} = U\tau U^\dagger$ (and similarly τ^u) into a sparse form, where only a relatively small number of selected elements need to be computed using Eq. 3.47. The number of required non-zero screened integrals scales linearly with system size. Different types of localized orbitals were used previously to solve the BSE, e.g. atomic-orbital basis sets [215], or maximally localized Wannier orbitals [239, 236]. However, there are several advantages of the localization technique used here: (i) it is adaptive, i.e. the orbitals can be localized in domains of different shapes and sizes; (ii) it allows to systematically control the localization error with a single parameter, and (iii) it is consistently applied to reduce the number of screened integrals and, at the same time, to speed up hybrid-DFT calculations[127, 68]. Hence the workload of our calculations is of $O(N^4)$ for the evaluation of $\tau_{vv'}$ and of $O(N^3)$ for the evaluation of Eq. 3.46, *irrespective of whether semilocal or hybrid functionals are used*. This is an important achievement, especially for the study of optical properties of materials, e.g. complex oxides, for which semi-local functionals do not even represent a qualitatively correct starting point to solve the BSE. In addition, we note that the computational gain of the method presented here increases as the size of the system increases, that is the prefactor in our calculations is increasingly smaller, compared to that of density functional perturbation theory calculations, as the size of the system increases (see Section 3.2.4).

3.2.3 Results

To demonstrate the accuracy of the FF-BSE methodology, we first calculated the neutral singlet excitation energies for the Thiel's set [343, 344], which consists of 28 small organic molecules. We compared our results with the best theoretical estimates as obtained from quantum chemistry calculations, i.e. coupled cluster and complete active space second-order perturbation theory using the aug-cc-pVTZ atomic basis set [343, 344]. This molecular set was recently used to benchmark GW-BSE [47, 297, 165] and TD-DFT calculations (with PBE0 [165] and dielectric-dependent hybrid functionals [45]). We evaluated the screened integrals in Eq. 3.47 with and without the RPA, and using either the Perdew–Burke–Ernzerhof (PBE) [279] or the PBE0 hybrid functional [4]. As shown in Fig.3.16, we obtained a good agreement with benchmark calculations, thus validating our methodology for molecules. A small change is observed when we compute the screened integrals with and without the Random Phase Approximation (RPA). Our results also show that BSE calculations based on G_0W_0 starting from the PBE (PBE0) ground state underestimate excitation energies by ~ 0.7 eV (~ 0.1 eV). The improvement observed with the PBE0 functional underscores the importance of an accurate ground state starting point. We also validated our method for solid LiF and compared our calculations with experiment and previous results (Section 3.2.4).

Next, we show how the use of bisected orbitals can reduce the computational cost of BSE calculations of optical spectra of the C_{60} fullerene in the gas phase. The computed electronic gap at the optimized PBE geometry and at the G_0W_0@PBE level of theory is 4.23 eV. This value is smaller than that obtained at the experimental geometry (4.55 eV) at the same level of theory, consistent with Ref. 296, and it is ~ 0.7 eV lower than the experimental value, estimated as the energy difference between the measured ionization potential and the electronic affinity [421, 389]. To evaluate the exciton binding energy, E_b^{ex}, we computed the energy difference between the electronic gap and the lowest optically-allowed singlet excited state (the lowest neutral eigenstate has T_g^1 symmetry). C_{60} has 120 doubly occupied valence

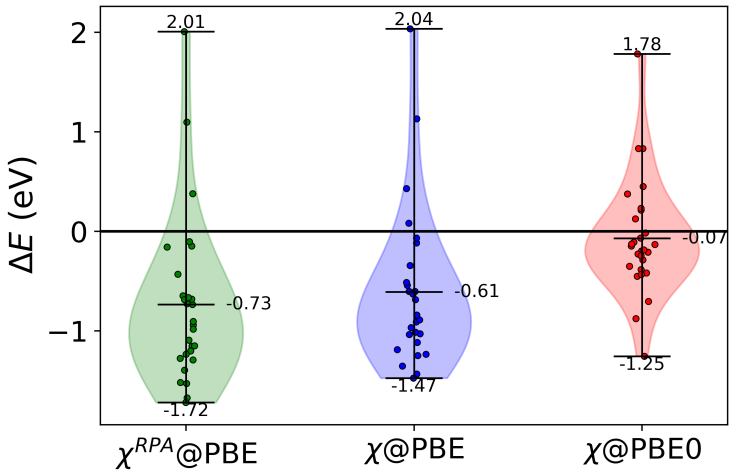

Figure 3.16: The lowest singlet excitation energies of the 28 molecules of the Thiel's set computed by solving the Bethe Salpeter equation in finite field (FF-BSE) with (green) and without (blue) the Random Phase Approximation (RPA), using the PBE and the PBE0 hybrid functional (red). Results are compared (ΔE) with the best theory estimates obtained using quantum chemistry methods [343, 344]. The horizontal lines denote the maximum, mean, and minimum of the distribution of results, compared with quantum chemistry methods. χ denotes the response function computed with and without the RPA. The numerical values are reported in Section 3.2.4.

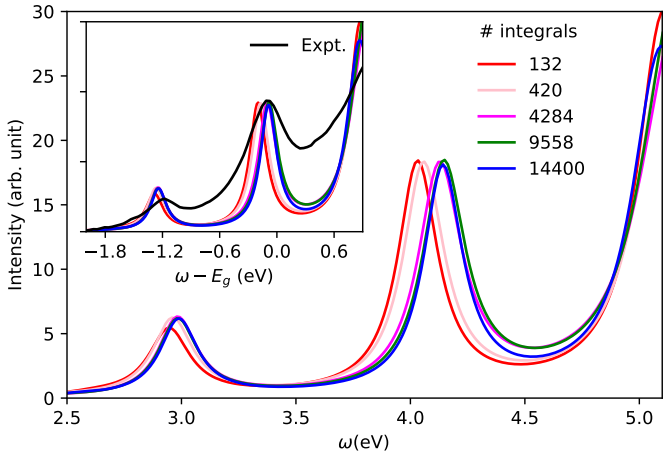

Figure 3.17: Optical absorption spectra of C_{60} in the gas phase computed by solving the BSE with several thresholds ξ for the screened exchange integrals. The resulting number of integrals is indicated. The inset shows the same spectra plotted as a function of $\omega - E_g$, and compared with experiment [176]. E_g is the electronic gap. Note that an accurate spectrum is obtained when using 4,284 integrals instead of the total number which is more than three times larger (14,400).

states, and in principle 14,400 integrals should be evaluated. As shown in Fig. 3.17, the number of screened integrals entering Eq. 3.47 can be greatly reduced without hardly any loss for accuracy in the computed absorption spectrum.

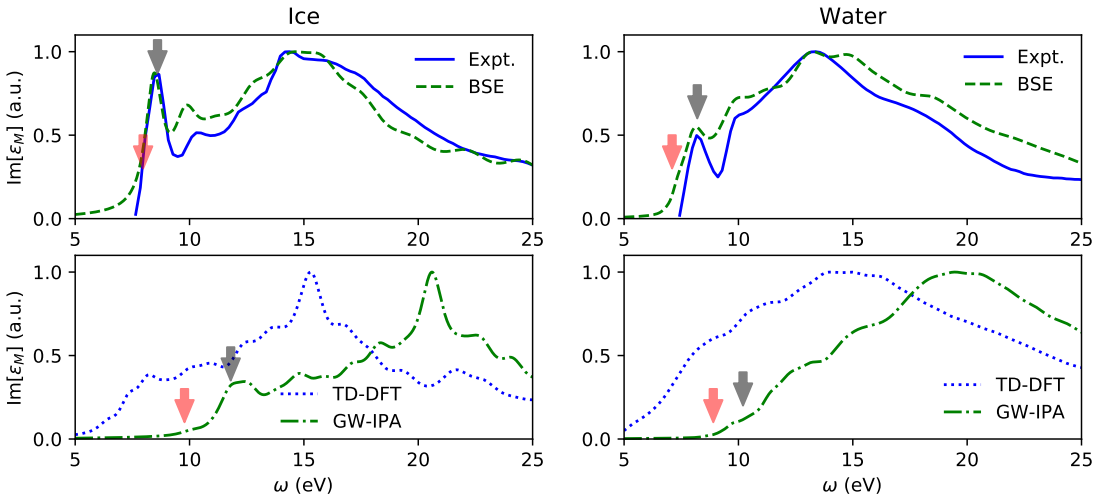

Figure 3.18: Imaginary part of the macroscopic dielectric constant (ϵ_M) as a function of the photon frequency (ω) for a proton-disorder hexagonal ice model (left panel) and liquid water (right panel) computed as an average over nine samples extracted from path-integral molecular dynamics (PIMD) trajectories [95] generated with the MBPol potential. Experimental results (from Refs. 136 and 187 for water and ice, respectively) are shown by the blue solid lines. The black and red arrows indicate the positions of the first excitonic peak and the onset of the spectra, respectively.

Finally, we report results for the optical absorption spectra of liquid water and ice. Even though the first measurement of these spectra dates back to 1974 [187, 136, 179], experimental estimates of the exciton binding energy, E_b^{ex}, are yet uncertain due to uncertainties in the values of ice and water electronic gaps [93, 95] and to the presence of a low energy tail in the absorption spectra ($\sim$ 1.0 eV) [187, 136, 179] hampering a precise determination of the onset energy. Thus far, only a few GW-BSE computations of the optical spectra of water and ice have been carried out; several theoretical studies used rather small unit cells ($\simeq$ 17 water molecules) and approximations for the static dielectric matrix [100, 139, 140, 128, 101] (e.g. homogeneous electron gas model). Here, we performed calculations for several samples of 64 water molecules of liquid water, extracted from MD trajectories [95]

and for 96 water molecules of a proton-disorder hexagonal ice model [94], whose structure was optimized with the PBE0 functional at 0 K [94]. In Fig.3.18, we compare our results with experiments [187, 136]. Due to the underestimation of the G_0W_0@PBE [288, 55, 93] electronic gaps of both systems, GW-BSE absorption spectra are red-shifted with respect to the experimental one. Hence we aligned the first peak of the computed GW-BSE spectrum with experiment, and we shifted the TD-DFT and GW-IPA (independent particle) spectra by the same energy. We found a remarkable agreement between GW-BSE and experiment both for the relative energy positions and intensities of the peaks over a wide range of energy. As expected, the TD-DFT and GW-IPA approximations predict significantly different spectra. We examined the influence of the DFT wavefunctions and eigenvalues chosen as starting point of the calculation, finding a good qualitative agreement between spectra for one water configuration computed at the DFT-PBE and dielectric hybrid (dielectric-dependent hybrid (DDH)[346]) level of theory (see Section 3.2.4). We also investigated the effect of different structural models on the computed spectra, by comparing results obtained using trajectories generated with the MB-pol potential [15] and path integral MD, with those computed for PBE trajectories, extracted from the PBE400 set [69]. Our results show a broadening of the averaged PIMD absorption spectrum, and a red-shift of $\sim$ 0.5 eV with respect to the averaged FPMD@PBE spectrum (see Section 3.2.4).

The exciton binding energies of liquid water and ice were computed using 64 and 96 water molecules, and were evaluated as the energy differences between the onset (E_{b1}^{ex}) and the first main peak (E_{b2}^{ex}) of the absorption spectra (marked by black and red arrows respectively in Fig. 3.18). We obtained $E_{b1}^{ex} = 1.64$ eV and 1.82 eV, and $E_{b2}^{ex} = 2.3$ eV and 3.12 eV for water and ice, respectively. The values for E_{b2}^{ex} are consistent with those reported in previous calculations, i.e. 2.5 [101] and 3.2 [128] eV. Finally, we also performed calculations for a larger supercell including 256 water molecules (2048 valence electrons) and concluded that size effects, although not fully negligible, are rather minor on the value of the exciton binding energies (of the order of $\sim$0.2-0.3 eV).

3.2.4 Technical details

Solution of the Bethe Salpeter equation within density matrix perturbation theory

Within density matrix perturbation theory (DMPT) [386, 304], the first order variation of the density matrix is expressed as:

$$\Delta\hat{\rho} = \left(\hat{P}_v + \hat{P}_c\right)\Delta\hat{\rho}\left(\hat{P}_v + \hat{P}_c\right) \tag{3.48}$$

$$= \hat{P}_c\Delta\hat{\rho}\hat{P}_v + \hat{P}_v\Delta\hat{\rho}\hat{P}_c\,, \tag{3.49}$$

where $\hat{P}_v = \sum_{i=1}^{N_{\rm occ}} |\varphi_i\rangle\langle\varphi_i|$, $\hat{P}_c = 1 - \hat{P}_v$, N_{occ} is the number of occupied states, and φ_i is the i-th occupied state of the unperturbed Hamiltonian (with energy ε_i). In Eq. 3.48 we have used the completeness of the eigenvectors of the unperturbed Hamiltonian, and in Eq. 3.49 we have used the property: $\hat{P}_v\Delta\hat{\rho}\hat{P}_v = \hat{P}_c\Delta\hat{\rho}\hat{P}_c = 0$. Introducing the following functions in Eq. 3.49:

$$|a_v\rangle = \hat{P}_c\Delta\hat{\rho}\,|\varphi_v\rangle \tag{3.50}$$

$$|b_v\rangle = \hat{P}_c\Delta\hat{\rho}^\dagger\,|\varphi_v\rangle\,, \tag{3.51}$$

we obtain an expression for $\Delta\hat{\rho}$ that does not contain any explicit summation over empty states:

$$\Delta\hat{\rho} = \sum_{v=1}^{N_{\rm occ}} \left(|a_v\rangle\langle\varphi_v| + |\varphi_v\rangle\langle b_v|\right)\,. \tag{3.52}$$

The function a_v and b_v are obtained solving the linearized Liouville equation:

$$\omega\Delta\hat{\rho} - [\hat{H}^o, \Delta\hat{\rho}] - [\Delta\hat{V}_{\rm H}, \hat{\rho}^o] - [\Delta\hat{\Sigma}, \hat{\rho}^o] = -[\hat{\phi}, \hat{\rho}^o]\,. \tag{3.53}$$

Multiplying Eq. 3.53 and its Hermitian conjugate by $\hat{P}_c$ to the left, and by $|\varphi_v\rangle$ to the right, we obtain:

$$\left(\omega\hat{I} - \hat{H}^o + \varepsilon_v\right)|a_v\rangle - \hat{P}_c\left[\Delta\hat{V}_{\rm H} + \Delta\hat{\Sigma}, \hat{\rho}^o\right]|\varphi_v\rangle = -\hat{P}_c\hat{\phi}\,|\varphi_v\rangle \tag{3.54}$$

$$\left(\omega\hat{I} + \hat{H}^o - \varepsilon_v\right)|b_v\rangle + \hat{P}_c\left[\Delta\hat{V}^\dagger_{\rm H} + \Delta\hat{\Sigma}^\dagger, \hat{\rho}^o\right]|\varphi_v\rangle = \hat{P}_c\hat{\phi}\,|\varphi_v\rangle\ , \tag{3.55}$$

where $\hat{I}$ is the identity operator. Because the two commutators in Eq. 3.54 and in Eq. 3.55 couple the set of a_v and b_v, we introduce the following matrix notation:

$$\begin{pmatrix} \omega\mathcal{I} - \mathcal{D} - \mathcal{K}^{1e} + \mathcal{K}^{1d} & -\mathcal{K}^{2e} + \mathcal{K}^{2d} \\ \mathcal{K}^{2e} - \mathcal{K}^{2d} & \omega\mathcal{I} + \mathcal{D} + \mathcal{K}^{1e} - \mathcal{K}^{1d} \end{pmatrix} \begin{pmatrix} \mathcal{A} \\ \mathcal{B} \end{pmatrix} = \begin{pmatrix} \left\{-\hat{P}_c\hat{\phi}\,|\varphi_v\rangle\right\} \\ \left\{\hat{P}_c\hat{\phi}\,|\varphi_v\rangle\right\} \end{pmatrix}\ , \tag{3.56}$$

where $\mathcal{A} = \{|a_v\rangle\}$, $\mathcal{B} = \{|b_v\rangle\}$, $v \in [1..N_{\rm occ}]$ and

$$\mathcal{I}\mathcal{A} = \mathcal{A}\,,\quad \mathcal{I}\mathcal{B} = \mathcal{B}\,, \tag{3.57}$$

$$\mathcal{D}\mathcal{A} = \left\{\hat{P}_c(\hat{H}^o - \epsilon_v\hat{I})\,|a_v\rangle : v \in [1..N_{\rm occ}]\right\}\ , \tag{3.58}$$

$$\mathcal{K}^{1e}\mathcal{A} = \left\{2\int d\mathbf{r}' P_c(\mathbf{r},\mathbf{r}')\varphi_v(\mathbf{r}')\sum_{v'}^{N_{\rm occ}}\int d\mathbf{r}'' v_c(\mathbf{r}',\mathbf{r}'')\varphi^*_{v'}(\mathbf{r}'')a_{v'}(\mathbf{r}'') : v \in [1..N_{\rm occ}]\right\}\ , \tag{3.59}$$

$$\mathcal{K}^{2e}\mathcal{A} = \left\{2\int d\mathbf{r}' P_c(\mathbf{r},\mathbf{r}')\varphi_v(\mathbf{r}')\sum_{v'}^{N_{\rm occ}}\int d\mathbf{r}'' v_c(\mathbf{r}',\mathbf{r}'')a^*_{v'}(\mathbf{r}'')\varphi_{v'}(\mathbf{r}'') : v \in [1..N_{\rm occ}]\right\}\ , \tag{3.60}$$

$$\mathcal{K}^{1d}\mathcal{A} = \left\{ \int d\mathbf{r}' P_c(\mathbf{r},\mathbf{r}') \sum_{v'}^{N_{\rm occ}} a_{v'}(\mathbf{r}') \int d\mathbf{r}'' W(\mathbf{r}',\mathbf{r}'') \varphi^*_{v'}(\mathbf{r}'') \varphi_v(\mathbf{r}'') : v \in [1..N_{\rm occ}] \right\}, \tag{3.61}$$

$$\mathcal{K}^{2d}\mathcal{A} = \left\{ \int d\mathbf{r}' P_c(\mathbf{r},\mathbf{r}') \sum_{v'}^{N_{\rm occ}} \varphi_{v'}(\mathbf{r}') \int d\mathbf{r}'' W(\mathbf{r}',\mathbf{r}'') a^*_{v'}(\mathbf{r}'') \varphi_v(\mathbf{r}'') : v \in [1..N_{\rm occ}] \right\}. \tag{3.62}$$

Equations for the application of $\mathcal{D}$, $\mathcal{K}^{1e}$, $\mathcal{K}^{2e}$, $\mathcal{K}^{1d}$, and $\mathcal{K}^{2d}$ on $\mathcal{B}$ can be obtained substituting a_v with b_v in Eq.s 3.58-3.62, where W and v_c are the screened and bare Coulomb interactions, respectively. In Eqs. 3.58, $\hat{H}^o$ is defined in terms of the G_0W_0 quasiparticle energies $\epsilon_m^{\rm QP}$, the KS eigenvalues $\epsilon_m^{\rm KS}$ and KS wavefunctions $|\varphi_m\rangle$ as:

$$\hat{H}^{\rm o} = \hat{H}^{\rm o}_{KS} + \sum_{m=1}^{N_{\rm cut}} |\varphi_m\rangle(\epsilon_m^{\rm QP} - \epsilon_m^{\rm KS} - \Delta\varepsilon)\langle\varphi_m| + \Delta\varepsilon\hat{I}, \tag{3.63}$$

In our calculations, G_0W_0 eigenvalues are obtained for all the occupied states and for some of the empty states up to a given number $N_{\rm cut}$. For the systems studied in this work, $N_{\rm cut}$ was chosen to correspond to energies about $\sim$ 10 eV and $\sim$ 20 eV above the conduction band minimum for the molecules of the Thiel's set, and for water and ice, respectively. For the remaining states higher in energy, we approximated $\Delta\varepsilon = \epsilon^{\rm QP}_{N_{\rm cut}} - \epsilon^{\rm KS}_{N_{\rm cut}}$.

In Eqs. 3.61 and 3.62, W is the statically screened Coulomb potential:

$$W = \epsilon^{-1} v_c = v_c + (v_c + f_{xc})\chi v_c, \tag{3.64}$$

where χ is the density-density response function, v_c is the bare Coulomb potential, and f_{xc} is the functional derivative of the xc potential with respect to the electron density.

Within the plane wave basis set, the bare Coulomb potential, $v_c = \frac{4\pi e^2}{|\mathbf{q}+\mathbf{G}|^2}\delta_{\mathbf{G}\mathbf{G}'}$ (δ is

the Kronecker delta), is divergent in the long wavelength limit ($\mathbf{q} \to \mathbf{0}$). The divergence in Eq. (3.64) occurring when $\mathbf{G} = \mathbf{G}' = \mathbf{0}$ can be numerically integrated as:

$$W(\mathbf{0},\mathbf{0}) = v_c(\mathbf{0},\mathbf{0}) + 4\pi e^2 \int_{R_{q=0}} \frac{d\mathbf{q}}{(2\pi)^3} \frac{\epsilon_M^{-1} - 1}{q^2}, \tag{3.65}$$

where $\epsilon_M = \frac{1}{\epsilon^{-1}_{\mathbf{00}}}$ is the macroscopic dielectric constant. The first term, $v_c(\mathbf{0},\mathbf{0})$, in the right-hand side of Eq. 3.65 was formally treated with the Gygi-Baldereschi method [126] to compute the Fock exact exchange matrix elements in reciprocal space. The integration in the second term is evaluated in the region $R_{q=0}$ of the first Brillouin zone (BZ) enclosing the Γ-point (i.e. $\mathbf{q} = \mathbf{0}$). The integration in Eq. (3.65) can be evaluated approximating the BZ with a sphere, or by using a Monte Carlo integration method to take into account the specific shape of the BZ [117]. ϵ_M is evaluated using the Qbox code [124] by computing the variation of macroscopic polarization of the system in response to a macroscopic electric field.

Finally, in this work we considered an Hermitian form of $\Delta\hat{\rho}$ (i.e. $|b_v\rangle = |a_v\rangle$), which is referred to as the Tamm-Dancoff [65] approximation and has been extensively discussed in the literature [306, 365, 318].

Finite field algorithm

In this section, we describe the steps followed when solving the BSE using the finite field (FF) approach and bisection techniques; we also discuss the scaling of the algorithm.

Step 1: Ground state calculation

The first step of the calculation involves the solution of the KS equations to obtain ground state single particle orbitals and energies. KS equations may be solved using local or semi-local exchange-correlation functionals (we call this approximation simply DFT) or hybrid-exchange correlation functionals (we call this approximation hybrid-DFT). Within a plane-wave implementation, the solution of the KS equations is of $O(N^3)$ with both local or

hybrid functionals. N is the number of valence electrons. However hybrid-DFT calculations are computationally much more expensive, due to different prefactors and different relative weights of the various parts of the calculations, as indicated in Table 3.5. In our work, the efficiency of solving the KS equations with hybrid functionals is greatly improved by using the bisection algorithm of Refs. 125, 127.

Table 3.5: The scaling of GGA and hybrid-DFT calculations is illustrated for the two main parts involved in the solution of the KS equations: the calculations of $\hat{H}^o_{KS}|\varphi_i\rangle$ (application of the KS Hamiltonian to single particle orbitals) and $\langle\varphi_i|\varphi_j\rangle = \delta_{ij}$ (orbital orthogonalzation). M denotes the number of plane waves. With (hybrid-DFT)$_b$ we denote hybrid calculations carried out using the bisection technique [125, 127]; α^b is the number of non zero orbital pairs included in the calculations of the exchange potential and energy. α^b is usually much smaller than N. We note that in (hybrid-DFT)$_b$ the workload to evaluate $\hat{H}^o_{KS}|\varphi_i\rangle$ can be reduced to $O(N)$ by computing the overlap integrals only in the domain where the bisected orbitals are non zero (not yet implemented; work is in progress to estimate how the implementation may affect parallelization).

	GGA	Hybrid-DFT	(Hybrid-DFT)$_b$
$\hat{H}^o\|\varphi_i\rangle$	$NM\log(M)$	$N^2M\log(M)$	$\alpha^b NM\log(M)\log(N)$
$\langle\varphi_i\|\varphi_j\rangle$	N^2M	N^2M	N^2M height

Step 2: Excited state energies

Excited state energies have been obtained within the G_0W_0 approximation starting from DFT ground states (for water and ice) or from hybrid-DFT (for the molecules belonging to the Thiel's set and for one snapshot of water). The scaling of G_0W_0 calculations is of $O(N^4)$, while that of hybrid-DFT, as mentioned above, is of $O(N^3)$.

In the following, factors $\log(M)$ and $\log(N)$ will be neglected.

Step 3: Solution of the Bethe Salpeter equation

Two main operations are involved in the solution of the BSE within a DMPT [304, 305, 291] approach: the evaluation of the screened Coulomb interaction W, Eq.(3.64) and the application of the matrix in Eq. 3.56.

3.1 Calculation of W

Using density functional perturbation theory (DFPT) [21] to obtain the spectral decomposition [400, 399] of the dielectric matrix ϵ, the scaling of the calculation is of $O(N^4)$,

namely proportional to $N_{\mathrm{PDEP}}N^3$ where N_{PDEP} is the number of eigenpotentials included in the spectral decomposition of ϵ. We define $\alpha^{\mathrm{DFPT}} = \frac{N_{\mathrm{PDEP}}}{N}$.

Using the FF method, the workload to compute W is proportional to N^2 multiplied by the workload of either DFT or hybrid-DFT calculations, hence it is of $O(N^5)$. However it can be decreased to $O(N^4)$ using the bisection technique [125], and it becomes proportional to $\alpha^b \times N^4$, where in general $\alpha^b < \alpha^{\mathrm{DFPT}}$ and, importantly, the larger the system, the smaller is the ratio $\frac{\alpha^b}{\alpha^{\mathrm{DFPT}}}$. Most importantly, the scaling of FF computations is the same for DFT and hybrid-DFT calculations. The screening in the Random-Phase Approximation (RPA) can be recovered within FF by skipping updates of the xc potential during self-consistency.

3.2 Application of the Liouville superoperator

The scaling of this step is $O(N^3)$, similar to the method of M. Marsili et al. [236], with a pre-factor greatly reduced when using bisected orbitals, compared to calculations using Bloch orbitals.

In addition to the overall scaling discussed above, pre-factors and parallelization techniques play an important role in determining the feasibility and efficiency of any algorithm. Our FF calculations is fully parallelized via coupling the WEST [117] and Qbox [124] codes operating in client-server mode; the WEST code prepares simultaneously multiple unscreened exchange integrals $\tau^u_{vv'}$; the calculations of the perturbed KS equations are performed by different Qbox instances, which in return yield the response densities, thus enabling WEST to evaluate the screened exchange integrals $\tau_{vv'}$.

Convergence of BSE calculations as a function of bisection threshold

We used the bisection technique[125, 127, 68] to obtain localized orbitals from the KS wavefunctions by applying a unitary transformation U: $|\tilde{\varphi}_m\rangle = \sum_v U_{mv}|\varphi_v\rangle$. We then defined the transformed screened integral matrix $\tilde{\tau} = U\tau U^\dagger$, and leveraged the sparsity of the latter to compute the FF response only for selected elements. In the bisection method [125], the degree of localization of an orbital $\tilde{\varphi}_m$ in a subdomain $\Omega^{(k)}$ is given by the singular value

$c_m^{(k)}$ of the Walsh projector[387] $P^{(k)}$ associated with the m-th orbital. Elements of $\tilde{\tau}$ are computed only if the corresponding orbitals have a sizable 2-norm in a common subdomain, i.e. they are neglected if $\exists P^{(k)}$: $\left(c_m^{(k)}\right)^2 < \xi$ and $\left(c_n^{(k)}\right)^2 > (1-\xi)$ or $\left(c_m^{(k)}\right)^2 > (1-\xi)$ and $\left(c_n^{(k)}\right)^2 < \xi$, where $\xi \in [0,1]$ is the bisection threshold[127].

In Fig. 3.19, we show the convergence of the BSE spectra of water as a function of the number of screened exchange integrals included in the calculations. We show results for three different snapshots. Note the similarity of the spectra computed with $\simeq 5,000$ and $\simeq 10,000$ integrals and the nearly identical results in the low part of the spectra (below 7.5 eV). The total number of integrals for the system shown in Fig. 3.19 (64 water molecules at the experimental density) is 65,536.

In Tab. 3.6, we show the convergence of the exciton binding energy of C_{60} as a function of the number of screened exchange integrals included in the calculations.

We found that a convenient way to determine the threshold ξ for which spectra are reasonably well converged is by determining the convergence of the Fock energy, $\tilde{E}_x$, as a function of ξ. In Tables 3.7, 3.8 and 3.9, we show how the Fock energy and the relative error $r = \left|[\tilde{E}_{\rm x}(\xi) - \tilde{E}_{\rm x}(\xi=0)]/\tilde{E}_{\rm x}(\xi=0)\right|$, vary as a function of the bisection threshold, ξ, for C_{60}, water and ice samples. See also Fig. 3.20, 3.21, and 3.22.

Table 3.6: The number of screened exchange integrals ($N_{\rm int}$) entering Eq. 3.46 and the computed exciton energy of the first singlet transition of the C_{60} molecule as a function of the bisection threshold, ξ, compared with experiment. The bisection orbitals were obtained using 5 bisection layers in each direction.

ξ	$N_{\rm int}$	$E^{\rm ex}$ (eV)
0.500	132	3.05
0.282	420	3.03
0.032	4284	3.01
0.010	9558	3.00
0.000	14400	3.00
Expt.	–	3.01

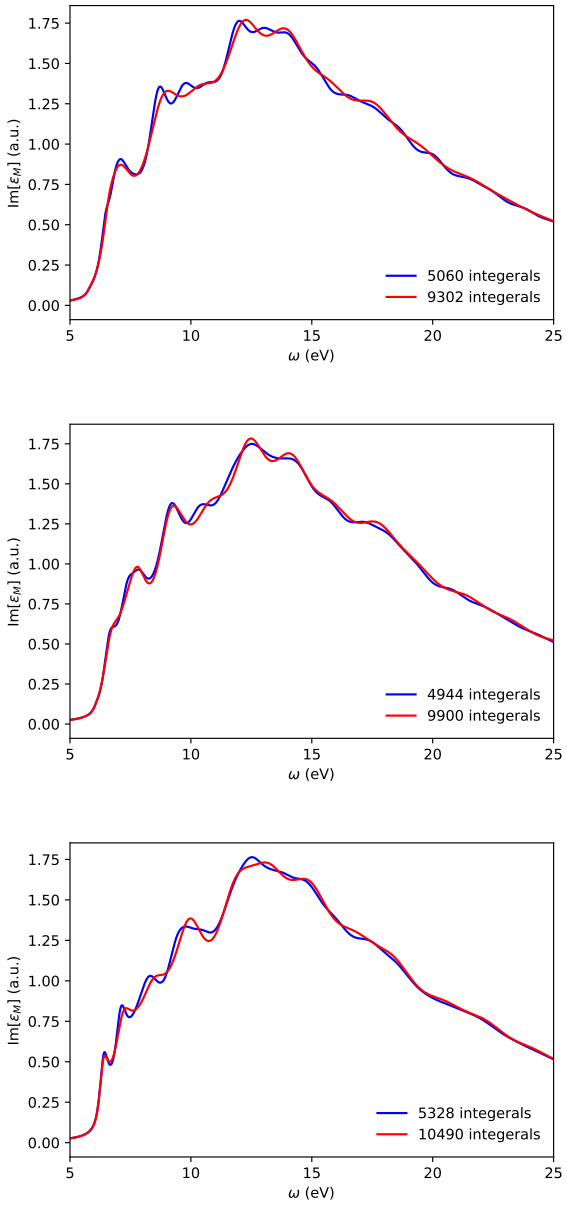

Figure 3.19: Imaginary part of the macroscopic dielectric constant (ϵ_M) of three snapshots representing liquid water, as a function of the photon frequency (ω), computed with two different bisection thresholds of 0.07 and 0.02. The number of the screened exchange integrals corresponding to these threshold values are shown in the inset of each panel. The bisection orbitals were obtained using 2 bisection layers in each direction.

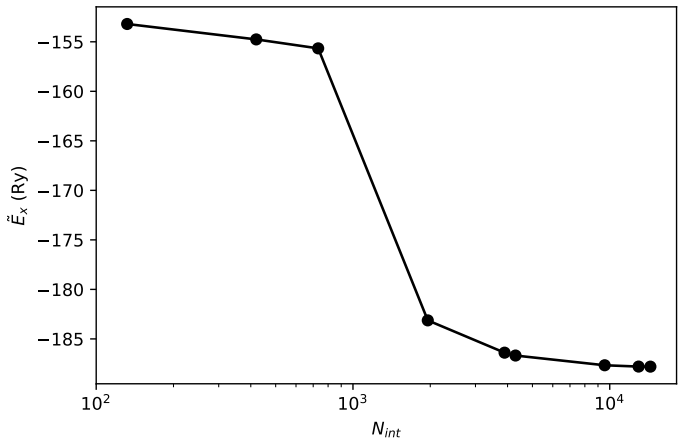

Figure 3.20: The Fock energy, $\tilde{E}_x$, as a function of the number of screened exchange integrals (N_{int}), for the C_{60} molecule.

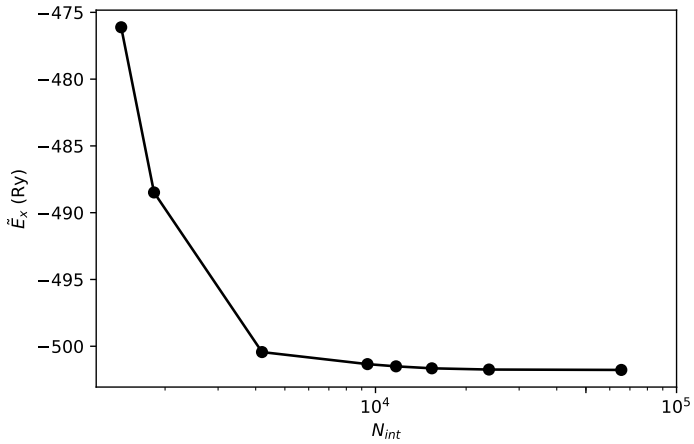

Figure 3.21: The Fock energy, $\tilde{E}_x$, as a function of the number of screened exchange integrals (N_{int}), for a representative liquid water sample.

Table 3.7: The number of the screened exchange integrals ($N_{\rm int}$) and the Fock energy $\tilde{E}_{\rm x}$ as function of the bisection threshold, ξ. The last two columns show $s = N_{\rm int}(\xi = 0)/N_{\rm int}(\xi)$ and the relative error $r = \left|[\tilde{E}_{\rm x}(\xi) - \tilde{E}_{\rm x}(\xi = 0)]/\tilde{E}_{\rm x}(\xi = 0)\right|$ (in %), for the C_{60} molecule (see also in Table 3.6). The bisection orbitals were obtained using 5 bisection layers in each direction. The function $\tilde{E}_{\rm x}(N_{\rm int})$ is shown in Fig.(3.20).

ξ	$N_{\rm int}$	$\tilde{E}_{\rm x}$ (Ry)	s	$r(\%)$
0.0000	14400	-187.79985	1.00000	0.00000
0.0032	12954	-187.79268	1.11163	0.00382
0.0100	9558	-187.66025	1.50659	0.07433
0.0316	4296	-186.67825	3.35196	0.59723
0.0400	3894	-186.38910	3.69800	0.75120
0.1000	1956	-183.12780	7.36196	2.48778
0.2000	732	-155.66261	19.67213	17.11250
0.2815	420	-154.75853	34.28571	17.59390
0.5000	132	-153.20143	109.09091	18.42303

Table 3.8: The same quantities as in Table 3.7 are reported for a liquid water snapshot. The bisection orbitals were obtained using 2 bisection layers in each direction. The function $\tilde{E}_{\rm x}(N_{\rm int})$ is shown in Fig.(3.21).

ξ	$N_{\rm int}$	$\tilde{E}_{\rm x}$ (Ry)	s	$r(\%)$
0.0000	65536	-501.77258	1.00000	0.00000
0.0032	23818	-501.74415	2.75153	0.00567
0.0100	15388	-501.65208	4.25890	0.02402
0.0200	11700	-501.50407	5.60137	0.05351
0.0316	9404	-501.33773	6.96895	0.08666
0.1000	4198	-500.43546	15.61124	0.26648
0.3162	1838	-488.48393	35.65615	2.64834
0.4472	1430	-476.11718	45.82937	5.11296

Table 3.9: The same quantities as in Table 3.7 are reported for the ice model. The bisection orbitals were obtained using 2 bisection layers in each direction. The function $\tilde{E}_{\rm x}(N_{\rm int})$ is shown in Fig.(3.22).

ξ	$N_{\rm int}$	$\tilde{E}_{\rm x}$ (Ry)	s	$r(\%)$
0.0000	147456	-755.46176	1.00000	0.00000
0.0032	20878	-755.37680	7.06275	0.01125
0.0100	10416	-755.26208	14.15668	0.02643
0.0200	7622	-754.94636	19.34610	0.06822
0.0316	6194	-754.53863	23.80626	0.12219
0.1000	3318	-750.97496	44.44123	0.59391
0.3162	2948	-746.69768	50.01900	1.16010
0.4472	2368	-728.21575	62.27027	3.60654

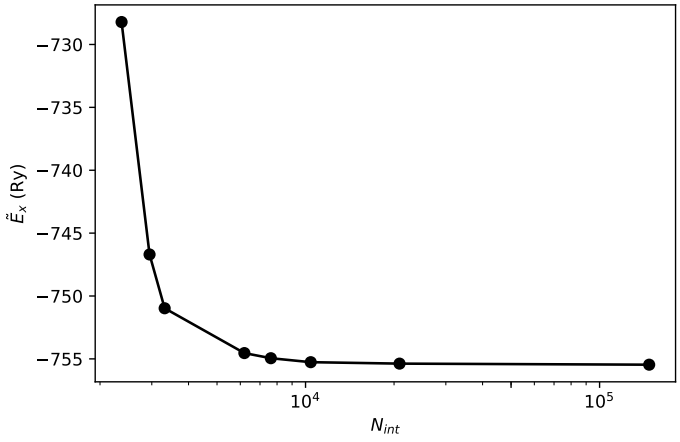

Figure 3.22: The Fock energy, $\tilde{E}_x$, as a function of the number of screened exchange integrals (N_{int}), for the ice model used in this work.

Computational setup for the calculation of neutral excitation energies of molecules belonging to the Thiel's set

The coordinates of the 28 organic molecules were taken from the supplementary material of Ref. 327, where geometrical relaxations were performed at the Møller-Plesset second-order perturbation theory level with the 6-31G* basis (MP2/6-31G level). We performed DFT calculations using both the Perdew–Burke–Ernzerhof (PBE) generalized gradient density functional [279] and the PBE0 hybrid functional [4] with the optimized norm-conserving Vanderbilt (ONCV) pseudopotentials [324] to model the interaction between ionic cores and electrons. The kinetic energy cutoff for the plane-wave basis set expansion was set to 60 Ry (240 Ry for the charge density). We used periodic boundary conditions and orthorhombic cells with the smallest distance between atoms belonging to different replicas equal to 15 Å in each direction.

The quasi-particle energies of the molecules were computed with the G_0W_0 method using the WEST code [117]. We used $10 \times N$ projective dielectric eigenpotentials (PDEPs) to represent the dielectric matrix (N is the number of valance electrons). Based on the convergence tests performed for the GW100 set [118], $10 \times N$ is sufficient to converge the

computed vertical ionization potential (VIP) and vertical electron affinity (VEA) within 0.1 eV. We note that G_0W_0 calculations may also be carried out in finite field, without the need of determining eigenpotentials of the dielectric matrix [220].

Table 3.10 shows the G_0W_0 VIP energy of the molecules of the Thiel's set [343, 344] computed using the PBE and PBE0 functional ground state wavefunctions. The G_0W_0 VIP energy of the molecules are in close agreement with experiments, with a mean absolute deviation (MAD) of 0.59 (PBE) and 0.26 (PBE0) eV, respectively.

Table 3.11 shows the BSE singlet excitation energies of the molecules of the Thiel's set [343, 344] computed using PBE and PBE0 hybrid functionals, and using different levels of theory for W corresponding to different approximations for f_{xc} and χ.

Table 3.10: Vertical ionization potentials (eV) of 28 molecules computed using DFT-PBE, G_0W_0@PBE and G_0W_0@PBE0. Experimental values were taken from the NIST Computational Chemistry Comparison and Benchmark Database (with the exception of propanamide for which no experiment was available). The last two rows show the mean absolute deviation (MAD) and root mean squared deviation (RMSD) between the computed energies and experimental values.

Molecule	DFT-PBE	G_0W_0@PBE	G_0W_0@PBE0	Expt.
Ethene	6.61	10.25	10.39	10.68
Butadiene	5.71	8.69	8.89	9.07
Hexatriene	5.25	7.81	8.06	8.30
Octatetraene	5.05	7.28	6.31	7.79
Cyclopropene	5.93	9.62	9.75	9.86
Cyclopentadiene	5.16	8.17	8.34	8.61
Norbornadiene	5.10	8.17	8.38	8.38
Benzene	6.14	8.87	9.06	9.25
Naphthalene	5.27	7.61	7.82	8.14
Furan	5.47	8.52	8.71	8.90
Pyrrole	4.96	7.90	8.07	8.23
Imidazole	5.53	8.57	8.74	8.96
Pyridine	5.73	8.90	9.44	9.51
Pyrazine	5.70	9.00	9.47	9.63
Pyrimidine	5.80	9.04	9.53	9.73
Pyridazine	5.26	8.50	9.07	9.31
Triazine	6.37	9.73	10.22	10.40
Tetrazine	5.67	9.11	9.61	9.70

Continued on next page

Table 3.10: Continued.

Molecule	DFT-PBE	G_0W_0@PBE	G_0W_0@PBE0	Expt.
Formaldehyde	6.14	10.24	10.67	10.88
Acetone	5.51	8.93	9.46	9.80
Benzoquinone	6.15	8.88	9.77	10.11
Formamide	5.90	9.35	10.02	10.16
Acetamide	5.60	8.96	9.57	10.00
Propanamide	5.60	8.86	9.47	–
Cytosine	5.52	8.11	8.53	8.90
Thymine	5.83	8.50	8.88	9.10
Uracil	6.00	8.98	9.26	9.50
Adenine	5.30	7.77	8.08	8.40
MAD	3.65	0.59	0.27	
RMSD	3.69	0.63	0.37	

Table 3.11: The BSE singlet excitation energies (eV) of the Thiel's molecular set, computed with different levels of theory for the screened Coulomb interaction W [see Eq. 3.64]: W^{RPA} is obtained with χ evaluated within the Random Phase Approximation (RPA), and $f_{xc} = 0$ in Eq. 3.64. $\tilde{W}^{\mathrm{RPA}}$ is obtained with χ evaluated within RPA and $f_{xc} \neq 0$ in Eq. 3.64. W is obtained with χ evaluated beyond RPA and $f_{xc} = 0$. $\tilde{W}$ is obtained with χ evaluated beyond RPA and $f_{xc} \neq 0$ in Eq. 3.64. All BSE calculations were performed using PBE wavefunctions except for those maked as W@PBE0, where we used PBE0 wavefunctions. The BSE results were compared with the best theory estimates (BTE) reported in Ref. 344, and with the results of BSE@G_0W_0@PBE0 reported in Ref. 165. The last two rows show the mean deviation (MD) and mean absolute deviation (MAD) between BSE and BTE energies for the data presented in the table.

Molecule	State	BSE						BTE
		W^{RPA}	$\tilde{W}^{\mathrm{RPA}}$	W	$\tilde{W}$	W@PBE0	Ref. 165	Ref. 344
Ethene	$1B_{1u}$	7.65	7.61	7.88	7.87	8.18	7.02	7.80
E-Butadiene	$1B_u$	5.53	5.57	5.64	5.70	6.11	5.36	6.18
E-Butadiene	$2A_g$	5.39	5.47	5.44	5.54	5.99	6.20	6.55
E-Hexatriene	$1B_u$	4.55	4.56	4.65	4.67	5.11	4.41	5.10
E-Hexatriene	$2A_g$	4.36	4.41	4.40	4.47	5.31	5.53	5.09
E-Octatetraene	$2A_g$	3.53	3.57	3.57	3.62	4.12	4.93	4.47
E-Octatetraene	$1B_u$	3.89	3.89	3.98	3.99	4.83	3.80	4.66
Cyclopropene	$1B_1$	5.99	5.95	6.16	6.13	6.56	6.22	6.67
Cyclopropene	$1B_2$	5.59	5.57	5.71	5.74	6.13	5.82	6.68
Cyclopentadiene	$1B_2$	5.39	5.56	5.43	5.61	5.78	4.58	5.55
Cyclopentadiene	$2A_1$	5.31	5.38	5.37	5.45	6.01	6.07	6.28

Continued on next page

Table 3.11: Continued.

Molecule	State	BSE						BTE
		W^{RPA}	$\tilde{W}^{\mathrm{RPA}}$	W	$\tilde{W}$	W@PBE0	Ref. 165	Ref. 344
Norbornadiene	$1A_2$	4.64	4.62	4.77	4.75	5.17	4.61	5.37
Norbornadiene	$1B_2$	4.89	5.03	4.92	5.07	5.26	5.45	6.21
Benzene	$1B_{2u}$	4.39	4.45	4.48	4.55	4.93	4.76	5.08
Benzene	$1B_{1u}$	6.07	6.19	6.15	6.29	6.50	5.59	6.54
Naphthalene	$1B_{3u}$	3.82	3.81	3.91	3.90	4.38	3.93	4.25
Naphthalene	$1B_{2u}$	3.57	3.60	3.63	3.68	4.04	3.96	4.82
Naphthalene	$2A_g$	4.91	4.94	4.98	5.02	5.27	5.45	5.90
Naphthalene	$1B_{1g}$	4.61	4.65	4.67	4.71	5.48	5.14	5.75
Naphthalene	$2B_{3u}$	5.45	5.41	5.55	5.52	6.04	5.35	6.11
Naphthalene	$2B_{2u}$	5.37	5.39	5.45	5.48	5.95	5.58	6.36
Naphthalene	$2B_{1g}$	5.40	5.42	5.45	5.51	6.29	–	6.46
Naphthalene	$3A_g$	5.57	5.62	5.59	5.66	6.37	–	6.49
Furan	$1B_2$	5.66	5.83	5.69	5.87	6.04	5.50	6.32
Furan	$2A_1$	5.57	5.64	5.62	5.71	5.98	5.98	6.57
Furan	$3A_1$	7.00	7.19	7.01	7.22	7.40	–	8.13
Pyrrole	$2A_1$	5.28	5.33	5.34	5.42	5.49	5.57	6.37
Pyrrole	$1B_2$	4.90	5.06	4.95	5.11	5.29	6.38	6.57
Pyrrole	$3A_1$	6.17	6.37	6.20	6.40	6.64	–	7.91
Imidazole	$2A^{'}$	5.27	5.30	5.34	5.39	5.55	5.61	6.25
Imidazole	$1A^{''}$	4.64	4.80	4.67	4.84	4.93	–	6.65
Imidazole	$3A^{'}$	5.74	5.87	5.76	5.94	6.10	6.39	6.73
Pyridine	$1B_2$	3.89	3.78	4.06	3.96	4.82	4.81	4.85
Pyridine	$1B_1$	4.49	4.54	4.52	4.60	5.04	4.34	4.59
Pyridine	$1A_2$	4.08	4.09	4.16	4.19	4.95	4.68	5.11
Pyridine	$2A_1$	5.44	5.57	5.47	5.63	6.13	5.77	6.26
Pyridine	$2B_2$	6.12	6.25	6.16	6.30	6.65	–	7.27
Pyridine	$3A_1$	5.65	5.63	5.76	5.72	6.33	–	7.18
Pyrazine	$1B_{3u}$	4.51	4.55	4.56	4.61	4.96	3.49	4.13
Pyrazine	$1A_u$	3.74	3.75	3.83	3.85	4.56	4.31	4.98
Pyrazine	$1B_{2u}$	4.37	4.21	4.59	4.44	3.98	4.61	4.97
Pyrazine	$1B_{2g}$	6.93	7.09	6.95	7.12	7.62	4.96	5.65
Pyrazine	$1B_{1g}$	5.05	5.10	5.12	5.18	6.11	5.89	6.69
Pyrazine	$1B_{1u}$	6.00	5.95	6.11	6.09	6.54	5.93	6.83
Pyrazine	$2B_{2u}$	6.44	6.62	6.46	6.63	7.11	–	7.81
Pyrazine	$2B_{1u}$	6.29	6.46	6.33	6.51	7.00	–	7.86
Pyrimidine	$1B_1$	3.28	3.22	3.46	3.41	5.26	3.80	4.43
Pyrimidine	$1A_2$	3.57	3.57	3.72	3.73	4.46	4.17	4.85
Pyrimidine	$1B_2$	4.65	4.71	4.74	4.82	4.19	5.02	5.34
Pyrimidine	$2A_1$	5.85	5.81	6.00	5.97	6.58	6.01	6.82
Pyridazine	$1B_1$	4.95	5.10	4.98	5.14	5.63	3.11	3.85

Continued on next page

Table 3.11: Continued.

Molecule	State	BSE						BTE
		W^{RPA}	$\tilde{W}^{\mathrm{RPA}}$	W	$\tilde{W}$	W@PBE0	Ref. 165	Ref. 344
Pyridazine	$1A_2$	3.13	3.12	3.27	3.28	4.08	3.75	4.44
Pyridazine	$2A_1$	4.61	4.66	4.69	4.77	5.11	4.86	5.20
Pyridazine	$2A_2$	4.33	4.22	4.55	4.44	5.49	5.04	5.66
s-Triazine	$1A_1''$	3.42	3.45	3.51	3.56	4.25	4.01	4.70
s-Tetrazine	$1B_{3u}$	4.47	4.52	4.50	4.56	2.25	1.73	2.46
s-Tetrazine	$1A_u$	2.56	2.55	2.65	2.66	3.41	3.11	3.78
s-Tetrazine	$1B_{1g}$	3.99	3.88	4.16	4.06	4.59	4.08	4.87
s-Tetrazine	$1B_{2u}$	1.40	1.31	1.56	1.47	5.06	4.70	5.08
s-Tetrazine	$1B_{2g}$	5.09	5.23	5.13	5.27	5.83	4.65	5.28
s-Tetrazine	$2A_u$	4.19	4.11	4.34	4.25	5.14	4.73	5.39
s-Tetrazine	$1B_{3g}$	4.18	4.12	4.31	4.26	5.07	–	5.76
Formaldehyde	$1A_2$	2.68	2.64	2.99	2.96	3.70	3.15	3.88
Formaldehyde	$1B_1$	5.50	5.77	5.52	5.83	6.15	8.11	9.04
Formaldehyde	$2A_1$	6.74	7.02	6.77	7.08	7.45	–	9.29
Acetone	$1A_2$	3.15	3.06	3.37	3.30	4.15	3.54	4.38
Acetone	$1B_1$	4.97	5.13	4.99	5.16	5.61	8.46	9.04
Acetone	$2A_1$	6.28	6.46	6.31	6.49	6.95	8.16	8.90
p-Benzoquinone	$1B_{1g}$	1.35	1.24	1.51	1.41	2.61	2.12	2.74
p-Benzoquinone	$1A_u$	1.35	1.24	1.52	1.41	2.71	2.19	2.86
p-Benzoquinone	$1B_{3g}$	4.16	4.17	4.22	4.23	5.46	3.66	4.44
p-Benzoquinone	$1B_{1u}$	4.55	4.56	4.61	4.63	5.20	4.58	5.47
p-Benzoquinone	$1B_{3u}$	5.56	5.69	5.59	5.72	6.65	5.17	5.55
p-Benzoquinone	$2B_{3g}$	5.55	5.48	5.69	5.62	6.76	6.60	7.16
Formamide	$1A''$	4.02	3.95	4.30	4.24	5.13	5.01	5.55
Formamide	$2A'$	5.14	5.33	5.19	5.41	5.93	6.93	7.35
Acetamide	$1A''$	3.95	3.87	4.19	4.11	4.37	5.02	5.62
Acetamide	$2A'$	4.94	5.13	4.97	5.16	5.56	6.85	7.14
Propanamide	$1A''$	3.93	3.85	4.18	4.10	5.64	5.04	5.65
Propanamide	$2A'$	4.97	5.14	5.00	5.18	4.37	6.87	7.09
Cytosine	$2A'$	3.76	3.78	3.82	3.85	4.41	4.12	4.66
Cytosine	$1A''$	3.83	3.83	3.92	3.93	4.73	4.49	4.87
Cytosine	$2A''$	4.11	4.04	4.21	4.21	4.91	4.98	5.26
Cytosine	$3A'$	4.53	4.57	4.59	4.64	5.18	5.02	5.62
Thymine	$1A''$	3.53	3.44	3.70	3.63	4.69	4.20	4.82
Thymine	$2A'$	4.28	4.29	4.34	4.37	5.01	4.57	5.20
Thymine	$3A'$	5.06	5.08	5.12	5.15	5.86	5.65	6.27
Thymine	$2A''$	4.64	4.55	4.81	4.73	5.25	5.41	6.16
Thymine	$4A'$	5.49	5.52	5.54	5.60	6.06	–	6.53

Continued on next page

Table 3.11: Continued.

Molecule	State	BSE						BTE
		W^{RPA}	$\tilde{W}^{\mathrm{RPA}}$	W	$\tilde{W}$	W@PBE0	Ref. 165	Ref. 344
Uracil	$1A''$	3.48	3.40	3.65	3.58	4.61	4.16	5.00
Uracil	$2A'$	4.38	4.40	4.45	4.48	5.16	4.68	5.25
Uracil	$3A'$	4.97	5.01	5.02	5.07	5.40	5.60	6.26
Uracil	$2A''$	4.57	4.49	4.74	4.67	5.56	5.37	6.10
Uracil	$4A'$	5.49	5.57	5.52	5.62	5.69	–	6.70
Uracil	$3A''$	5.03	5.13	5.07	5.18	6.27	–	6.56
Adenine	$1A''$	3.97	3.95	4.08	4.08	4.69	4.59	5.12
Adenine	$2A'$	4.21	4.23	4.28	4.31	4.85	4.59	5.25
Adenine	$3A'$	4.42	4.42	4.50	4.51	4.92	4.70	5.25
Adenine	$2A''$	4.52	4.47	4.57	4.62	5.01	5.19	5.75
MD (eV)		-1.11	-1.08	-1.02	-0.97	-0.42	-0.58	
MAD (eV)		1.21	1.18	1.12	1.09	0.62	0.60	

Computational setup for the C_{60} fullerene

The geometry of C_{60} was relaxed at the DFT-PBE level of theory, and the calculations were carried out in a supercell of edge 21 Å. We used a ONCV pseudopotential [324], a kinetic energy cut-off for the plane-wave basis of 30 Ry (120 Ry for the charge density). In G_0W_0 calculations, we employed 2048 PDEPs to represent the dielectric matrix. G_0W_0 corrections were computed for 800 states above the lowest unoccupied molecular orbital, and they were used to construct the effective G_0W_0 Hamiltonian (see Eq. 3.63).

Computational setup for liquid water and ice

We used an ice model with 96-water molecules which was optimized using the PBE0 functional (Ref. 94). We considered two water models based on 64 water molecule samples. The first one includes nine snapshots extracted from 1 ns trajectories obtained using the MB-Pol potential and path integral molecular dynamics (PIMD); the snapshots were taken from Ref. 95. The second model includes five equilibrated water snapshots, extracted from the PBE400 dataset [69]. This dataset consists of simulations of an ensemble of 32 indepen-

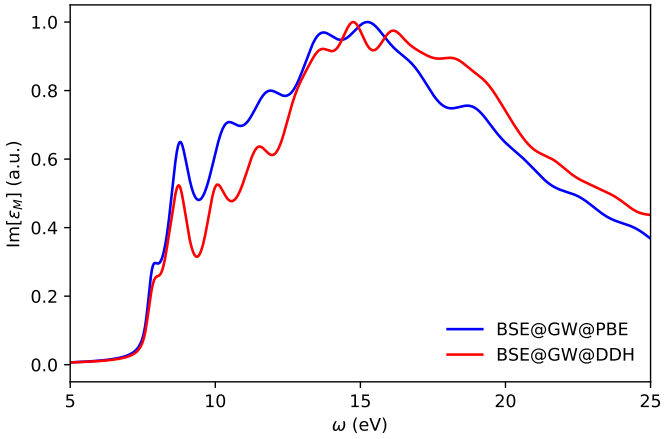

Figure 3.23: Imaginary part of the macroscopic dielectric constant (ϵ_M) as a function of the photon frequency (ω) for liquid water done on the same snapshot, computed using GW-BSE starting from PBE and from dielectric-dependent hybrid (DDH)[346] functional ground states. We used a global dielectric hybrid functional with the parameter determining the fraction of exact exchange equal to the high frequency dielectric constant.

dent samples of liquid water performed using first-principles molecular dynamics simulations (FPMD) at 400 K with the PBE functional[69]. The ground state calculations for ice and water models were carried out with the PBE functional, using ONCV pseudopotentials [324] and a plane-wave kinetic energy cutoff set to 60 Ry. For one water snapshot (see Fig. 3.23) we also conducted calculations with dielectric dependent hybrid functionals. The quasiparticle energies of the systems were obtained with the G_0W_0 approximation, where quasi-particle corrections were computed for 800 electronic states (corresponding to $\sim$ 20 eV) above the conduction band minimum, and they were used to construct the effective G_0W_0 Hamiltonian, see Eq. 3.63. G_0W_0 calculations were performed using the WEST code [117] and were carried out with 2048 PDEPs. In Fig. 3.24 and 3.25 we show the energy gaps and averaged spectra computed for different PIMD and FPMD snapshots, respectively.

Computational setup for solid LiF

The calculation of solid LiF was carried out using a 216 atom cubic supercell with an edge length of 22.83 a.u. We used ONCV pseudopotentials [324], a kinetic energy cut-off for the

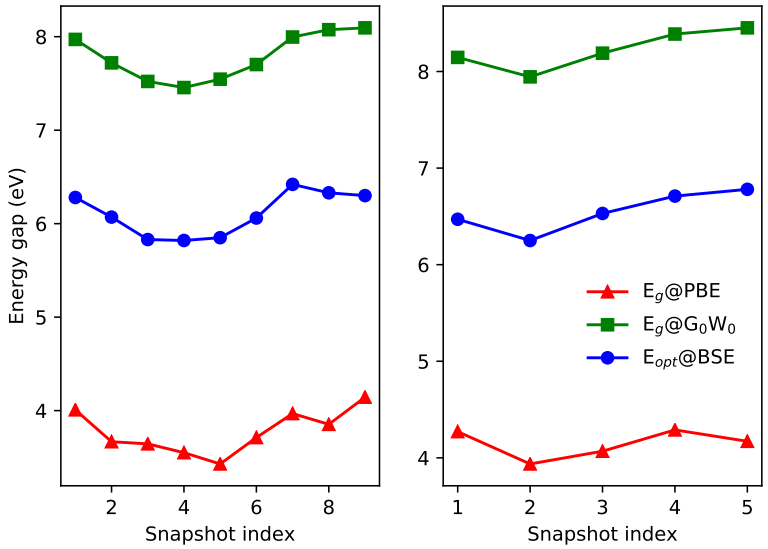

Figure 3.24: The BSE optical (E_{opt}) gap and the electronic (E_{g}) gaps computed with PBE and G_0W_0@PBE for different snapshots extracted from PIMD simulations with the MBPol potential (left-panel) and FPMD with the PBE functional (right-panel).

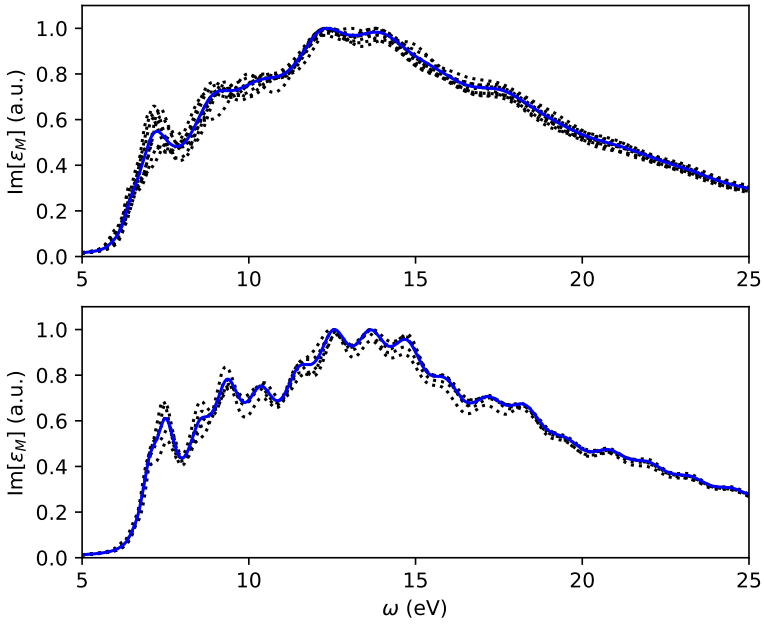

Figure 3.25: Imaginary part of the frequency-dependent macroscopic dielectric constant (ϵ_M) for liquid water computed as an average (blue line) over nine different snapshots (black-dotted lines) extracted from the PIMD-MBPol trajectories [95] (top panel) and from FPMD-PBE trajectories [69] (bottom panel).

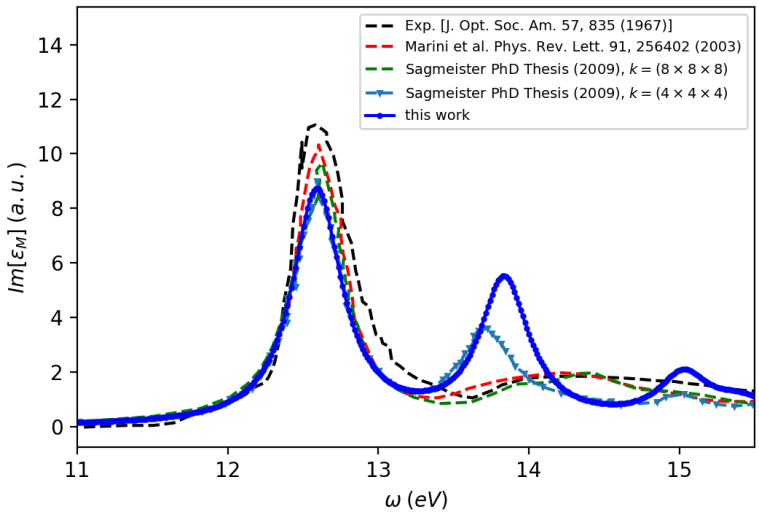

Figure 3.26: Imaginary part of the frequency-dependent macroscopic dielectric constant (ϵ_M) for solid LiF.

plane-wave basis of 60 Ry (240 Ry for the charge density). In G_0W_0 calculations, we employed 2160 PDEPs to represent the dielectric matrix. G_0W_0 corrections were computed for 1800 states, and they were used to construct the effective G_0W_0 Hamiltonian (see Eq. 3.63). The optical absorption spectrum obtained with the proposed methodology is reported in Fig. 3.26, and compares well with the theoretical results reported by Sagmeister[316] using a $(4 \times 4 \times 4)$ sampling of the Brillouin Zone. In the figure we also report theoretical results obtained by Marini *et al.*[231], and by Sagmeister[316] using a $(8 \times 8 \times 8)$ Brillouin zone sampling. As is common procedure in the literature and adopted in ref. 316, we aligned the position of the first peak to experiment[307]. The differences between our results and those of Sagmeister[316] are due to a difference on k-point sampling (e.g. the spurious peak at about 14 eV), which are also responsible for the difference between the results with two different k-meshes reported by Sagmeister[316].

3.2.5 Conclusions

In summary, we have presented a novel method to solve the BSE in finite field, which not only avoids the calculations of virtual electronic states, but avoids all together the calculation of dielectric matrices. In addition, our formulation uses linear combinations of Bloch orbitals that are localized in appropriate regions of real space, leading to substantial computational savings. There are several advantages of the method presented here: calculations beyond the RPA are straightforward and the complexity and scaling of solving the BSE is *the same* when using local or hybrid-DFT starting points. As a consequence, the method proposed here leads to an improvement in both accuracy and efficiency in the calculations of optical spectra of large molecular and condensed systems, and to the ability of coupling such computations with first principles molecular dynamics.

CHAPTER 4

QUANTUM EMBEDDING AND QUANTUM SIMULATIONS OF STRONGLY-CORRELATED ELECTRONIC STATES

Density functional theory (DFT) and post-DFT methods such as many-body perturbation theory have been successfully applied to simulate a wide range of molecular and materials systems. However, DFT fails to give accurate descriptions of electronic structure in certain cases. One of the outstanding challenges for DFT is the strongly-correlated (multireference) electronic states, which are states that cannot be represented as a single determinant of one-electron orbitals. Methods tailored for strongly-correlated states are usually computationally expensive and thus limited to relatively small systems. Fortunately, in many important chemical and materials systems, the strongly-correlated electronic states are localized in certain regions of the space, which motivates a multi-scale description of the system where the active region of the system is described by a high level of theory, with the rest of the system (environment) treated with a low level of theory such as DFT.

In this chapter, we present a quantum embedding theory based on the concept of dielectric screening. The quantum embedding theory is capable of constructing effective models of the active region of the system, with the environment acting as a dielectric screening media described as DFT level. We show that the quantum embedding theory can be used to generate effective models for realistic materials science problems, which can be solved by both classical and quantum computers.

Adapted with permission from H. Ma, M. Govoni, and G. Galli. npj Computational Materials. 6, 85 (2020). Copyright (2020) by Springer Nature. https://doi.org/10.1038/s41524-020-00353-z.

4.1 Introduction

In the last three decades, atomistic simulations based on the solution of the basic equation of quantum mechanics have played an increasingly important role in predicting the properties of functional materials, encompassing catalysts and energy storage systems for energy applications, and materials for quantum information science. Especially in the case of complex, heterogeneous materials, the great majority of first-principles simulations are conducted using density functional theory (DFT), which is in principle exact but in practice requires approximations to enable calculations. Within its various approximations, DFT has been extremely successful in predicting numerous properties of solids, liquids and molecules, and in providing key interpretations to a variety of experimental results; however it is often inadequate to describe so-called strongly-correlated electronic states [61, 358]. We will use here the intuitive notion of strong correlation as pertaining to electronic states that cannot be described by static mean-field theories. Several theoretical and computational methods have been developed over the years to treat systems exhibiting strongly-correlated electronic states, including dynamical mean-field theory [103, 194] and quantum Monte-Carlo [53, 384]; in addition, *ab initio* quantum chemistry methods, traditionally developed for molecules, have been recently applied to solid state problems as well [360]. Unfortunately, these approaches are computationally demanding and it is still challenging to apply them to complex materials containing defects and interfaces, even using high-performance computing architectures.

Quantum computers hold promise to enable efficient quantum mechanical simulations of weakly and strongly-correlated molecules and materials alike [11, 43, 14, 181, 252, 266, 347, 348, 25]; in particular when using quantum computers, one is able to simulate systems of

interacting electrons exponentially faster than using classical computers. Thanks to decades of successful experimental efforts, we are now entering the noisy intermediate-scale quantum (NISQ) era [295], with quantum computers expected to have on the order of 100 quantum bits (qubits); unfortunately this limited number of qubits still prevents straightforward quantum simulations of realistic molecules and materials, whose description requires hundreds of atoms and thousands to millions of degrees of freedom to represent the electronic wavefunctions. An important requirement to tackle complex chemistry and material science problems using NISQ computers is the reduction of the number of electrons treated explicitly at the highest level of accuracy [313, 409]. For instance, building on the idea underpinning dynamical mean field theory [103, 194], one may simplify complex molecular and material science problems by defining active regions (or building blocks) with strongly-correlated electronic states, embedded in an environment that may be described within mean-field theory [26, 196, 315].

In this work, we present a quantum embedding theory built on DFT, which is scalable to large systems and which includes the effect of exchange-correlation interactions of the environment on active regions, thus going beyond commonly adopted approximations. In order to demonstrate the effectiveness and accuracy of the theory, we compute ground and excited state properties of several spin-defects in solids including the negatively charged nitrogen-vacancy (NV) center [67, 308, 75, 242, 58, 76, 112], the neutral silicon-vacancy (SiV) center [79, 98, 120, 312, 119, 370] in diamond, and the Cr impurity (4+) in 4H-SiC [352, 189, 72]. These spin-defects are promising platforms for solid-state quantum information technologies, and they exhibit strongly-correlated electronic states that are critical for the initialization and read-out of their spin states [392, 334, 335, 160, 81, 6]. Our quantum embedding theory yields results in good agreement with existing measurements. In addition, we present theoretical predictions for the position and ordering of the singlet states of SiV and of Cr, and we provide an interpretation of experiments which have so far remained unexplained.

Importantly, we report calculations of spin-defects using a quantum computer [2]. Based

on the effective Hamiltonian derived from the quantum embedding theory, we investigated the strongly-correlated electronic states of the NV center in diamond using quantum phase estimation algorithm (PEA) [3, 11] and variational quantum eigensolvers (VQE) [282, 244, 173], and we show that quantum simulations yield results in agreement with those obtained with classical full configuration interaction (FCI) calculations. Our findings pave the way to the use of near term quantum computers to investigate the properties of realistic heterogeneous materials with first-principles theories.

4.2 Formalism

4.2.1 General strategy

We summarize our strategy in Fig. 4.1. Starting from an atomistic structural model of materials (e.g. obtained from DFT calculations or molecular dynamics simulations), we identify active regions with strongly-correlated electrons, which we describe with an effective Hamiltonian that includes the effect of the environment on the active region. This effective Hamiltonian is constructed using the quantum embedding theory described below, and its eigenvalues can be obtained by either classical algorithms such as exact diagonalization (FCI) or quantum algorithms.

4.2.2 Embedding theory

A number of interesting quantum embedding theories have been proposed over the past decades [361]. For instance, density functional embedding theory has been developed to improve the accuracy and scalability of DFT calculations [152, 115, 164, 102, 395]. Density matrix embedding theory (DMET) [185, 401, 284] and various Green's function based approaches [205, 83], e.g. dynamical mean field theory (DMFT), have been developed to describe systems with strongly-correlated electronic states. At present, *ab initio* calculations of materials using DMET and DMFT have been limited to relatively small unit cells (a few

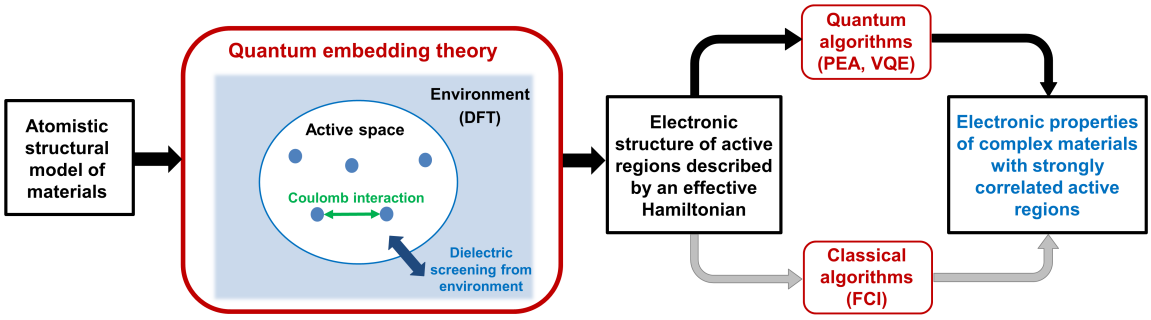

Figure 4.1: General strategy for quantum simulations of materials using quantum embedding. The full system is separated into an active space and its environment, with the electronic states in the active space described by an effective Hamiltonian solved with either classical (e.g. full configuration interaction, FCI) or quantum algorithms (e.g. phase estimation algorithm (PEA), variational quantum eigensolver (VQE)). The effective interaction between electrons in the active space includes the bare Coulomb interaction and a polarization term arising from the dielectric screening of the environment, which is evaluated including exchange-correlation interactions.

tens of atoms) of *pristine* crystals, due to their high computational cost [420, 62]. In this work, we present a quantum embedding theory that is applicable to strongly-correlated electronic states in realistic *heterogeneous* materials and we apply it to systems with hundreds of atoms. The theory, inspired by the constrained random phase approximation (cRPA) approach [9, 247, 143], does not require the explicit evaluation of virtual electronic states [399, 117], thus making the method scalable to materials containing thousands of electrons. Furthermore, cRPA approaches contain a specific approximation (RPA) to the screened Coulomb interaction, which neglects exchange-correlation effects and may lead to inaccuracies in the description of dielectric screening. Our embedding theory goes beyond the RPA by explicitly including exchange-correlation effects, which are evaluated with a recently developed finite-field algorithm [220, 261].

The embedding theory developed here aims at constructing an effective Hamiltonian operating on an active space (A), defined as a subspace of the single-particle Hilbert space:

$$H^{\text{eff}} = \sum_{ij}^{\text{A}} t_{ij}^{\text{eff}} a_i^\dagger a_j + \frac{1}{2} \sum_{ijkl}^{\text{A}} V_{ijkl}^{\text{eff}} a_i^\dagger a_j^\dagger a_l a_k. \tag{4.1}$$

Here t^{eff} and V^{eff} are one-body and two-body interaction terms that take into account the effect of all the electrons that are part of the environment (E) in a mean-field fashion, at the DFT level. An active space can be defined, for example, by solving the Kohn-Sham equations of the full system and selecting a subset of eigenstates among which electronic excitations of interest take place (e.g. defect states within the gap of a semiconductor or insulator). To derive an expression for V^{eff} that properly accounts for all effects of the environment including exchange and correlation interactions, we define the environment density response function (reducible polarizability) $\chi^{\text{E}} = \chi_0^E + \chi_0^{\text{E}} f \chi^E$, where $\chi_0^{\text{E}} = \chi_0 - \chi_0^{\text{A}}$ is the difference between the polarizability of the Kohn-Sham system χ_0 and its projection onto the active space χ_0^{A} (see Section 4.2.3). χ^{E} thus represents the density response outside the active space. The term $f = V + f_{\text{xc}}$ is often called the Hartree-exchange-correlation kernel, where V is the Coulomb interaction and the exchange-correlation kernel f_{xc} is defined as the derivative of the exchange-correlation potential with respect to the electron density. We define the effective interactions between electrons in A as

$$V^{\text{eff}} = V + f \chi^{\text{E}} f, \tag{4.2}$$

given by the sum of the bare Coulomb potential and a polarization term arising from the density response in the environment E. When the RPA is adopted, the exchange-correlation kernel f_{xc} is neglected in Eq. 4.2 and the expression derived here reduces to that used within cRPA. We represent χ^{E} and f on a compact basis obtained from a low-rank decomposition of the dielectric matrix [399, 117] that allows us to avoid the evaluation and summation over virtual electronic states. Once V^{eff} is defined, the one-body term t^{eff} can be computed by subtracting from the Kohn-Sham Hamiltonian a term that accounts for Hartree and exchange-correlation effects in the active space (see Section 4.2.3).

4.2.3 Derivation of the embedding formalism

Within density functional theory (DFT), the single-particle electronic structure of a physical system is determined by the Kohn-Sham (KS) equation

$$H^{\mathrm{KS}} \left|\psi_m\right\rangle = \varepsilon_m \left|\psi_m\right\rangle , \tag{4.3}$$

where the Kohn-Sham Hamiltonian $H^{\mathrm{KS}} = T + V_{\mathrm{ion}} + V_{\mathrm{H}} + V_{\mathrm{xc}}$ includes the kinetic operator as well as ionic, Hartree and exchange-correlation potentials; ε_m and ψ_m are eigenvalues and eigenvectors of H^{KS}. The density response function of the Kohn-Sham system is

$$\chi_0(\boldsymbol{x}_1, \boldsymbol{x}_2) = 2 \sum_{i<j} (f_i - f_j) \frac{\langle\psi_i|\hat{n}(\boldsymbol{x}_1)|\psi_j\rangle \, \langle\psi_j|\hat{n}(\boldsymbol{x}_2)|\psi_i\rangle}{\varepsilon_i - \varepsilon_j} \tag{4.4}$$

where $\hat{n}(\boldsymbol{x})$ is the density operator at $\boldsymbol{x} = \boldsymbol{r}\sigma$ and $\boldsymbol{r}$ and σ are coordinate and spin indeces, respectively, f_i denotes the occupation number of the spin orbital i (not to be confused with the Hartree-exchange-correlation kernel f).

The set of Kohn-Sham orbitals constitutes a complete orthogonal basis of the one-particle Hilbert space. In this work we define an active space (denoted as A) as a subset of the orthogonal basis where relevant electronic excitations take place. We note that such a definition is closely related to the notion of active spaces in multireference quantum chemistry methods, in the sense that it is a set of single-particle orbitals among which all possible excitations are explicitly taken into account; however, in the embedding theory developed here, the environmental effects manifest as a renormalization of one-body and two-body terms in the Hamiltonian, and we do not keep track of wavefunctions in the environment after effective Hamiltonians are constructed.

For a given definition of A, χ_0 can be partitioned into two parts:

$$\chi_0(\boldsymbol{x}_1, \boldsymbol{x}_2) = \chi_0^{\mathrm{A}}(\boldsymbol{x}_1, \boldsymbol{x}_2) + \chi_0^{\mathrm{E}}(\boldsymbol{x}_1, \boldsymbol{x}_2) \tag{4.5}$$

$$\chi_0^{\mathrm{A}}(\boldsymbol{x}_1,\boldsymbol{x}_2) = 2\sum_{i\in\mathrm{A}}\sum_{\substack{j>i\\ j\in\mathrm{A}}}(f_i-f_j)\frac{\langle\psi_i|\hat{n}(\boldsymbol{x}_1)|\psi_j\rangle\,\langle\psi_j|\hat{n}(\boldsymbol{x}_2)|\psi_i\rangle}{\varepsilon_i-\varepsilon_j} \tag{4.6}$$

$$\begin{aligned}\chi_0^{\mathrm{E}}(\boldsymbol{x}_1,\boldsymbol{x}_2) = {} & 2\sum_{i\in\mathrm{A}}\sum_{\substack{j>i\\ j\notin\mathrm{A}}}(f_i-f_j)\frac{\langle\psi_i|\hat{n}(\boldsymbol{x}_1)|\psi_j\rangle\,\langle\psi_j|\hat{n}(\boldsymbol{x}_2)|\psi_i\rangle}{\varepsilon_i-\varepsilon_j}\\ & +2\sum_{i\notin\mathrm{A}}\sum_{\substack{j>i\\ j\in\mathrm{A}}}(f_i-f_j)\frac{\langle\psi_i|\hat{n}(\boldsymbol{x}_1)|\psi_j\rangle\,\langle\psi_j|\hat{n}(\boldsymbol{x}_2)|\psi_i\rangle}{\varepsilon_i-\varepsilon_j}\\ & +2\sum_{i\notin\mathrm{A}}\sum_{\substack{j>i\\ j\notin\mathrm{A}}}(f_i-f_j)\frac{\langle\psi_i|\hat{n}(\boldsymbol{x}_1)|\psi_j\rangle\,\langle\psi_j|\hat{n}(\boldsymbol{x}_2)|\psi_i\rangle}{\varepsilon_i-\varepsilon_j}\end{aligned} \tag{4.7}$$

where the superscript E denotes the environment of the active space.

Within the RPA, one can define the partial screened Coulomb interaction $W_{\mathrm{RPA}}^{\mathrm{E}}$ as

$$W_{\mathrm{RPA}}^{\mathrm{E}} = V + V\chi_0^{\mathrm{E}}W_{\mathrm{RPA}}^{\mathrm{E}} \tag{4.8}$$

where V represents the bare Coulomb interaction. In the cRPA formalism, $W_{\mathrm{RPA}}^{\mathrm{E}}$ is used as effective electron interactions in A, and has the property that the full RPA screened Coulomb interaction W_{RPA} can be obtained by further screening $W_{\mathrm{RPA}}^{\mathrm{E}}$ with χ_0^{A}

$$W_{\mathrm{RPA}} = W_{\mathrm{RPA}}^{\mathrm{E}} + W_{\mathrm{RPA}}^{\mathrm{E}}\chi_0^{\mathrm{A}}W_{\mathrm{RPA}} \tag{4.9}$$

To derive a formalism that goes beyond the RPA and includes exchange-correlation interactions between electrons, we consider a system subject to a perturbative potential δV_{bare}. The corresponding screened potential is denoted as δV_{scf}. We define self-consistent and bare charge density responses as

$$\delta n_{\mathrm{scf}} = \chi\delta V_{\mathrm{bare}} = \chi_0\delta V_{\mathrm{scf}} \tag{4.10}$$

$$\delta n_{\mathrm{bare}} = \chi_0\delta V_{\mathrm{bare}} \tag{4.11}$$

In the presence of a perturbation, the Hartree-exchange-correlation potential of the sys-

tem changes by $\delta V_{\mathrm{Hxc}} = f\delta n_{\mathrm{scf}}$, where $f = \frac{\delta V_{\mathrm{Hxc}}}{\delta n_{\mathrm{scf}}} = V + f_{\mathrm{xc}}$ is the Hartree-exchange-correlation kernel introduced previously.

The functional derivative of δV_{Hxc} with respect to δn_{bare} is equal to the screened Coulomb interaction W

$$W = \frac{\delta V_{\mathrm{Hxc}}}{\delta n_{\mathrm{bare}}} = f + f\chi f \tag{4.12}$$

We note that W defined above represents the interaction between electrons in the system (i.e. it is the electron-electron screened Coulomb interaction) and is widely used in first-principles theories of electron-phonon coupling [108, 243]. W should not be confused with test-charge test-charge screened Coulomb interaction $W_{\mathrm{TC-TC}}$ or electron-test-charge screened Coulomb interaction $W_{\mathrm{E-TC}}$ [157, 350]. W, $W_{\mathrm{TC-TC}}$, and $W_{\mathrm{E-TC}}$ all reduce to W_{RPA} when $f_{\mathrm{xc}} = 0$, but represent different types of screened Coulomb interactions beyond the RPA.

From Eq. 4.12, δV_{Hxc} can be written as

$$\begin{aligned}
\delta V_{\mathrm{Hxc}} &= W\delta n_{\mathrm{bare}} \\
&= f\delta n_{\mathrm{bare}} + f\chi_0 W\delta n_{\mathrm{bare}} \\
&= \left(\frac{\delta V_{\mathrm{H}}}{\delta n_{\mathrm{scf}}} + \frac{\delta V_{\mathrm{xc}}}{\delta n_{\mathrm{scf}}}\right)\delta n_{\mathrm{bare}} + \left(\frac{\delta V_{\mathrm{H}}}{\delta n_{\mathrm{scf}}} + \frac{\delta V_{\mathrm{xc}}}{\delta n_{\mathrm{scf}}}\right)\chi_0 W\delta n_{\mathrm{bare}} \\
&= \left(\frac{\delta V_{\mathrm{H}}}{\delta n_{\mathrm{scf}}} + \frac{\delta V_{\mathrm{xc}}}{\delta n_{\mathrm{scf}}}\right)\delta n_{\mathrm{bare}} + \left(\frac{\delta V_{\mathrm{H}}}{\delta n_{\mathrm{scf}}} + \frac{\delta V_{\mathrm{xc}}}{\delta n_{\mathrm{scf}}}\right)\delta n_{\mathrm{scr}}
\end{aligned} \tag{4.13}$$

where we defined the screening density

$$\delta n_{\mathrm{scr}} = \chi_0 W\delta n_{\mathrm{bare}} = \chi f\delta n_{\mathrm{bare}} \tag{4.14}$$

and the self-consistent charge density response is simply the sum of bare and screening contributions:

$$\delta n_{\mathrm{scf}} = \delta n_{\mathrm{bare}} + \delta n_{\mathrm{scr}} \tag{4.15}$$

Now we consider a bare change of density in the A space, denoted by $\delta n^{\mathrm{A}}_{\mathrm{bare}}$, and we

consider a constrained screening process that only occurs in the E space, characterized by $\chi_0^{\mathrm{E}} = \frac{\delta n_{\mathrm{scf}}^{\mathrm{E}}}{\delta V_{\mathrm{scf}}}$. The resulting screening density δn_{scr} thus belongs to the E space, and we denote it by

$$\delta n_{\mathrm{scr}}^{\mathrm{E}} = \chi^{\mathrm{E}} f \delta n_{\mathrm{bare}}^{\mathrm{A}} \tag{4.16}$$

where χ^{E} is defined as

$$\chi^{\mathrm{E}} = \chi_0^{\mathrm{E}} + \chi_0^{\mathrm{E}} f \chi^{\mathrm{E}} \tag{4.17}$$

The resulting change of the Hartree-exchange-correlation potential, denoted by $\delta V_{\mathrm{Hxc}}^{\mathrm{c}}$ (c stands for constrained, indicating the fact that screening processes in A are not included), is given by:

$$\begin{aligned}
\delta V_{\mathrm{Hxc}}^{\mathrm{c}} &= \left(\frac{\delta V_{\mathrm{H}}}{\delta n_{\mathrm{scf}}} + \frac{\delta V_{\mathrm{xc}}}{\delta n_{\mathrm{scf}}} \right) \delta n_{\mathrm{bare}}^{\mathrm{A}} + \left(\frac{\delta V_{\mathrm{H}}}{\delta n_{\mathrm{scf}}} + \frac{\delta V_{\mathrm{xc}}}{\delta n_{\mathrm{scf}}} \right) \delta n_{\mathrm{scr}}^{\mathrm{E}} \\
&= \left[\frac{\delta V_{\mathrm{H}}}{\delta n_{\mathrm{scf}}} \delta n_{\mathrm{bare}}^{\mathrm{A}} + \left(\frac{\delta V_{\mathrm{H}}}{\delta n_{\mathrm{scf}}} + \frac{\delta V_{\mathrm{xc}}}{\delta n_{\mathrm{scf}}} \right) \delta n_{\mathrm{scr}}^{\mathrm{E}} \right] + \frac{\delta V_{\mathrm{xc}}}{\delta n_{\mathrm{scf}}} \delta n_{\mathrm{bare}}^{\mathrm{A}} \\
&= \frac{\delta V_{\mathrm{H}}^{\mathrm{eff}}}{\delta n_{\mathrm{scf}}} \delta n_{\mathrm{bare}}^{\mathrm{A}} + \frac{\delta V_{\mathrm{xc}}}{\delta n_{\mathrm{scf}}} \delta n_{\mathrm{bare}}^{\mathrm{A}}
\end{aligned} \tag{4.18}$$

where we grouped terms in the square bracket and formally defined:

$$\frac{\delta V_{\mathrm{H}}^{\mathrm{eff}}}{\delta n_{\mathrm{scf}}} = \frac{\delta V_{\mathrm{H}}}{\delta n_{\mathrm{scf}}} + \left(\frac{\delta V_{\mathrm{H}}}{\delta n_{\mathrm{scf}}} + \frac{\delta V_{\mathrm{xc}}}{\delta n_{\mathrm{scf}}} \right) \frac{\delta n_{\mathrm{scr}}^{\mathrm{E}}}{\delta n_{\mathrm{bare}}^{\mathrm{A}}} \tag{4.19}$$

Recall that $f = \frac{\delta V_{\mathrm{Hxc}}}{\delta n_{\mathrm{scf}}}$. Thus, for a general change of density δn_{scf}, the resulting change of the Hartree-exchange-correlation potential is

$$\delta V_{\mathrm{Hxc}} = \frac{\delta V_{\mathrm{H}}}{\delta n_{\mathrm{scf}}} \delta n_{\mathrm{scf}} + \frac{\delta V_{\mathrm{xc}}}{\delta n_{\mathrm{scf}}} \delta n_{\mathrm{scf}} \tag{4.20}$$

By comparing Eq. 4.18 with Eq. 4.20, we see that the constrained change of Hartree-exchange-correlation potential $\delta V_{\mathrm{Hxc}}^{\mathrm{c}}$ induced by $\delta n_{\mathrm{bare}}^{\mathrm{A}}$ is equivalent to the unconstrained change of Hartree-exchange-correlation potential δV_{Hxc} induced by δn_{scf} in a system with

effective electron-electron interaction:

$$\begin{aligned} V^{\text{eff}} &= \frac{\delta V_{\text{H}}^{\text{eff}}}{\delta n_{\text{scf}}} = \frac{\delta V_{\text{H}}}{\delta n_{\text{scf}}} + \left(\frac{\delta V_{\text{H}}}{\delta n_{\text{scf}}} + \frac{\delta V_{\text{xc}}}{\delta n_{\text{scf}}} \right) \frac{\delta n_{\text{scr}}^{\text{E}}}{\delta n_{\text{bare}}^{\text{A}}} \\ &= V + f \chi^{\text{E}} f \end{aligned} \tag{4.21}$$

We represent χ^{E}, f and other relevant quantities on a compact basis obtained through a low-rank decomposition of the dielectric matrix [399, 400, 260, 286, 117] obtained using density functional perturbation theory [21], and evaluate f_{xc} with a finite-field algorithm [220, 261].

After V^{eff} is obtained, the effective one-particle term t_{ij}^{eff} is computed from the Kohn-Sham Hamiltonian by subtracting a double-counting term [39] computed at the Hartree-Fock level

$$t_{ij}^{\text{eff}} = H_{ij}^{\text{KS}} - \left(\sum_{kl} V_{ikjl}^{\text{eff}} \rho_{kl} - \sum_{kl} V_{ijkl}^{\text{eff}} \rho_{kl} \right) \tag{4.22}$$

where ρ is the one-electron density matrix.

We note that throughout this work we used the following index notation for V:

$$V_{ijkl} = \int d\boldsymbol{x}_1 d\boldsymbol{x}_2 \frac{\varphi_i^*(\boldsymbol{x}_1) \varphi_j^*(\boldsymbol{x}_2) \varphi_k(\boldsymbol{x}_1) \varphi_l(\boldsymbol{x}_2)}{|\boldsymbol{r}_1 - \boldsymbol{r}_2|} \tag{4.23}$$

where φ's are spin orbitals spanning the active space.

4.3 Application of embedding theory to spin-defects

The embedding theory presented above is general and can be applied to a variety of systems for which active regions, or building blocks, with strongly-correlated electronic states may be identified: for example active sites in inorganic catalysts or organic molecules or defects in solids and liquids (e.g. solvated ions in water). Here we apply the theory to spin-defects including NV and SiV in diamond and Cr in 4H-SiC. Most of these defects' excited states are strongly-correlated (they cannot be represented by a single Slater determinant of single-

particle orbitals), as shown e.g. for the NV center in diamond by Bockstedte et al.[39] using cRPA calculations. We demonstrate that our embedding theory can successfully describe the many-body electronic structure of different types of defects including transition metal atoms; our results not only confirm existing experimental observations but also provide a detailed description of the electronic structure of defects not presented before, which sheds light into their optical cycles.

We first performed spin-restricted DFT calculations using hybrid functionals [346] to obtain a mean-field description of the defects and of the whole host solid. The spin restriction ensures that both spin channels are treated on an equal footing and that there is no spin-contamination when building effective Hamiltonians. Based on our DFT results, we then selected active spaces that include single-particle defect wavefunctions and relevant resonant and band edge states. We verified that the size of the chosen active spaces yields converged excitation energies (see Section 4.3.2). We then constructed effective Hamiltonians (Eq. 4.1-4.2) by taking into account exchange-correlation effects, and we obtained many-body ground and excited states using classical (FCI) and, for selected cases, quantum algorithms (PEA, VQE). All calculations were performed at the spin triplet ground state geometries obtained by spin-unrestricted DFT calculations, thus obtaining vertical excitation energies (equal to the sums of zero phonon line (ZPL) and Stokes energies). It is straightforward to extend the current approach to compute potential energy surfaces at additional geometries For example, one may follow the strategy of Ref. [39] and compute excited states of defects along given normal modes, which are usually obtained from delta-SCF calculations. This type of treatment, albeit approximate, provides valuable insights into the vibrational properties of defects in excited states., so as to include relaxations and Jahn-Teller effects [39, 370]. In Fig. 4.2 we present atomistic structures, single-particle defect levels and the many-body electronic structure of three spin-defects. Several relevant vertical excitation energies are reported in Table 1, and additional ones are given in the 4.3.1. In the following discussion, lower-case symbols represent single-particle states obtained from DFT and upper-case symbols represent

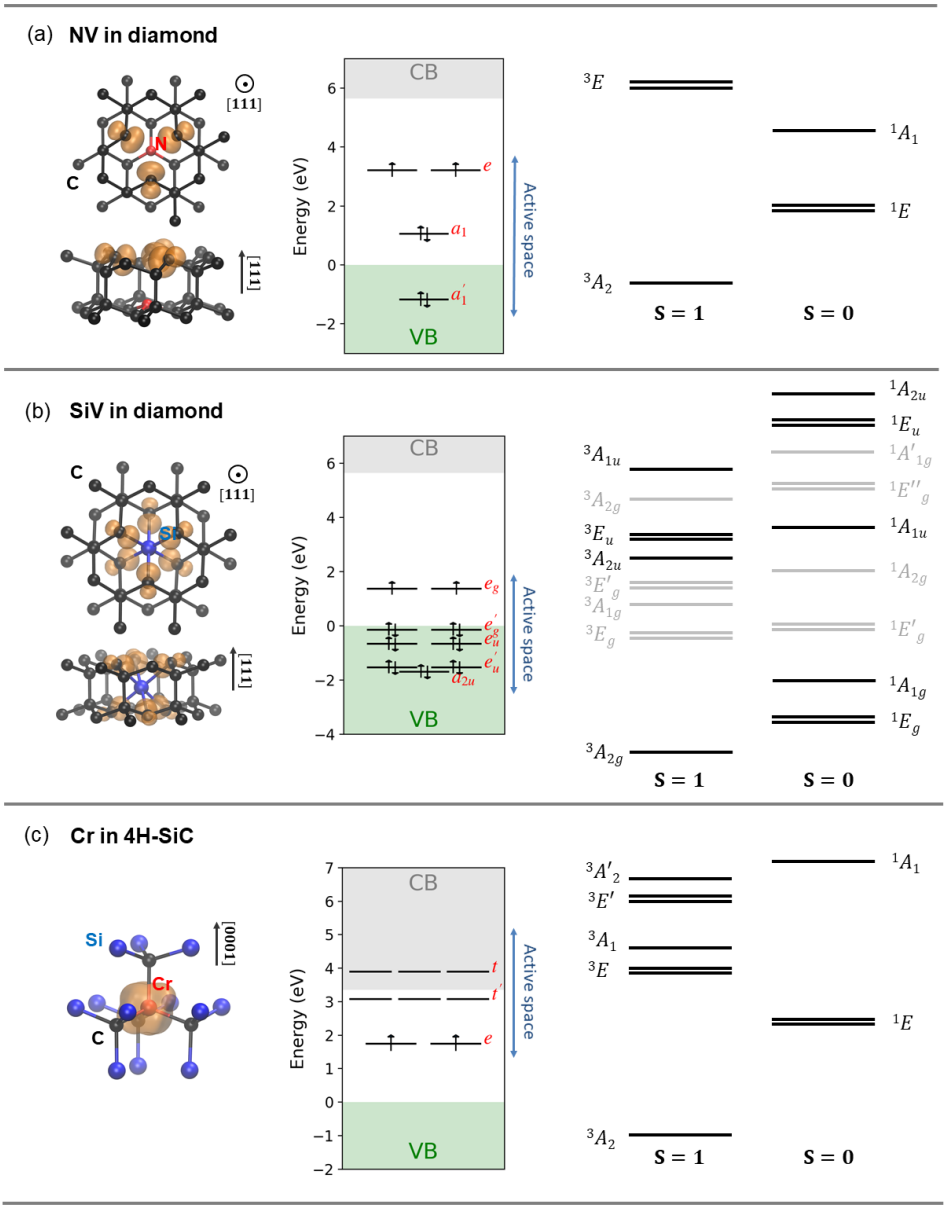

Figure 4.2: Electronic structure of spin-defects. Panels (a), (b), and (c) present results for the negatively-charged nitrogen vacancy (NV) in diamond, the neutral silicon vacancy (SiV) in diamond, and the Cr impurity (4+) in 4H-SiC, respectively. Left panels show spin densities obtained from spin unrestricted DFT calculations. Middle panels show the position of single-particle defect levels computed by spin restricted DFT calculations. States included in active spaces are indicated by blue vertical lines. Right panels show the symmetry and ordering of the low-lying many-body electronic states obtained by exact diagonalization (FCI calculations) of effective Hamiltonians constructed with exchange-correlation interactions included.

many-body states.

Table 4.1: Vertical excitation energies (eV) of the negatively charged nitrogen vacancy (NV) and neutral silicon vacancy (SiV) in diamond and Cr (4+) in 4H-SiC, obtained using the random phase approximation (RPA: third column) and including exchange-correlation interactions (beyond RPA: fourth column). Experimental measurements of zero-phonon-line (ZPL) energies are shown in brackets in the fifth column. Reference vertical excitation energies are computed from experimental ZPL when Stokes energies are available.

System	Excitation	RPA	Beyond-RPA	Expt.
NV	$^3A_2 \leftrightarrow {}^3E$	1.921	2.001	2.180[a] (1.945[a])
	$^3A_2 \leftrightarrow {}^1A_1$	1.376	1.759	
	$^3A_2 \leftrightarrow {}^1E$	0.476	0.561	
	$^1E \leftrightarrow {}^1A_1$	0.900	1.198	(1.190[b])
	$^1A_1 \leftrightarrow {}^3E$	0.545	0.243	(0.344-0.430[c])
SiV	$^3A_{2g} \leftrightarrow {}^3E_u$	1.590	1.594	1.568[d] (1.31[e])
	$^3A_{2g} \leftrightarrow {}^3A_{1u}$	1.741	1.792	
	$^3A_{2g} \leftrightarrow {}^1E_g$	0.261	0.336	
	$^3A_{2g} \leftrightarrow {}^1A_{1g}$	0.466	0.583	
	$^3A_{2g} \leftrightarrow {}^1A_{1u}$	1.608	1.623	
	$^3A_{2g} \leftrightarrow {}^1E_u$	2.056	2.171	
	$^3A_{2g} \leftrightarrow {}^1A_{2u}$	2.365	2.515	
	$^3A_{2u} \leftrightarrow {}^3E_u$	0.003	0.011	(0.007[e])
Cr	$^3A_2 \leftrightarrow {}^3E$	1.365	1.304	
	$^3A_2 \leftrightarrow {}^3A_1$	1.480	1.406	
	$^3A_2 \leftrightarrow {}^3E'$	1.597	1.704	
	$^3A_2 \leftrightarrow {}^3A_2'$	1.635	1.755	
	$^3A_2 \leftrightarrow {}^1E$	0.860	1.090	(1.190[f])
	$^3A_2 \leftrightarrow {}^1A_1$	1.560	1.937	

[a]Ref [67]. [b]Ref [308]. [c]Estimated by Ref [112] with a model for intersystem crossing. [d]Computed with Stokes energy from Ref [370]. [e]Ref [119]. [f]Ref [352].

For the NV in diamond, we constructed effective Hamiltonians (Eq. 4.1) by using an active space that includes a_1 and e single-particle defect levels in the band gap and states near the valence band maximum (VBM). Our FCI calculations correctly yield the symmetry and ordering of the low-lying $^3A_2$, ^3E, ^1E and $^1A_1$ states. The vertical excitation energies reported in Table 4.1 show that including exchange-correlation effects yields results in better agreement with experiments than those obtained within the RPA. The results obtained

within RPA (0.476/1.376/1.921 eV for ${}^1E/{}^1A_1/{}^3E$ states) are in good agreement with cRPA results reported in Ref. [39] (0.47/1.41/2.02 eV).

In the case of the SiV in diamond, we built effective Hamiltonians using an active space with the e_u and e_g defect levels and states near the VBM, including resonant e'_u and e'_g states. Effective Hamiltonians including or neglecting exchange-correlation effects yield similar results, with the excitation energies obtained beyond RPA being slightly higher. We predicted the first optically-allowed excited state to be a ${}^3E_u$ state with vertical excitation energy of 1.59 eV, in good agreement with the sum of 1.31 eV ZPL measured experimentally [79] and 0.258 eV Stokes shift estimated using an electron-phonon model [370]. Our calculations predicted a ${}^3A_{2u}$ state 11 meV below the ${}^3E_u$ state, in qualitative agreement with a recent experimental observation by Green et al. [119], which proposed a ${}^3A_{2u}$-${}^3E_u$ manifold with 7 meV separation in energy. The small difference in energy splitting between our results and experiment is likely due to geometry relaxation effects not yet taken into account in our study. In addition to states of u symmetry generated by $e_u \rightarrow e_g$ excitations, we observed a number of optically dark states of g symmetry (grey levels in Fig. 4.2b) originating from the excitation from the e'_g level and the VBM states to the e_g level.

Despite significant efforts [120, 312, 119, 370], several important questions on the singlet states of SiV remain open. These states are crucial for a complete understanding of the optical cycle of the SiV center. Our predicted ordering of singlet states of SiV is shown in Fig. 4.2b. We find the vertical excitation energies of the ${}^1A_{1u}$ state to be slightly higher than that of the ${}^3A_{2u}$-${}^3E_u$ triplet manifold, suggesting that the intersystem crossing (ISC) from ${}^3A_{2u}$ or ${}^3E_u$ to singlet states may be energetically unfavorable (first-order ISC to lower ${}^1E_g$ and ${}^1A_{1g}$ states are forbidden). We note that the ${}^1E_u$ and ${}^1A_{2u}$ states are much higher in energy than ${}^1A_{1u}$ and are not expected to play a significant role in the optical cycle. In addition the first-order ISC process from the lowest energy singlet state ${}^1E_g$ to the ${}^3A_{2g}$ ground state is forbidden by symmetry. Overall our results indicate that the ${}^3A_{2g}$ state is populated through higher-order processes and therefore the spin-selectivity of the full

optical cycle is expected to be low. While more detailed studies including spin-orbit coupling are required for definitive conclusions, our predictions shed light on the strongly-correlated singlet states of SiV and provide a possible explanation for the experimental difficulties in measuring optically-detected magnetic resonance (ODMR) of SiV.

We now turn to Cr in 4H-SiC, where we considered the hexagonal configuration. We constructed effective Hamiltonians with the half-filling e level in the band gap and states near the conduction band minimum (CBM) including resonance states. Upon solving the effective Hamiltonian, we predict the lowest excited state to be a ^1E state arising from $e \rightarrow e$ spin-flip transition, with excitation energy of 1.09 (0.86) eV based on embedding calculations beyond (within) the RPA. Results including exchange-correlation effects are in better agreement with the measured ZPL of 1.19 eV [352], where the Stokes energy is expected to be small given the large Debye-Waller factor [72]. There is currently no experimental report for the triplet excitation energies of Cr in 4H-SiC, but our results are in good agreement with existing experimental measurements for Cr in GaN, a host material with a crystal field strength similar to that of 4H-SiC [189]. We predict the existence of a $^3E + {}^3A_1$ manifold at $\simeq 1.4$ eV and a $^3E' + {}^3A_2'$ manifold at $\simeq 1.7$ eV above the ground state (Fig. 4.2c), resembling the $^3T_2$ manifold (1.2 eV) and $^3T_1$ manifold (1.6 eV) for Cr in GaN observed experimentally [134]. We note that in many cases it is challenging to study materials containing transition metal elements with DFT [8]. The agreement between FCI results and experimental measurements clearly demonstrates that the embedding theory developed here can effectively describe the strongly-correlated part of the system, while yielding at the same time a quantitatively correct description of the environment.

4.3.1 Excitation energies of defects

In the following tables we list low-energy FCI solutions of the effective Hamiltonian for defects. VBM and CBM denote valence band maximum and conduction band minimum, respectively.

Table 4.2: Energies (eV), symmetries and characters of low-energy eigenstates obtained from FCI calculation of effective Hamiltonians for the NV center in diamond. Effective Hamiltonians are constructed within and beyond the random phase approximation (RPA). The ground state energy is set to zero. GS indicates ground state, GS-SF indicates spin-flip excitations within the ground state orbital configuration.

State	RPA			Beyond-RPA		
	Energy	Symmetry	Character	Energy	Symmetry	Character
0	0.000	${}^3A_2$	GS	0.000	${}^3A_2$	GS
1	0.476	${}^1E$	GS-SF	0.561	${}^1E$	GS-SF
2	1.376	${}^1A_1$	GS-SF	1.759	${}^1A_1$	GS-SF
3	1.921	${}^3E$	$a_1 \to e$	2.001	${}^3E$	$a_1 \to e$
4	2.996	${}^1E$	$a_1 \to e$	3.461	${}^1E$	$a_1 \to e$

Table 4.3: Energies (eV), symmetries and characters of low-energy eigenstates obtained from FCI calculation of effective Hamiltonians for the SiV in diamond. The ground state energy is set to zero. GS indicates ground state, GS-SF indicates spin-flip excitations within ground state orbital configurations.

State	RPA			Beyond-RPA		
	Energy	Symmetry	Character	Energy	Symmetry	Character
0	0.000	${}^3A_{2g}$	GS	0.000	${}^3A_{2g}$	GS
1	0.261	${}^1E_g$	GS-SF	0.336	${}^1E_g$	GS-SF
2	0.466	${}^1A_{1g}$	GS-SF	0.583	${}^1A_{1g}$	GS-SF
3	1.254	${}^3E_g$	VBM $\to e_g$	1.347	${}^3E_g$	VBM $\to e_g$
4	1.268	${}^1E_g$	VBM $\to e_g$	1.363	${}^1E_g$	VBM $\to e_g$
5	1.424	${}^3A_{1g}$	$e'_g \to e_g$	1.508	${}^3A_{1g}$	$e'_g \to e_g$
6	1.441	${}^3E_g$	$e'_g \to e_g$	1.530	${}^3E_g$	$e'_g \to e_g$
7	1.469	${}^1A_{2g}$	$e'_g \to e_g$	1.563	${}^1A_{2g}$	$e'_g \to e_g$
8	1.545	${}^3A_{2g}$	$e'_g \to e_g$	1.583	${}^3A_{2u}$	$e_u \to e_g$
9	1.587	${}^3A_{2u}$	$e_u \to e_g$	1.594	${}^3E_u$	$e_u \to e_g$
10	1.590	${}^3E_u$	$e_u \to e_g$	1.623	${}^1A_{1u}$	$e_u \to e_g$
11	1.608	${}^1A_{1u}$	$e_u \to e_g$	1.636	${}^3A_{2g}$	$e'_g \to e_g$
12	1.619	${}^1E_g$	$e'_g \to e_g$	1.723	${}^1E_g$	$e'_g \to e_g$
13	1.692	${}^1A_{1g}$	$e'_g \to e_g$	1.792	${}^3A_{1u}$	$e_u \to e_g$
14	1.741	${}^3A_{1u}$	$e_u \to e_g$	1.812	${}^1A_{1g}$	$e'_g \to e_g$
15	2.056	${}^1E_u$	$e_u \to e_g$	2.171	${}^1E_u$	$e_u \to e_g$
16	2.365	${}^1A_{2u}$	$e_u \to e_g$	2.515	${}^1A_{2u}$	$e_u \to e_g$

4.3.2 Convergence of the active space size

In previous sections we report results obtained with active spaces sufficiently large to converge the excitation energies; they include 21/38/23 spatial orbitals (42/76/46 spin orbitals) for

Table 4.4: Energies (eV), symmetries and characters of low-energy eigenstates obtained from FCI calculation of effective Hamiltonians for Cr in 4H-SiC. The ground state energy is set to zero. GS indicates ground state, GS-SF indicates spin-flip excitations within ground state orbital configuration. Excitations from e level to the CBM are positioned more than 3 eV above the ground state.

State	RPA			Beyond-RPA		
	Energy	Symmetry	Character	Energy	Symmetry	Character
0	0.000	$^3A_2$	GS	0.000	$^3A_2$	GS
1	0.860	^1E	GS-SF	1.090	^1E	GS-SF
2	1.365	^3E	$e \rightarrow t'$	1.304	^3E	$e \rightarrow t'$
3	1.480	$^3A_1$	$e \rightarrow t'$	1.406	$^3A_1$	$e \rightarrow t'$
4	1.560	$^1A_1$	GS-SF	1.704	^3E	$e \rightarrow t'$
5	1.597	^3E	$e \rightarrow t'$	1.755	$^3A_2$	$e \rightarrow t'$
6	1.635	$^3A_2$	$e \rightarrow t'$	1.937	$^1A_1$	GS-SF
7	1.770	^1E	$e \rightarrow t'$	1.948	^1E	$e \rightarrow t'$

NV/SiV/Cr defects, respectively. As an example, in Fig. 4.3 we show the convergence of FCI eigenvalues of the NV center as a function of the size of the active space. The minimum model $\{a_1, e\}$ already yields excitation energies within 0.2 eV of the converged results. Inclusion of a_1' level and other valence band states near the VBM yields results that converge rapidly. Including empty states does not affect the computed excitation energies.

4.4 Quantum simulations

The results presented in the previous section were obtained using classical algorithms. We now turn to the use of quantum algorithms. To perform quantum simulations with PEA and VQE, we constructed a minimum model of an NV center including only a_1 and e orbitals in the band gap. This model (4 electrons in 6 spin orbitals) yields excitation energies within 0.2 eV of the converged results using a larger active space. In Fig. 4.4 we show the results of quantum simulations.

We first performed PEA simulations with a quantum simulator (without noise) [2] to compute the energy of $^3A_2$, ^3E, ^1E and $^1A_1$ states. We used molecular orbital approximations of these states derived from group theory [75] as initial states for PEA, which are single

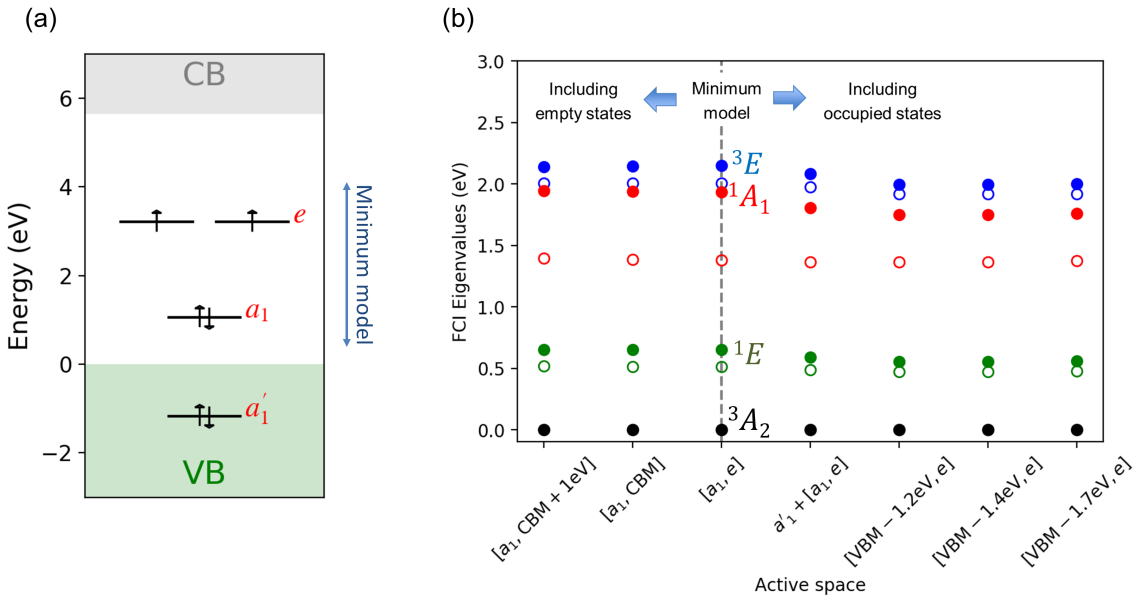

Figure 4.3: (a) Single-particle level diagrams for the NV center in diamond. The minimum model for the NV center includes the a_1 and e levels in the band gap. (b) Convergence of FCI eigenvalues as functions of the size of active space (represented by intervals between the lowest and highest single-particle levels). Empty and full circles represent RPA and beyond-RPA results, respectively.

Slater determinant for $^3A_2$ ($M_S = 1$) and ^3E ($M_S = 1$) states, and superpositions of two Slater determinants for ^1E and $^1A_1$ states. As shown in Fig. 4.4a, PEA results converge to classical FCI results with an increasing number of ancilla qubits.

We then performed VQE simulations with a quantum simulator and with the IBM Q 5 Yorktown quantum computer. We estimated the energy of the $^3A_2$ ground state manifold by performing VQE calculations for both the single-Slater-determinant $M_S = 1$ component and the strongly-correlated $M_S = 0$ component. Within a molecular orbital notation, $M_S = 1$ and $M_S = 0$ ground states can be represented as $|a\bar{a}e_x e_y\rangle$ and $\frac{1}{2}\left(|a\bar{a}e_x\bar{e}_y\rangle + |a\bar{a}\bar{e}_x e_y\rangle\right)$, respectively, where a, e_x, e_y (spin-up) and $\bar{a}$, $\bar{e}_x$, $\bar{e}_y$ (spin-down) denote a_1 and e orbitals. To obtain the $M_S = 0$ ground state, we used a closed-shell Hartree-Fock state $|a\bar{a}e_x\bar{e}_x\rangle$ as reference; the $M_S = 1$ ground state is itself an open-shell Hartree-Fock state, so we started with a higher energy reference state $|ae_x\bar{e}_x e_y\rangle$ in the ^3E manifold. We used unitary coupled-cluster single and double (UCCSD) ansatzes [282] to represent the trial wavefunctions. Fig.

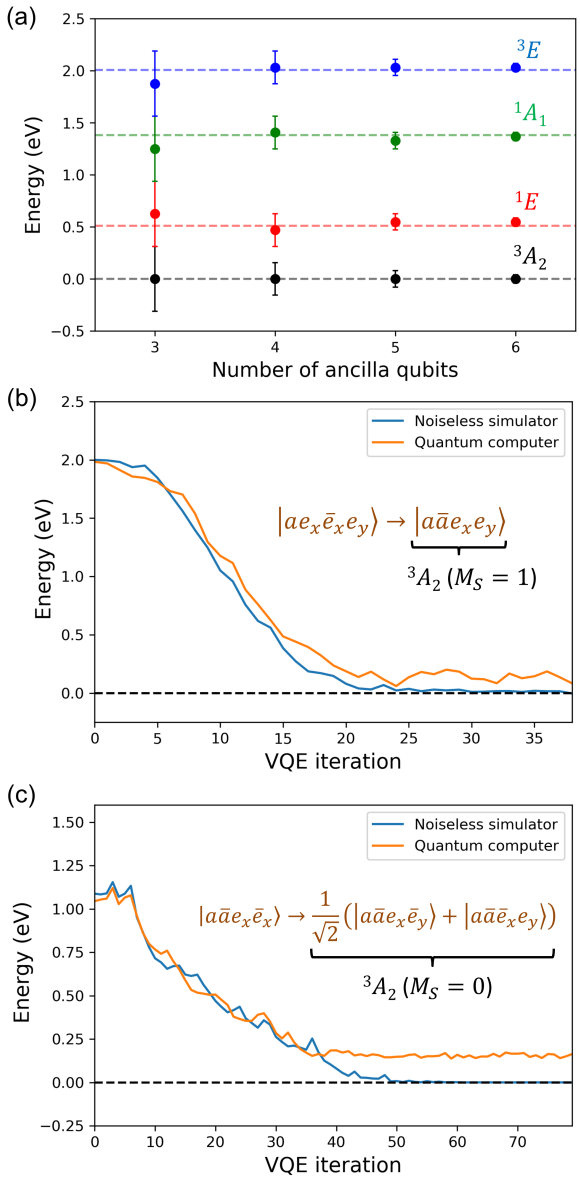

Figure 4.4: Quantum simulations of a minimum model of the NV center in diamond using the phase estimation algorithm (PEA) and a variational quantum eigensolver (VQE). The energy of the $^3A_2$ ground state manifold is set to zero for convenience. (a) PEA estimation of ground and excited states of the NV center. Error bars represent the uncertainties due to the finite number of ancilla qubits used in the simulations; dashed lines show classical FCI results. (b) VQE estimation of ground state energy, starting from $|ae_x\bar{e}_xe_y\rangle$ state ($M_S = 1$). (c) VQE estimation of ground state energy, starting from $|a\bar{a}e_x\bar{e}_x\rangle$ state ($M_S = 0$); strongly-correlated $\frac{1}{2}\left(|a\bar{a}e_x\bar{e}_y\rangle + |a\bar{a}\bar{e}_xe_y\rangle\right)$ state ($M_S = 0$ state in the $^3A_2$ manifold) is obtained with VQE.

4.4b and Fig. 4.4c show the estimated ground state energy as a function of the number of VQE iterations, where VQE calculations performed with the quantum simulator correctly converges to the ground state energy in both the $M_S = 1$ and $M_S = 0$ case. Despite the presence of noise, whose characterization and study will be critical to improve the use of quantum algorithms [174], the results obtained with the quantum computer converge to the ground state energy within a 0.2 eV error. Calculations of excited states with quantum algorithms will be the focus of future works.

4.5 Technical details

Density Functional Theory

All ground state DFT calculations are performed with the Quantum Espresso code [106] using the plane-wave pseudopotential formalism. Electron-ion interactions are modeled with norm-conserving pseudopotentials from the SG15 library [324]. A kinetic energy cutoff of 50 Ry is used. All geometries are relaxed with spin-unrestricted DFT calculations using the Perdew–Burke-Ernzerhof (PBE) functional [279] until forces acting on atoms are smaller than 0.013 eV/Å. NV and SiV in diamond are modeled with 216-atom supercells; Cr in 4H-SiC is modeled with a 128-atom supercell. The Brillouin zone is sampled with the Γ point.

Construction of effective Hamiltonians

Construction of effective Hamiltonians is performed with the WEST code [117], starting from wavefunctions of spin-restricted DFT calculations. For this step, we remark that the use of hybrid functional is important for an accurate mean-field description of defect levels, even though the geometry of defects are well represented at the PBE level. We used a dielectric dependent hybrid (DDH) functional [346] which self-consistently determines the fraction of exact exchange based on the dielectric constant of the host material. In particular, 17.8 %

and 15.2 % of exact exchange were used for the calculations of defects in diamond and 4H-SiC, respectively. The DDH functional was shown to yield accurate band gaps of diamond and silicon carbide, as well as optical properties of defects [334, 335, 285, 349, 104]. After hybrid functional solutions of the Kohn-Sham equations are obtained, iterative diagonalizations of χ_0 are performed, and density response functions and f_{xc} of the system are represented on a basis consisting of the first 512 eigenpotentials of χ_0. Finite field calculations of f_{xc} are performed by coupling the WEST code with the Qbox [124] code. FCI calculations [186] on the effective Hamiltonian are carried out using the PySCF [360] code.

Quantum simulations

In order to carry out quantum simulations, a minimum model of the NV center is constructed by applying the embedding theory with a_1 and e orbitals beyond the RPA.

In PEA simulations, the Jordan-Wigner transformation [170] is used to map the fermionic effective Hamiltonian to a qubit Hamiltonian, and Pauli operators with prefactors smaller than 10^{-6} a.u. are neglected to reduce the circuit depth, which results in less than 10^{-4} a.u. (0.003 eV) change in eigenvalues. In order to achieve optimal precision, the Hamiltonian is scaled such that 0 and 2.5 eV are mapped to phases $\phi = 0$ and $\phi = 1$ of the ancilla qubits, respectively. We used the first-order Trotter formula to split time evolution operators into 4 time slices.

In VQE simulations, the parity transformation [43] is adopted. For the simulation of the $M_S = 1$ state, the resulting qubit Hamiltonian acts on 4 qubits and there are 2 variational parameters in the UCCSD ansatz. For the simulation of the $M_S = 0$ state, we fixed the occupation of the a orbital and the resulting qubit Hamiltonian acts on 2 qubits. We replicated the exponential excitation operator twice, with parameters in both replicas variationally optimized. Such a choice results in 6 variational parameters, providing a sufficient number of degrees of freedom for an accurate representation of the strongly-correlated $M_S = 0$ state. Parameters in the ansatz are optimized with the COBYLA algorithm [294].

Quantum simulations are performed with the QASM simulator and the IBM Q 5 Yorktown quantum computer using the IBM Qiskit package [2]. Each quantum circuit is executed 8192 times to obtain statistically reliable sampling of the measurement results.

4.6 Discussion

With the goal of providing a strategy to solve complex materials problems on NISQ computers, we proposed a first-principles quantum embedding theory where appropriate active regions of a material and their environment are described with different levels of accuracy, and the whole system is treated quantum mechanically. In particular, we used hybrid density functional theory for the environment, and we built a many-body Hamiltonian for the active space with effective electron-electron interactions that include dielectric screening and exchange-correlation effects from the environment. Our method overcomes the commonly used random phase approximation, which neglects exchange-correlation effects; importantly it is applicable to heterogeneous materials and scalable to large systems, due to the algorithms used here to compute response functions [220, 261]. We emphasize that the embedding theory presented here provides a flexible framework where multiple effects of the environment may be easily incorporated. For instance, dynamical screening effects can be included by considering a frequency-dependent screened Coulomb interaction, evaluated using the same procedure as the one outlined here for static screening; electron-phonon coupling effects can be incorporated by including phonon contributions in the screened Coulomb interactions. Furthermore, for systems where the electronic structure of the active region is expected to influence that of the host material, a self-consistent cycle in the calculation of the screened Coulomb interaction of the environment can be easily added to the approach.

We presented results for spin-defects in semiconductors obtained with both classical and quantum algorithms, and we showed excellent agreement between the two sets of techniques. Importantly, for selected cases we showed results obtained using a quantum simulator and a quantum computer, which agree within a relatively small error, in spite of the presence

of noise in the quantum hardware. We made several predictions for excited states of SiV in diamond and Cr in SiC, which provide important insights into their full optical cycle. We also demonstrated that a treatment of the dielectric screening beyond the random phase approximation leads to an accurate prediction of excitation energies.

The method proposed in our work enables calculations of realistic, heterogeneous materials using the resources of NISQ computers. We demonstrated quantum simulations of strongly-correlated electronic states in considerably larger systems (with hundreds of atoms) than previous studies combining quantum simulation and quantum embedding [313, 409, 26, 196, 315]. We have studied solids with defects, not just pristine materials, which are of great interest for quantum technologies. The strategy adopted here is general and may be applied to a variety of problems, including the simulation of active regions in molecules and materials for the understanding and discovery of catalysts and new drugs, and of aqueous solutions containing complex dissolved species. We finally note that our approach is not restricted to strongly-correlated active regions and will be useful also in the case of weakly correlated systems, where different regions of a material may be treated with varying levels of accuracy. Hence we expect the strategy presented here to be widely applicable to carry out quantum simulations of materials on near-term quantum computers.

CHAPTER 5

FIRST-PRINCIPLES CALCULATION OF SPIN PROPERTIES OF MOLECULES AND MATERIALS

Many important physical and chemical processes involve the magnetic interactions among electron and nuclear spins. Such interactions are relativistic in nature and are not directly accessible from the solution of the nonrelativistic electronic structure problem. This chapter discusses density functional theory (DFT) calculation of spin properties of paramagnetic molecules and semiconductor defects including the hyperfine interaction, zero-field splitting and nuclear quadruple interaction. These properties are numerically difficult to compute using usual basis sets such as plane waves or Gaussian orbitals. In Section 5.1 we describe a novel approach based on finite-element basis sets, which enables all-electron DFT calculation of spin properties and leads to results that can be systematically converged as a function of basis set size. In Section 5.2 we present an extension of the formalism in Section 5.1 where only selected atoms need to be treated at the all-electron level and the rest of the system can be treated with pseudopotentials. This mixed all-electron-pseudopotential approach is highly scalable and allows for calculations of spin properties for systems containing more than one thousand atoms.

5.1 All-electron calculation of spin properties using finite-element DFT

https://doi.org/10.1103/PhysRevMaterials.3.043801

The interaction between electronic and nuclear spins in the presence of external magnetic fields can be described by a spin Hamiltonian, with parameters obtained from first principles, electronic structure calculations. We describe an approach to compute these parameters, applicable to both molecules and solids, which is based on Density Functional Theory (DFT) and real-space, all-electron calculations using finite elements (FE). We report results for hyperfine tensors, zero field splitting tensors (spin-spin component) and nuclear quadrupole tensors of a series of molecules and of the nitrogen-vacancy center in diamond. We compare our results with those of calculations using Gaussian orbitals and plane-wave basis sets, and we discuss their numerical accuracy. We show that calculations based on FE can be systematically converged with respect to the basis set, thus allowing one to establish reference values for the spin Hamiltonian parameters, at a given level of DFT.

5.1.1 Introduction

Electron spins in molecules, nanostructures and solids are important resources in many areas including spintronics [158] and quantum information science [392]. For instance, high-spin magnetic molecules can be utilized as single-molecule magnets and are promising platforms for next-generation data storage devices [122]; in the solid state, spin-carrying deep centers in semiconductors can serve as quantum bits for quantum information processing [190]. In order to understand the physical properties of electron spins in molecules and solids, one needs to describe the interaction of electron and nuclear spins, in the presence of external electromagnetic fields. Such a description may be achieved by using spin Hamiltonians, with

parameters derived from experiments or from calculations. For systems with a single effective electron spin, the leading terms in the spin Hamiltonian are [331, 131, 1]:

$$H = \mu_B \boldsymbol{B} \cdot \boldsymbol{g} \cdot \boldsymbol{S} + \sum_N \gamma_N \boldsymbol{B} \cdot \boldsymbol{I}_N + \sum_N \boldsymbol{S} \cdot \boldsymbol{A}_N \cdot \boldsymbol{I}_N + \boldsymbol{S} \cdot \boldsymbol{D} \cdot \boldsymbol{S} + \sum_N \boldsymbol{I}_N \cdot \boldsymbol{P}_N \cdot \boldsymbol{I}_N \quad (5.1)$$

where μ_B is Bohr magneton; $\boldsymbol{S}$ is the effective electron spin; $\boldsymbol{B}$ is the external magnetic field; $\boldsymbol{I}_N$ and γ_N are the spin and gyromagnetic ratio of the N^{th} nucleus; $\boldsymbol{g}$, $\boldsymbol{A}$, $\boldsymbol{D}$, and $\boldsymbol{P}$ are rank-2 tensors that characterize the strength of electron Zeeman interaction, hyperfine interaction, zero-field splitting and nuclear quadrupole interaction, respectively. Nuclear spin-spin interactions and the chemical shielding effect in nuclear Zeeman interactions are neglected in Eq. 5.1.

The spin Hamiltonian parameters $\boldsymbol{g}$, $\boldsymbol{A}$, $\boldsymbol{D}$ and $\boldsymbol{P}$ may be obtained by electron paramagnetic resonance (EPR), nuclear quadrupole resonance (NQR) and related spectroscopic techniques [393]. Theoretically their values can be determined by first-principles electronic structure calculations, which also provide important information complementary to experiments. For example, in the case of spin defects in solids often times the atomistic structure and charge state of the defect are not straightforward to determine, experimentally. Comparing the computed spin Hamiltonian parameters for candidate structures and charge states with experimental results is a useful means to identify the properties of the defect. In addition, first-principles calculations can provide insights into the structure-property relations of molecules and spin defects, thus facilitating the rational design of molecules and materials with desirable spin properties. Finally, by simulating spin systems under external perturbations such as mechanical strain or applied electromagnetic fields, one can obtain valuable information and guidance for the experimental manipulation of electron spins [86, 396].

Therefore, in order to devise predictive computational strategies, the development of robust methods for the calculation of spin Hamiltonian parameters is an important task. In spite of important progress in the fields of materials science [377, 35, 289, 290, 16, 298, 40, 31]

and quantum chemistry [267, 208, 345, 255, 301, 193, 256], there is not yet a general and well established computational protocol that can reliably predict various spin Hamiltonian parameters with high accuracy for broad classes of systems. At present, the method most often adopted for spin Hamiltonian parameter calculations is Density Functional Theory (DFT). While calculations using *ab initio* wavefunction-based methods have also appeared in the literature [321, 359], they have so far been limited to relatively small molecular systems due to their high computational cost. To solve the Kohn-Sham equations in DFT, single particle electronic wavefunctions are usually represented using basis sets, with Gaussian-type orbitals (GTO) and plane-waves (PW) being among the most popular choices for molecular and extended systems, respectively. In PW-based DFT calculations, pseudopotentials are employed and the electronic wavefunctions near the nuclei are not explicitly evaluated, and one generally needs to perform a so-called projected augmented wave (PAW) reconstruction [34] to extract all-electron wavefunctions for the calculation of certain spin Hamiltonian parameters. Besides PW, there are studies exploring other basis sets including numerical atomic orbitals [171], linearized augmented plane-wave [330], linear muffin-tin orbitals [63, 274], and GTO [78] for the calculation of A-tensors and V-tensors (electric field gradient tensor) for solids.

In this work we present calculations of spin Hamiltonian parameters carried out, for the first time, using a real-space finite-element (FE) formulation of DFT [251]. The FE basis is a piece-wise continuous polynomial basis [46] that allows for systematic convergence of calculations with increasing polynomial order and decreasing element size. An important attribute of the FE basis is its spatial adaptivity that can provide increased resolution in specific regions of interest in real space, while using coarser descriptions elsewhere. In the present context, the FE basis can be chosen to have higher resolution in the core region to accurately describe the highly oscillatory nature of the single particle wavefunctions, and a coarser resolution far from the core where the orbitals are smoother. Further, FE-based calculations can be performed with either open or periodic boundary conditions, and

therefore molecular and extended systems can be treated on an equal footing. There are several advantages in using FE-based DFT calculations for computing spin Hamiltonian parameters. The cusp of the wavefunctions near the nuclei can be more efficiently represented than with GTO basis sets, and this is an important requisite to compute quantities such as the Fermi contact component of the A-tensor. In addition, FE-based calculations can be systematically converged with respect to the basis set size in a more straightforward manner than GTO-based calculations, and they do not mandate the use of pseudopotentials and PAW reconstructions, as required when using PWs.

Here we specifically consider the isotropic (Fermi contact) and the spin dipolar contribution to the hyperfine A-tensor, the spin-spin component of the zero-field splitting D-tensor, and the nuclear quadrupole P-tensor.

5.1.2 Formalism

Hyperfine tensor

The isotropic (Fermi contact) and the spin dipolar component of the A-tensor are given by:

$$A^{\text{iso}} = -\frac{1}{3S}\mu_0\gamma_e\gamma_N\hbar^2 n_s(\boldsymbol{r}_N), \tag{5.2}$$

$$A^{\text{dip}}_{ab} = \frac{1}{2S}\frac{\mu_0}{4\pi}\gamma_e\gamma_N\hbar^2\int\frac{|\boldsymbol{r}-\boldsymbol{r}_N|^2\delta_{ab} - 3(\boldsymbol{r}-\boldsymbol{r}_N)_a(\boldsymbol{r}-\boldsymbol{r}_N)_b}{|\boldsymbol{r}-\boldsymbol{r}_N|^5}n_s(\boldsymbol{r})d\boldsymbol{r}, \tag{5.3}$$

where $a, b = x, y, z$, S is the effective electron spin ($S = 0$ for a singlet, $\frac{1}{2}$ for a doublet, etc.); n_s is the electron spin density; $\boldsymbol{r}_N$ is the position of the nucleus; $(\boldsymbol{r}-\boldsymbol{r}_N)_a$ is the a-direction component of $\boldsymbol{r}-\boldsymbol{r}_N$; γ_e and γ_N are gyromagnetic ratios for electron and nuclei, respectively.

As can be seen from Eq. 5.2, the isotropic (Fermi contact) component of the A-tensor exhibits a strong dependence on the electron spin density at the nuclei. An all-electron A-tensor calculation in real-space requires very refined finite elements near the nuclei to ac-

curately compute the electron spin density. The spatial adaptivity of the finite element mesh (h refinement) is hence extremely useful here. On the other hand, the dipolar component of the A-tensor involves an integration with $\frac{1}{r^5}$ and $\frac{1}{r^3}$ kernels. This requires high accuracy in the electronic spin density within a certain region surrounding the nuclei, which can be systematically improved through the p-refinement.

Zero-field splitting tensor

The spin-spin component of the D-tensor evaluated using the Kohn-Sham wavefunctions, is given by [245, 298]

$$D_{ab} = \frac{1}{2S(2S-1)} \frac{\mu_0}{4\pi} (\gamma_e \hbar)^2 \left[\sum_{i<j}^{occ.} \chi_{ij} \int \int \Phi_{ij}^*(\mathbf{r}, \mathbf{r}^{'}) \frac{\tilde{r}^2 \delta_{ab} - 3\tilde{r}_a \tilde{r}_b}{r^5} \Phi_{ij}(\mathbf{r}, \mathbf{r}^{'}) d\mathbf{r} d\mathbf{r}^{'} \right] , \quad (5.4)$$

where the summation is over all pairs of occupied orbitals, and $\Phi_{ij}(\mathbf{r}, \mathbf{r}^{'})$ are 2×2 determinants formed from orbitals ϕ_i and ϕ_j, $\Phi_{ij}(\mathbf{r}, \mathbf{r}^{'}) = \frac{1}{\sqrt{2}} \Big[\phi_i(\mathbf{r}) \phi_j(\mathbf{r}^{'}) - \phi_i(\mathbf{r}^{'}) \phi_j(\mathbf{r}) \Big]$; $\chi_{ij} = \pm 1$ for parallel and antiparallel spins respectively; $\tilde{r}$ is a scalar representing $|\mathbf{r} - \mathbf{r}^{'}|$; $\tilde{r}_a$ represents the a-direction component of the vector $\mathbf{r} - \mathbf{r}^{'}$. The operator $\frac{\tilde{r}^2 \delta_{ab} - 3\tilde{r}_a \tilde{r}_b}{r^5}$ is the ab element of the Hessian of the Green's function of $-\frac{1}{4\pi} \nabla^2$, i.e. $G(\mathbf{r}, \mathbf{r}^{'}) = \frac{1}{|\mathbf{r} - \mathbf{r}^{'}|}$. Since the operator, $\frac{\partial^2 G(\mathbf{r}, \mathbf{r}^{'})}{\partial r_a \partial r_b^{'}}$, is invariant under particle exchange, the real-space integrals in Eq. 5.4 can be split into direct ($M_{ab}^{ij,D}$) and exchange terms ($M_{ab}^{ij,E}$) given by

$$M_{ab}^{ij,D} = \int \int \phi_i(\mathbf{r}) \phi_j(\mathbf{r}^{'}) \frac{\partial^2 G(\mathbf{r}, \mathbf{r}^{'})}{\partial r_a \partial r_b^{'}} \phi_i^*(\mathbf{r}) \phi_j^*(\mathbf{r}^{'}) d\mathbf{r} d\mathbf{r}^{'} , \quad (5.5)$$

and

$$M_{ab}^{ij,E} = \int \int \phi_i(\mathbf{r}) \phi_j(\mathbf{r}^{'}) \frac{\partial^2 G(\mathbf{r}, \mathbf{r}^{'})}{\partial r_a \partial r_b^{'}} \phi_i^*(\mathbf{r}^{'}) \phi_j^*(\mathbf{r}) d\mathbf{r} d\mathbf{r}^{'} . \quad (5.6)$$

Equation 5.5 and Eq. 5.6 can be rewritten as

$$M_{ab}^{ij,D} = \int\int \frac{\partial(\phi_i(\mathbf{r})\phi_i^*(\mathbf{r}))}{\partial r_a} G(\mathbf{r},\mathbf{r}^{'}) \frac{\partial(\phi_j(\mathbf{r}^{'})\phi_j^*(\mathbf{r}^{'}))}{\partial r_b^{'}} d\mathbf{r} d\mathbf{r}^{'}\,, \tag{5.7}$$

and

$$M_{ab}^{ij,E} = \int\int \frac{\partial(\phi_i(\mathbf{r})\phi_j^*(\mathbf{r}))}{\partial r_a} G(\mathbf{r},\mathbf{r}^{'}) \frac{\partial(\phi_i^*(\mathbf{r}^{'})\phi_j(\mathbf{r}^{'}))}{\partial r_b^{'}} d\mathbf{r} d\mathbf{r}^{'}\,. \tag{5.8}$$

While the equivalence of Eqs. 5.5-5.6 with Eqs. 5.7-5.8 is trivial to see for molecular systems (using integration by parts), showing the equivalence for periodic systems requires a more complex manipulation (see Sec. 5.1.4).

In order to evaluate the double integrals in Eq. 5.7 and Eq. 5.8, we note that the kernel of extended interactions is the Green's function of $-\frac{1}{4\pi}\nabla^2$, and we take recourse to the solution of the Poisson equation. Thus, we obtain,

$$M_{ab}^{ij,D} = \int \frac{\partial(\phi_i(\mathbf{r})\phi_i^*(\mathbf{r}))}{\partial r_a} \Lambda_b^{jj,D}(\mathbf{r}) d\mathbf{r} \tag{5.9}$$

and

$$M_{ab}^{ij,E} = \int \frac{\partial(\phi_i(\mathbf{r})\phi_j^*(\mathbf{r}))}{\partial r_a} \Lambda_b^{ij,E}(\mathbf{r}) d\mathbf{r}\,, \tag{5.10}$$

where $\nabla^2\Lambda_b^{jj,D}(\mathbf{r}) = -4\pi\frac{\partial(\phi_j(\mathbf{r})\phi_j^*(\mathbf{r}))}{\partial r_b}$ and $\nabla^2\Lambda_b^{ij,E}(\mathbf{r}) = -4\pi\frac{\partial(\phi_i^*(\mathbf{r})\phi_j(\mathbf{r}))}{\partial r_b}$. Thus, finally, the D-tensor can be expressed as

$$D_{ab} = \frac{1}{2S(2S-1)}\frac{\mu_0}{4\pi}(\gamma_e\hbar)^2 \sum_{i<j}^{occ.} \chi_{ij}(M_{ab}^{ij,D} - M_{ab}^{ij,E})\,. \tag{5.11}$$

The computationally expensive part of the D-tensor calculation involves the solution of Poisson problems, which are solved on the same FE mesh that represents the KS wavefunctions. However, this computation is embarrassingly parallel over the pairs of orbitals ϕ_i and ϕ_j. We note that, unlike the A-tensor, the dipole-dipole integral entering the D-tensor expression (Eq. 5.4) does not explicitly depend on the nuclear coordinates, and thus we expect

the D-tensor to be less sensitive to the cusps in the spin density at the nuclei. Therefore, a p-refinement is ideal to systematically improve the accuracy in the calculation of D.

Electric Field Gradient Tensor

The nuclear quadrupole interaction P-tensor is directly related to the electric field gradient (EFG) V-tensor. We denote the nuclear quadrupole moment by Q and the quantum number (a component) of the nuclear spin as I (I_a); the nuclear quadrupole Hamiltonian is given by [331]

$$\begin{aligned} H_Q &= \boldsymbol{I} \cdot \boldsymbol{P} \cdot \boldsymbol{I} \\ &= \frac{eQ}{6I(2I-1)} \sum_{a,b} V_{ab} \left[\frac{3}{2}(I_a I_b + I_b I_a) - \delta_{ab} I(I+1) \right], \end{aligned} \tag{5.12}$$

where the EFG V-tensor is the second derivative of the electrostatic potential at the nucleus:

$$\begin{aligned} V_{ab} &= [\nabla_a \nabla_b V(\boldsymbol{r})]|_{\boldsymbol{r}=\boldsymbol{r}_N} \\ &= \left\{ \nabla_a \nabla_b \left[-\int d\boldsymbol{r}' \frac{n(\boldsymbol{r}')}{|\boldsymbol{r}-\boldsymbol{r}'|} + \sum_{I \neq N} \frac{Z_I}{|\boldsymbol{r}-\boldsymbol{r}_I|} \right] \right\} \Bigg|_{\boldsymbol{r}=\boldsymbol{r}_N} \end{aligned} \tag{5.13}$$

Here n is the electron density (defined as positive), and Z_I and $\boldsymbol{r}_I$ are the charge and position of the I^{th} nucleus in the system, respectively.

Calculation of the nuclear contribution to the V-tensor (second term in Eq. 5.13) is trivial, and only requires the knowledge of the nuclear charges and the respective positions of the nuclei. We note that the electronic contribution to the V-tensor is given by the Hessian of the electrostatic potential. To this end, from a converged self-consistent DFT calculation, we extract the Hartree potential and compute the Hessian at the FE quadrature points. By construction, every nucleus is on an FE node in the FE mesh. Thus, the value of the Hessian at each nucleus is obtained via a projection of the quadrature point values to nodal value. As the V-tensor involves point-wise second-order derivatives, a careful convergence study of

both h and p refinement is required.

5.1.3 Results

We carried out calculations of spin Hamiltonian parameters for a series of molecules/radicals and the nitrogen-vacancy (NV) center in diamond. For the calculation of the NV center, the -1 charge state was considered, which is the most relevant charge state for NV-based quantum information processing. A 64-atom supercell of diamond and Γ-point sampling of the Brillouin zone were used. In the following discussion of A and V-tensors of the NV center, we focus on the nitrogen atom and the three carbon atoms with dangling bonds (DB). All calculations were performed with the PBE functional [279]. When treating charged systems we included a neutralizing jellium background. All structures were optimized with plane-wave DFT using the `QUANTUM ESPRESSO` code [106] and the same structures were used for all-electron calculations.

All-electron FE calculations were performed with the `DFT-FE` code using adaptive real-space meshes. The tensor elements were converged with respect to the FE basis through h and p refinements, within 1-2 MHz for the A-tensor, $5 \times 10^{-4}\,\mathrm{cm}^{-1}$ for the D-tensor and 0.05 a.u. for the V-tensor of molecules. Convergence of the spin Hamiltonian parameters for the NV center with respect to the FE basis is presented later in the discussion.

In order to verify our FE results, we also performed PW-based calculations for all systems and GTO-based calculations for molecules. PW calculations of the A and V tensors were carried out with the `GIPAW` code using the GIPAW pseudopotentials (PP). PW calculations of the D-tensor were conducted with two different PP: GIPAW and ONCV [324]. We followed the numerical method in Ref. 298 to evaluate Eq. 5.4 in reciprocal space, using normalized pseudo-wavefunctions [162, 86, 335, 396] (without PAW reconstructions) from the `QUANTUM ESPRESSO` code. A kinetic energy cutoff of 200 Ry was used for PW calculations of molecules; for the NV center we used 100 Ry for computational efficiency. GTO calculations of A, D and P tensors were carried out with the `ORCA` code [257]. Two Gaussian basis sets were

considered: EPR-III [299] and IGLO-III [204], both of which are designed for an accurate representation of core electrons. We also tested a series of general-purpose basis sets from Dunning and co-workers (cc-pVDZ, cc-pVTZ, cc-pVQZ and cc-pV5Z) [82], but we found that the values of A, D and P tensors converge poorly as a function of the basis set and the poor convergence prevented any meaningful extrapolation to the complete basis set limit. We present GTO results obtained with cc- basis sets in Sec. 5.1.4.

Table-I and Table-II show the isotropic (Fermi contact) and spin dipolar component of the A-tensor for several molecules (CN, BO, AlO, NH) and the NV center. Due to the symmetry of the systems considered here, the dipolar A-tensor has only one independent component (except for DB carbons in the NV center). Denoting the principal values of the dipolar A-tensor as $A_{11}^{\rm dip}, A_{22}^{\rm dip}, A_{33}^{\rm dip}$ ($|A_{11}^{\rm dip}| = |A_{22}^{\rm dip}| = \frac{1}{2}|A_{33}^{\rm dip}|$), we show $A_{33}^{\rm dip}$ in Table-II. In PW calculations we tested three different treatments of core relaxation (Slater exchange-only, exchange-only and exchange-correlation) implemented in the `GIPAW` code [16]. Experimental values are also shown in the Tables for reference. We note that all of the results presented here, in addition to numerical errors which are quantified and discussed in detail below, suffer from systematic errors introduced by the use of a specific, approximate exchange-correlation functional, the PBE functional. A previous study has shown that more advanced functionals, such as certain hybrid and meta-GGA functionals, may improve the agreement with experiments, relative to GGA functionals, for the A-tensor of small radicals and transition metal complexes [193]. However, there is yet no consensus on which functional is the most accurate one, in general, for the calculation of the A-tensor or other spin Hamiltonian parameters.

Table 5.1: Isotropic hyperfine tensor (see Eq. 5.2) (MHz) computed by DFT with finite-element (FE), Gaussian-type orbital (GTO) and plane-wave (PW) basis sets. For PW calculations three different treatments of the core-relaxation effect are considered, which include Slater exchange (Slater-X), exchange (X), and exchange+correlation (XC) in the perturbative potential for the calculation of spin densities at the core region.

System	Atom	FE	GTO (EPR-III)	GTO (IGLO-III)	PW (Slater-X)	PW(X)	PW(XC)	Exp
CN ($S=\frac{1}{2}$)	^{13}C	504.21	500.50	509.63	539.55	536.04	566.57	588 [84]
	^{14}N	-12.81	-12.47	-12.25	-14.87	-15.15	-12.43	-13 [84]
BO ($S=\frac{1}{2}$)	^{11}B	1007.71	998.17	1002.34	983.68	980.02	1009.31	1027 [366]
	^{17}O	-7.34	-7.18	-7.26	-7.83	-8.13	-7.24	
AlO ($S=\frac{1}{2}$)	^{27}Al	590.80		646.95	564.18	560.09	626.93	766 [184]
	^{17}O	11.47		12.20	-15.22	-14.78	-22.99	
NH ($S=1$)	^{14}N	11.27	10.20	9.77	24.24	22.00	33.60	20 [394]
	^{1}H	-53.52	-53.13	-47.74	-51.60	-51.60	-51.60	-70 [394]
Diamond NV ($S=1$)	^{14}N	-2.32			-2.60	-2.60	-2.56	2.23 [132], -2.51 [87], -2.53 [412]
	DB ^{13}C	98.72			100.27	99.05	108.51	146.7 [87]

Table 5.2: Spin dipolar hyperfine tensor (see Eq. 5.3) (MHz) computed by DFT with finite-element (FE), Gaussian-type orbital (GTO) and plane-wave (PW) basis sets. The eigenvalue with the largest absolute value is shown.

System	Atom	FE	GTO(EPR-III)	GTO(IGLO-III)	PW	Exp
CN ($S = \frac{1}{2}$)	^{13}C	115.33	118.47	117.43	124.20	89.9 [84]
	^{14}N	44.51	42.62	42.40	45.25	30.8 [84]
BO ($S = \frac{1}{2}$)	^{11}B	53.71	53.38	53.76	55.37	54.254 [366]
	^{17}O	-47.83	-46.47	-45.97	-51.55	
AlO ($S = \frac{1}{2}$)	^{27}Al	114.23		111.67	112.51	106 [184]
	^{17}O	-122.65		-116.42	-127.57	
NH ($S = 1$)	^{14}N	-47.87	-45.82	-46.01	-49.59	-46 [394]
	^{1}H	58.08	58.50	59.92	58.02	60 [394]
Diamond NV ($S = 1$)	^{14}N	-0.07			-0.05	-0.13 [132], 0.37 [87], 0.33 [412]
	DB ^{13}C	54.87			58.34	52.9 [87]

We found that in general, GTO results obtained with EPR-III and IGLO-III basis sets are similar, with a mean absolute deviation (MAD) of 3.2 (0.6) MHz for A^{iso} (A^{dip}) for the systems considered here. FE and GTO results agree well: the MAD between FE and GTO@EPR-III results is 2.5 (1.5) MHz for A^{iso} (A^{dip}). However, for the Al atom in AlO, FE and GTO@IGLO-III yield different values of A^{iso} by 56 MHz (9%). We expect the difference to originate from inaccuracies of the IGLO-III basis set used in GTO calculation; for example, we found that GTO calculations using different cc- basis sets yield large variations, between 580 to 520 MHz, for the A^{iso} value of Al. Overall, the agreement between FE and GTO results serves as a verification of our FE implementation for the calculation of the A-tensor. We note that EPR-III and IGLO-III sets are specialized GTO basis designed for spin Hamiltonian parameter calculations, and they are not available for all elements (for instance, an EPR-III basis set for Al is not available). FE-based calculations, on the other hand, can be performed for any element in the periodic table and the results can be systematically converged with respect to the basis set.

We found that PW calculations agree well with all-electron FE and GTO calculations for A^{dip}, while they deviate slightly for A^{iso}. For A^{dip}, the MAD between FE and PW results is 2.7 MHz, while the MAD for A^{iso} ranges from 13-17 MHz depending on the treatment of core relaxation in PW calculations. Notably, in the case of the AlO molecule, PW calculations predicted a different sign for the A^{iso} of the O atom compared to all-electron FE and GTO calculations.

PW and FE calculations for the NV center yielded qualitatively similar values for A^{iso} and A^{dip} for both nitrogen and DB carbons. The larger value of A^{iso} compared to A^{dip} for the nitrogen atom reveals a strong s character of the spin density on the nitrogen. The spin density on the DB carbons has instead a significant p-type contribution as revealed by the comparable values of A^{iso} and A^{dip}. There is a sizable difference between DFT results and experimental values for the A^{iso} of DB carbons (30%), which might be due to the use of a small (64-atom) supercell for the NV center.

In Table-III we present the computed zero field splitting D-tensor for several spin-triplet molecules/radicals (O_2, CH_2, NH, $C_5H_5{}^+$) as well as for the NV center. We report the scalar parameter $D = \frac{3}{2}D_{33}$, where D_{11}, D_{22}, D_{33} are principal values of the D-tensor such that $|D_{11}| \leq |D_{22}| \leq |D_{33}|$. For low symmetry systems such as the CH_2 carbene, we additionally report the scalar parameter $E = \frac{1}{2}(D_{11} - D_{22})$.

Table 5.3: The spin-spin component of the zero-field splitting tensor (see Eq. 5.4) (cm^{-1}) computed by DFT with finite-element (FE), Gaussian-type orbital (GTO) and plane-wave (PW) basis sets. Scalar parameters $D = \frac{3}{2}D_{33}$ are reported. Scalar parameters $E = \frac{1}{2}(D_{22} - D_{11})$, if non-zero, are reported in brackets.

System	FE	GTO(EPR-III)	GTO(IGLO-III)	PW(GIPAW)	PW(ONCV)	Exp
O_2 ($S = 1$)	1.894	1.893	1.843	1.642	1.695	3.960 [154][a]
CH_2 ($S = 1$)	0.894 (0.051)	0.895 (0.052)	0.895 (0.052)	0.896 (0.052)	0.908 (0.049)	0.760 (0.068) [390]
NH ($S = 1$)	1.861	1.862	1.857	1.795	1.815	1.860 [73]
$C_5H_5^+$ ($S = 1$)	0.123	0.120	0.110	0.123	0.123	0.187 [320]
Diamond NV ($S = 1$)	0.100			0.101	0.100	0.096 [216]

[a] Experimental value for O_2 is dominated by the spin-orbit component. The spin-spin component is estimated to be $1.57\,cm^{-1}$ by *ab initio* wavefunction-based calculations [345].

Overall, GTO results show a weak dependence on the basis set, with a MAD of 0.016 cm^{-1} between values obtained with EPR-III and IGLO-III basis sets. PW calculations show a weak dependence on the chosen pseudopotential, with a MAD of 0.017 cm^{-1} between ONCV and GIPAW results. Similar to the case of the A-tensor, GTO and FE results agree well, with a MAD of 0.001 cm^{-1} between FE and GTO@EPR-III values. Due to the use of pseudo-wavefunctions for the evaluation of Eq. 5.4 and the lack of PAW reconstruction, PW results deviate from all-electron ones, with a MAD of 0.064 cm^{-1} between FE and PW@GIPAW values. For the case of the NV center, results from FE, PW and experiments appear to be in good agreement.

Table-IV summarizes the electric field gradient V-tensor for several closed-shell molecules (HCN, NCCN, N_2, H_2O) and for the NV center. Following the convention of the NQR spectroscopy literature, we report the quadrupole coupling constants eQV_{33}, where V_{11}, V_{22}, V_{33} are principal values of the V-tensor such that $|V_{11}| \leq |V_{22}| \leq |V_{33}|$. For low symmetry systems, we additionally report $\eta = \left|\frac{V_{22}-V_{11}}{V_{33}}\right|$.

Table 5.4: Quadrupole coupling constants eQV_{33} (see Eq. 5.13) (MHz) computed by DFT with finite-element (FE), Gaussian-type orbital (GTO) and plane-wave (PW) basis sets. The scalar parameters $\eta = \left|\frac{V_{22}-V_{11}}{V_{33}}\right|$, if non-zero, are reported in brackets.

System	Atom	FE	GTO(EPR-III)	GTO(IGLO-III)	PW	Exp
HCN ($S=0$)	^{2}H	0.20	0.21	0.22	0.20	
	^{11}C	-2.95	-2.87	-2.77	-3.73	
	^{14}N	-4.72	-4.85	-4.79	-5.07	-4.02 [208]
NCCN ($S=0$)	^{14}N	-4.72	-4.80	-4.75	-4.99	-4.27 [208]
	^{11}C	-1.84	-1.95	-1.76	-2.72	
N_2 ($S=0$)	^{14}N	-5.08	-5.52	-5.46	-5.77	-4.65 [208]
H_2O ($S=0$)	^{2}H	0.31 (0.12)	0.31 (0.13)	0.32 (0.13)	0.30 (0.13)	0.31 (0.14) [380]
	^{17}O	10.10 (0.81)	10.69 (0.74)	10.90 (0.74)	10.85 (0.72)	10.17 (0.75) [380]
Diamond NV ($S=1$)	^{14}N	-7.30			-7.47	-6.68 [87][a]
	DB ^{11}C	1.96 (0.03)			-1.77 (0.10)	

[a] Computed from $P_{\|}$ parameter reported in Ref. 87 by $eQV_{33} = 4I(2I-1)P_{\|}/3$.

Unlike the A tensor, which depends on charge density differences, the V-tensor depends on the absolute value of the charge density and thus it is more sensitive to the details of the electronic structure. Differences are indeed observed for GTO calculations with different basis sets (MAD = 0.09 MHz), as well as between GTO and FE calculations (MAD = 0.18 MHz between FE and GTO@EPR-III). PW results significantly deviate from all-electron GTO and FE results, with a MAD of 0.76 MHz between FE and PW values. In the case of the NV center, PW and FE yield similar nuclear quadrupole coupling for nitrogen, in qualitative agreement with experiment, while for DB carbons the predicted V_{33} values using PW and FE have opposite signs.

Finally, to demonstrate the convergence of the FE results with respect to the basis set, in Table-V we show A-, D- and V-tensors for the NV center computed with different FE polynomial degrees. We denote calculations with n^{th}-order polynomials as FEn. For the A-tensor and V-tensor calculations a mesh size of 0.1 Bohr was used surrounding the nuclei, while for the D-tensor calculation the mesh size was 0.5 Bohr. We see in Table-V that our results for the A-tensor are well converged at the FE6 level, as indicated by the small difference (less than 3%) between FE5 and FE6 results. Similarly, D-tensor values are well converged at the FE5 level. The numerical value of the V tensor is sensitive to the details of the electronic wavefunctions around the nuclei, as mentioned previously, and its convergence is indeed more challenging compared to that of the A- and D-tensors. We performed V-tensor calculations with polynomial degrees up to 7. At the FE7 level, most of the computed V tensor elements are converged within 10%, based on asymptotic estimates obtained by power law extrapolations.

Table 5.5: The principle values of A (top, in MHz), D (center, in cm^{-1}), and V (bottom, in a.u.) tensors for the NV center computed by FE-based DFT using different finite-element polynomial degrees.

	^{14}N				DB ^{13}C			
	A_{11}^{dip}	A_{22}^{dip}	A_{33}^{dip}	A^{iso}	A_{11}^{dip}	A_{22}^{dip}	A_{33}^{dip}	A^{iso}
FE3	0.033	0.033	-0.066	-2.362	-27.303	-27.592	54.896	100.492
FE4	0.034	0.034	-0.067	-2.307	-27.199	-27.654	54.853	99.708
FE5	0.035	0.035	-0.070	-2.319	-27.189	-27.664	54.854	99.016
FE6	0.035	0.035	-0.070	-2.316	-27.171	-27.696	54.867	98.721

	D_{11}	D_{22}	D_{33}
FE3	-0.0327	-0.0327	0.0654
FE4	-0.0321	-0.0321	0.0642
FE5	-0.0329	-0.0329	0.0658

	N			DB C		
	V_{11}	V_{22}	V_{33}	V_{11}	V_{22}	V_{33}
FE5	0.865	0.865	-1.731	-0.033	-0.127	0.160
FE6	0.804	0.804	-1.609	-0.081	-0.136	0.217
FE7	0.761	0.761	-1.520	-0.122	-0.129	0.251

5.1.4 Technical details

Real space computation of D-tensor for crystalline solids

Here, we describe the mathematical formulation behind translating Eq. 5.5 (Eq. 5.6) to Eq. 5.7 (Eq. 5.8) for crystalline solids. Eq. 5.5, in a periodic system, has the following the form given by

$$M_{ab}^{ij,D} = \int_{\Omega}\int_{\mathbb{R}^3} f(\mathbf{r})\frac{\partial^2 G(\mathbf{r},\mathbf{r}')}{\partial r_a \partial r_b'} h(\mathbf{r}')d\mathbf{r}'d\mathbf{r}\,, \tag{5.14}$$

with $h(\mathbf{r}') = \phi_j(\mathbf{r}')\phi_j^*(\mathbf{r}')$ and $f(\mathbf{r}) = \phi_i(\mathbf{r})\phi_i^*(\mathbf{r})$. Ω is the volume representing the unit cell. Integrating by parts with respect to $\mathbf{r}$, we arrive at

$$M_{ab}^{ij,D} = -\int_{\Omega}\frac{\partial f(\mathbf{r})}{\partial r_a}\int_{\mathbb{R}^3}\frac{\partial G(\mathbf{r},\mathbf{r}')}{\partial r_b'}h(\mathbf{r}')d\mathbf{r}'d\mathbf{r} + \oint_{S(\Omega)} f(\mathbf{r})\Big(\int_{\mathbb{R}^3}\frac{\partial G(\mathbf{r},\mathbf{r}')}{\partial r_b'}h(\mathbf{r}')d\mathbf{r}'\Big)d(\hat{\mathbf{a}}.\mathbf{S})\,. \tag{5.15}$$

Now noting the fact that $\frac{\partial G(\mathbf{r},\mathbf{r}^{'})}{\partial r_b^{'}} = -\frac{\partial G(\mathbf{r},\mathbf{r}^{'})}{\partial r_b}$, we can rewrite the second term on the right hand side of Eq. 5.15 as

$$M_{ab,2}^{ij,D} = -\oint_{S(\Omega)} f(\mathbf{r}) \frac{\partial}{\partial r_b} \Big(\int_{\mathbb{R}^3} G(\mathbf{r},\mathbf{r}^{'}) h(\mathbf{r}^{'}) d\mathbf{r}^{'} \Big) d(\hat{\mathbf{a}}.\mathbf{S}) \,. \tag{5.16}$$

The term within the parenthesis (let us denote it as $\Phi(\mathbf{r})$) can be obtained from the solution of the PDE, $\nabla^2 \Phi(\mathbf{r}) = -4\pi h(\mathbf{r})$, with periodic boundary conditions on the unit cell domain, provided $\int_\Omega h(\mathbf{r}) d\mathbf{r} = 0$. However, this condition is not valid while computing the direct part of the D-tensor, as $\int_\Omega h(\mathbf{r}) d\mathbf{r} = 1$. Thus, we rewrite Eq. 5.3 as the sum of two terms, given by

$$\begin{aligned} M_{ab,2}^{ij,D} = &-\oint_{S(\Omega)} f(\mathbf{r}) \frac{\partial}{\partial r_b} \Bigg(\int_{\mathbb{R}^3} G(\mathbf{r},\mathbf{r}^{'}) \Big(h(\mathbf{r}^{'}) - \frac{1}{\Omega} \Big) d\mathbf{r}^{'} \Bigg) d(\hat{\mathbf{a}}.\mathbf{S}) \\ &- \frac{1}{\Omega} \oint_{S(\Omega)} f(\mathbf{r}) \Big(\int_{\mathbb{R}^3} \frac{\partial G(\mathbf{r},\mathbf{r}^{'})}{\partial r_b} d\mathbf{r}^{'} \Big) d(\hat{\mathbf{a}}.\mathbf{S}) \,. \end{aligned} \tag{5.17}$$

Considering the second term on the right hand side of Eq. 5.4, it is straightforward to show that the integral within the parenthesis (over $\mathbb{R}^3$) vanishes. Further, noting that the convolution integral within the parenthesis (over $\mathbb{R}^3$) of the first term of Eq. 5.17 is the given by the solution of the Poisson equation, the resulting field is periodic on the unit cell. Thus, the surface integral in the first term of Eq. 5.17 vanishes owing to the periodicity of the functions. Thus, Eq. 5.15 can be rewritten as

$$M_{ab}^{ij,D} = -\int_\Omega \frac{\partial f(\mathbf{r})}{\partial r_a} \int_{\mathbb{R}^3} \frac{\partial G(\mathbf{r},\mathbf{r}^{'})}{\partial r_b^{'}} h(\mathbf{r}^{'}) d\mathbf{r}^{'} d\mathbf{r} \,, \tag{5.18}$$

which, again, through integration by parts can be written as

$$M_{ab}^{ij,D} = \int_\Omega \int_{\mathbb{R}^3} \frac{\partial f(\mathbf{r})}{\partial r_a} G(\mathbf{r},\mathbf{r}^{'}) \frac{\partial h(\mathbf{r}^{'})}{\partial r_b^{'}} d\mathbf{r}^{'} d\mathbf{r} \,, \tag{5.19}$$

which is same as Eq. 5.7 of. We note that the boundary term, resulting from integration by parts, in the above equation vanishes as $G(\mathbf{r}, \mathbf{r}^{'}) \to 0$ as $\mathbf{r}^{'} \to \infty$.

The treatment of the exchange term is similar. In this case, we define $h(\mathbf{r}^{'}) = \phi_i(\mathbf{r}^{'})\phi_j^*(\mathbf{r}^{'})$, and $f(\mathbf{r}) = \phi_i(\mathbf{r})\phi_j^*(\mathbf{r})$, $\forall\ i \neq j$. Thus, the condition $\int_\Omega h(\mathbf{r})d\mathbf{r} = 0$ holds from the orthogonality of the Kohn-Sham wavefunctions, and one need not split Eq. 5.16 into two parts as above. The rest of the arguments are identical.

Convergence tests for GTO calculations with cc- basis sets

In this section we present A^{iso}, A_{33}^{dip}, D and V_{33} computed with GTO DFT as a function of basis sets: cc-pVDZ ($\zeta = 2$), cc-pVTZ ($\zeta = 3$), cc-pVQZ ($\zeta = 4$), cc-pV5Z ($\zeta = 5$). According to the following plots, in many cases spin Hamiltonian parameters do not converge with respect to basis in a reasonable manner. Therefore, it is challenging to extrapolate the results to the complete basis set (CBS) limit, as is usually done for the calculation of DFT total energies.

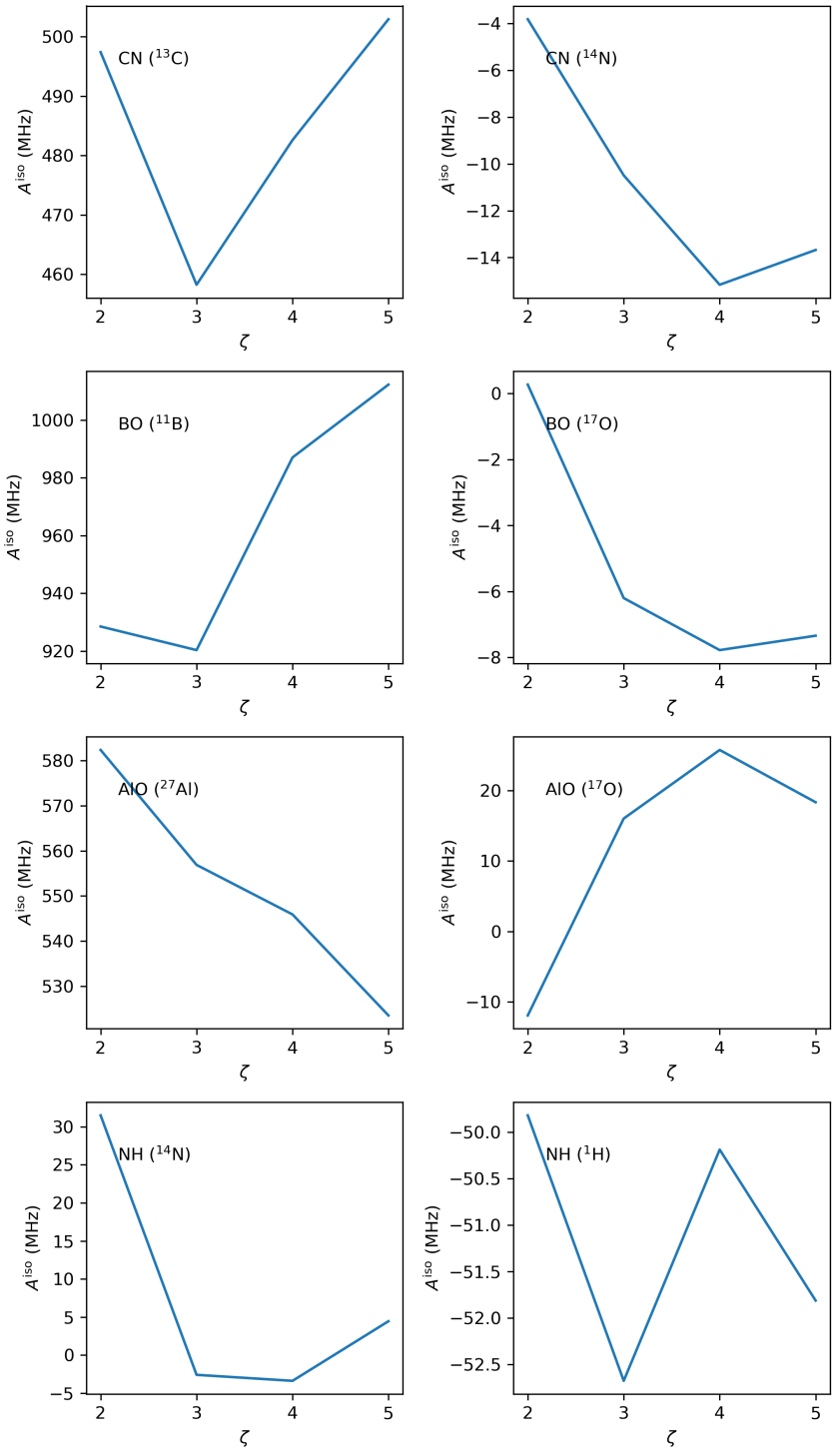

Figure 5.1: A^{iso} as a function of basis set.

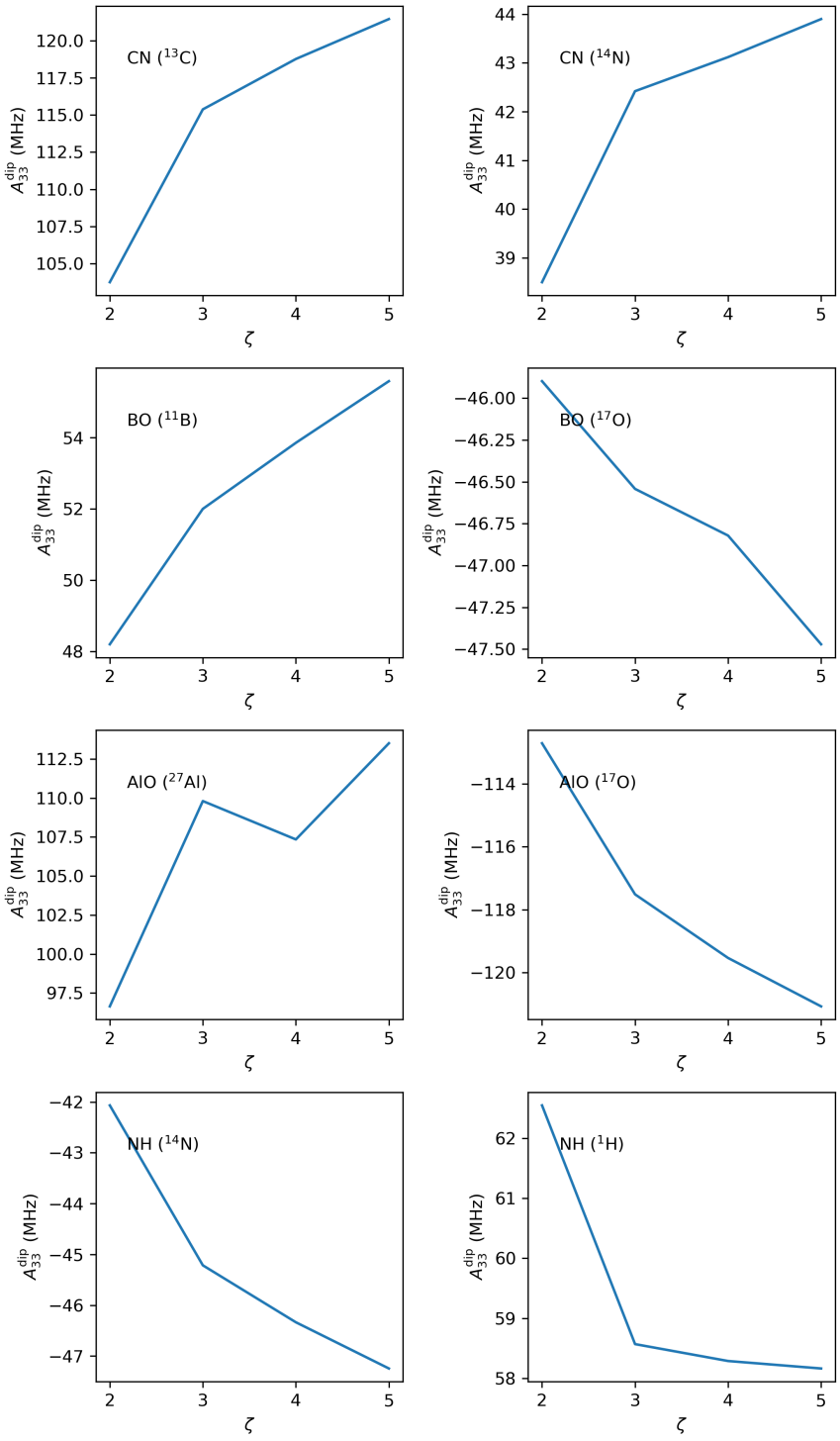

Figure 5.2: A_{33}^{dip} as a function of basis set.

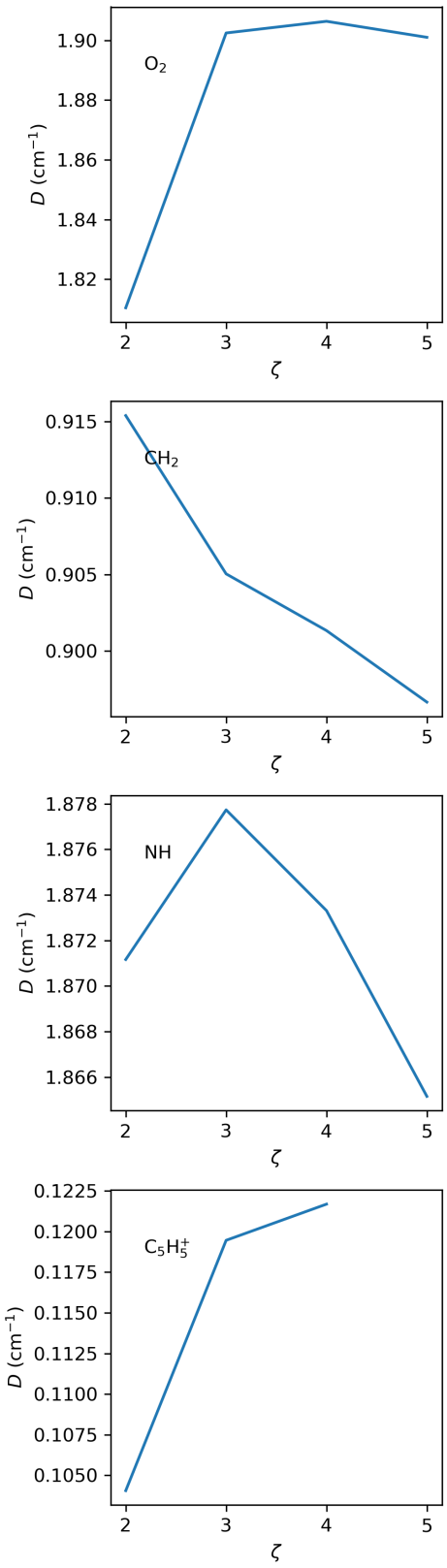

Figure 5.3: D as a function of basis set. cc-pV5Z calculation for $C_5H_5^+$ is not performed due to computational cost.

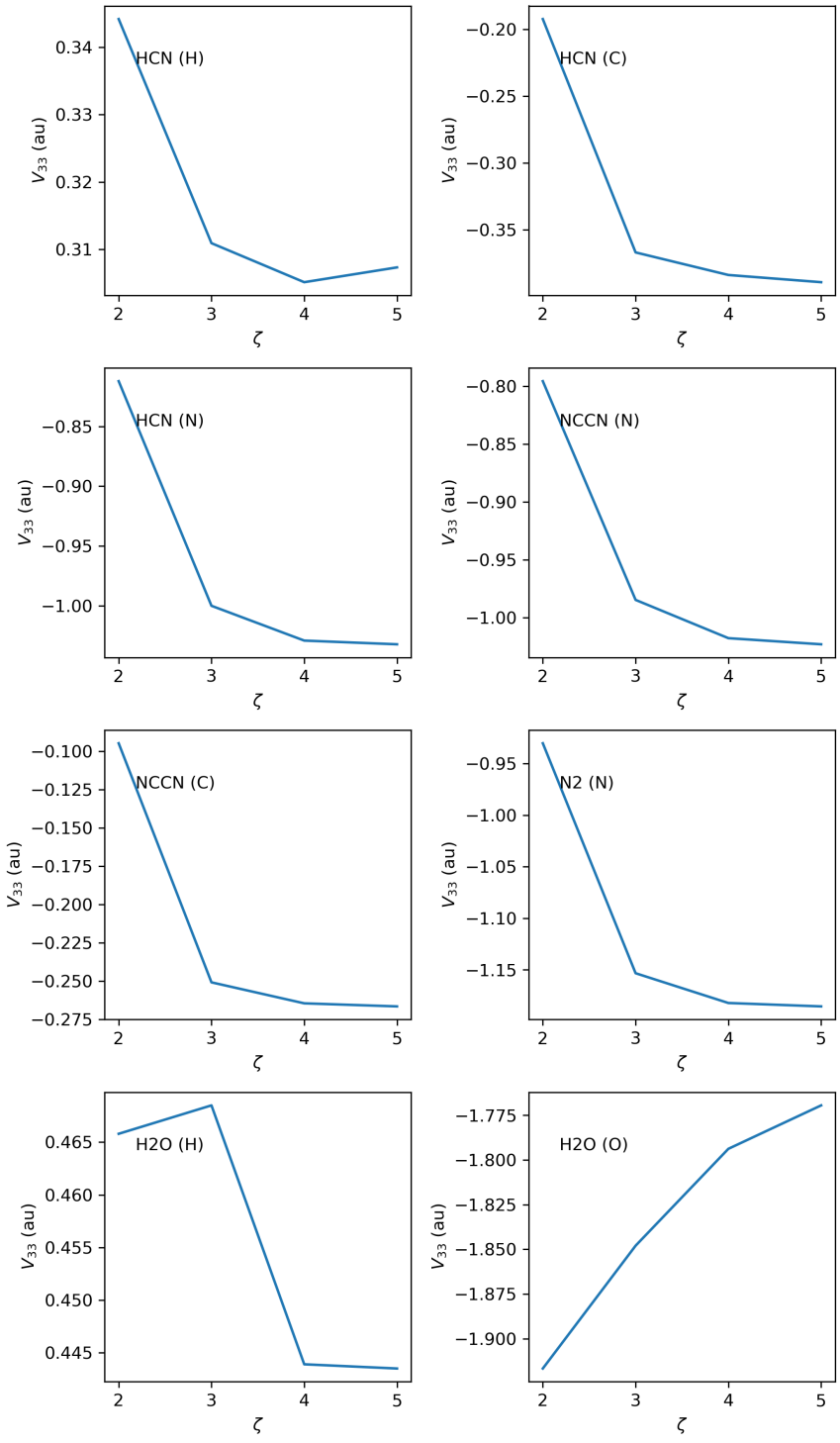

Figure 5.4: V_{33} as a function of basis set.

5.1.5 Conclusions

To summarize, we presented an approach to compute spin Hamiltonian parameters based on DFT, which uses all-electron calculations and finite element basis sets to solve the Kohn-Sham equations. The approach can be applied to both solids and molecules and offers the important advantage of straightforward convergence of the calculations with respect to the basis set, which can be systematically achieved by refinement of the finite element basis.

We reported calculations of the Fermi contact and dipolar component of the A-tensor, the spin-spin component of the D-tensor and the nuclear quadrupole P-tensor for several molecules and for the NV center in diamond. We presented detailed comparisons of results obtained using FE, GTO and PW basis. For molecules, we showed that all-electron results obtained with FE basis sets are in good agreement with those obtained with GTO basis sets.

The approach introduced in our work represents the first step towards building a robust protocol for the first-principles prediction of various spin Hamiltonian parameters based on finite element density functional theory. There are multiple prospects of future work in this direction, both in terms of the level of physics and computational efficiency. It is important to extend the current formalism to include relativistic effects since proper treatment of scalar relativistic effects will be crucial for accurate calculations of spin Hamiltonian parameters of heavy elements. The ability to include spin-orbit coupling effects will also allow for the computation of additional spin Hamiltonian parameters, including the g-tensor and the spin-orbit component of the A and D-tensor. Further, it would be interesting to develop and test more advanced density functionals, such as meta-GGAs and hybrid functionals, and to establish which functional performs better, compared to experiments. With regards to the computational efficiency, the FE basis functions can be enriched using compactly supported precomputed enrichment functions [175], which will drastically reduce the computational cost, while providing systematic convergence. Finally, we plan to utilize a combination of all-electron and pseudopotential based calculation under the same framework, where certain atoms of interest are treated at all-electron level and other atoms are treated using pseudopo-

tential approximation, which will enable the computation of spin Hamiltonian parameters in systems involving thousands of atoms.

5.2 Mixed all-electron-pseudopotential calculation of spin properties

Adapted from K. Ghosh, H. Ma, M. Onizhuk, V. Gavini, and G. Galli. To be submitted.

Spin-defects in semiconductors are promising quantum bits (qubits) for quantum information technologies including quantum computation, quantum communication and quantum sensing. The prime example of spin-defect is the nitrogen-vacancy (NV) center in diamond, which can be optically initialized and read-out, and possesses millisecond coherence time even at room temperature. In recent years, great efforts have been devoted to the search for novel spin-defects in industrially friendly host materials with similar or superior properties to diamond NV centers for quantum information applications. For instance, several promising spin-defects have been investigated in silicon carbide, including the divacancy (VV), Cr impurity, V impurity, etc. There are also growing interests in discovering and designing spin qubits in aluminum nitride, zinc oxide, and 2D materials.

First-principles simulations based on density functional theory (DFT) have played an important role in the discovery and identification of novel spin-defects. In particular, DFT simulations can predict various thermodynamic and spin properties of spin-defects, which provide critical information for the interpretation of optical and magnetic measurements, and the determination of atomistic configuration and electronic structure of unknown defects. Among various properties DFT can compute, spin properties are among the most important predictors for promising defect spin qubits. The spin properties of a point defect in a certain electronic state (such as the ground state) can be summarized by its spin Hamiltonian (SH), which describes the interaction between electron spins, nuclei spins and external fields. A typical SH for a spin-defect is

$$H = \mu_B \boldsymbol{B} \cdot \boldsymbol{g} \cdot \boldsymbol{S} + \sum_N \boldsymbol{S} \cdot \boldsymbol{A}_N \cdot \boldsymbol{I}_N + \boldsymbol{S} \cdot \boldsymbol{D} \cdot \boldsymbol{S} \tag{5.20}$$

where $\boldsymbol{g}$-tensor characterizes the coupling strength between the electron and the external

magnetic field, hyperfine $\boldsymbol{A}$-tensors characterize the coupling between electron and nuclei spins, and zero field splitting $\boldsymbol{D}$-tensor characterizes the energy splitting between different spin states at zero magnetic field. We have neglected other terms with smaller magnitudes. The $\boldsymbol{A}$-tensor and $\boldsymbol{D}$-tensor are particularly important descriptors of novel defects: large hyperfine couplings limit the coherence time of electron spin, but may benefit the use of nuclear spins as quantum memories; the dependence of $\boldsymbol{D}$-tensor on external environment characterizes the coupling between electron spins and other degrees of freedom such as lattice strain, electric field and temperature, and are important for quantum sensing applications.

The great majority of existing DFT calculations of SH parameters are based on the plane-wave pseudopotential formalism. Other formalism exists but is often limited to small systems. In the plane-wave pseudopotential formalism, pseudopotentials are used to approximate interactions between valence electrons and nuclei, and wavefunctions of core electrons are not explicitly evaluated. Based on the results of plane-wave pseudopotential calculations, one generally needs to perform a so-called projected augmented wave (PAW) reconstruction to extract all-electron wavefunctions for the calculation of SH parameters. Such calculations yield results dependent on the choice of pseudopotentials. In the previous section, we proposed and benchmarked a real-space all-electron DFT framework based on finite-element (FE) basis sets for accurate prediction of SH parameters in molecules and solids. This framework enables all-electron calculations of SH parameters and leads to results that can be systematically converged with respect to basis sets. In this work, we propose a novel computational scheme that combines the all-electron and pseudopotential formalism, and we demonstrate calculations of systems with $\sim$1000 atoms. In particular, the new scheme proposed here treats selected atoms in the system on the all-electron level, while treating the rest of atoms using pseudopotentials (see Figure 5.5). We applied the mixed all-electron pseudopotential scheme to compute the $\boldsymbol{A}$-tensor and $\boldsymbol{D}$-tensor of NV in diamond and VV in 4H-SiC. Remarkably, we show that by only treating a few atoms around the defect on the all-electron level, one can already obtain results almost identical to those obtained with

pure all-electron calculations.

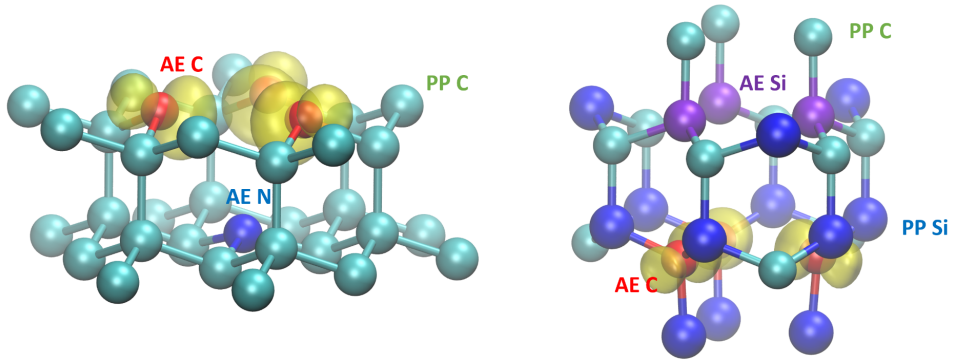

Figure 5.5: Structure and spin density of nitrogen-vacancy (NV) center in diamond (left) and divacancy in 4H-SiC (right). In both systems, the spin density is localized around three carbon atoms with dangling bonds. By only treating a few atoms near the defect at the all-electron (AE) level, one can obtain accurate predictions of spin Hamiltonian parameters, while the remaining atoms can be treated using the pseudopotential (PP) approximation.

CHAPTER 6

FIRST-PRINCIPLES SIMULATION OF SPIN-DEFECTS FOR QUANTUM INFORMATION SCIENCE

In this chapter, we present several studies where we apply first-principles methods to investigate spin-defects for quantum information science (QIS). Spin-defects in semiconductors are point defects that carry electron spins, whose spin sublevels can be harnessed to encode quantum information. Compared to other physical realization of quantum bits (qubits), spin-defects combines several desirable features such as long coherence time, room temperature operability and optical addressibility. Spin-defects have been widely used in QIS fields including quantum sensing, quantum communication and hybrid quantum architectures.

The research summarized in this chapter can be partitioned into two topics. The first topic is the computational design and characterization of novel spin-defects. Currently, the most studied spin-defect is the nitrogen-vacancy (NV) center in diamond, and a lot of efforts have been devoted to explore novel spin-defects in diamond and other materials, with the hope of finding novel defects with distinct (hopefully improved) properties from NV centers in diamond. In Section 6.1 we proposed several novel transition metal ion-vacancy complexes in silicon carbide and aluminum nitride as promising spin qubits. In Section 6.2 we present a computational study of strongly-correlated electronic states of group-4 vacancy centers in diamond.

The second topic of this chapter is the computational study of existing spin-defects, where first-principles calculations are used to interpret experimental measurements and to provide guidance for the design of new experiments. In Section 6.3 we present a joint experimental-computational study of divacancy (VV) defects in silicon carbide under mechanical waves, where DFT and group theory are used to derive a complete microscopic theory of spin-phonon interaction of VV. In Section 6.4 we briefly introduce quantum dynamics simulations of spin-defects using the cluster correlation expansion (CCE) method, which allowed us to predict

the coherence time of spin-defects in the bath of nuclear spins and other spin-defects.

6.1 Discovery of novel spin qubits in silicon carbide and aluminum nitride

https://doi.org/10.1103/PhysRevMaterials.1.075002

The development of novel quantum bits is key to extend the scope of solid-state quantum information science and technology. Using first-principles calculations, we propose that large metal ion - vacancy pairs are promising qubit candidates in two binary crystals: 4H-SiC and w-AlN. In particular, we found that the formation of neutral Hf- and Zr-vacancy pairs is energetically favorable in both solids; these defects have spin-triplet ground states, with electronic structures similar to those of the diamond NV center and the SiC di-vacancy. Interestingly, they exhibit different spin-strain coupling characteristics, and the nature of heavy metal ions may allow for easy defect implantation in desired lattice locations and ensure stability against defect diffusion. In order to support future experimental identification of the proposed defects, we report predictions of their optical zero-phonon line, zero-field splitting and hyperfine parameters. The defect design concept identified here may be generalized to other binary semiconductors to facilitate the exploration of new solid-state qubits.

6.1.1 Introduction

Optically active spin defects in wide-gap semiconductors are important resources for solid-state quantum technologies [12, 57, 138, 99]. One well-known spin defect is the nitrogen-vacancy (NV) center in diamond [76], which may be used for applications ranging from quantum information processing [385] to quantum sensing [71, 406]. Recently, alternative defect qubits in wide-gap binary semiconductors have been proposed [188, 397, 351, 18]. In particular, di-vacancies in SiC were shown to have several desired properties similar to the diamond NV center [188, 59, 60] and to exhibit a quantum coherence time much longer than

that of the diamond NV [59, 333, 410]. In a previous study, we showed that the binary nature of SiC is responsible for the improved coherence time [333]. Given the attractive properties of SiC - i.e., much cheaper than diamond and with well-established synthesis procedures - and the promising properties of its point defects, it is interesting to explore whether additional defects may be engineered in SiC as qubit candidates [392, 190].

In recent years, first-principles calculations have played a key role in the search of defect qubits in wide-gap semiconductors. For example, by using density functional theory (DFT), Gali pointed out similarities between the divacancy spin in SiC and the diamond NV center [96], originating from the same C_{3v} configuration of C $2sp^3$ dangling bonds in the two materials [163]. An experimental investigation of the divacancy by Koehl *et al.* readily followed [188]. Weber *et al.* formulated criteria for the systematic identification of qubits in wide-gap semiconductors and proposed to realize 'NV centers' in SiC [392]. Later, Bardeleben *et al.* experimentally verified the existence of the NV center in SiC [382], which were followed by further experimental and theoretical characterizations [416, 381]. First-principles DFT calculations have also been used to investigate Si vacancies (VSi) in SiC and to identify the role of C $2sp^3$ dangling bonds in determining the properties of the optically addressable solid-state qubit [355].

The realization of 'NV-like' qubits in SiC, based on C $2sp^3$ dangling bonds, may lead to several advantageous properties [138, 392, 190], nevertheless a number of drawbacks are present. For example, the SiC divacancy, similar to the diamond NV center, may exhibit low optical read-out fidelity [76, 356] and small ground-state spin-transverse strain coupling [209, 86], which is unfavorable for certain hybrid quantum applications [222, 30, 329, 114, 373]. In addition, the implementation of spin qubits using C $2sp^3$ dangling bonds is not generalizable to other binary materials, e.g. nitrides. In the case of nitrides, theoretical studies have suggested that defects based on N $2sp^3$ dangling bonds, e.g. $V_{Al}O_N$ may be potential qubit candidates [373]. However, in a previous study on AlN [334], we showed that the occupied spin-orbitals of $V_{Al}O_N$ are in strong resonance with the valence band of the host, which

make them unfavorable for spin qubit applications.

Therefore, it is desirable to explore the possibility of realizing qubits that are based on novel defects rather than on C or N $2sp^3$ dangling bonds. Recent theoretical studies have proposed spin defects in SiC and AlN based on cationic dangling bonds, e.g. Al $3sp^3$ states and Si $3sp^3$ states [334, 362, 379]. In a previous work, we showed that the negatively charged N vacancy in w-AlN could have an optically addressable spin-triplet state under a uniaxial or biaxial strain [334]. Varley *et al.* considered impurity-vacancy pairs in w-AlN based on Group-IV elements including Ge, Sn, Ti, and Zr [379]. They suggested that Zr- and Ti-vacancy pairs would be good candidates for spin qubits in w-AlN. In the case of 4H-SiC, Szasz *et al.* proposed that the $S = 1$ state of the carbon-antisite vacancy defect may be stable, and hence may be a valuable qubit [362].

Using a combination of first-principles calculations, here we propose that large metal ion - vacancy (LMI-vacancy) pairs are promising qubit candidates in both 4H-SiC and w-AlN. In particular, we selected Y, La, Zr, and Hf ions for two reasons: (i) They have ionic radii larger than those of Si and Al [339], and hence they may favorably pair with anion vacancies, i.e. N vacancies in w-AlN and C vacancies in 4H-SiC. Such pairing was previously investigated for Nb in SiC [161] and Ce in AlN [212] are lower than those of Al (1.6), Si (1.9), possibly leading to the stabilization of desired charge states for the defect complexes. We found that neutral Hf- and Zr-vacancy pairs are promising candidates for spin qubits in both 4H-SiC and w-AlN. Our calculations showed that these defect complexes are energetically stable and exhibit a spin-triplet ground state localized in the band gap of SiC and AlN, which could be optically addressable. In addition, we predicted the optical zero-phonon line, spin zero-field splitting, and hyperfine coupling parameters of the defects, to assist future experimental detection.

The rest of the paper is organized as follow. In Section 6.1.2, we describe the first-principles computational methods used in this work. Our main results are presented in Section 6.1.3. In Section 6.1.4, we discuss the unique features of the defects proposed here

as potential qubits in 4H-SiC and w-AlN and we summarize our results.

6.1.2 Methods

Density functional theory and G_0W_0 calculations

We performed DFT calculations with semi-local and hybrid functionals using plane-wave basis sets (with an energy cutoff of 75 Ry), optimized norm-conserving Vanderbilt (ONCV) pseudopotentials [129, 324] and the Quantum Espresso code [106]. We used the PBE semi-local functional [279] and the dielectric-dependent hybrid (DDH) functional proposed in Ref. 346 with the self-consistent Hartree-Fock mixing parameter (α) determined in Ref. 346 for SiC ($\alpha_{\mathrm{SiC}} = 0.15 = 1/\epsilon_{\infty,\mathrm{SiC}}$, where $\epsilon_{\infty,\mathrm{SiC}} = 6.5$ was self-consistently computed by including the full response of the electronic density to the perturbing external electric field). For AlN, we used the PBE0 hybrid functional [4], whose choice for AlN was extensively verified in Ref. 334 (For PBE0, $\alpha_{\mathrm{AlN}} = 0.25$, close to the self-consistently determined mixing parameter; $1/\epsilon_{\infty,\mathrm{AlN}} = 1/4.16 = 0.2446$). Bulk properties of 4H-SiC (see Table 6.1) and w-AlN (reported in our previous study [334]) computed with the DDH functionals were found to be in excellent agreement with experimental data [212, 278]. In addition, we also performed calculations with the Heyd-Scuseria-Ernzerhof (HSE06) range-separated hybrid functional 141 and projector-augmented-wave (PAW) pseudopotentials [34] to cross-check some of our results obtained with the DDH functional.

The calculation of the defect formation energy [90] of charged point defects in a crystal was carried out with the charge correction scheme developed by Freysoldt, Neugebauer, and Van de Walle [91]. We employed supercells with 480 atoms and 96 atoms for PBE and DDH calculations, respectively, and we sampled the Brillouin zone with the Gamma point only for the largest supercell and with a $2 \times 2 \times 2$ k-point for the smallest one. Convergence studies as a function of cell size and k-meshes were reported in a previous paper [334].

The zero-phonon line (ZPL) of the LMI-vacancy pairs was obtained by calculating total

Table 6.1: Computed bulk properties of the 4H-SiC calculated at the PBE and the DDH-DFT levels of theory along using ONCV pseudopotentials [129, 324]. Experimental values are from Ref. 212, 278.

	Lattice parameters		Dielectric constants	
	a (Å)	c (Å)	Electronic ($\epsilon_{\infty,\parallel}$ /$\epsilon_{\infty,\perp}$)	Static ($\epsilon_{0,\parallel}$ /$\epsilon_{0,\perp}$)
PBE	3.096	10.136	6.938 / 7.251	10.306 / 10.938
DDH	3.087	10.089	6.396 / 6.623	9.663 / 9.926
Experiment	3.073	10.053	6.52 / 6.70	9.66 / 10.03

Table 6.2: Computed band-gaps (eV) of the crystals considered in this study calculated at the G_0W_0@PBE, the DDH hybrid, and the HSE06 hybrid functional levels of theory.

Host crystals	DD-hybrid (eV)	HSE06 (eV)	G_0W_0@PBE (eV)	Experiment
Diamond	5.59	5.42	4.25	5.48 [180]
4H-SiC	3.28	3.19	3.29	3.23 [212]
w-AlN	6.39	5.67	6.12	6.03 - 6.28 [302]

energy differences (ΔSCF method) with 480-atom supercells with the PBE semi-local functional and 240-atom supercells with the hybrid functionals (DDH and HSE06). We found that energy differences computed with 480- and 240-atom supercells at the PBE level differed by less than 50 meV.

We also calculated defect level diagrams of the LMI-vacancy pairs in 4H-SiC and w-AlN within the G_0W_0@PBE approximation [133, 156] using the WEST code [117] with 240-atom supercells and the Γ point only. Table 6.2 compares the band-gap of diamond, 4H-SiC, and w-AlN obtained with the G_0W_0@PBE as well as with hybrid DFT calculations, showing excellent agreement with experiment.

Spin Hamiltonian: zero-field splitting and hyperfine parameters

The properties of a defect in a crystal with spin $S > 1/2$, interacting with a nuclear spin I can be described by the following spin Hamiltonian [331]:

$$H = \boldsymbol{S} \cdot \boldsymbol{D} \cdot \boldsymbol{S} + \boldsymbol{S} \cdot \boldsymbol{A} \cdot \boldsymbol{I} \tag{6.1}$$

where $\boldsymbol{D}$ is the zero-field splitting (ZFS) tensor describing the splitting and the mixing of levels with different values of magnetic spin quantum number (e.g. $m_s = 0, \pm 1$ for $S = 1$), occuring even in the absence of an applied magnetic field and $\boldsymbol{A}$ is the hyperfine tensor describing the coupling between the electron spin and the nuclear spin. The first term of Eq. 6.1 can be written as:

$$H_{\mathrm{ZFS}} = D_{xx}S_x^2 + D_{yy}S_y^2 + D_{zz}S_z^2 = D\left(S_z^2 - \frac{S(S+1)}{3}\right) + E(S_x^2 - S_y^2) \tag{6.2}$$

where $D = 3D_{zz}/2$ and $E = (D_{xx} - D_{yy})/2$ are called the axial and rhombic ZFS parameters, respectively, and the ZFS tensor $\boldsymbol{D}$ is traceless [331]. Hence, in the case of spin $S = 1$, the D term describes the energy splitting between the $m_s = \pm 1$ and $m_s = 0$ spin sub-levels, while the E term mixes the spin sub-levels. In the case of $\mathrm{C_{3v}}$ symmetry, the E term is zero and the $\mathrm{C_{3v}}$ axis aligns with the spin quantization axis of the D tensor.

For a defect spin in a crystal composed of light elements (such as Si and C), the interactions contributing to the ZFS tensor are known to be dominated by the magnetic dipole-dipole interaction between the constituent electron spins (H_{dd}) [131]. For instance, for a defect system with $S = 1$ composed of only two unpaired electrons ($s_1 = 1/2$, $s_2 = 1/2$, and $S = s_1 + s_2$), the general form of the magnetic dipole-dipole coupling is given by:

$$H_{dd} = \frac{\mu_0}{4\pi}\frac{(\gamma_e\hbar)^2}{|\boldsymbol{r}_1 - \boldsymbol{r}_2|^5}(r^2\boldsymbol{s}_1 \cdot \boldsymbol{s}_2 - 3(\boldsymbol{s}_1 \cdot (\boldsymbol{r}_1 - \boldsymbol{r}_2))(\boldsymbol{s}_2 \cdot (\boldsymbol{r}_1 - \boldsymbol{r}_2))) \tag{6.3}$$

where μ_0 is the vacuum magnetic permeability, γ_e is the electron gyromagnetic ratio, $\hbar$ is the Planck constant divided by 2π, $\boldsymbol{s}_1$ and $\boldsymbol{s}_2$ are the spin-1/2 operators for the two electrons, $\boldsymbol{r}_1$ and $\boldsymbol{r}_2$ are the positions of the electrons, and r is the distance between them. Using the total spin ($\boldsymbol{S} = \boldsymbol{s}_1 + \boldsymbol{s}_2$) and averaging over the spatial coordinates, one can derive an expression for the ZFS tensor's components originating from the magnetic dipole-dipole interaction of Eq. 6.3:

$$D_{ab} = \frac{1}{2}\frac{\mu_0}{4\pi}(\gamma_e\hbar)^2 \langle \Psi_{ij}(\boldsymbol{r}_1, \boldsymbol{r}_2)| \frac{r^2\delta_{ab} - 3r_a r_b}{r^5} |\Psi_{ij}(\boldsymbol{r}_1, \boldsymbol{r}_2)\rangle \tag{6.4}$$

where a and b label the Cartesian coordinates and $\Psi_{ij}(\boldsymbol{r}_1, \boldsymbol{r}_2)$ is the wavefunction of the two-electron system.

For many-electron systems such as the LMI-vacancy spins considered here, we computed the D-tensor's components following Ref. 298:

$$D_{ab} = \frac{1}{2}\frac{\mu_0}{4\pi}(\gamma_e \hbar)^2 \frac{1}{S(2S-1)} \sum_{i>j}^{\text{occupied}} \chi_{ij} \langle \Psi_{ij}(\boldsymbol{r}_1, \boldsymbol{r}_2) | \frac{r^2 \delta_{ab} - 3 r_a r_b}{r^5} | \Psi_{ij}(\boldsymbol{r}_1, \boldsymbol{r}_2) \rangle \qquad (6.5)$$

where $\Psi_{ij}(\boldsymbol{r}_1, \boldsymbol{r}_2)$ is a Slater-determinant approximated by using the i-th and j-th Kohn-Sham wavefunctions of a given spin defect. The sum in Eq. 6.5 is over all the possible pairs of occupied Kohn-Sham wavefunctions. χ_{ij} is +1 (-1) for parallel (antiparallel) spins. As suggested in Ref. 298, we computed Eq. 6.5 in Fourier space; we used PBE wavefunctions obtained with a 480-atom supercell with the Γ point only.

Our results for diamond and SiC, obtained with the ONCV norm-conserving pseudopotentials (see Table 6.5) systematically overestimate the experimental ZFS parameters by 200 $\sim$ 300 MHz [166, 85].

The hyperfine parameters were calculated by first obtaining the ground-state wavefunctions of a LMI-vacancy spin at the PBE level of theory, with the PAW pseudopotentials, and the 480-atom supercell (Gamma-only calculations). We then calculated the hyperfine parameters by using the gauge-including projector-augmented wave method [289] (GIPAW) as implemented in the GIPAW module of the Quantum Espresso code. The core polarization effects [16] were included throughout all of our calculations.

6.1.3 Results

Electronic properties of metal ion-vacancy pairs

As a validation step of the computational strategy applied to LMI-vacancy pairs, we first applied the DDH hybrid functionals to the diamond NV center and a divacancy defect

(the (hh)-divacancy) in 4H-SiC, which have the same C_{3v} symmetry as that of the defect complexes studied here; we compared our results with those already present in the literature [86, 97, 116] and found good agreement.

We then computed the atomic and electronic structure of the Hf- and Zr-vacancy in 4H-SiC using the DDH functionals. For the LMI-vacancy pairs considered in this study, we note that we only consider (hh) axial configuration and C_{3v} symmetry: for Hf-vacancy pairs in SiC, Hf substitutes Si at an h-site and it pairs with a C vacancy at the nearest neighboring h-site. Fig. 6.1a shows the structure of a Hf-vacancy defect complex in 4H-SiC in a neutral charge state. Our hybrid functional calculation showed that substitutional Hf does not occupy the original Si site, rather it is significantly off-centered (by 0.41 A), closer to the C vacancy site, which provides extra space to accommodate the large substitutional Hf. As noted earlier, the electronegativity of this Hf (1.341) is smaller than that of Si (1.9), indicating that substitutional Hf would transfer four valence electrons to the nearest neighboring C and Si dangling bonds, thus remaining in a 4+ oxidation state. Therefore, the defect geometry includes three passivated C sp^3 dangling bonds around substitutional Hf, and three Si $3sp^3$ dangling bonds in the C_{3v} symmetry, with one e^- from each Si dangling bond and one e^- transferred from Hf.

Fig. 6.1b and 1c show the defect level diagram of the neutral Hf-vacancy complex in 4H-SiC and its spin density, respectively, with a fully occupied a state and two degenerate ex and ey states with two unpaired electrons localized within the band gap of the crystal. Although there are significant contributions from Hf and the nearby C atoms to the defect spin density, the major contribution arises from the Si $3sp^3$ dangling bonds. Hence, one may qualitatively understand the level diagram of Fig. 6.1b, as originating from a C_{3v} configuration of three Si dangling bonds with four electrons, corresponding to a $^3A_2$ spin-triplet state, analogous to that of the diamond NV or the SiC (hh)-divacancy. A spin-conserving intra-defect optical excitation would then be allowed, by promoting an a electron to the e manifold in the spin-down channel, leading to a ^3E excited state [97]. We also found that the Zr-vacancy showed

very similar properties in terms of geometrical and electronic structures (Zr belongs to the same row of the periodic table as Hf).

The energy levels of the occupied and unoccupied doubly degenerate e states of these defects were also computed with the G_0W_0@PBE method and the HSE06 functionals (see Table 6.3) for validation purposes. We found that all three methods yielded consistent results for the position of the levels, which are calculated to be about 1 eV above the valence band edge in SiC.

We note that the same type of defect may also be considered for optically addressable spin qubits in w-AlN as the electronegativities41 of Hf (1.3) and Zr (1.3) are smaller than those of Al (1.6) and N (3.0) and their ionic radii are larger than that of Al [339]. Fig. 6.2a shows the defect level diagram of a Hf-vacancy complex in w-AlN, in which substitutional Hf is paired with a N vacancy along the [0001] direction. The metal ion passivates the N $2sp^3$ dangling bonds and transfers one electron to the nearest neighboring Al $3sp^3$ dangling bonds in the C_{3v} configuration. The defect level diagram is qualitatively the same as that of the Hf-vacancy in 4H-SiC. Using the G_0W_0@PBE method and hybrid functionals, we calculated the energy levels of the occupied e states to be about 3 eV below the conduction band edge (See Table 6.3). As shown in Fig. 6.2b, the dominant contribution to the ground-state spin density originates from the Al $3sp^3$ dangling bonds, but there are also significant contributions from substitutional Hf and the nearby N atoms.

Similar defect complexes may be obtained with other LMIs, for example, La-vacancy and Y-vacancy pairs. La and Y have large ionic radii [339] and small electronegativities [212], but only three valence electrons. Hence, they may behave similar to the neutral Hf-vacancy when negatively charged. The defect level diagrams of the negatively charged La-vacancy and Y-vacancy pairs in 4H-SiC and w-AlN are reported in Fig. S3 and S4, respectively, showing, as expected, the presence of localized e states similar to Fig. 6.1b and 2a. We now turn to discuss the energetic stability of LMI-vacancy pairs in 4H-SiC and w-AlN.

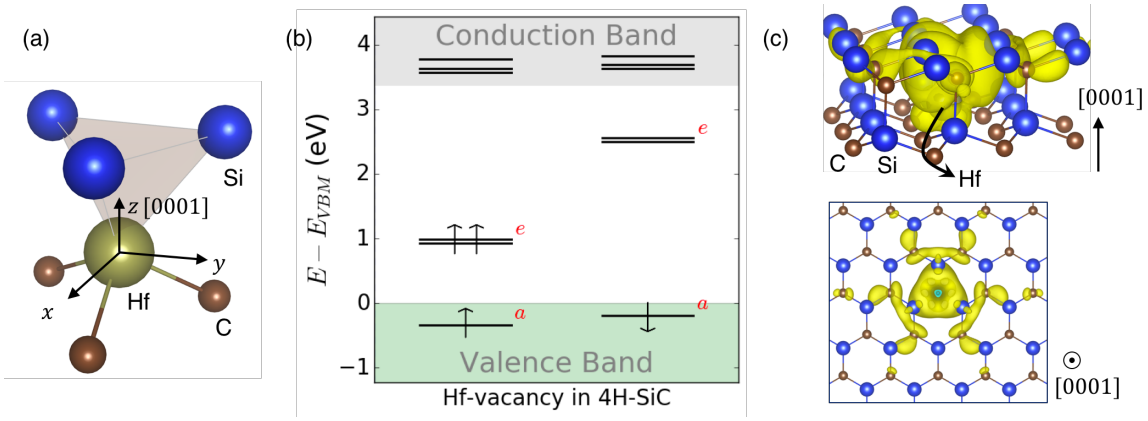

Figure 6.1: Hf-vacancy complex in 4H-SiC. (a) Proposed defect structure of a Hf-vacancy complex in 4H-SiC with (hh) axial configuration and C_{3v} symmetry: Hf substitutes Si at an h-site and it pairs with a C vacancy at the nearest neighboring h-site. Only the nearest neighboring Si and C atoms are shown for clarity. (b) The defect level diagram of the Hf-vacancy complex calculated at the DFT- DDH hybrid level of theory. The totally symmetric a state is located at -0.34 eV and -0.19 eV below the valence band edge in the spin-up and the spin-down channel, respectively. (c) Side (up) and top (down) views of the ground-state spin density of the Hf-vacancy defect calculated at the DDH level of theory.

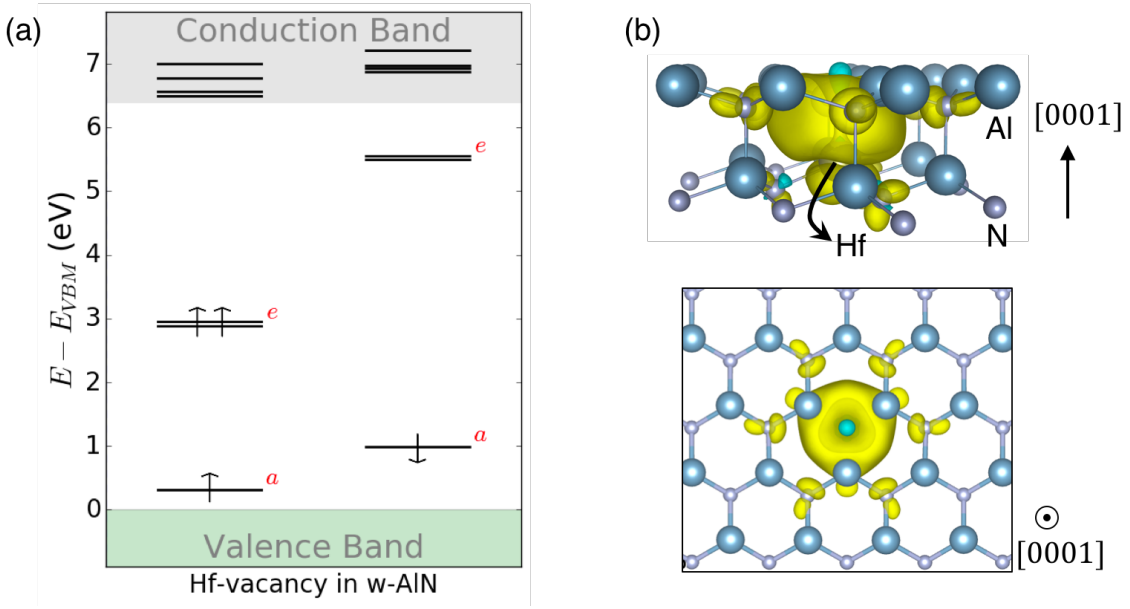

Figure 6.2: Hf-vacancy complex in w-AlN. (a) The defect level diagram of an axial Hf-vacancy in w-AlN calculated at the DDH level of theory. The symmetry of the state is $^3A_2$. In this study, we only consider the axial defect configuration in C_{3v} symmetry. In principle, however, a basal configuration in C1h symmetry is also possible. (b) Side (top) and top (bottom) views of the ground-state spin density of the Hf-vacancy in w-AlN calculated at the DDH level of theory.

Table 6.3: Computed energy levels (eV) of the occupied spin-up (left number) and unoccupied spin-down (right number) e-manifolds of the LMI-vacancy pairs in 4H-SiC and w-AlN with respect to the valence band edge using the G_0W_0@PBE, the DDH functional, and the HSE06 hybrid functional levels of theory. The experimental band gap (E_g) of the materials are given. The computed band gaps are reported in Table 6.2.

Host crystals	Defects	G_0W_0 (eV)	DD-hybrid (eV)	HSE06 (eV)
4H-SiC (E_g = 3.3 eV)	Hf-vacancy	0.97 / 2.26	0.96 / 2.54	0.99 / 2.48
	Zr-vacancy	1.05 / 2.35	0.93 / 2.54	0.97 / 2.50
w-AlN (E_g = 6.2 eV)	Hf-vacancy	2.92 / 4.96	2.92 / 5.53	2.90 / 4.78
	Zr-vacancy	3.01 / 5.12	2.83 / 5.56	2.82 / 4.82

Defect stability

We investigated the stability of the LMI-vacancy defects by (1) examining the stability of the C_{3v} $S = 1$ high-spin state against potential symmetry-lowering structural distortions; and (2) investigating defect formation energies as a function of charge states. We then computed the charge transition levels and the ionization energies of the defects, which we compared to their optical zero-phonon lines (ZPLs).

In Table S1, we report the total energy differences between the $S = 0$ singlet state (C1h structure) and the $S = 1$ state (C_{3v} structure) of the LMI-vacancy defects in w-AlN and 4H-SiC calculated using the DDH-DFT. We found that in all cases, the $S = 1$ state is lower in energy than the $S = 0$ state, e.g. by 205 (380) meV for the Hf-vacancy in 4H-SiC (w-AlN). In addition, we tested the stability of the defect geometry against perturbation to the metal ion position, to investigate whether other low-energy configurations of the defect were accessible, with small or no energy barriers, close to the proposed $S = 1$ state. We considered in- and out-of-plane displacements of the metal ion: the former would lower the defect symmetry while the latter would lead to a different electronic structure due to a different interaction between the metal ion and the Si or Al dangling bonds. We found that the C_{3v} structure shown in Fig. 6.1a is the lowest energy minimum structure of the defects in 4H-SiC and w-AlN at $T = 0$ K, indicating the robustness of the $S = 1$ state against structural distortions.

Next, we examined additional charge states. Fig. 6.3a and 3b show the defect formation energy of the LMI-vacancy pairs (Hf and Zr, and La, respectively) in 4H-SiC in the C-poor limit. The results for the C-rich case and those of Y-related defects are reported in Fig. S5 and S6.

In all cases, we found that the formation energy of a LMI-vacancy complex is lower than the sum of the formation energies of an isolated LMI impurity and an isolated C vacancy across the entire Fermi level range, regardless of the charge state. As shown in Fig. 6.3a (Hf and Zr in SiC), the energy gain by forming a LMI-vacancy complex is $\sim$1 eV near the valence band maximum (VBM), and larger than $\sim$2 eV near the conduction band minimum (CBM). For the La case, the energy gain is larger than for the Hf-vacancy: $\sim$2 eV and $\sim$ 3 eV near the VBM and CBM, respectively. The energy differences are the same in the C-rich limit as shown in Fig. S5. In addition, we found that the LMI-vacancy defect formation energies are lower than that of the divacancy, which was shown to be a stable defect in SiC65. This result strongly supports our hypothesis that the pairing of large metal ions with C vacancies leads to the formation of stable defect complexes in SiC.

The results of Fig. 6.3 also show the relative stability of different charge states. We recall that the slope of the defect formation energy as a function of the Fermi level represents the charge state of a given defect: a neutral state and a negative state are stable in a Fermi level range where the defect formation energy with slope of 0 and -1, respectively, has the lowest energy. In particular, Fig. 6.3a shows that the neutral Hf- and Zr-vacancy pairs with $S = 1$ are stable in the mid-gap region of 4H-SiC, with (+1/0) charge transition levels (CTLs) of 1.84 eV and 1.87 eV, respectively, with respect to the CBM. This indicates that the neutral Hf-vacancy and Zr-vacancy pairs may exist in highly insulating 4H-SiC crystals. The negatively charged state of the La- and Y-vacancy, with $S = 1$ is stable near the conduction band edge with the (0/-1) CTLs of 0.86 eV and 0.99 eV, respectively.

Our results for the formation energies of the LMI-vacancy pairs in w-AlN are similar to those for SiC, as shown in Fig. 6.4. The Hf- and the La-vacancy are stable in neutral

and negatively charged states, and the formation energy of the Zr-vacancy is similar to that of the Hf-vacancy. The (+1/0) CTL of the Hf- and the Zr-vacancy are 2.76 eV and 2.84 eV, respectively, with respect to the CBM. The stability region for the neutral Hf- and Zr-vacancies is shown in Fig. 6.4a as a grey shaded area, and it overlaps with that of the neutral N vacancy, which has been previously detected in experiment66. Furthermore, the defect formation energy of the neutral Hf-vacancy is smaller than the sum of an isolated Hf impurity and an isolated N vacancy formation energies, indicating that realizing the $S = 1$ state of the Hf-vacancy complex is indeed possible. The same conclusion was obtained for the Zr-vacancy. The negative charge state of the La-vacancy is stable near the CBM, with the (0/-1) CTL position 1.43 eV below the CBM. We also found a significant energy gain (1$\sim$2 eV) upon formation of the La-vacancy complex from an isolated La impurity and an isolated N vacancy across the entire band gap.

Zero-phonon lines of the LMI-vacancy pairs

The optical initialization and readout of the diamond NV center and the SiC divacancy relies on the spin-conserving excitation to a ^3E spin-triplet excited state and its spin-selective decay [406, 166]. We found that the same spin-conserving excitation scheme may occur in the LMI-vacancy pairs in 4H-SiC and w-AlN, as shown in Table 6.4, where we report calculated ZPLs using total energy differences (ΔSCF calculations) at the PBE, the DDH, and the HSE06 levels of theory. We note that the DDH and HSE06 calculations yielded similar results.

The calculated ZPLs are 1.7 eV (PBE) and 2.2 eV (Hybrids) for the diamond NV center and 1.0 eV (PBE) and 1.3 eV (Hybrids) for the SiC (hh)-divacancy; our PBE results underestimate the experimental ZPLs (1.945 eV and 1.094 eV) and our hybrid functional results consistently overestimate them by 0.2$\sim$0.3 eV. We computed the ZPLs of the Hf-vacancy and Zr-vacancy pairs in 4H-SiC to be $\sim$2.0 eV using the DDH and HSE06 functionals. These calculations were not conducted at the PBE level of theory as the occupied a state is deep

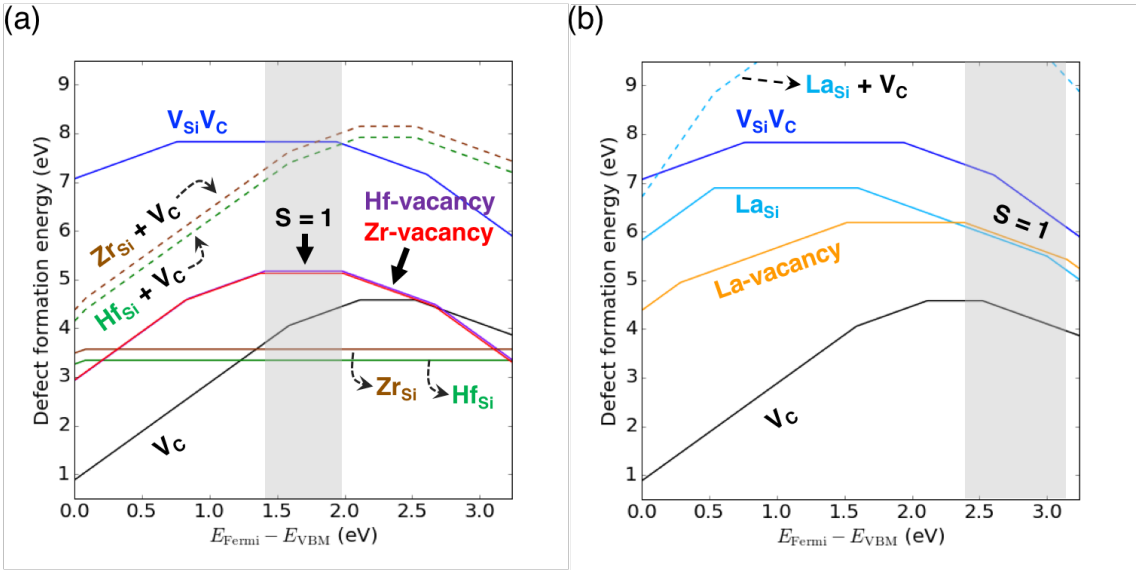

Figure 6.3: Defect formation energy of spin defects in 4H-SiC. (a,b) Defect formation energy of Hf- and Zr-related defects in 4H-SiC (a), and that of La-related defects in 4H-SiC (b) as a function of Fermi level referred to the valence band maximum (VBM). Calculations were conducted at the DFT-DDH level of theory. The defect formation energy of the (hh)-divacancy is included for comparison. For simplicity, the results of Y-related defects are reported in Fig. S6. The dotted lines are the sum of the formation energies of substitutional impurity (either Hf_{Si}, Zr_{Si}, or La_{Si}) and C vacancy to be compared to that of the corresponding LMI-vacancy defect complex. The grey shaded area in each plot indicates a Fermi-level range, in which the LMI-vacancy pairs exhibit a stable $^3A_2$ spin-triplet ($S = 1$) ground state in 4H-SiC.

in the valence band due to the PBE band gap underestimation. We expect our hybrid functional results to provide an upper bound to the measured ZPLs of the Hf- and Zr-vacancy in 4H-SiC, similar to our diamond NV and SiC divacancy results; we would estimate the measured ZPLs to be close to ∼1.7 eV. Similarly, we suggest that the measured ZPLs of the Hf- and Zr-vacancy in w-AlN are between ∼2.3 eV (PBE, lower bound) and ∼3.0 eV (hybrid, upper bound).

For the negatively charged La-vacancy, the corresponding computed ZPLs are 1.20 (1.57) eV and 2.24 (2.82) eV in 4H-SiC and w-AlN, at the PBE (DDH) level of theory. However, the (0/-1) CTLs of the La-vacancy in 4H-SiC and w-AlN were found to be 0.86 eV and 1.43 eV, respectively, with respect to the CBM. This indicates that the ^3E excited state of the negatively charged La-vacancy is above the conduction band edge in both 4H-SiC and

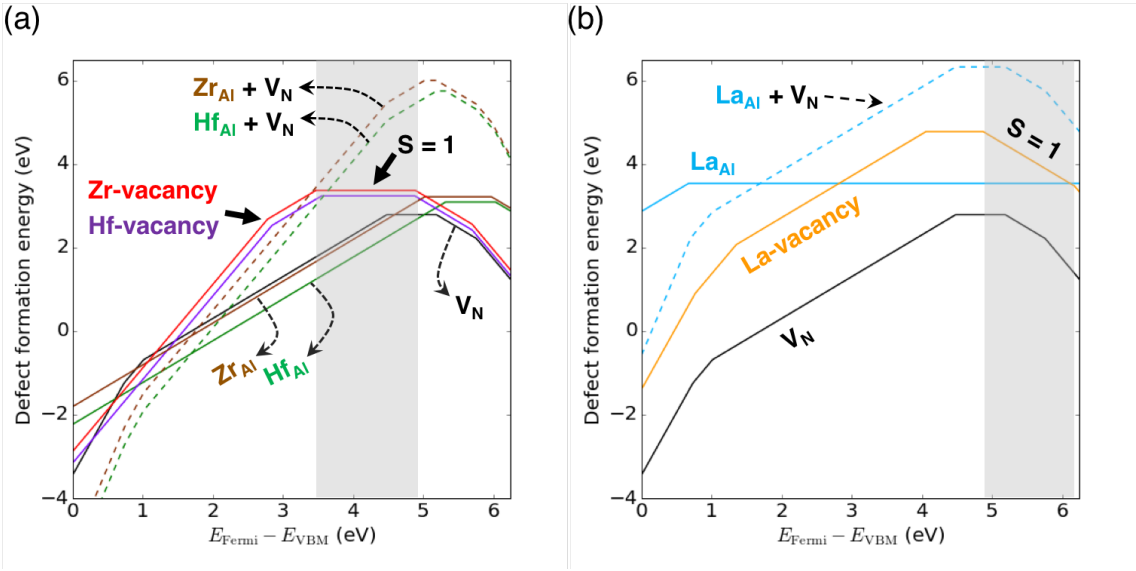

Figure 6.4: Defect formation energy of spin defects in w-AlN. (a,b) Defect formation energy of Hf- and Zr-related defects in w-AlN (a), and that of La-related defects in w-AlN (b) The DDH-DFT was used. The formation energy of N vacancy, which is a common defect in w-AlN, is included for comparison. The dotted lines are the sum of the formation energies of a substitutional impurity (either Hf_{Al} or Zr_{Al}) and a N vacancy to be compared to that of the corresponding LMI-vacancy defect complex. The grey shaded area in each plot indicates a Fermi-level range where the LMI-vacancy pairs have stable $^3A_2$ spin-triplet ($S = 1$) ground state in w-AlN.

w-AlN, which may lead to the ionization of the defect center. This turned to be also the case for the negatively charged Y-vacancy as its (0/-1) CTL is very shallow. Therefore, in what follows we do not further consider the negatively charged La-vacancy and Y-vacancy pairs, and focus on the Hf-vacancy and the Zr-vacancy pairs for use as potential qubits in 4H-SiC and w-AlN.

Spin Hamiltonian parameters: Zero-field splitting and hyperfine interaction

Electron paramagnetic resonance (EPR) is a powerful technique to detect and characterize paramagnetic defects in solids [331]. The zero-field splitting D tensor and the hyperfine A tensor are key components of the spin Hamiltonian that determines the EPR spectrum (see Eq. 6.5). For the Hf-vacancy and Zr-vacancy in SiC (AlN), we found $D = 1.40$ (2.96) GHz and 1.10 (3.05) GHz, respectively, using the ONCV pseudopotentials, as reported in Table

Table 6.4: Computed zero-phonon lines (eV) of the (hh)-divacancy and the LMI-vacancy pairs (Hf and Zr only) in 4H-SiC and w-AlN using various levels of theory; the semi-local PBE functional, the DDH functional, and the HSE06 hybrid functional. Spin-conserving intra-defect excitation between the $^3A_2$ ground state and the ^3E excited state was considered.

Host crystals	Defects	PBE (eV)	DD-hybrid (eV)	HSE06 (eV)	Experiment (eV)
Diamond	NV center	1.72	2.22	2.23	1.945 [76]
4H-SiC	(hh)-divacancy	1.03	1.30	1.33	1.094 [188]
	Hf-vacancy	n/a	2.04	2.13	n/a
	Zr-vacancy	n/a	1.96	2.05	n/a
w-AlN	Hf-vacancy	2.46	3.07	2.88	n/a
	Zr-vacancy	2.33	2.98	2.79	n/a

6.5. These values are comparable to those of the diamond NV and the SiC divacancy, which were measured to be 2.9 GHz [166] and 1.3 GHz [85], respectively.

In order to study the coupling between defect spin qubits and lattice strain, we computed D as a function of hydrostatic pressure, $D(P)$ [77]. In particular, we investigated the role of different dangling bonds (e.g. C $2sp^3$ vs. Si $3sp^3$) and different type of host crystals (e.g. diamond vs. SiC or AlN) in determining the coupling characteristic of spin to strain. We considered hydrostatic pressure, which may yield an isotropic compressive strain around the defect centers, thus preserving the C_{3v} symmetry. Defect qubits under hydrostatic pressure could also be easily accessible in diamond anvil cell experiments [77]. We first compare $D(P)$ of the diamond NV and the SiC divacancy, and then discuss $D(P)$ of the LMI-vacancy pairs. Fig. 6.5a shows that in diamond, $D(P)$ is linear up to 100 GPa, while in SiC, $D(P)$ deviates from a linear behavior already at 50 GPa (SiC is known to be stable under pressure up to 100 GPa [414]). The linear behavior found for the diamond NV is in good agreement with previous experimental [77] and theoretical [162] results. We found a slope of 10.91 MHz/GPa, compared to an experimental value of 14.58 MHz/GPa [77] and a previous theoretical value of 9.52 MHz/GPa [162]. One may distinguish two contributions to the variation of D as a function of P: purely geometrical changes around the defect center and the variation of the defect's spin density. The former may be described using the 'compressed-orbital' model,

introduced by Ivady *et al.* [162], according to which D is scaled by a geometrical factor (d/d_0) determined by atomic relaxations under pressure, in proximity of the defect; d and d_0 are neighbor distances under P and at equilibrium, respectively. As shown in Fig. 6.5a, the compressed-orbital model describes well $D(P)$ in the case of diamond, showing a negligible contribution of spin density changes.

In contrast, $D(P)$ of the SiC divacancy is not well described by the compressed orbital model. As expected from the bulk modulus of SiC, which is substantially smaller than that of diamond, the divacancy defect structure relaxes significantly under pressure: d/d_0 (P) is 0.70 for P=100 GPa, compared to the value of 0.88 found for diamond NV under the same conditions. This relaxation allows for significant hybridization between the divacancy dangling bonds leading to large deviations of $D(P)$ from the values obtained with the compressed-orbital model. The slope of $D(P)$ close to ambient pressure is 16.34 MHz/GPa for the SiC divacancy.

Fig. 6.5b shows that the $D(P)$ of the Hf- and Zr-vacancy spins in 4H-SiC exhibits a behavior different from that reported in Fig.4: $D(P)$ deviates significantly from that predicted by a compressed orbital model, with a parabolic behavior and maxima around 70 GPa and 30 GPa for the Hf-vacancy and Zr-vacancy, respectively. In addition, close to P = 0 GPa, the slope of $D(P)$ is about a factor of two smaller than that observed for the divacancy: 7.637 (2.835) MHz/GPa for the Hf-(Zr)vacancy. We note that the structural relaxation of the Hf- and the Zr-vacancy under pressure are relatively limited due to the presence of the LMIs, compared to the divacancy relaxation. At 100 GPa, d/d_0 is 0.84 for both Hf- and Zr-vacancy, to be compared to 0.7 of the SiC divacancy.

Fig. 6.5c shows $D(P)$ for Hf- and Zr-vacancies in w-AlN up to 30 GPa (w-AlN is known to undergo a structural phase transition above 20 GPa70). The figure indicates a greater sensitivity of $D(P)$ with respect to the corresponding defects in SiC, with slopes of 19.24 MHz/GPa and 15.03 MHz/GPa for the Hf- and the Zr-vacancy, respectively, in w-AlN. Our results show that the coupling characteristics of a defect spin qubit to lattice strain can vary

over a wide range depending on its constituent electronic states (i.e. dangling bonds) and its host crystal as well.

Finally, as a guide for future EPR-based defect detections and to support development of the LMI-vacancy-based defects, we report computed hyperfine parameters (A) (see Eq. 6.1). The Hf- and Zr-vacancy defects may have intrinsic nuclear spins by implanting different isotopes: ^{177}Hf (I = 7/2, 18.6%), ^{179}Hf (I = 9/2, 13.62%), and 91Zr (I = 5/2, 11.2%). The values of A are given in Table 6.6, for the ^{14}N nuclear spin in diamond NV71 and the LMI-vacancy defects. In 4H-SiC and w-AlN, there are also other intrinsic nuclear spins associated with ^{29}Si (I = 1/2, 4.7%), ^{13}C (I = 1/2, 1.1%), ^{27}Al (I = 5/2, 100%), and ^{14}N (I = 1, 99.63%). We report the hyperfine parameters for these intrinsic lattice nuclear spins coupled with the Hf-vacancy and the Zr-vacancy in 4H-SiC and w-AlN in Table S2 and S3, respectively.

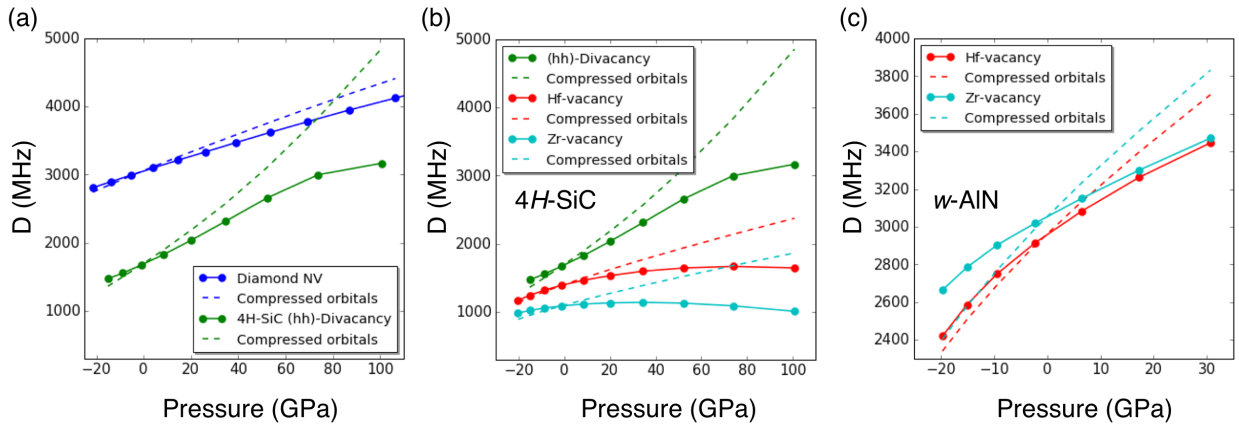

Figure 6.5: Zero-field splitting (ZFS) of the spin defects in 4H-SiC and w-AlN. (a) ZFS parameters (D) of the diamond NV and the SiC divacancy as a function of hydrostatic pressure. (b, c) ZFS parameters (D) of the Hf-vacancy and the Zr-vacancy as a function of hydrostatic pressure in 4H-SiC (b) and in w-AlN (c). For the defects in 4H-SiC, we also show D of the divacancy for comparison. We considered a pressure range from -20 GPa to 100 GPa, in which 4H-SiC is known to be stable. For defects in w-AlN under pressure, we considered a pressure range from -20 to to 30 GPa as w-AlN is known to undergoes a structural phase transition above 20 $\sim$ 30 GPa.

Table 6.5: Computed Zero-field splitting parameters (D) of the diamond NV center, the divacancy spins in 4H-SiC, and the Hf- and Zr-vacancy pairs in 4H-SiC and w-AlN. The LMI-vacancy pairs considered in this study are the (hh) axial defects in C_{3v} symmetry. The single-particle wavefunctions for the defects were calculated using the Quantum Espresso code with the ONCV [129, 324] and the PAW [34] pseudopotentials.

Host crys-tals	Defects	Theory (GHz) (This work) (QE + ONCV)	Theory (GHz) (This work) (QE + PAW)	Theory (GHz) (Previous work [86]) (VASP + PAW)	Exp. [166, 85] (GHz)
Diamond	NV center	3.03	2.90	2.854	2.88
4H-SiC	(hh)-divacancy	1.682	1.387	1.358	1.336
	(hk)-divacancy	1.580	1.306	1.320	1.222
	(kh)-divacancy	1.641	1.356	1.376	1.334
	(kk)-divacancy	1.635	1.349	1.321	1.305
	Hf-vacancy	1.403	1.291	n/a	n/a
	Zr-vacancy	1.096	1.035	n/a	n/a
w-AlN	Hf-vacancy	2.962	2.896	n/a	n/a
	Zr-vacancy	3.053	2.925	n/a	n/a

Table 6.6: Computed hyperfine parameters (MHz) for the Hf-vacancy and Zr-vacancy pairs in 4H-SiC and w-AlN. For comparison, the computed hyperfine parameters of the diamond NV center are also reported along with the experimental data [87] in parenthesis. Other hyperfine parameters are reported in Table S2 and S3.

Host crystals	Defects	Nuclear spin	A_{xx} (MHz)	A_{yy} (MHz)	A_{zz} (MHz)
Diamond	NV center	^{14}N (I=1, 99.6%)	-2.02 (-2.14)	-2.02 (-2.14)	-2.15 (-2.70)
4H-SiC	Hf-vacancy	^{177}Hf (I=7/2, 18.6%)	7.58	7.91	-8.60
		^{179}Hf (I=9/2, 13.62%)	-4.76	-4.97	5.40
	Zr-vacancy	^{91}Zr (I=5/2, 11.2%)	1.92	1.70	17.57
w-AlN	Hf-vacancy	^{177}Hf (I=7/2, 18.6%)	26.05	26.20	10.53
		^{179}Hf (I=9/2, 13.62%)	-16.36	-16.46	-6.62
	Zr-vacancy	^{91}Zr (I=5/2, 11.2%)	6.21	6.12	15.59

6.1.4 Conclusions

In this work, we proposed that large metal ion-vacancy pairs may be promising defect qubits in 4H-SiC and w-AlN. In particular, we considered Hf, Zr, La, and Y as they have larger ionic radii and smaller electronegativities than those of Si and Al. By using density functional theory, we showed that, similar to the diamond NV center and the SiC divacancy, the neutral Hf- and Zr-vacancy pairs are stable defects, with a $^3A_2$ spin-triplet ground state and an ^3E excited state, both with energies in the band gap of 4H-SiC and w-AlN. In addition, we found that the negatively charged La-vacancy and Y-vacancy pairs have a spin-triplet ground state, similar to the diamond NV center. However, in either 4H-SiC or w-AlN, the negative charge state of La- and Y-vacancy pairs is much shallower with respect to the CBM than the corresponding ones for the Hf- and Zr-vacancies. As a result, the $^3A_2$ - ^3E zero-phonon line excitation may ionize the La-vacancy defect center, making it unfavorable for use as optically addressable spin qubit. In order to guide future experiments, we calculated experimental observable of the Hf- and the Zr-vacancy in 4H-SiC and w-AlN, including optical zero-phonon lines, hyperfine parameters, and the zero-field splitting parameters.

Recently, Varley, Janotti, and Van de Walle also investigated impurity-vacancy pairs in w-AlN, including Ge, Sn, Ti, and Zr [379]. Using computational methods similar to those employed here, they suggested that Zr- and Ti-vacancy pairs would be good candidates for spin qubits in w-AlN. Their prediction on the Zr-vacancy is consistent with ours. In addition, Varley *et al.* have shown that the Ge-vacancy and the Sn-vacancy do not favor the $S = 1$ state in w-AlN. We confirm this finding for 4H-SiC as well; our results show that in both crystals the $S = 1$ state of the Ge-vacancy and the Sn-vacancy is much higher in energy than their $S = 0$ state, which is stabilized by charge transfer from neighboring dangling bonds.

The proposed LMI-vacancy defects may provide new opportunities to defect-based quantum technologies due to several unique features. For example, these defects may couple with various types of lattice strain [209, 273, 86, 222, 77]: we showed that the Hf-vacancy in w-AlN shows a large spin-pressure coupling which is about twice as large as that of the diamond

NV, making it a good candidate for nano-scale pressure sensors [77]. Instead, the D parameter of the Zr-vacancy in 4H-SiC showed the smallest sensitivity to pressure, which may be useful in applications requiring spin sub-level structure insensitive to pressure. Work is in progress to explore spin responses to uniaxial strains, which may be useful in applications ranging from nano-scale sensing [182] to creation of hybrid quantum systems [30, 329, 114].

Nuclear spins associated with different isotopes of Hf and Zr (^{177}Hf ($I = 7/2$, 18.60%), ^{179}Hf ($I = 9/2$, 13.62%), 91Zr ($I = 5/2$, 11.22%)) may also be used as quantum resources73. For example, Klimov *et al.*, demonstrated a coherent coupling between a divacancy-related (PL5) spin and native nuclear spins associated with ^{13}C and ^{29}Si isotopes at room temperature [183]. This study was a milestone towards developing SiC-based hybrid quantum systems. However, it is still challenging to find ^{29}Si and ^{13}C nuclear spins strongly coupled to a divacancy spin due to their natural abundances: 4.7% for ^{29}Si and 1.1% for ^{13}C. The nuclear spins of Hf and Zr may resolve this issue and provide intrinsic nuclear spins at a well-defined position of the LMI-vacancy pairs. Finally, the use of LMIs may be beneficial for defect localization. For example, in the case of divacancy or Si vacancy in SiC, it is hard to control the position of the defects as both C vacancies and Si vacancies are highly mobile. The mobility of Hf and Zr in SiC would be much lower than that of the C vacancy and the Si vacancy due to their large mass.

In summary, optically addressable spins bound to point defects in solids have a great potential for quantum information processing, quantum communications, and hybrid quantum systems. The defect complexes proposed here would provide alternative quantum systems in heterogeneous materials such as 4H-SiC and w-AlN that could broaden the scope of defect-based quantum technologies.

6.2 First-principles study of strongly-correlated states for spin-defects in diamond

https://doi.org/10.1039/D0CP04585C

Using a recently developed quantum embedding theory, we present first principles calculations of strongly correlated states of spin defects in diamond. Within this theory, effective Hamiltonians are constructed, which can be solved by classical and quantum computers; the latter promise a much more favorable scaling as a function of system size than the former. In particular, we report a study of the neutral group-IV vacancy complexes in diamond, and we discuss their strongly-correlated spin-singlet and spin-triplet excited states. Our results provide valuable predictions for experiments aimed at optical manipulation of these defects for quantum information technology applications.

6.2.1 Introduction

Electron spins in molecular and condensed systems are important resources for the storage and process of quantum information [392]. In the past decades, several spin-defects in wide band gap semiconductors and insulators have been widely studied, in particular in diamond [76], silicon carbide [391, 59], and aluminum nitride [334, 335]. The prototype example of spin-defects is the negatively-charged nitrogen-vacancy center (NV) center in diamond [67, 308, 75, 242, 58, 112]. The NV center exhibits spin-triplet ground state with long spin coherence time even at room temperature [17]. Different spin states of the electron spin can be used to encode quantum information, and transitions between spin states can be driven by microwave fields. To date, spin-defects have found many applications both in fundamental science and cutting-edge quantum technologies. For instance, spin-defects have been used to demonstrate fundamental principles of quantum mechanics such as the Berry phase [407] and

Bell inequality [137]. Spin-defects are also extensively used as quantum sensors due to their sensitivity to external electric, magnetic and temperature fields [151, 92]. Furthermore, the spin states of defects can be coupled with various optical [250] and mechanical [396] degrees of freedom, making them important components in hybrid quantum architectures for quantum communication and quantum computation.

First-principles simulations based on density functional theory (DFT) have been playing an important role in the identification and characterization of spin-defects [334, 335]. For instance, ground state DFT calculations can predict the formation energies of defects, thus enabling, e.g. the identification of the atomistic structure and charge states of unknown defects [160]. Using ground state DFT wavefunctions, several spin properties can be computed that are critical for the prediction of qubit state splitting and coherence time, such as the zero-field splitting and the hyperfine coupling [105, 218]. However accurate predictions of excited states are challenging, when using DFT, especially in the case of strongly correlated states which may not be approximated by a single Slater determinant of spin-electron orbitals. Multi-reference electronic states have been an important subject of research in quantum chemistry for decades [135]. Unfortunately, most *ab initio* multireference methods are computationally very demanding, preventing their straightforward application to spin-defects in solids, whose description requires periodic supercells containing hundreds of atoms.

In the past decades, quantum embedding theories emerged as promising approaches to apply a high-level theory (such as multireference methods) to the description of strongly correlated active regions of a solid or molecule, where the environment is treated with a lower level of theory. Different quantum embedding schemes have been proposed[361], using, e.g. the electron density [153, 152, 115, 164, 102, 395], density matrices [185, 401, 284] or based on Green's function approaches[205, 83, 420, 9, 10, 247, 159, 142, 143]. Spin-defects in semiconductors can be viewed as atom-like systems embedded in bulk crystals, and the states used to encode quantum information are usually localized around the defects.

Therefore, spin-defects are promising systems for the application of quantum embedding theories. For instance, Bochstedte and coworkers investigated strongly correlated excited states of NV in diamond and divacancies in silicon carbide using the constrained random phase approximation (cRPA) [39]. In the cRPA approach [9, 247, 143], the low-energy excited states of the active site are obtained by solving an effective Hamiltonian that is constructed from effective electron-electron interactions. The cRPA approach is based on the random phase approximation (RPA), which neglects exchange-correlation effects in the calculation of dielectric screening. Recently, we developed a quantum embedding theory [219] similar to cRPA, albeit going beyond the RPA description of dielectric screening by including exchange-correlation effects evaluated using a finite-field algorithm [220, 261]. In addition, the quantum embedding theory of Ref.[219] has the important advantage that no explicit summation over empty electronic orbitals is necessary [399, 260, 286, 117], making it scalable to systems with hundreds of atoms. We demonstrated the efficiency and accuracy of such a computational approach for spin-defects in diamond and silicon carbide, and carried out calculations on both classical and quantum computers.

In this work, we apply the quantum embedding theory of Ref.[219] to several defects in diamond (Fig. 6.6). In particular, we consider the group-IV vacancy complexes in diamond, i.e. XV where X=Si, Ge, Sn, Pb, in addition to the NV center. These vacancy complexes have attracted substantial interests recently due to their excellent optical properties [79, 98, 369, 119, 370, 419]. We performed quantum embedding calculations based on DFT results obtained with different exchange-correlation functionals [279, 346] and demonstrated the importance of using hybrid functionals to obtain accurate results. While the NV and SiV centers were discussed in part in ref. [219], here we report the first to-date simulation of the strongly-correlated excited states of the neutral GeV, SnV and PbV defects in both the spin singlet and spin triplet manifold, which are both required to predict their operation as optically-addressable qubits.

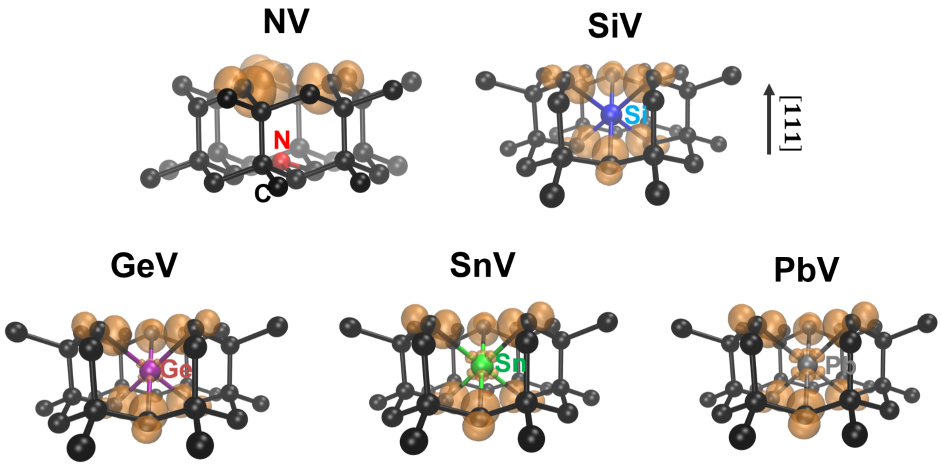

Figure 6.6: Structures and spin polarization densities of spin-defects in diamond, including the negatively-charged nitrogen-vacancy (NV) center, and the neutral group-IV vacancy complexes XV (with X=Si, Ge, Sn, and Pb).

6.2.2 Methods

Quantum embedding theory

For a system of interacting electrons, the non-relativisitic Hamiltonian is given by

$$H = \sum_{ij} t_{ij} a_i^\dagger a_j + \frac{1}{2} \sum_{ijkl} v_{ijkl} a_i^\dagger a_j^\dagger a_l a_k \tag{6.6}$$

where $a^\dagger$ and a are creation and annihilation operators acting on single-electron orbitals i, j, k, l; the one-electron term t includes the kinetic energy and the electron-nuclei interaction; the two-electron term v represents the *bare* Coulomb interaction between electrons. The exact solution of H is generally limited to small systems due to the high computational cost.

For systems where important electronic excitations are restricted to an active space (A) such as frontier orbitals of molecules or energy levels near the Fermi level of solids, it is

desirable to construct an effective Hamiltonian that operates only on the active space

$$H^{\text{eff}} = \sum_{ij}^{\text{A}} t_{ij}^{\text{eff}} a_i^\dagger a_j + \frac{1}{2} \sum_{ijkl}^{\text{A}} v_{ijkl}^{\text{eff}} a_i^\dagger a_j^\dagger a_l a_k. \tag{6.7}$$

and the physical processes outside the active space are included through a renormalization of t and v. The renormalized effective Hamiltonian parameters t^{eff} and v^{eff} should properly incorporate dielectric screening and exchange-correlation effects outside the active space. In the cRPA approach, the two-body term in the effective Hamiltonian v^{eff} is computed as a partially screened Coulomb interaction

$$v^{\text{eff}} = v + v\chi_{\text{rpa}}^{\text{E}} v \tag{6.8}$$

where $\chi_{\text{rpa}}^{\text{E}} = \chi_0^{\text{E}} + \chi_0^{\text{E}} v \chi_{\text{rpa}}^{\text{E}}$ is the reducible polarizability of the environment within the RPA; $\chi_0^{\text{E}} = \chi_0 - \chi_0^{\text{A}}$ is the irreducible density response function for the environment (E), with χ_0^{A} being the projection of χ_0 inside the active space.

The cRPA approach neglects the exchange-correlation effect in the calculation of the dielectric screening. In Ref. [219], we proposed an expression for v^{eff} that properly accounts for exchange and correlation interactions in the environment

$$v^{\text{eff}} = v + f\chi^{\text{E}} f \tag{6.9}$$

where the reducible density response function χ^{E} of the environment is evaluated beyond the RPA as $\chi^{\text{E}} = \chi_0^E + \chi_0^{\text{E}} f \chi^E$, with $f = v + f_{\text{xc}}$ being the Hartree-exchange-correlation kernel. The exchange-correlation kernel f_{xc}, defined as the derivative of the exchange-correlation potential with respect to the electron density, is evaluated with a finite-field algorithm described in Ref. [220, 261]. By representing χ^{E} and f on a compact basis obtained from a low-rank decomposition of the dielectric matrix [399, 117], one can avoid the evaluation and summation over virtual electronic orbitals. Finally, the one-body term t^{eff} can be computed

by properly subtracting from the Kohn-Sham Hamiltonian a term that accounts for Hartree and exchange-correlation effects in the active space [219].

Computational setup

We first carried out spin-unrestricted DFT calculations to obtain the ground state geometries of defects in their host materials. Using ground state geometries, we then performed spin-restricted DFT calculations [346] to obtain their electronic structure (Fig. 6.7) at the mean-field level, which serves as the starting point for the construction of the effective Hamiltonian described in the previous section. The spin restriction ensures that both spin channels are treated on equal footing and the eigenstates of the resulting effective Hamiltonian are eigenstates of S^2. Once mean-field DFT single particle eigenvalues and wavefunction are obtained, an effective Hamiltonian was constructed using the quantum embedding theory described in Section 6.2.2. The active space is defined by a set of selected Kohn-Sham orbitals, that are chosen to include relevant defect levels in the band gap of the host material, as well as resonance orbitals and orbitals close in energy to band edges. The choice of the active space was tested to yield converged excitation energies (see Section 6.2.4). Full configuration-interaction (FCI) calculations [186] were performed for the effective Hamiltonian to compute low-energy eigenstates and vertical excitation energies.

We performed DFT calculations using the Quantum Espresso code [106]. We used a plane-wave basis set with a kinetic energy cutoff of 50 Ry. Norm-conserving pseudopotentials from the SG15 library [324] are used to represent electron-ion interactions; these pseudopotentials include scalar relativistic effects. In the calculations of PbV including spin-orbit coupling, we used the fully relativistic version of SG15 pseudopotentials [322]. Defects are modeled with 215-atom supercells of diamond with the Γ-point sampling of the Brilliouin zone. Quantum embedding theory calculations are performed from two different DFT starting points, obtained respectively with PBE [279] and a dielectric-dependent hybrid functional (DDH) [346], using geometries optimized with the PBE functional. For selected

cases we also tested the HSE06 functional [141, 197], which was found to yield results similar to those of the DDH functional (see Section 6.2.4). Quantum embedding calculations were carried out with the WEST code [117]. Density response functions were evaluated using a basis set including the first 512 eigenvectors of χ_0. In calculations beyond the RPA, the exchange-correlation kernel f_{xc} was computed with a finite-field algorithm using the WEST code coupled to the Qbox code [124]. FCI calculations were carried out using the PySCF code [360].

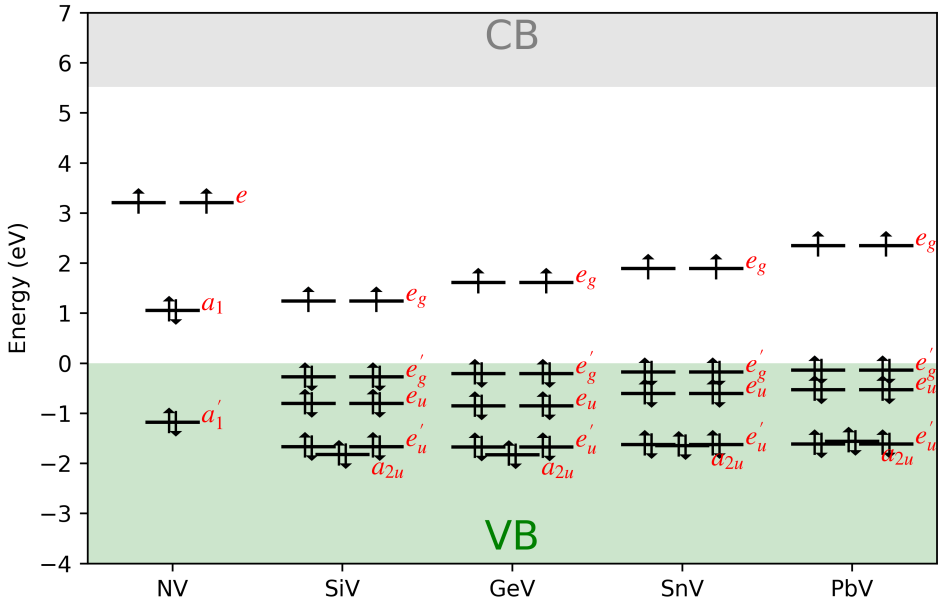

Figure 6.7: Mean-field electronic structure of spin-defects in diamond obtained with spin-restricted DFT calculations using the dielectric-dependent hybrid functional (DDH)[346]. VB (CB) denotes the valence (conduction) band. The symmetry of important defect orbitals is indicated following group theory notation.

6.2.3 Results

In Table 6.7 we summarize several vertical excitation energies of spin-defects obtained from FCI calculations with the Hamiltonian defined in Section 6.2.2. Overall, the excitation energies obtained using the DFT@DDH energies and wavefunctions are significantly larger than those obtained at the DFT@PBE level of theory, and DDH results are in better agreement

with available reference values. Our findings highlight the importance of using DFT@DDH as a starting point for embedding calculations.

The NV in diamond has a spin-triplet ground state of C_{3v} symmetry. Fig. 6.8 shows its vertical excitation energies computed within and beyond the RPA, using the PBE and DDH functionals. In all cases, quantum embedding calculations predict the correct energy level structure of $^3A_2$, ^1E, $^1A_1$ and ^3E, with ^1E and $^1A_1$ being strongly-correlated states that cannot be directly computed by DFT. Results obtained beyond the RPA using the DDH functional yield the best agreement with experimental values (Table 6.7).

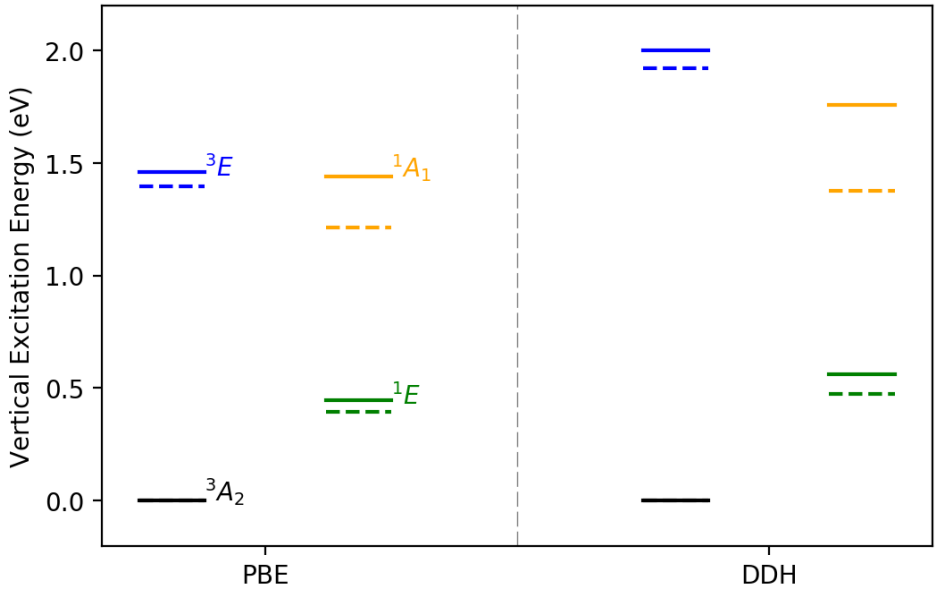

Figure 6.8: Many-electron energy levels of negatively charged nitrogen-vacancy (NV) center in diamond. Calculations are performed starting from PBE and dielectric-dependent hybrid (DDH) functionals, with dielectric screening evaluated within (dashed lines) and beyond (solid lines) the random phase approximation (RPA).

Group-IV vacancy centers (SiV, GeV, SnV and PbV) in diamond have spin-triplet ground states with D_{3d} symmetry. The spin-flip excitations within e_g single-particle defect levels in the band gap and the excitations from e_u to e_g orbitals yield a rich set of many-electron excited states, many of which are strongly-correlated. Experimentally, it has been shown that the lowest spin-triplet excitations of SiV lead to a $^3A_{2u}$-^3E_u manifold [119]. Much less is known about spin singlet excited states. Here we provide the first predictions of the singlet

states of GeV, SnV and PbV obtained with first-principles simulations.

Fig. 6.9 presents the vertical excitation energies of many-electron states of group-IV vacancy centers. First, we note that the excitation energies from $^3A_{2g}$ state to ^3E_u state increase from SiV to PbV (1.594/2.105/2.091/2.493 eV for SiV/GeV/SnV/PbV), which is consistent with the trend of increasing e_u-e_g energy level splitting in their mean-field descriptions (Fig. 6.7). In the spin singlet manifold, the positions of ^1E_g, $^1A_{1g}$ and $^1A_{1u}$ are also increasing in energy from SiV to PbV. These singlet states originate from spin-flip transitions of e_g defect orbitals located in the band gap of diamond, and thus their excitation energies strongly depend on the Coulomb repulsion of electrons in e_g orbitals. The increasing excitation energies indicate an increase in strength of the effective Coulomb interactions, as the element becomes heavier (the bond length between impurity atom and nearest neighbor carbon atom is 1.99/2.03/2.10/2.13 Å for SiV/GeV/SnV/PbV, respectively).

In the case of PbV, we investigated the influence of spin-orbit coupling by performing fully relativistic DFT calculations with noncollinear spin. We found that the effect of spin-orbit coupling (SOC) on the position and splitting of defect levels (see Section 6.2.4) is negligible. For instance, the e_g orbitals of PbV in the band gap of diamond are split by less than 0.02 eV due to the SOC effect. We further carried out projected density of states calculations (see Section 6.2.4), which indicate that defect orbitals are hybrid orbitals with a major component coming from the host carbon atoms instead of the impurity atom. This prominent carbon character of the orbitals is responsible for the small SOC splitting observed in the PbV case. Therefore, we concluded that spin-orbit coupling could be neglected in our quantum embedding calculations.

Comparing results obtained with PBE and DDH functionals, we again found that the DDH functional yields larger excitation energies and is in closer agreement with experiments than those obtained with PBE. Beyond-RPA calculations yield larger singlet excitation energies than those obtained with RPA, similar to our findings for NV. Unlike singlet excitation energies, triplet excitation energies of group-IV vacancy centers are found to be insensitive

to the description of dielectric screening and mainly depend on the mean-field starting point.

Experimentally, it has been challenging to realize optical spin polarization for the neutral SiV; however important progress in that direction has been recently reported by Zhang et al. [419], who performed optically detected magnetic resonance measurements enabled by optical spin polarization via higher-lying excited states. Our results for SiV indicate that the experimental difficulties may arise from the position of the $^1A_{1u}$ state being slightly higher in energy than that of the $^3A_{2u}$-^3E_u manifold, thus making the intersystem crossing (ISC) from triplet to singlet manifolds energetically unfavorable [219]. However, when moving from SiV to PbV in group IV, the the $^1A_{1u}$ state becomes slightly lower in energy than the $^3A_{2u}$-^3E_u manifold, suggesting that the ISC may become energetically more favorable for heavier defects, such as the PbV.

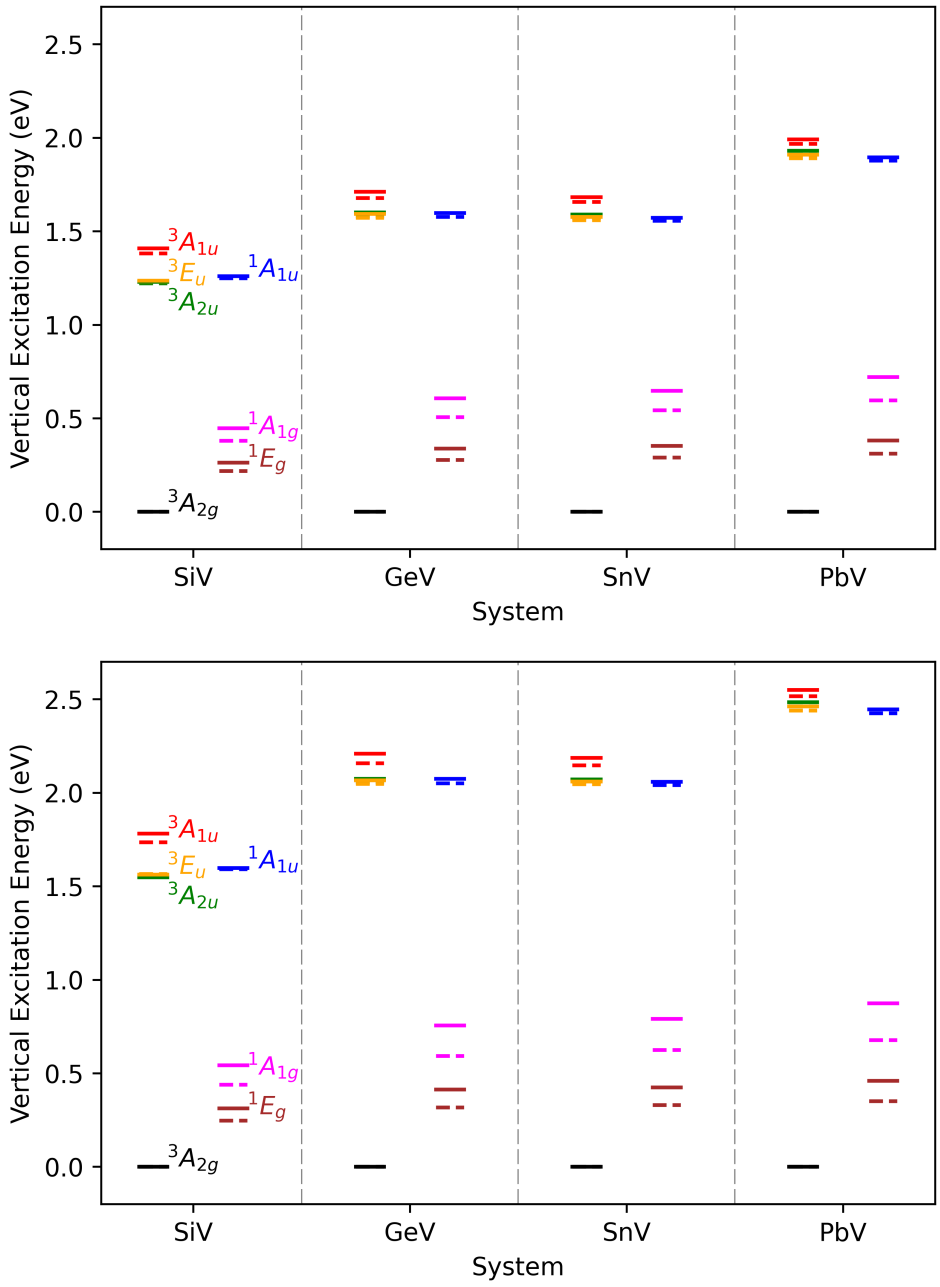

Figure 6.9: Many-electron energy levels of the neutral silicon-vacancy (SiV), germanium-vacancy (GeV), tin-vacancy (SnV) and lead-vacancy (PbV) center in diamond. Calculations are performed starting from PBE (top) and dielectric-dependent hybrid (DDH) (bottom) functionals, with dielectric screening evaluated within (dashed lines) and beyond (solid lines) the random phase approximation (RPA).

Table 6.7: Vertical excitation energies (eV) of spin-defects including the negatively charged nitrogen-vacancy (NV) and neutral silicon-vacancy (SiV), germanium-vacancy (GeV), tin-vacancy (SnV), and lead-vacancy (PbV) center in diamond. Calculations are performed using PBE and DDH functionals to obtain mean-field energy levels, and dielectric screening is evaluated within and beyond the random phase approximation (RPA). Reference vertical excitation energies are computed from experimental zero-phonon lines (ZPL) when Stokes energies are available. Reference experimental values for ZPLs are shown in brackets in the Ref column.

		PBE		DDH		Ref
		RPA	Beyond-RPA	RPA	Beyond-RPA	
System	Excitation					
NV	${}^3E \leftrightarrow {}^3A_2$	1.395	1.458	1.921	2.001	2.180 [67] (1.945 [67])
	${}^1A_1 \leftrightarrow {}^3A_2$	1.211	1.437	1.376	1.759	
	${}^1E \leftrightarrow {}^3A_2$	0.396	0.444	0.476	0.561	
	${}^1A_1 \leftrightarrow {}^1E$	0.815	0.993	0.900	1.198	(1.190 [308])
	${}^3E \leftrightarrow {}^1A_1$	0.184	0.020	0.545	0.243	(0.344-0.430 [112])
SiV	${}^3E_u \leftrightarrow {}^3A_{2g}$	1.247	1.258	1.590	1.594	1.568 [370] (1.31 [119])
	${}^3A_{1u} \leftrightarrow {}^3A_{2g}$	1.386	1.416	1.741	1.792	
	${}^1E_g \leftrightarrow {}^3A_{2g}$	0.232	0.281	0.261	0.336	
	${}^1A_{1g} \leftrightarrow {}^3A_{2g}$	0.404	0.478	0.466	0.583	
	${}^1A_{1u} \leftrightarrow {}^3A_{2g}$	1.262	1.277	1.608	1.623	
	${}^3E_u \leftrightarrow {}^3A_{2u}$	-0.000	0.002	0.003	0.011	(0.007 [119])
GeV	${}^3E_u \leftrightarrow {}^3A_{2g}$	1.595	1.619	2.076	2.105	
	${}^3A_{1u} \leftrightarrow {}^3A_{2g}$	1.689	1.726	2.173	2.231	
	${}^1E_g \leftrightarrow {}^3A_{2g}$	0.288	0.355	0.329	0.434	
	${}^1A_{1g} \leftrightarrow {}^3A_{2g}$	0.529	0.639	0.617	0.797	
	${}^1A_{1u} \leftrightarrow {}^3A_{2g}$	1.595	1.621	2.076	2.110	
	${}^3E_u \leftrightarrow {}^3A_{2u}$	-0.012	-0.011	-0.012	-0.009	
SnV	${}^3E_u \leftrightarrow {}^3A_{2g}$	1.579	1.599	2.069	2.091	
	${}^3A_{1u} \leftrightarrow {}^3A_{2g}$	1.667	1.696	2.160	2.207	
	${}^1E_g \leftrightarrow {}^3A_{2g}$	0.302	0.368	0.341	0.444	
	${}^1A_{1g} \leftrightarrow {}^3A_{2g}$	0.565	0.678	0.649	0.830	
	${}^1A_{1u} \leftrightarrow {}^3A_{2g}$	1.570	1.591	2.060	2.086	
	${}^3E_u \leftrightarrow {}^3A_{2u}$	-0.017	-0.017	-0.017	-0.014	
PbV	${}^3E_u \leftrightarrow {}^3A_{2g}$	1.910	1.934	2.464	2.493	
	${}^3A_{1u} \leftrightarrow {}^3A_{2g}$	1.980	2.008	2.533	2.574	
	${}^1E_g \leftrightarrow {}^3A_{2g}$	0.321	0.396	0.360	0.476	
	${}^1A_{1g} \leftrightarrow {}^3A_{2g}$	0.615	0.750	0.697	0.910	
	${}^1A_{1u} \leftrightarrow {}^3A_{2g}$	1.894	1.916	2.446	2.476	
	${}^3E_u \leftrightarrow {}^3A_{2u}$	-0.023	-0.024	-0.025	-0.025	

6.2.4 Technical details

Convergence tests of active space

A minimum model of 9 defect orbitals and 16 electrons can be constructed for group-IV vacancy centers. The 9 defect orbitals for SiV are visualized in Fig. 6.10; the corresponding orbitals for GeV, SnV, and PbV are similar in shape.

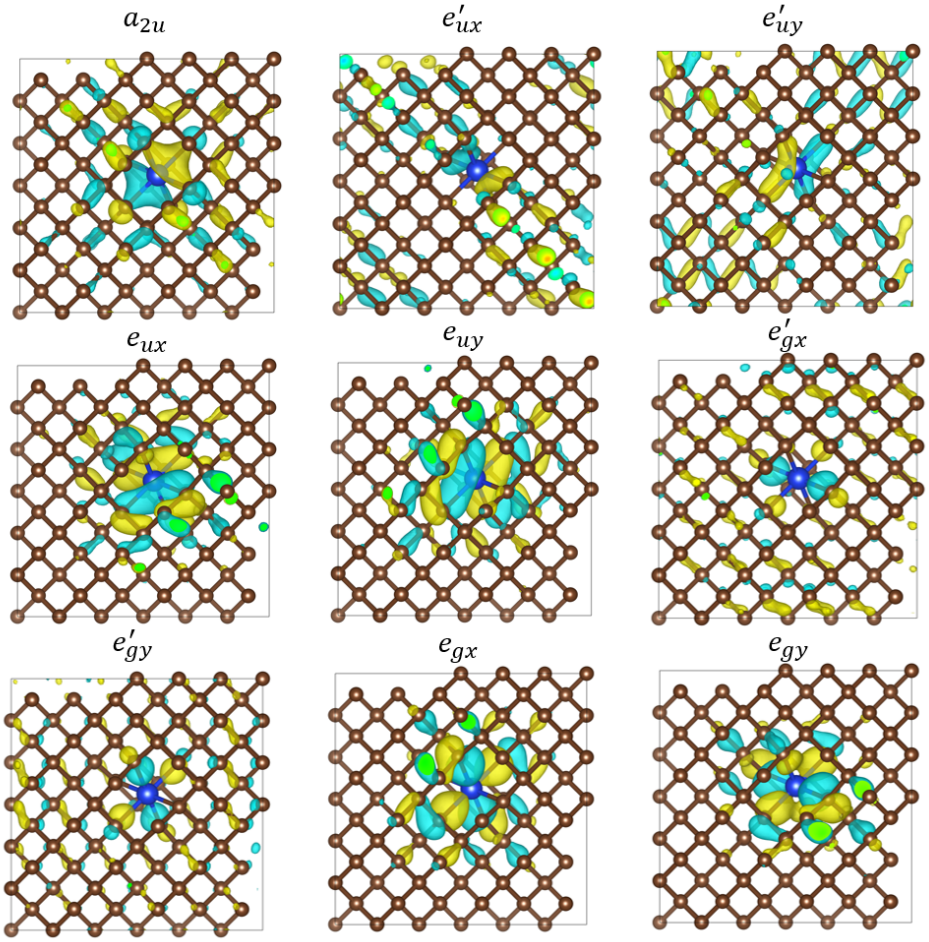

Figure 6.10: Shape of orbitals in the minimum model of SiV. a_{2u}, e_u and e_g are defect orbitals localized around the Si atom, e'_u and e'_g are resonance orbitals.

Active spaces that are larger than the minimum model are obtained by including in the active space valence and conduction orbitals. In the following figures, active spaces are denoted by a tuple of electron number and orbital number, and the minimum model

is marked with dashed lines. Following each figure a precise definition of active spaces with band indices is given. All results shown in this section are obtained with the dielectric dependent hybrid (DDH) functional. In all cases, FCI eigenvalues are found to be insensitive to the choice of active spaces.

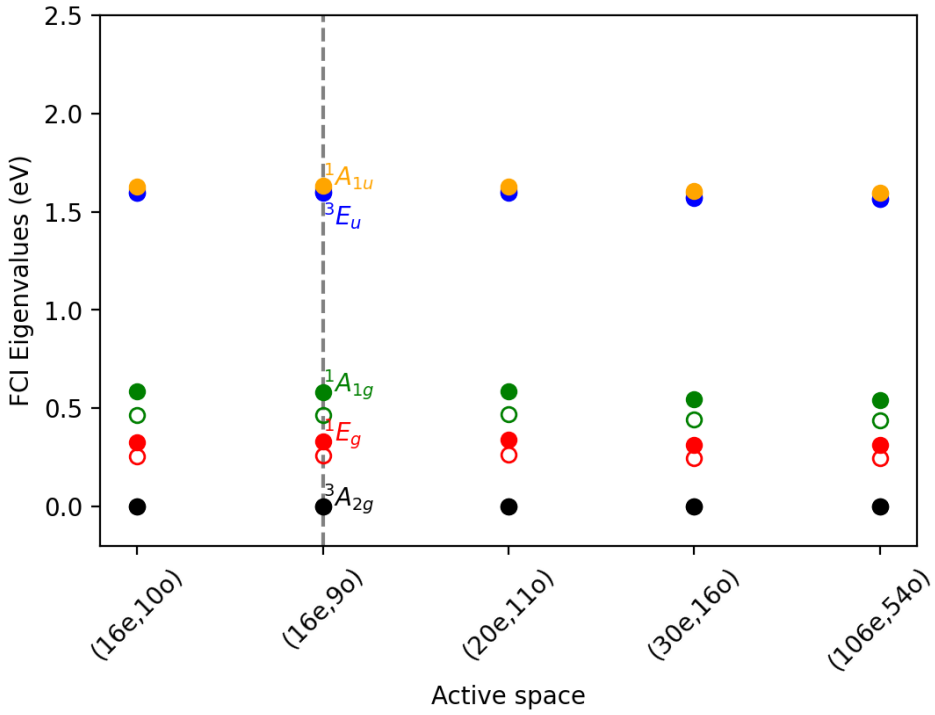

Figure 6.11: Convergence of vertical excitation energies of SiV in diamond as a function of active space size.

(16e,9o): minimal model including band indices 412, 415-416, 425-428, 430-431

(16e,10o): minimal model + index 450

(20e,11o): minimal model + indices 413-414

(30e,16o): minimal model + indices 378-382, 413-414

(106e,54o): indices 378-431

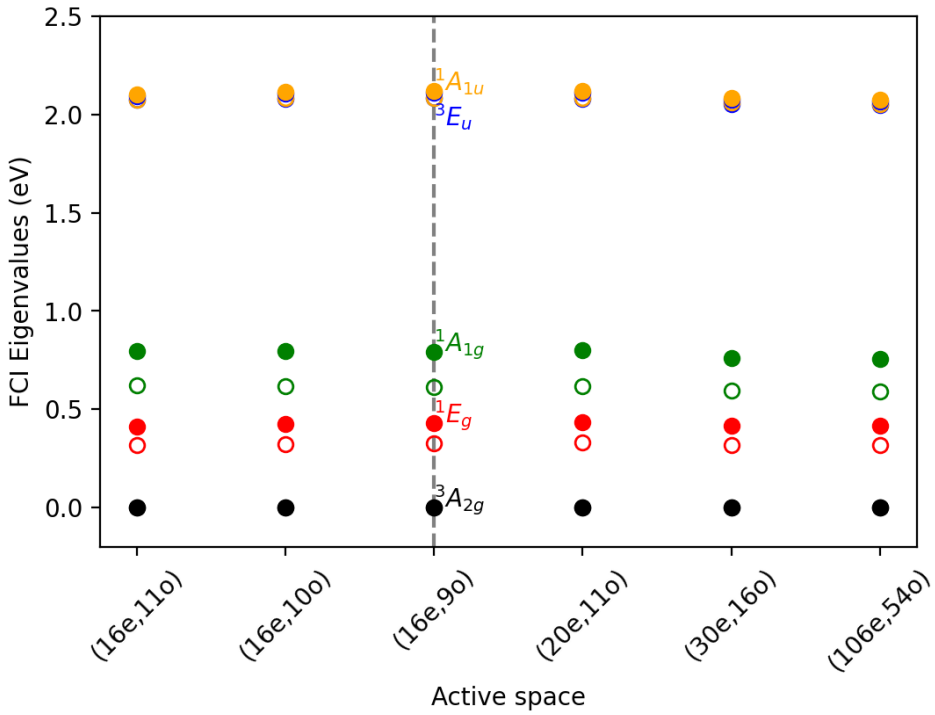

Figure 6.12: Convergence of vertical excitation energies of GeV in diamond as a function of active space size.

(16e,9o): minimal model including band indices 417, 420-421, 430-433, 435-436

(16e,11o): minimal model + indices 443, 455

(16e,10o): minimal model + index 443

(20e,11o): minimal model + indices 418-419

(30e,16o): minimal model + indices 383-387, 418-419

(106e,54o): indices 383-436

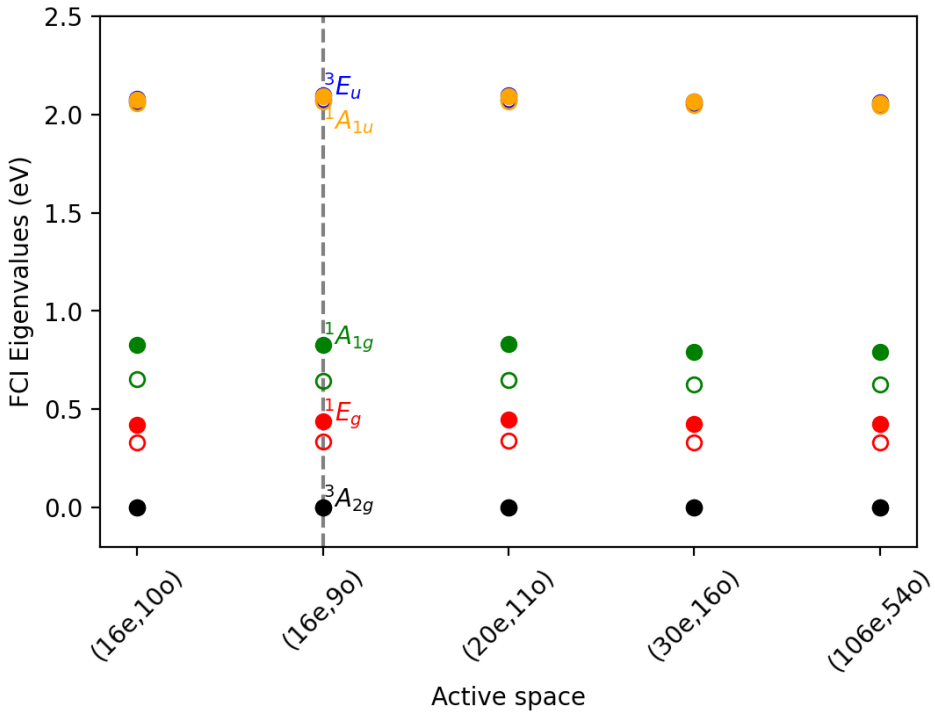

Figure 6.13: Convergence of vertical excitation energies of SnV in diamond as a function of active space size.

(16e,9o): minimal model including band indices 419-421, 430-433, 435-436

(16e,10o): minimal model + index 458

(20e,11o): minimal model + indices 417-418

(30e,16o): minimal model + indices 383-387, 417-418

(106e,54o): indices 383-436

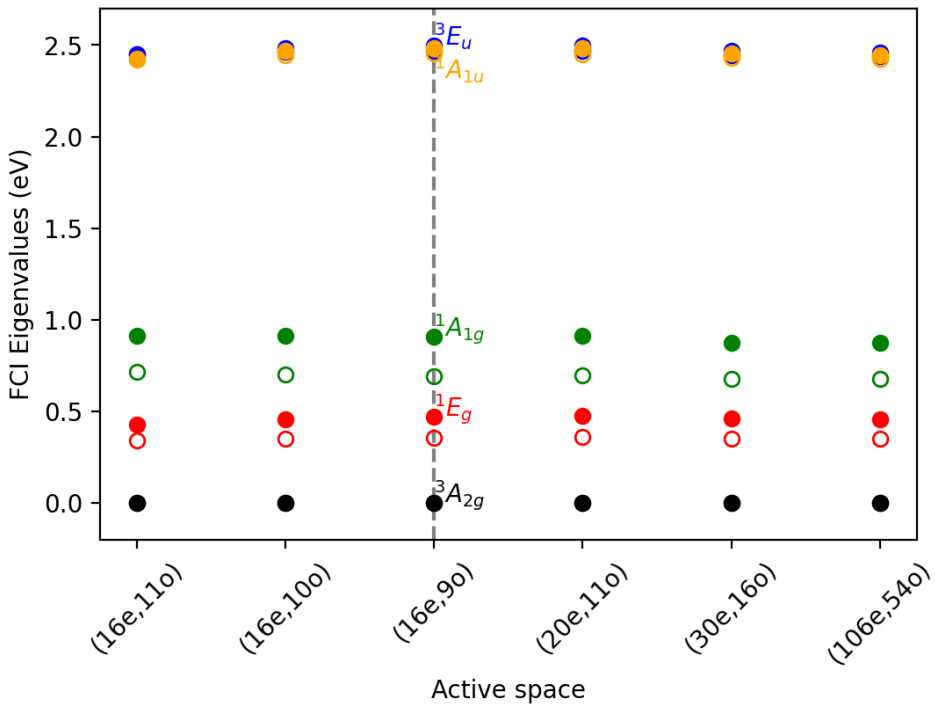

Figure 6.14: Convergence of vertical excitation energies of PbV in diamond as a function of active space size.

(16e,9o): minimal model including band indices 419-420, 422, 430-433, 435-436

(16e,11o): minimal model + indices 443, 455

(16e,10o): minimal model + index 443

(20e,11o): minimal model + indices 417-418

(30e,16o): minimal model + indices 383-387, 418-419

(106e,54o): indices 383-436

Results using HSE functional

Table 6.8: Vertical excitation energies (eV) of the negatively charged nitrogen vacancy (NV) in diamond (64-atom supercell), obtained using different DFT starting points.

	PBE		HSE		DDH	
	RPA	Beyond-RPA	RPA	Beyond-RPA	RPA	Beyond-RPA
Excitation						
${}^3E \leftrightarrow {}^3A_2$	1.512	1.655	1.941	2.162	2.057	2.281
${}^1A_1 \leftrightarrow {}^3A_2$	1.222	1.590	1.371	1.933	1.367	1.941
${}^1E \leftrightarrow {}^3A_2$	0.452	0.552	0.520	0.677	0.530	0.695
${}^1A_1 \leftrightarrow {}^1E$	0.770	1.038	0.850	1.256	0.837	1.247

Projected density of states

The following figures show the projected density of states (PDOS) of SiV, GeV, SnV and PbV obtained with spin-unrestricted DFT calculations using the PBE functional. The e_g defect orbitals in the band gap of diamond are dominated by C character.

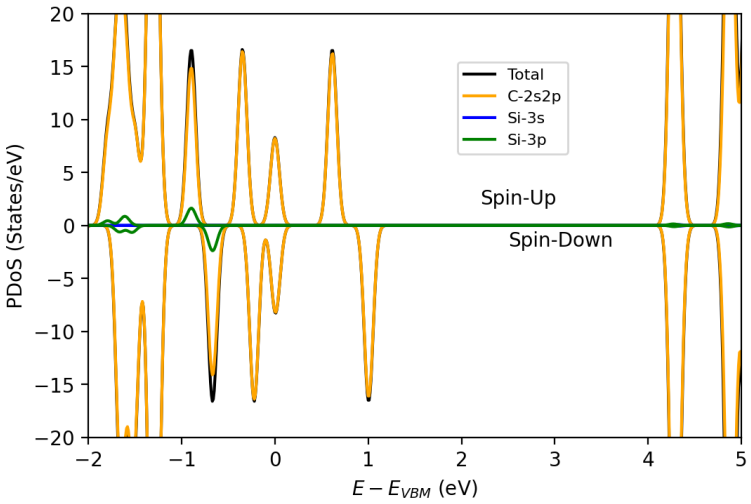

Figure 6.15: Projected density of states of SiV in diamond.

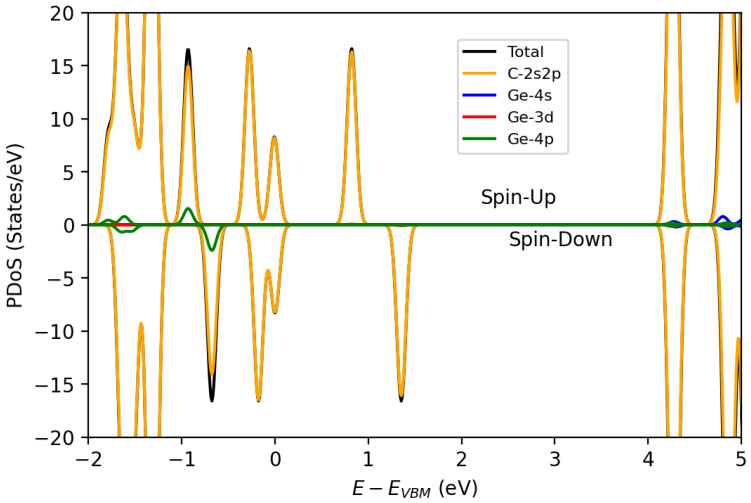

Figure 6.16: Projected density of states of GeV in diamond.

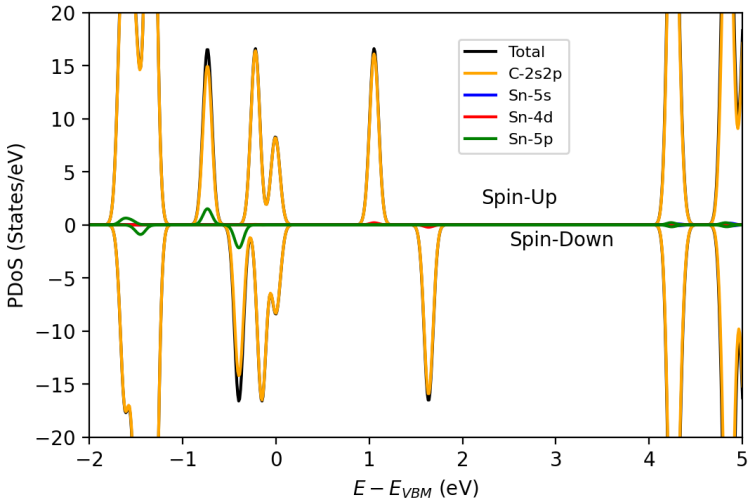

Figure 6.17: Projected density of states of SnV in diamond.

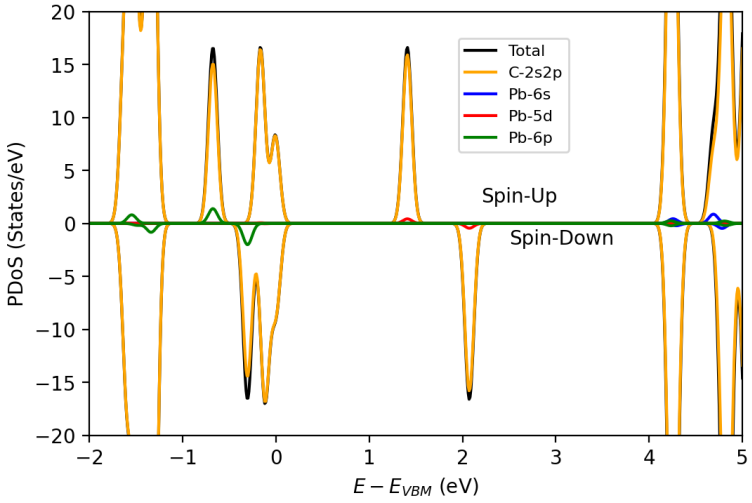

Figure 6.18: Projected density of states of PbV in diamond.

Fully relativistic calculations of PbV

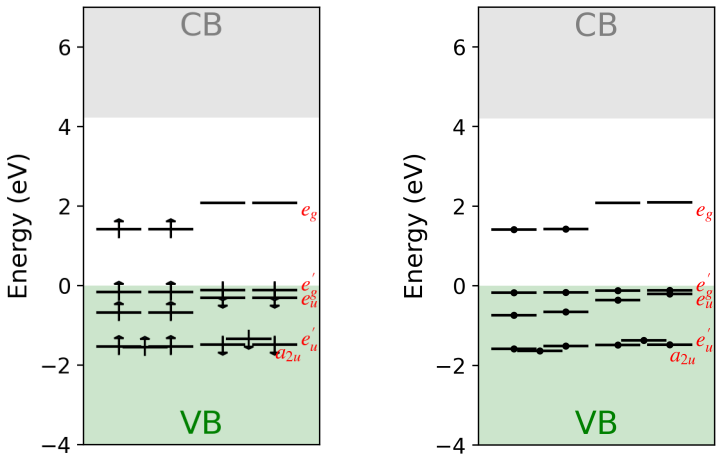

Figure 6.19: Kohn-Sham eigenvalues for important defect levels of PbV obtained by (unrestricted) collinear-spin DFT calculation (left) and fully relativistic noncollinear-spin DFT calculations (right). The split of degenerate e_g orbitals in the band gap induced by spin-orbit coupling is less than 0.02 eV.

6.2.5 Conclusion

In summary, we presented a study of strongly-correlated electronic states of several spin-defects in diamond using the quantum embedding theory described in Ref [219]. We reported the first prediction of strongly-correlated electronic states of neutral GeV, SnV and PbV defects based on first-principles calculations. In addition, we compared results obtained starting from different functionals and with different approximations in the treatment of the dielectric screening, and we showed the importance of using hybrid functional starting points and beyond-RPA dielectric screening for the construction of effective models of spin-defects. Our results indicate that optical spin polarization may be easier to realize in neutral vacancy complexes with elements heavier than Si, e.g. Pb, due to a more energetically favorable ISC. Finally we note that the quantum embedding results obtained in this work are based on the exact diagonalization of effective Hamiltonians, which can be effectively performed on near-term quantum computers with a relatively small number of qubits, as shown in Ref [219].

6.3 Microscopic theory for spin-phonon interactions in silicon carbide

Adapted with permission from S. J. Whiteley, G. Wolfowicz, C. P. Anderson, A. Bourassa, H. Ma, M. Ye, G. Koolstra, K. J. Satzinger, M. V. Holt, F. J. Heremans, A. N. Cleland, D. I. Schuster, G. Galli, and D. D. Awschalom. Nature Physics. (2019). https://doi.org/10.1038/s41567-019-0420-0

Hybrid spin-mechanical systems provide a platform for integrating quantum registers and transducers. Efficient creation and control of such systems require a comprehensive understanding of the individual spin and mechanical components as well as their mutual interactions. Point defects in silicon carbide (SiC) offer long-lived, optically addressable spin registers in a wafer-scale material with low acoustic losses, making them natural candidates for integration with high quality factor mechanical resonators. Here, we show Gaussian focusing of a surface acoustic wave in SiC, characterized by a novel stroboscopic X-ray diffraction imaging technique, which delivers direct, strain amplitude information at nanoscale spatial resolution. Using *ab initio* calculations, we provide a more complete picture of spin-strain coupling for various defects in SiC with C_{3v} symmetry. This reveals the importance of shear for future device engineering and enhanced spin-mechanical coupling. We demonstrate all-optical detection of acoustic paramagnetic resonance without microwave magnetic fields, relevant to sensing applications. Finally, we show mechanically driven Autler-Townes splittings and magnetically forbidden Rabi oscillations. These results offer a basis for full strain control of three-level spin systems.

6.3.1 Introduction

Hybrid quantum systems [201] leverage the strengths of various modalities of representing quantum information, including optical photons for sending quantum states across long distances, spins for information storage, and microwave superconducting circuits for com-

putation, with the potential of using nanomechanics as an intermediary quantum bus. For instance, coherently exchanging quantum information between optically active defect spins and mechanical resonators [209] provides a route to couple optical photons to microwave frequency phonons in a hybrid quantum system. Optically active defect spins in SiC, such as the neutral divacancy [188], have recently been shown to support long-lived spin states [59, 398, 334] a variety of quantum controls [138], and spin-photon interfaces [60] compatible with quantum entanglement protocols. Importantly, SiC is a piezoelectric material and supports mature fabrication processes for production of high quality micro-electromechanical systems (MEMS). Although progress has been made coupling spins to mechanics in similar defect systems, including the NV center in diamond with coherent sensing using single spins [192, 148], strain tuning[368, 273], and mechanical driving [224, 20, 223, 19] defects in SiC are well positioned to solve the materials challenges of coherently manipulating spins with strain and strong coupling of spins with phonons.

While static strain will generate shifts in ground state ($s = 1$) energy sublevels, resonant a.c. strain can coherently drive electron spin transitions. Large in-plane dynamic strains can be generated by surface acoustic wave (SAW) devices, which are well developed for radio frequency filters and offer simple engineering approaches for fabricating low loss resonators. SAW devices have also been proposed as hybrid quantum transducers [328] and used to demonstrate coupling to superconducting qubits [228, 248, 319] along with optomechanical interactions involving defect excited states [114, 113].

Here, we demonstrate acoustically driven $\Delta m_{\mathrm{s}} = \pm 1$ spin transitions, where $m_{\mathrm{s}} = 0, \pm 1$ is the spin projection, on divacancy spin ensembles in 4H-SiC. We further demonstrate $\Delta m_{\mathrm{s}} = \pm 2$ spin transitions through the Autler-Townes effect, mechanical Rabi oscillations, and comparing the relative coupling strengths of inequivalent divacancy defects. These results are well described by our theoretical model developed from a combination of direct experimental observations and Density Functional Theory (DFT) calculations of anisotropic spin-strain coupling coefficients. We find that uniaxial strain and shear drive divacancy spins

with coupling strengths of similar magnitude, but with generally different relative phase and selection rules. These experiments utilize a patterned Gaussian SAW phonon resonator that focuses strain and reduces resonator mode volumes in analogy to Gaussian optics. To image the mechanical modes of our Gaussian SAW devices, we use a unique nanoscale scanning X-ray diffraction technique that directly measures acoustic lattice perturbations. In addition, spatial responses of Autler-Townes splittings are well explained by ensemble averaging shear and uniaxial strain from the SAW mode. Shear provides an important way of controlling three-level spins (qutrits) with phonons and opens avenues for coupling spins with MEMS.

6.3.2 Experimental control of divacancy spins using surface accoustic waves

Gaussian SAW Devices for Spin Manipulation

We first describe device design and characterization with a nanoscale X-ray diffraction imaging method, followed by spin manipulation. To amplify the piezoelectric response of the SiC substrate, we use a thin, sputtered aluminum nitride (AlN) layer on the SiC surface before fabricating a SAW resonator to create radio frequency mechanical strain. Standard planar SAW resonator designs span wide apertures, often greater than 100 acoustic wavelengths (λ), distributing the strain across large crystal areas. Since AlN and 4H-SiC have isotropic in-plane Rayleigh wave velocities [363] (5790 and 6830 m/s, respectively), we fabricate simple Gaussian geometries, inspired by Gaussian optics, to focus strain while also suppressing acoustic diffraction losses (Fig. 6.20a,b). A patterned aluminum interdigitated transducer transmits SAWs ($\lambda = 12$ μm), while grooves in AlN form Bragg gratings that act as SAW cavity mirrors to support a resonator frequency $\omega_{\mathrm{m}}/2\pi \approx 560$ MHz and loaded quality factor of $\sim 16,000$ (Fig. 6.20c) at 30 K. The Gaussian SAW resonator internal quality factor ($Q_{\mathrm{i}} \approx 22,400$ at 30 K) is likely limited by the polycrystalline AlN layer at low temperatures. In our experiments the Gaussian geometries for enhanced strain focusing and reduced res-

onator mode volumes facilitate larger strains for fast coherent manipulation of electron spin states.

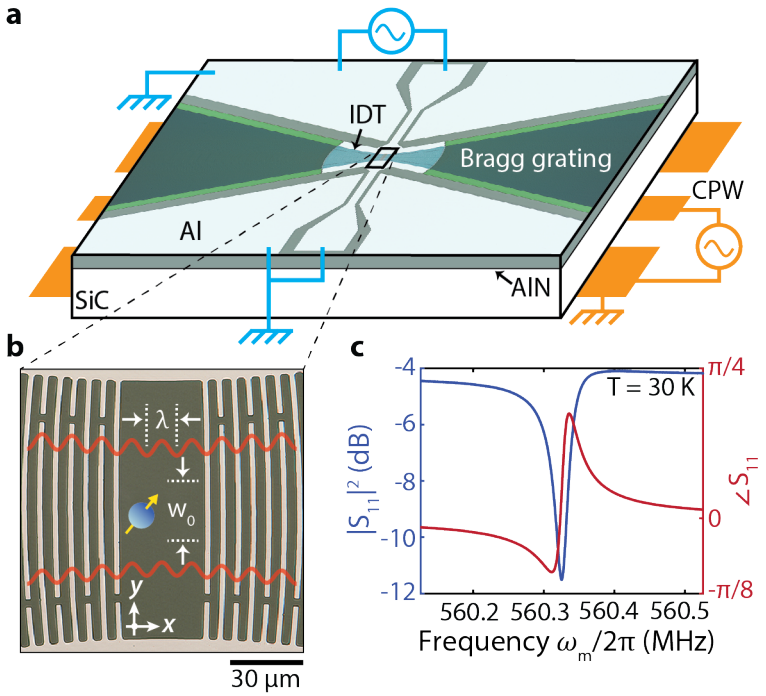

Figure 6.20: **Strain focusing with a Gaussian SAW resonator.** **a**. Schematic of the SAW device geometry fabricated on sputtered AlN on a 4H-SiC substrate. Microwaves drive spin transitions mechanically through the SAW resonator (cyan) and magnetically from the backside coplanar waveguide (orange). **b**. Optical micrograph of the Gaussian SAW resonator's acoustic focus ($\lambda = 12$ μm, $w_0 = 2\lambda$) with red lines illustrating the wave's out-of-plane displacement (u_z). **c**. Magnitude (blue) and phase (red) measurements of the 1-port reflection of the Gaussian SAW resonator used in spin experiments.

To directly visualize the Gaussian mechanical mode, we use stroboscopic scanning X-ray diffraction microscopy (s-SXDM) to image the phonons with nanoscale resolution. This technique utilizes coherent X-rays from a synchrotron radiation light source, generated at 8.00 keV and focused to a 25 nm spot size (3σ), and Bragg diffraction contrast to enable local measurements of lattice curvature and strain along a particular crystal orientation [147, 150]. We frequency match the radio frequency excitation to a Gaussian interdigitated transducer with the timing structure of the synchrotron storage ring in order to measure the peak-to-peak amplitude of the acoustic standing wave. Due to the frequency matching requirements for s-SXDM, we use a SAW transducer without a cavity, which is designed to produce a

spatial strain mode similar to resonators used in spin experiments. Scanning the nano-focused X-ray beam in real space clearly shows the SAW profile (Fig. 6.21a) is consistent with the fabricated geometry and approximately nanometer Rayleigh wave displacements. The dynamic transverse lattice slope (Fig. 6.21b), caused by a local lattice plane tilt towards the $\pm y$ direction, is expected from a Gaussian focus and SAW confinement. These X-ray measurements confirm that the SAW out-of-plane displacement (in phase with the in-plane uniaxial strain required for spin driving) is maximized at the resonator's precise center and demonstrate the value of using X-ray diffraction microscopy for studying quantum devices [276] and materials.

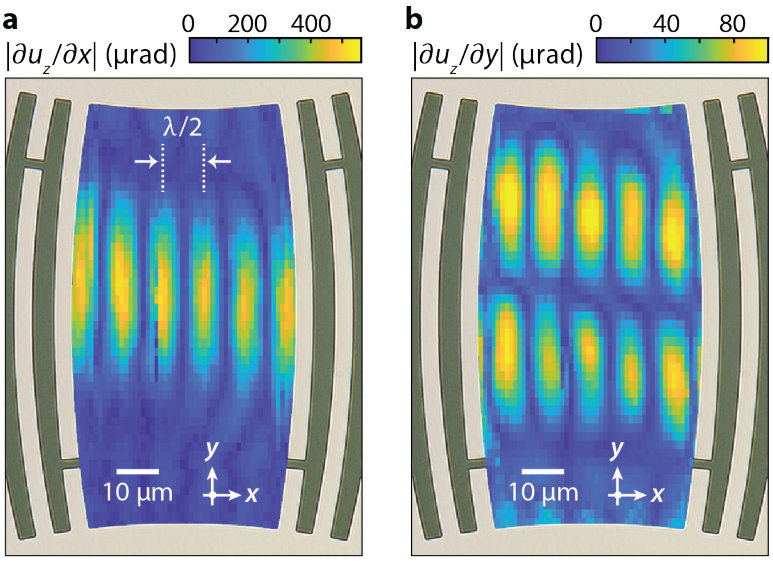

Figure 6.21: **Nanoscale X-ray imaging of the Gaussian acoustic mode.** Mechanical mode from a similar Gaussian SAW device ($\lambda = 19$ μm, $w_0 = 1.25\lambda$), directly measured with s-SXDM using the 4H-SiC [0004] Bragg peak. This quantifies the SAW peak-to-peak longitudinal (**a**) and transverse (**b**) lattice slopes at the acoustic beam waist. The image is skewed vertically due to sample drift during measurements.

Optically Detected Acoustic Paramagnetic Resonance

Electron spin ground state sublevels of divacancy defects are typically measured using optically detected magnetic resonance (ODMR) with $\Delta m_s = \pm 1$ transitions magnetically driven by microwave fields. Due to the defect's intersystem crossing, ODMR probes the spin pro-

jections of $|\pm 1\rangle$ versus $|0\rangle$ through changes in photoluminescence. The ground state spin Hamiltonian neglecting hyperfine interactions takes the form, z z

$$H/h = \gamma \mathbf{B} \cdot \mathbf{S} + \mathbf{S} \cdot \mathbf{D} \cdot \mathbf{S} \tag{6.10}$$

where h is the Planck constant, γ is the electron gyromagnetic ratio ($\mu_{\mathrm{B}} \approx 2.8$ MHz/G), $\mathbf{B}$ is the external magnetic field vector, and $\mathbf{D}$ is the zero-field splitting tensor (also referred to as D_{ij}). In the absence of lattice strain, the divacancy spin-spin interaction simplifies to $D_0 S_z^2$ where $D_0 \approx 1.336$ and 1.305 GHz, depicted in Fig. 6.22a, for c-axis oriented defect configurations [85] hh and kk, respectively. The zero-field splitting Hamiltonian is sensitive to local lattice perturbations [86] such as thermal disorder, an applied electric field, or strain. When the lattice is perturbed by a small strain, characterized by a tensor ϵ_{kl}, the zero-field splitting tensor is generally modified by $\Delta D_{ij} = G_{ijkl}\epsilon_{kl}$, where G_{ijkl} is the spin-strain coupling tensor. The symmetry of the spin-strain coupling tensor is determined by the local $\mathrm{C_{3v}}$ symmetry of the hh and kk configurations for divacancy and also applies to the NV center in diamond [375]. We utilize off-diagonal Hamiltonian elements containing ΔD_{ij} to drive resonant spin transitions with phonons, and consider both $\Delta m_{\mathrm{s}} = \pm 1$ and ± 2 transitions for full ground state $s = 1$ spin control.

We first demonstrate mechanical driving of $\Delta m_{\mathrm{s}} = \pm 1$ spin transitions with the Gaussian SAW resonator. The point group symmetries of the divacancy in SiC allow for non-zero spin-strain coupling coefficients for zero-field splitting terms that contain the anticommutators $\{S_x, S_z\}$ and $\{S_y, S_z\}$. In order to probe acoustic paramagnetic resonance, we tune the axial magnetic field (B_0) such that the spin $|0\rangle$ to $|-1\rangle$ transition frequency is matched with the SAW resonator (Fig. 6.22a). It is critical to design an experimental measurement sequence insensitive to stray magnetic fields from electrical currents in the interdigitated transducer. To disentangle these effects, we use an interlaced pump/laser probe sequence as well as lock-in amplification to measure the difference in luminescence when the spin resonance frequency is shifted away from the cavity resonance via modulation of B_0 with a small coil. Spin rotations

are primarily driven and detected during the SAW cavity ring down period without radio frequency driving, although the spin ensemble will also encounter some residual magnetic resonance when the drive is turned back on due to lingering optical-spin polarization. We detect higher photoluminescence contrast when the radio frequency drive is matched to our SAW cavity resonance (Fig. 6.22b), whereas smaller, residual contrast is detected when the drive is far off the SAW resonance. When the photoluminescence contrast is normalized by ODMR experiments from magnetic driving, the kk/hh mechanical drive rate ratio is 0.89 ± 0.10, which agrees with our theoretical model and DFT calculations (ratio ~ 1.0) where shear couples more strongly to $\Delta m_\mathrm{s} = \pm 1$ transitions than does uniaxial strain. The transverse spatial dependence (Fig. 6.22c) confirms that the photoluminescence contrast we measure on resonance matches our Gaussian resonator's mechanical mode shape. Magnetic field driving from the transducer, on the other hand, results in a flat profile. The long cavity ring up time prevents us from performing pulsed Rabi oscillations, though this could be solved using fast B_0 pulses to tune the spin resonance frequency. Our demonstration of $\Delta m_\mathrm{s} = \pm 1$ transitions by phonons enables direct photoluminescence contrast (optical detection) of resonant spin-strain coupling for sensing applications without electromagnetic microwaves.

Coherent Magnetically Forbidden Spin Transitions

To complement $\Delta m_\mathrm{s} = \pm 1$ spin driving, we further use the strain coupling terms $S_x^2 - S_y^2$ and $\{S_x, S_y\}$ in the zero-field splitting Hamiltonian to show $\Delta m_\mathrm{s} = \pm 2$ spin transitions. For these transitions, photoluminescence contrast from ODMR cannot directly measure resonant strain without extra electromagnetically driven spin resonance because photoluminescence contrast is insensitive to differences between $|+1\rangle$ and $|-1\rangle$ states. The mechanical transition rate (Ω_m) is instead measured using Autler-Townes (AC Stark) splittings, where in the dressed basis, the new eigenstates are split in energy by Ω_m. This splitting can be observed in the ODMR spectrum. We use a continuous magnetic microwave pump (Rabi frequency

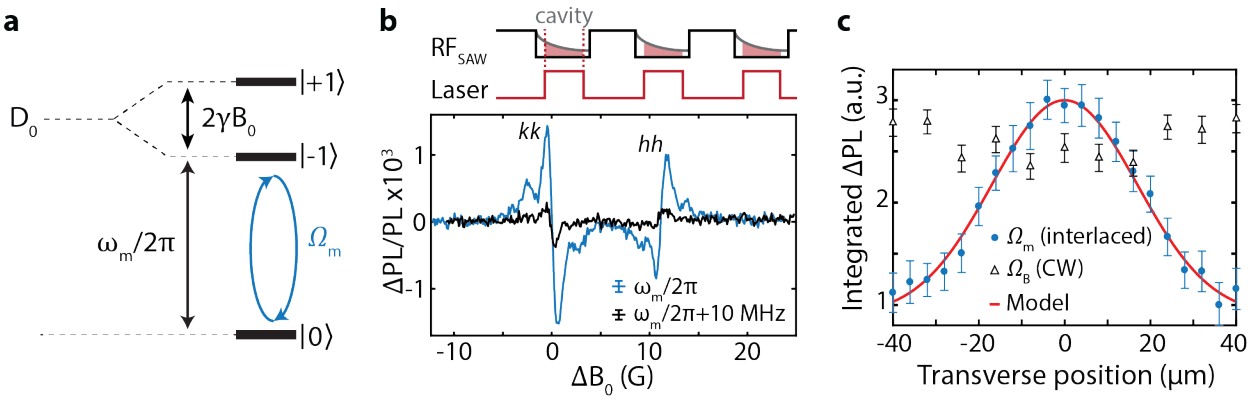

Figure 6.22: **Optically detected acoustic paramagnetic resonance in silicon carbide.** **a**. Energy level diagram showing the SAW frequency on resonance with the spin transition between the $|0\rangle$ and $|-1\rangle$ states. **b**. (Top) Interlaced pump-probe sequence during magnetic field-modulation. (Bottom) Photoluminescence (PL) contrast at 30 K when electrical excitation is on and off cavity resonance ($\omega_m/2\pi = 559.6$ MHz). Radio frequency power is 32 mW at sample, and ΔB_0 is in reference to the drive frequency. **c**. Integrated photoluminescence contrast from kk resonance (evaluated at $\Delta B_0 = 0$) as a function of the SAW resonator transverse position. Driving on-resonance ("Ω_m") uses the interlaced sequence from (**b**), whereas off-resonance data ("Ω_B") uses a continuous, non-interlaced sequence. The radio frequency power is 200 mW at the sample, and the beam waist model is $\exp[-y^2/(w_0^2)]$, using fabrication parameters and a scaled amplitude. All error bars are 95% confidence intervals.

$\Omega_B : \pm 1 \sim$ MHz) for $|0\rangle$ to $|\pm 1\rangle$ transitions while the SAW is driven at a constant frequency $\omega_m/2\pi$ (Fig. 6.23a). Dressed state level anti-crossings are most clearly seen when the $|\pm 1\rangle$ spin sublevels are tuned to the SAW resonance frequency. The dressed spin eigenstate energies observed for a 400 mW drive power on the Gaussian SAW resonator closely match predictions for $\Omega_m/2\pi \approx 4$ MHz (Fig. 6.23b). Additionally, the Autler-Townes splitting scales linearly with square-root of radio frequency drive power delivered to the SAW, which is expected as Ω_m is linearly proportional to strain (Fig. 6.23c). The resolved Autler-Townes splitting shows that the mechanical drive rate is faster than the ensemble spin inhomogeneous linewidth (decoherence rate), allowing for measurement of coherent Rabi oscillations.

We mechanically drive coherent Rabi oscillations of kk electron spins using the pulse sequence in Fig. 6.23d to differentiate between populations transferred to $|+1\rangle$ versus $|-1\rangle$ spin states. The spin ensemble inhomogeneous linewidth ($\sim$ 1 MHz) and relatively long

cavity ring up time ($2Q_{\mathrm{i}}/\omega_m \approx 16\mu$s) prevent fast mechanical pulsing, so we keep the mechanical drive on continuously. A pair of magnetic microwave π pulses defines the effective mechanical pulse time τ seen by the spin ensemble (Fig. 6.23d). Using this pulse sequence and positive ODMR contrast of kk defects, normalized photoluminescence values of ± 1 can be interpreted as $|\mp 1\rangle$ spin populations, respectively, before the second magnetic π pulse. We find that three-level system dynamics are necessary to explain the observed mechanical Rabi oscillations shown in Fig. 6.23e, in particular the ensemble population at $\tau = 0$. Specifically, during each magnetic π pulse, the simultaneous mechanics Ω_{m} drives some unintended population transfer between the $|+1\rangle$ and $|-1\rangle$ spin states, which leads to a modified initial projection of the population at $\tau = 0$.

The observed Rabi oscillations qualitatively agree with spin simulations predicted using a physical model consisting of spin-strain coupling parameters from DFT calculations and experimental knowledge, including (i) the ensemble spin resonance spectrum from ODMR, (ii) spin-mechanical drive amplitudes from fitted Autler-Townes splittings, (iii) spatial distribution of spins in the SiC bulk and implanted layer, (iv) finite element analysis of strain and shear distributions from Rayleigh waves, and (v) optical point spread function. Our physical model reproduces the mechanically driven Rabi oscillation rates, asymmetric decay shape, higher frequency features from hyperfine detuned spins, and initial spin population at $\tau = 0$. This demonstrates we can mechanically drive $\Delta m_{\mathrm{s}} = \pm 2$ transitions with a Rabi frequency about four times greater than the ensemble ODMR linewidth. During Rabi oscillations with 400 mW radio frequency power, we estimate from input-output theory applied on a SAW model that the mechanical field strength is approximately 10^{-3} strain order of magnitude, in agreement with DFT simulation results. Short Rabi decay times are primarily explained by SAW strain inhomogeneity across the ensemble, though another source of damping may be present in the experiments. Manipulation of single divacancies [59, 60] will offer the opportunity to extend coherent Rabi oscillations up to or beyond the spin T_2^*. Coherent Rabi oscillations in ensembles for quantum phononics applications could be improved by using

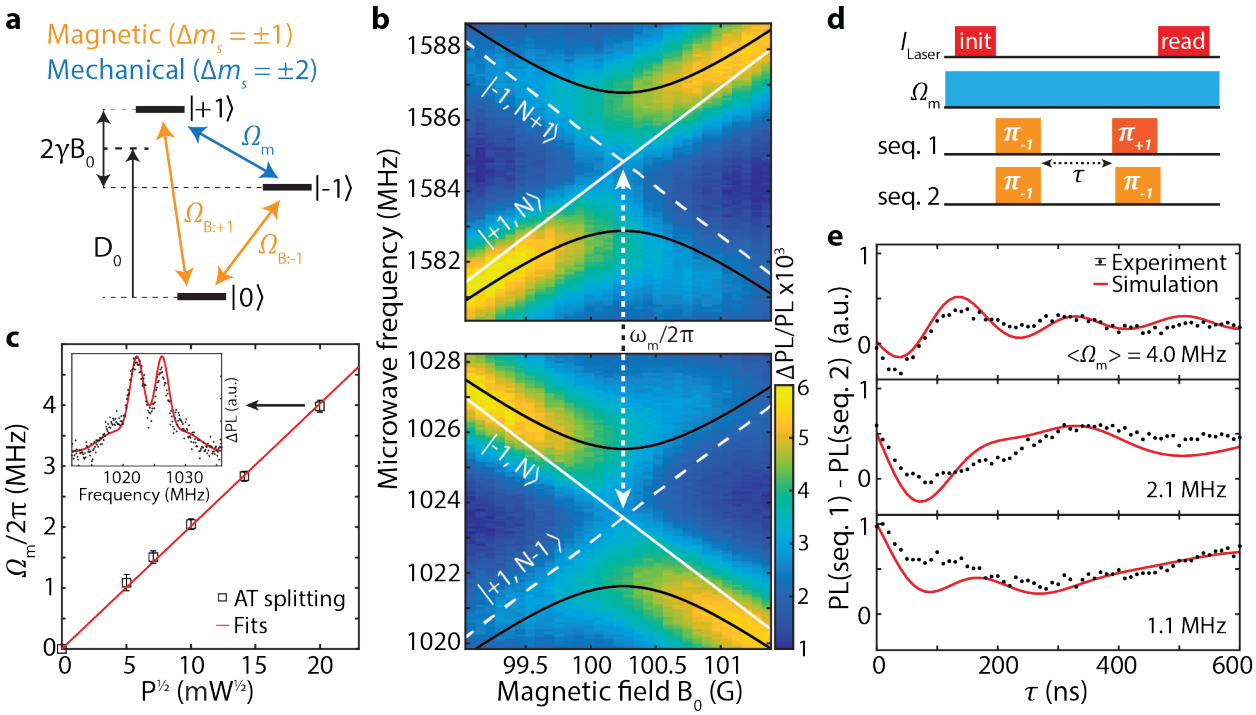

Figure 6.23: **Coherent mechanical driving of kk spin ensembles.** **a**. Divacancy ground state illustration with magnetic ($\Omega_{\mathrm{B:}\pm1}$) and electromechanical (Ω_{m}) drives shown. **b**. Autler-Townes measurement on a kk ensemble at 30 K; dressed for N phonons (black) and undressed (white) spin transitions. The mechanically dressed eigenstates and corresponding transitions are split by Ω_{m}. **c**. Mechanical transition rates obtained from Autler-Townes splittings agree with a linear fit to the square-root of drive power. Error bars are 95% confidence intervals from fits. Inset shows an Autler-Townes splitting measurement (black) at $B_0 \approx 100$ G, with Gaussian fits (red) to the divacancy electron spin and weakly coupled nearby nuclear spins. **d**. Pulse sequence for mechanically driven Rabi oscillations. **e**. Mechanically driven Rabi oscillations at ∼400, 100, and 25 mW, respectively, and typical error bars are 95% confidence intervals. The photoluminescence signal for each Rabi oscillation is normalized by a global factor, and simulations are ensemble average predictions with inhomogeneous strain distributions from finite element modeling.

higher quality material and controlled aperture implantations [372] for more homogeneous strain distributions.

Quantum Sensing of Gaussian Acoustics

We spatially map the Gaussian SAW mode in order to show that $\Delta m_{\mathrm{s}} = \pm 2$ transitions occur due to the mechanical driving and not due to any stray electromagnetic fields [182]. We map changes in the Autler-Townes splitting, shown in Fig. 6.24a, at a constant mag-

netic field while sweeping the laser position across the SAW beam waist. In the resonator's transverse direction, a clear Autler-Townes splitting maximum, and therefore resonant strain amplitude, is observed at the Gaussian acoustic focus. Ω_m as a function of transverse position is well described by a model Gaussian beam waist of the fundamental mode in the device geometry (FWHM = 3.3λ) and not due to predicted stray electric fields. Scanning the laser spot longitudinally (Fig. 6.24b), along the SAW propagation, reveals oscillations in the Autler-Townes splitting at the resonator's acoustic half wavelength. Surprisingly, in conflict with assumptions of a simple sinusoidal standing wave containing uniaxial strain nodes (Fig. 6.21a,b), we observe the mechanical drive rate oscillations are less than 5% peak-to-peak. This is contrary to expectations from previous theoretical work [74] neglecting the full strain tensor, so we interpret our experimental results using a spin Hamiltonian under anisotropic strains also including shear.

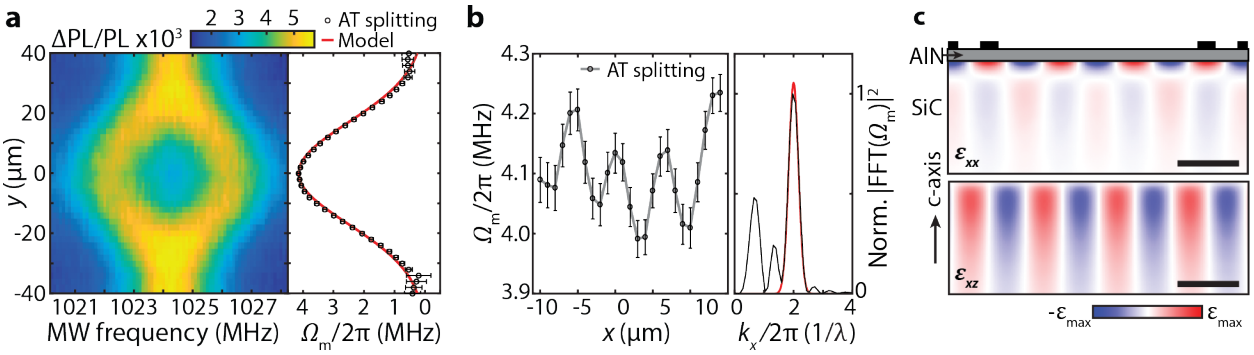

Figure 6.24: **Spatially mapping mechanical spin drive rates. a**. Autler-Townes splitting of kk $|-1\rangle$ sublevel as a function of transverse position (left) at $x = 0$ and the analyzed mechanical transition rates (right). The beam waist model only uses fabrication parameters with a scaled amplitude. **b**. Mechanical transition rate (left) as a function of longitudinal position at $y = 0$, plotted with a line through the experimental data. FFT (right) shows a peak and Gaussian fit in red at the expected acoustic periodicity $\lambda/2$ (6μm). **c**. Strain ϵ_{xx} and ϵ_{xz} of the SAW modeled with COMSOL Multiphysics.

The spatial mapping results can be understood by employing a combination of finite-element simulations in conjunction with DFT calculations of spin-strain interactions. The $\{\overline{1}120\}$ mirror plane symmetry in 4H-SiC is broken by shears ϵ_{xz} and ϵ_{xy}, which drive the spin out-of-phase with $\epsilon_{xx} - \epsilon_{yy}, \epsilon_{yz}$ (mirror symmetry preserving). In our experiments, the

Gaussian SAW beamwaist is oriented to propagate in the $\{1\bar{1}00\}$ plane (defined as the xz-plane). The mechanical transition rate is $\Omega_{\mathrm{m}} = \frac{1}{2}(G_{11}-G_{12})\epsilon_{xx}-2iG_{14}\epsilon_{xz}$ corresponding to $\Delta m_{\mathrm{s}} = \pm 2$ transitions, where the spin-strain coupling tensor $\mathbf{G}$ is written in Voigt notation. In Fig. 6.24c we show finite element simulation results for uniaxial strain ϵ_{xx} and shear ϵ_{xz} for a Rayleigh wave propagating along the x direction. We model the experimental results by converting the strain maps to Ω_{m} using G calculated from DFT, which is then convolved with both an optical point-spread function and estimated spatial distribution of the spins. In our model, spatial averaging causes the spin ensemble to experience similar transition rate magnitude $|\Omega_{\mathrm{m}}|$ from $(G_{11} - G_{12})\epsilon_{xx}$ and $G_{14}\epsilon_{xz}$ contributions at their respective spatial maxima. These uniaxial strain and shear components, which are spatially offset, do not interfere destructively since Ω_{m} is proportional to a linear combination of $\epsilon_{xx}(S_x^2 - S_y^2)$ and $\epsilon_{xz}(S_xS_y + S_yS_x)$. Consequently, in qualitative agreement with our calculations, we always experimentally measure a non-zero Autler-Townes splitting in Fig. 6.24b. Furthermore, our model explains the relative Ω_{m} amplitudes between kk and hh (4.0 : 1.1) observed in Fig. 6.25, and the results for $\Delta m_{\mathrm{s}} = \pm 2$ transitions are well described by the zero-field splitting tensor when the full strain tensor is taken into account. Lastly, we measure mechanical-spin driving on the PL6 defect species in SiC, previously used to demonstrate electron-nuclear spin entanglement in ambient conditions [183]. We find that PL6 experiences similar mechanical transition rates compared to hh and kk (Fig. 6.25); therefore, mechanical control of SiC spin ensembles should be possible at room temperature.

6.3.3 First-principles theory of spin-strain coupling

In this section we discuss symmetry properties of the spin-strain coupling tensor and present its values predicted by density functional theory (DFT). We mainly focus on the experimentally relevant divacancies (hh, kk)-VV in 4H-SiC. To validate the computational protocol of our DFT calculations, we also report the spin-strain coupling tensor for the NV center in diamond and compare with existing literature values.

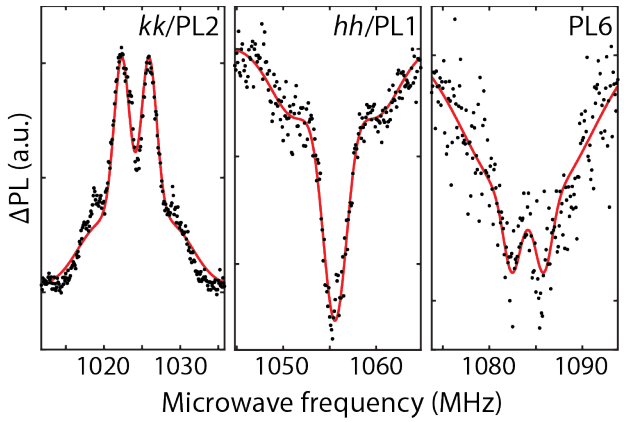

Figure 6.25: **Divacancy defect comparisons of mechanical drive rates.** Autler-Townes splitting measurements (black points) for kk, hh, and PL6 with Ω_{m} ∼4.0, 1.1, 3.4 MHz, respectively, under the same conditions. The fits (red lines) are from simultaneously fitting the data with ODMR spectra to common Gaussian distributions. All error bars are 95% confidence intervals from fitting and measurements are performed at 30 K.

In the following discussion we define the Cartesian frame for 4H-SiC to be x: $[\bar{1}\bar{1}20]$, y: $[1\bar{1}00]$, z: [0001], in consistence with the SAW experiment. The Cartesian frame for diamond is defined as x: $[\bar{1}10]$, y: $[\bar{1}\bar{1}2]$, z: [111]. Under this convention, there is a mirror plane perpendicular to the x axis for both 4H-SiC and diamond. The structures of (hh, kk)-VV and NV in their respective frames are shown in Fig 6.26.

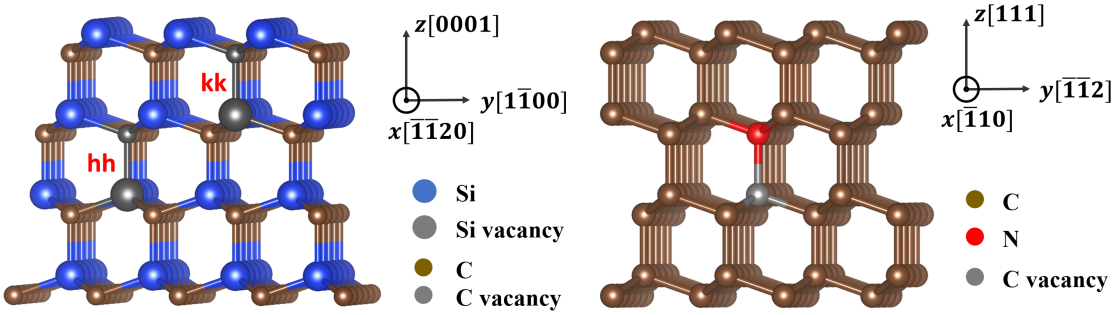

Figure 6.26: The structures of (hh, kk)-VV in 4H-SiC (left) and NV in diamond (right). Lattices are slightly rotated around z axis to show more details.

In the basis of $\{|m_S = 1\rangle, |m_S = 0\rangle, |m_S = -1\rangle\}$, the zero-field splitting (ZFS) Hamil-

tonian as a 3×3 matrix is

$$\mathcal{H}_{\mathrm{ZFS}} = \boldsymbol{S} \cdot \boldsymbol{D} \cdot \boldsymbol{S} \tag{6.11a}$$

$$= \begin{pmatrix} \frac{1}{2}(D_{xx}+D_{yy})+D_{zz} & \frac{1}{\sqrt{2}}(D_{xz}-iD_{yz}) & \frac{1}{2}(D_{xx}-D_{yy})-iD_{xy} \\ \frac{1}{\sqrt{2}}(D_{xz}+iD_{yz}) & D_{xx}+D_{yy} & \frac{1}{\sqrt{2}}(-D_{xz}+iD_{yz}) \\ \frac{1}{2}(D_{xx}-D_{yy})+iD_{xy} & \frac{1}{\sqrt{2}}(-D_{xz}-iD_{yz}) & \frac{1}{2}(D_{xx}+D_{yy})+D_{zz} \end{pmatrix} \tag{6.11b}$$

$$= \begin{pmatrix} \frac{1}{3}D & & \\ & -\frac{2}{3}D & \\ & & \frac{1}{3}D \end{pmatrix}. \tag{6.11c}$$

The last expression applies to defects with $\mathrm{C_{3v}}$ symmetry where the $\boldsymbol{D}$ tensor has only one independent component, and we used the conventional notation $D = \frac{3}{2}D_{zz}$. Off-diagonal elements of $\mathcal{H}_{\mathrm{ZFS}}$ are zero by symmetry. If a strain is applied to the system, the $\mathrm{C_{3v}}$ symmetry may be broken, leading to non-zero off-diagonal elements and transitions between states with different m_S.

The relation between strain and $\boldsymbol{D}$ is characterized by the spin-strain coupling tensor of the defect, which we denote as $\boldsymbol{G}$. $\boldsymbol{G}$ is defined as the derivative of $\boldsymbol{D}$ with respect to the strain tensor $\boldsymbol{\varepsilon}$

$$G_{abcd} = \frac{\partial D_{ab}}{\partial \varepsilon_{cd}} \tag{6.12}$$

where a, b, c, d represent the Cartesian coordinates x, y, z. The strain is defined as $\varepsilon_{ab} = \frac{1}{2}(\frac{u_a}{x_b} + \frac{u_b}{x_a})$. In this convention, compressive strains are negative.

In Voigt notation, both $\boldsymbol{D}$ and $\boldsymbol{\varepsilon}$ are written as 6-dimensional vectors in the order of (xx, yy, zz, yz, xz, xy), and $\boldsymbol{G}$ is represented by a 6×6 matrix. Within the linear response

regime, the change of $\boldsymbol{D}$ induced by strains are given by

$$\begin{pmatrix} \Delta D_{xx} \\ \Delta D_{yy} \\ \Delta D_{zz} \\ \Delta D_{yz} \\ \Delta D_{xz} \\ \Delta D_{xy} \end{pmatrix} = \begin{pmatrix} G_{11} & G_{12} & G_{13} & G_{14} & G_{15} & G_{16} \\ G_{21} & G_{22} & G_{23} & G_{24} & G_{25} & G_{26} \\ G_{31} & G_{32} & G_{33} & G_{34} & G_{35} & G_{36} \\ G_{41} & G_{42} & G_{43} & G_{44} & G_{45} & G_{46} \\ G_{51} & G_{52} & G_{53} & G_{54} & G_{55} & G_{56} \\ G_{61} & G_{62} & G_{63} & G_{64} & G_{65} & G_{66} \end{pmatrix} \begin{pmatrix} \varepsilon_{xx} \\ \varepsilon_{yy} \\ \varepsilon_{zz} \\ 2\varepsilon_{yz} \\ 2\varepsilon_{xz} \\ 2\varepsilon_{xy} \end{pmatrix}. \tag{6.13}$$

Under C_{3v} symmetry, $\boldsymbol{G}$ only has 6 independent components. In the reference frame defined in Fig 6.26, $\boldsymbol{G}$ has the following form

$$\boldsymbol{G} = \begin{pmatrix} G_{11} & G_{12} & G_{13} & G_{14} & & \\ G_{12} & G_{11} & G_{13} & -G_{14} & & \\ -G_{11}-G_{12} & -G_{11}-G_{12} & -2G_{13} & & & \\ G_{41} & -G_{41} & & G_{44} & & \\ & & & & G_{44} & G_{41} \\ & & & & G_{14} & (G_{11}-G_{12})/2 \end{pmatrix} \tag{6.14}$$

where independent components are chosen to be G_{11}, G_{12}, G_{13}, G_{14}, G_{41} and G_{44}. Combining the above equation with Eq. 6.11b, one can see that strains can induce both $\Delta m_S = \pm 1$ and $\Delta m_S = \pm 2$ transitions.

To compute the numerical values of $\boldsymbol{G}$ components, we assume that the zero-field splitting effects for VV and NV are dominated by the magnetic dipole-dipole interaction, and we neglect the spin-orbit coupling effect. The magnetic dipole-dipole interaction between the two unpaired electrons in the defect ground state is given by

$$\mathcal{H}_{\mathrm{dd}} = \frac{\mu_0}{4\pi}(\gamma_{\mathrm{e}}\hbar)^2 \, \frac{r^2 \boldsymbol{s}_1 \cdot \boldsymbol{s}_2 - 3(\boldsymbol{s}_1 \cdot \boldsymbol{r})(\boldsymbol{s}_2 \cdot \boldsymbol{r})}{r^5} \tag{6.15}$$

where μ_0 is the vacuum magnetic permeability, γ_e is the electron gyromagnetic ratio, $\hbar$ is the reduced Planck constant, $\boldsymbol{s}_1$ and $\boldsymbol{s}_2$ are spin-1/2 operators for the two unpaired electrons, $\boldsymbol{r}$ and r are the relative coordinate between two electrons and its norm. The $\boldsymbol{D}$ tensor is computed as the expectation value of the dipole-dipole interaction on the ground state from Kohn-Sham DFT calculations

$$D_{ab} = \frac{1}{2}\frac{1}{S(2S-1)}\frac{\mu_0}{4\pi}(\gamma_e\hbar)^2 \sum_{i\leq j}^{\text{occ.}} \chi_{ij} \langle\Psi_{ij}| \frac{r^2\delta_{ab} - 3r_a r_b}{r^5} |\Psi_{ij}\rangle \tag{6.16}$$

where S is the effective electron spin ($S = 1$ for triplet defects like VV or NV). The summation runs over all pairs of occupied Kohn-Sham orbitals, and $\chi_{ij} = \pm 1$ for parallel and anti-parallel electrons respectively. Ψ_{ij}'s are 2×2 Slater determinants of occupied Kohn-Sham orbitals, and expectation values of dipole-dipole interaction are evaluated following the recipe in Ref [298].

We performed DFT calculations for (hh, kk)-VV in 4H-SiC and NV in diamond with the PBE exchange-correlation functional[279]. The Projector Augmented Wave (PAW) method[34] with datasets compiled in the PSL1.0 library[64] are used to represent electron-ion interactions. When evaluating the expectation values in Eq. 6.16, we used normalized pseudo-wavefunctions[162][86][335]. We used 55 Ry kinetic energy cutoff and Γ-point sampling of the Brillioun zone. Structures are relaxed until forces on atoms are smaller than 5×10^{-4} eV $\cdot$ Å^{-1}. All DFT calculations are performed with the Quantum ESPRESSO code[106].

To simulate isolated defects, we create defects in large supercells built by periodic replication of hexagonal unit cells of 4H-SiC or diamond. The following figure shows the convergence of D value with respect to supercell size: For all results reported in the following, $7 \times 2 \times 2$ supercells are adopted, which contain 782 and 588 atoms for pristine 4H-SiC and diamond, respectively.

With the computational formalism described above, the D values obtained for (hh, kk)-

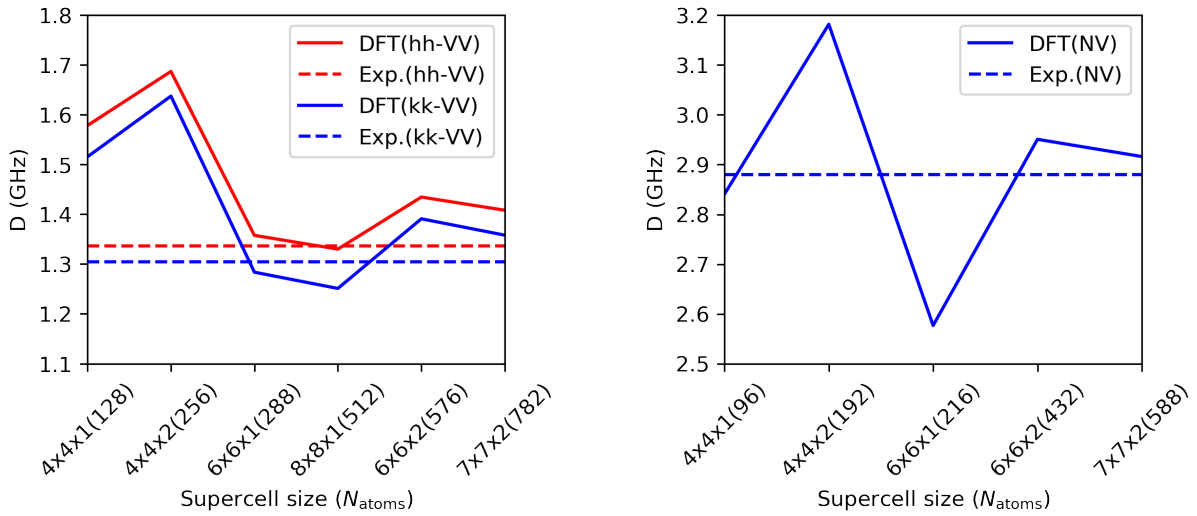

Figure 6.27: D value $(\frac{1}{2}(D_{xx}+D_{yy})-D_{zz})$ for VV in 4H-SiC (left) and NV in diamond (right) as functions of supercell sizes. Calculations are done without strain and thus all defects have C_{3v} symmetry. E values $(\frac{1}{2}(D_{xx}-D_{yy}))$ are smaller than 2 MHz for all calculations.

VV in 4H-SiC and NV in diamond agree very well with experimental results[166][85].

Table 6.9: D values for (hh, kk)-VV in 4H-SiC and NV in diamond (GHz).

	This work (DFT)	Ref (Exp.)[166][85]
hh-VV	1.41	1.34
kk-VV	1.36	1.31
NV	2.92	2.88

To compute spin-strain coupling tensor $\boldsymbol{G}$, $\boldsymbol{D}$ tensor is computed for defects in strained lattices with 0.0%, ± 0.25%, ± 0.5%, ± 0.75%, ± 1.0% amount of strain in each direction (xx, yy, zz, yz, xz, xy). Then a linear fitting for each $\boldsymbol{D}$ component and strain component is performed to extract the corresponding $\boldsymbol{G}$ component. Due to numerical noises, $\boldsymbol{G}$ tensors predicted by DFT do not exactly obey the symmetric form in Eq. 6.14. We symmetrized $\boldsymbol{G}$ tensors by projecting them onto the A_1 irreducible representation of the C_{3v} group. Table 6.10 presents the 6 independent components of symmetrized $\boldsymbol{G}$ tensors. For all values reported, the standard deviation of linear fitting are smaller than 0.1 GHz/strain.

To validate the computational protocol, we compared the results for the NV center in diamond with the work by Udvarhelyi *et al.* [375] and Barson *et al.* [23]. Udvarhelyi *et al.*

Table 6.10: Independent components of spin-strain coupling tensors for hh(kk)-VV in 4H-SiC and NV in diamond (GHz/strain).

	hh-VV	kk-VV	NV
G_{11}	-3.99	-3.35	-4.63
G_{12}	-0.42	-0.93	-1.67
G_{13}	1.74	1.26	1.23
G_{14}	0.34	1.93	-4.68
G_{41}	0.30	-0.10	0.48
G_{44}	0.46	0.47	0.80

computed the spin-strain and spin-stress coupling coefficients of NV centers by DFT. Barson *et al.* measured the coupling strength between spin and stress for NV centers in a diamond nanomechanical structure. To make direct comparison, we converted the 6 spin-strain coupling coefficients for NV centers in Table 6.10 into the 6 spin-stress coupling coefficients a_1, a_2, b, c, d, e as defined in their work [375][23]. In the conversion we used the compliance tensor of diamond in Ref [177]. Table 6.11 shows the comparison of spin-stress coupling coefficients from different works. Note that Ref [23] used a different sign convention for strain, and therefore their results are multiplied by a negative sign in the table.

Table 6.11: Spin-stress coupling coefficients for NV in diamond (MHz/GPa).

	This work (DFT)	Ref (DFT)[375]	Ref (Exp.)[23]
a_1	-3.82	-2.65	-4.4
a_2	3.80	2.52	3.7
b	1.80	1.94	2.3
c	-2.77	-2.84	-3.5
d	-0.23	-0.12	
e	0.60	0.67	

From Table 6.11 we find that our results match well with both references. The agreement is a validation for the computational setup we used for the calculations of $\boldsymbol{G}$.

Finally, we remark that the response of $\boldsymbol{D}$ to strain (2nd rank tensor) is different from its response to applied electric field (1st rank tensor). Similar to spin-strain coupling tensor,

we can define tensor $\boldsymbol{F}$ as the coupling between $\boldsymbol{D}$ and the electric field

$$F_{abc} = \frac{\partial D_{ab}}{\partial E_c}\,. \tag{6.17}$$

In Voigt notation, the response of $\boldsymbol{D}$ to an applied electric field $\boldsymbol{E}$ is given by

$$\begin{pmatrix} \Delta D_{xx} \\ \Delta D_{yy} \\ \Delta D_{zz} \\ \Delta D_{yz} \\ \Delta D_{xz} \\ \Delta D_{xy} \end{pmatrix} = \begin{pmatrix} F_{11} & F_{12} & F_{13} \\ F_{21} & F_{22} & F_{23} \\ F_{31} & F_{32} & F_{33} \\ F_{41} & F_{42} & F_{43} \\ F_{51} & F_{52} & F_{53} \\ F_{61} & F_{62} & F_{63} \end{pmatrix} \begin{pmatrix} E_x \\ E_y \\ E_z \end{pmatrix} = \begin{pmatrix} & F_{12} & F_{13} \\ & -F_{12} & F_{13} \\ & & -2F_{13} \\ & F_{42} & \\ F_{42} & & \\ F_{12} & & \end{pmatrix} \begin{pmatrix} E_x \\ E_y \\ E_z \end{pmatrix} \tag{6.18}$$

where C_{3v} symmetry was considered in the last equality. Combining the above equation with Eq. 6.11b, one can see that an applied electric field can drive $\Delta m_s = \pm 1$ and $\Delta m_s = \pm 2$ transitions, similar to the case of applying a strain. However, an electric field and a strain enters the Hamiltonian by different response tensors with different dimensions. $\boldsymbol{F}$ is 6×3 matrix while $\boldsymbol{G}$ is 6×6 matrix in Voigt notation. For C_{3v} defects, $\boldsymbol{F}$ has only 3 independent components while $\boldsymbol{G}$ has 6 independent components; $\boldsymbol{F}$ also has completely different symmetric form as $\boldsymbol{G}$ even if only the first 3 columns of $\boldsymbol{G}$ (corresponding to normal strains ε_{xx}, ε_{yy}, ε_{zz}) are considered.

6.3.4 Conclusions

In summary, we established a Gaussian surface acoustic wave platform for ground state spin control and imaged the phononic modes using a novel nanoscale X-ray imaging technique. Local defect symmetries are critical to understanding spin-phonon interactions in a general model of anisotropic lattice perturbations that we developed based on *ab initio* calculations. Surprisingly, shear and uniaxial strain couple to the ground state spin with equivalent

magnitudes and different relative phases depending on the strain tensor component. This property could be used to engineer material and device designs that capitalize on mechanical interactions. Since a complete model of spin-strain coupling with C_{3v} symmetry requires six independent coupling parameters, strain cannot necessarily be treated as an equivalent electric field vector. Even so, the zero-field splitting tensor is also affected by electric fields with three independent coupling parameters and can be used for both $\Delta m_s = \pm 1$ and $\Delta m_s = \pm 2$ spin transitions. In order to further enhance defect-phonon interaction strengths for hybrid quantum systems, defect excited state electronic orbitals [210, 54] and spins [225] could be utilized as opposed to ground state spins [23], and strain effects on defect hyperfine couplings have not been well explored. In addition, new defects [13] with greater spin-spin or spin-orbit coupling, with minimal cost to their spin coherence, may greatly improve spin-phonon coupling strengths and be advantageous for quantum control of phonons with optically addressable spins. Our combined theoretical understanding and demonstrations of spin-strain coupling with SiC divacancies provide a basis for quantum sensing with MEMS [374] as well as engineering strong interactions with single phonons for quantum transduction [201], spin squeezing [30], and phonon cooling [178] applications.

6.4 Quantum dynamics simulation of spin-defects

Coherence time is one of the most important properties for spin-defects. Theoretical prediction of coherence times for spin-defects involves the solution of the central spin problem, where a central electron spin is embedded in an environment consisting of external fields and other spins (e.g. nuclear spins or electron spins from other paramagnetic defects). This section discusses the simulation of the central spin problem using the cluster correlation expansion (CCE) method [411, 334, 413].

For a system consisting of a central electron spin with spin-1 and bath nuclear spins in external magnetic field, the Hamiltonian is given by

$$H = H_{\mathrm{e}} + H_{\mathrm{b}} + H_{\mathrm{eb}} \tag{6.19}$$

where H_{e}, H_{b} and H_{eb} denotes the electron Hamiltonian, bath Hamiltonian and the coupling between electron and bath

$$H_{\mathrm{e}} = -\gamma_e \boldsymbol{B} \cdot \boldsymbol{S} + \boldsymbol{S} \cdot \boldsymbol{D} \cdot \boldsymbol{S} \tag{6.20}$$

$$H_{\mathrm{b}} = -\sum_i \gamma_i \boldsymbol{B} \cdot \boldsymbol{I}_i + \sum_{i \neq j} \boldsymbol{I}_i \cdot \boldsymbol{P}_{ij} \cdot \boldsymbol{I}_j \tag{6.21}$$

$$H_{\mathrm{eb}} = \sum_i \boldsymbol{S} \cdot \boldsymbol{A} \cdot \boldsymbol{I}_i \tag{6.22}$$

where $\boldsymbol{B}$ is the external magnetic field; γ_e and γ_i are gyromagnetic ratios of the electron spin and the i-th nuclear spin, respectively; $\boldsymbol{S}$ and $\boldsymbol{I}_i$ denote electron and the i-th nuclear spin operators, respectively; $\boldsymbol{D}$ is the zero-field splitting tensor; $\mathbf{P}_{ij}$ is the magnetic dipole-dipole coupling tensor between bath spins i and j; $\mathbf{A}_i$ is the hyperfine coupling tensor that couples the electron spin with the i-th nuclear spin. The zero-field splitting and hyperfine coupling can be predicted through first-principles electronic structure calculations, as shown

in Chapter 5.

The quantum coherence of the central electron spin is characterized by the time evolution of the reduced density matrix of the electron spin governed by the Hamiltonian in Eq. 6.19. For pure dephasing processes, the diagonal elements of the reduced density matrix are unchanged during the time evolution, and the entire Hamiltonian in Eq. 6.19 can be decomposed into different components corresponding to different qubit states

$$H = \sum_{m_s} |m_s\rangle \langle m_s| \otimes H_{m_s} \tag{6.23}$$

where $|m_s\rangle$ denotes m_s spin state of the electron spin, H_{m_s} denotes the Hamiltonian acting on the bath spins when the electron spin is in $|m_s\rangle$ state. For instance, H_0 and H_1 governs the time evolution of bath spins when the electron spin is in $m_s = 0$ and $m_s = 1$ state, respectively.

The dephasing of electron spin is characterized by the decay of the coherence function $L(t)$, which is defined as

$$L(t) = \frac{\mathrm{Tr}\{\rho(t)S^+\}}{\mathrm{Tr}\{\rho(0)S^+\}} \tag{6.24}$$

where $\rho(t)$ denotes the reduced density matrix of the central electron spin.

If the qubit is prepared in initial state $\frac{1}{\sqrt{2}}(|0\rangle + |1\rangle)$, the coherence function can be expressed in terms of time evolution of bath spins under under H_0 and H_1

$$L(t) = \mathrm{Tr}\Big\{\rho_b U_0 U_1^\dagger\Big\} \tag{6.25}$$

where ρ_b is the density matrix for bath spins; U_0 and U_1 are propogators for bath spins under electron spin states $m_s = 0$ and $m_s = 1$, respectively. The exact form of U_0 and U_1 depends on the experimental setup for the measurement of coherence time. For free induction decay (T_2^* measurement),

$$U_0 = \exp\{-iH_0 t\} \tag{6.26}$$

$$U_1 = \exp\{-iH_1 t\} \tag{6.27}$$

For Hahn-Echo experiment (T_2 measurement),

$$U_0 = \exp\{-iH_0 t/2\} \exp\{-iH_1 t/2\} \tag{6.28}$$

$$U_1 = \exp\{-iH_1 t/2\} \exp\{-iH_0 t/2\} \tag{6.29}$$

Higher-order dynamical decoupling schemes correspond to more sophisticated forms of U_0 and U_1.

The exact calculation of $L(t)$ is computationally very demanding the number of bath spins is large. In the CCE method, the coherence function $L(t)$ is approximated as a product of cluster contributions

$$L(t) \approx \prod_C \tilde{L}_C(t) \tag{6.30}$$

where $\tilde{L}_C(t)$ is the irreducible contribution from cluster C. CCE calculations are normally performed up to a certain order, which defines the size of clusters considered for the evaluation of $L(t)$. For instance, a first-order CCE calculation considers only contributions from isolated nuclear spins; a second-order CCE calculation considers contributions from all clusters with up to 2 nuclear spins. The irreducible contribution $\tilde{L}_C(t)$ is defined recursively as

$$\tilde{L}_C(t) = \frac{L_C(t)}{\prod_{C'} \tilde{L}'_C(t)} \tag{6.31}$$

where $L_C(t)$ denotes the coherence function computed with only contributions from cluster C included; C' denotes clusters with sizes smaller than or equal to that of C.

Using the CCE method and its generalizations, we investigated the quantum coherence of divacancy electron spins in silicon carbide and predicted the coherence time of divacancy spins in the environment of nuclear spins and other paramagnetic defects [42, 272].

CHAPTER 7

CONCLUSION

In this dissertation, we presented research projects that fall within two interwoven themes: (1) the development of method and algorithms for quantum mechanical simulation of molecules and materials; (2) first-principles studies of the electronic structure and quantum dynamics of spin-defects in semiconductors for quantum information science.

In terms of method development, we first presented a finite-field approach to compute density response functions for molecules and materials. The approach is non-perturbative and can be used in a straightforward manner with both semilocal and orbital-dependent functionals. The finite-field approach allows us to explicitly compute the exchange-correlation kernel of a physical system and to perform GW and Bethe-Salpeter equation calculations beyond the random phase approximation. These developments enabled accurate and efficient many-body perturbation theory (MBPT) calculations of charged and neutral excitation energies of molecules and materials.

Based on the finite-field approach, we developed a quantum embedding theory for the study of strongly-correlated electronic states in condensed systems. The quantum embedding theory is capable of constructing effective models for a selected part of the physical system, with the environment acting as a dielectric screening media described at the density functional theory (DFT) level. The effective models can be solved by classical algorithms such as exact diagonalization, or by quantum algorithms such as variational quantum eigensolver. The quantum embedding theory presented here is a powerful tool to reduce a complex materials science problem into a simpler one, and is highly valuable for first-principles studies of strongly-correlated electronic states in condensed and molecular systems.

In addition to electronic properties, we presented a novel approach to compute certain spin properties (e.g. the hyperfine coupling) for paramagnetic systems. Calculations of spin properties such as hyperfine coupling require an accurate description of electronic wavefunction near nuclei, which is a challenging task for common basis sets such as plane waves

or Gaussian orbitals. We presented a novel approach to predict such spin properties from all-electron DFT calculations using finite element basis sets, and we demonstrated that the results can be systematically converged as a function of the basis set size. This development enabled robust all-electron calculations of spin properties for paramagnetic molecules and materials.

In terms of application, we presented a number of first-principles predictions for spin-defects in semiconductors, encompassing properties such as thermodynamics, excited states, spin-phonon coupling and quantum coherence. In particular, we applied DFT and MBPT to study the stability and excitation energies of several novel spin-defects in silicon carbide and aluminum nitride; we applied the quantum embedding theory to study the strongly-correlated excited states of group-4 vacancy centers in diamond; we applied DFT and group theory to construct a complete microscopic theory of spin-phonon coupling for divacancy spins in silicon carbide; we applied cluster correlation expansion method to simulate the quantum coherence dynamics of spin-defects in the environment of other electron spins and nuclear spins. These studies greatly expand our understanding of various physical properties of existing spin-defects as well as novel ones, and provided important guidance for the experimental realization and manipulation of these spin-defects as solid-state qubits.

The research presented in this dissertation heavily focused on solving real-world chemical and materials problems, which usually involve large, heterogeneous systems. For instance, an accurate description of spin-defects often requires a periodic cell including hundreds or even thousands of atoms. First-principles calculations of such systems require not only sophisticated theories but also robust and scalable software implementations that can harness the computational power of modern high-performance computing architectures. Theories and methods presented in this dissertation are implemented with a strong emphasis on efficiency and scalability, and are made available to the community through several open-source software (summarized in Appendix B).

Overall, this dissertation highlighted several advancements in quantum mechanical sim-

ulations of molecules and materials. It is my hope that the theories, algorithms and applications presented in this dissertation will benefit the greater chemistry and materials science community in large-scale, first-principles simulations of molecular and condensed systems.

APPENDIX A

PUBLICATIONS

List of publications:

1. **H. Ma**, M. Govoni, and G. Galli. Quantum simulations of materials on near-term quantum computers. *npj Computational Materials*. 6, 85 (2020).

2. **H. Ma**, N. Sheng, M. Govoni, and G. Galli. First-principles studies of strongly correlated states in defect spin qubits in diamond. *Physical Chemistry Chemical Physics*. Accepted (2020).

3. A. Bourassa, C. P. Anderson, K. C. Miao, M. Onizhuk, **H. Ma**, A. L. Crook, H. Abe, J. Ul-Hassan, T. Ohshima, N. T. Son, G. Galli, D. D. Awschalom. Entanglement and control of single quantum memories in isotopically engineered silicon carbide. *Nature Materials*. 10.1038/s41563-020-00802-6 (2020).

4. **H. Ma**, W. Wang, S. Kim, M. Cheng, M. Govoni, and G. Galli. PyCDFT: A Python package for constrained density functional theory. *Journal of Computational Chemistry*. 41, 1859–1867 (2020).

5. **H. Ma**, M. Govoni, and G. Galli. PyZFS: A Python package for first-principles calculations of zero-field splitting tensors. *Journal of Open Source Software*. 5(47), 2160 (2020).

6. S. J. Whiteley, G. Wolfowicz, C. P. Anderson, A. Bourassa, **H. Ma**, M. Ye, G. Koolstra, K. J. Satzinger, M. V. Holt, F. J. Heremans, A. N. Cleland, D. I. Schuster, G. Galli, and D. D. Awschalom. Spin-phonon interactions in silicon carbide addressed by Gaussian acoustics. *Nature Physics*. 10.1038/s41567-019-0420-0 (2019).

7. N. L. Nguyen, **H. Ma**, M. Govoni, F. Gygi, and G. Galli. A finite-field approach to solving the Bethe-Salpeter equation. *Physical Review Letters*. 122, 237402 (2019).

8. K. Ghosh, **H. Ma**, V. Gavini, and G. Galli. All-electron density functional calculations for electron and nuclear spin interactions in molecules and solids. *Physical Review Materials*. 3, 04380 (2019).

9. **H. Ma**, M. Govoni, F. Gygi, and G. Galli. A Finite-field approach for GW calculations beyond the random phase approximation. *Journal of Chemical Theory and Computations*. 15 (1), 154 (2019).

10. H. Seo, **H. Ma**, M. Govoni, and G. Galli. Designing defect-based qubit candidates in wide-gap binary semiconductors for solid-state quantum technologies. *Physical Review Materials*. 1, 075002 (2017).

APPENDIX B

SOFTWARE

List of software and contribution:

1. WEST code (west-code.org, contributor)
    - Finite-field algorithm
    - Quantum embedding theory
2. Qbox code (qboxcode.org, contributor)
    - DFT calculations under arbitrary finite electric field
3. PyZFS code (github.com/hema-ted/pyzfs, main developer)
4. PyCDFT code (github.com/hema-ted/pycdft, main developer)

Details of the `PyZFS` code and the `PyCDFT` code are discussed in Appendix B.1 and B.2, respectively.

B.1 PyZFS: A Python package for first-principles calculations of zero-field splitting tensors

This subsection presents `PyZFS`, a Python package for first-principles calculations of zero-field splitting tensors in plane-wave basis.

Reprinted from H. Ma, M. Govoni, and G. Galli. Journal of Open Source Software. 5(47), 2160 (2020). https://doi.org/10.21105/joss.02160

Electron spins in molecules and materials may be manipulated and used to store information, and hence they are interesting resources for quantum technologies. A way to understand the physical properties of electron spins is to probe their interactions with electromagnetic fields. Such interactions can be described by using a so-called spin Hamiltonian, with parameters derived from either experiments or calculations. For a single electron spin (e.g. associated to a point-defect in a semiconductor or insulator), the leading terms in the spin Hamiltonian are

$$H = \mu_B \mathbf{B} \cdot \mathbf{g} \cdot \mathbf{S} + \mathbf{S} \cdot \mathbf{D} \cdot \mathbf{S} \tag{B.1}$$

where μ_B is the Bohr magneton, $\mathbf{S}$ is the electron spin operator, $\mathbf{B}$ is an external magnetic field, $\mathbf{g}$ and $\mathbf{D}$ are rank-2 tensors that characterize the strength of the Zeeman interaction, and the zero-field splitting (ZFS), respectively. Experimentally, the spin Hamiltonian parameters $\mathbf{g}$ and $\mathbf{D}$ may be obtained by electron paramagnetic resonance (EPR). The ZFS tensor describes the lifting of degeneracy of spin sublevels in the absence of external magnetic fields, and is an important property of open-shell molecules and spin defects in semiconductors with spin quantum number $S \geq 1$. The ZFS tensor can be predicted from first-principles calculations, thus complementing experiments and providing valuable insight into the design of novel molecules and materials with desired spin properties. Furthermore, the comparison of computed and measured ZFS tensors may provide important information on the atomistic structure and charge state of defects in solids, thus helping to identify the defect configuration present in experimental samples. Therefore, the development of robust methods for the

calculation of the ZFS tensor is an interesting topic in molecular chemistry and materials science.

In this work we describe the code `PyZFS` for the calculation of the ZFS tensor **D** of molecules and solids, based on wave-functions obtained from density functional theory (DFT) calculations. For systems without heavy elements, i.e. where spin-orbit coupling is negligible, magnetic spin-spin interactions are the dominant ones in the determination of the ZFS tensor. For molecules and materials with magnetic permeability close to the vacuum permeability μ_0, the spin-spin ZFS tensor evaluated using the DFT Kohn-Sham wavefunctions, is given by:

$$D_{ab} = \frac{1}{2S(2S-1)} \frac{\mu_0}{4\pi} (\gamma_e \hbar)^2 \sum_{i<j}^{\text{occ.}} \chi_{ij} \langle \Phi_{ij} | \frac{r^2 \delta_{ab} - 3 r_a r_b}{r^5} | \Phi_{ij} \rangle \tag{B.2}$$

where $a, b = x, y, z$ are Cartesian indices; γ_e is the gyromagnetic ratio of electrons; the summation runs over all pairs of occupied Kohn-Sham orbitals; $\chi_{ij} = \pm 1$ for parallel and antiparallel spins, respectively; $\Phi_{ij}(\mathbf{r}, \mathbf{r'})$ are 2×2 determinants formed from Kohn-Sham orbitals ϕ_i and ϕ_j, $\Phi_{ij}(\mathbf{r}, \mathbf{r'}) = \frac{1}{\sqrt{2}} \Big[\phi_i(\mathbf{r}) \phi_j(\mathbf{r'}) - \phi_i(\mathbf{r'}) \phi_j(\mathbf{r}) \Big]$.

Several quantum chemistry codes (for example ORCA [257]) include the implementation of ZFS tensor calculations for molecules, where electronic wavefunctions are represented using Gaussian basis sets. However, few open-source codes are available to compute ZFS tensors using plane-wave basis sets, which are usually the basis sets of choice to study condensed systems. In `PyZFS` we implement the evaluation of spin-spin ZFS tensors using plane-wave basis sets. The double integration in real space is reduced to a single summation over reciprocal lattice vectors through the use of Fast Fourier Transforms [298].

We note that a large-scale DFT calculations can yield wavefunction files occupying tens of GB. Therefore, proper distribution and management of data is critical. In `PyZFS`, the summation over pairs of Kohn-Sham orbitals is distributed into a square grid of processors through the use of the Message Passing Interface (MPI), which significantly reduces the CPU time and memory cost per processor.

`PyZFS` can use wavefunctions generated by various plane-wave DFT codes as input. For

instance, it can directly read wavefunctions from Quantum Espresso [106] in the HDF5 format and from Qbox [124] in the XML format. The standard cube file format is also supported. `PyZFS` features a modular design and utilizes abstract classes for extensibility. Support for new wavefunction format may be easily implemented by defining subclasses of the relevant abstract class and overriding corresponding abstract methods.

Since its development, `PyZFS` has been adopted to predict ZFS tensors for spin defects in semiconductors, and facilitated the discovery of novel spin defects [335] and the study of spin-phonon interactions in solids [396]. `PyZFS` has also been adopted to generate benchmark data for the development of methods to compute the ZFS tensor using all electron calculations on finite element basis sets [105]. Thanks to the parallel design of the code, `PyZFS` can perform calculations for defects embedded in large supercells. For example, the calculations performed in [396] used supercells that contain more than 3000 valence electrons, and are among the largest first-principles calculations of ZFS tensors reported so far.

B.2 PyCDFT: A Python package for constrained density functional theory

Reprinted with permission from H. Ma, W. Wang, S. Kim, M. Cheng, M. Govoni, and G. Galli. Journal of Computational Chemistry. 41, 1859–1867 (2020). https://doi.org/10.1002/jcc.26354

This subsection presents `PyCDFT`, a Python package to compute diabatic states using constrained density functional theory (CDFT). `PyCDFT` provides an object-oriented, customizable implementation of CDFT, and allows for both single-point self-consistent-field calculations and geometry optimizations. `PyCDFT` is designed to interface with existing density functional theory (DFT) codes to perform CDFT calculations where constraint potentials are added to the Kohn-Sham Hamiltonian. Here we demonstrate the use of `PyCDFT` by performing calculations with a massively parallel first-principles molecular dynamics code, `Qbox`, and we benchmark its accuracy by computing the electronic coupling between diabatic states for a set of organic molecules. We show that `PyCDFT` yields results in agreement with existing implementations and is a robust and flexible package for performing CDFT calculations.

B.2.1 Introduction

The transfer of electronic charges plays a central role in many physical and chemical processes [241], such as those for cellular activity in biological processes [36] and catalytic activity in condensed phases [259]. In addition, the rate of charge transfer in a material directly impacts its carrier mobility and hence its use in e.g., electronic devices [167, 168].

Theoretical and computational modeling provides invaluable insights into the microscopic mechanism of charge transfer, and is playing an important role in the development of novel drugs, catalysts, and electronic materials. In the past few decades, many research efforts have been dedicated to the development of robust theoretical methods

and simulation strategies to describe charge transfer processes in molecules and materials [149, 169, 418, 107, 408, 326, 265]. Charge transfer can take place through a wide spectrum of mechanisms, with two important regimes being the band-like regime (where transport occurs through delocalized electronic states) and the hopping regime (where transport occurs through localized electronic states) [341, 24]. Here we focus on the hopping transfer, which is the dominant charge transfer mechanism in many organic crystals and conducting polymers, and in several metal oxides in the solid state, as well as in many nanoparticle solids [206, 364, 123, 415].

The classic theory of charge transfer in the hopping regime is Marcus theory [229, 230], which has seen many generalizations through the years [207, 417, 213, 254]. For a charge transfer between two sites A and B (e.g., a donor-acceptor pair consisting of two molecules or two fragments of the same molecular unit), Marcus theory predicts the charge transfer rate to be

$$k = \frac{2\pi}{\hbar}|H_{ab}|^2\sqrt{\frac{1}{4k_BT\pi\lambda}}\exp\left[-\frac{(\Delta G+\lambda)^2}{4\lambda k_BT}\right], \tag{B.3}$$

where the diabatic electronic coupling H_{ab} between A and B is one of the central quantities that determines transfer rates; k_B and T are the Boltzmann constant and temperature; ΔG is the free energy difference between states A and B, and λ is the reorganization energy. As shown in Fig. B.1, within Marcus theory the charge transfer process can be described using the free energy surfaces of two *diabatic states* as functions of a chosen reaction coordinate. Diabatic states are defined as a set of states among which the nonadiabatic derivative couplings vanish. Diabatic states have the property that their physical characters (such as charge localization) do not change along the reaction coordinate. For instance, the two diabatic states (Ψ_a/Ψ_b) involved in the charge transfer depicted in Fig. B.1 are constructed to have the charge localized on site A/B, and this charge localization character does not change as the reaction occurs.

In contrast to *adiabatic* states, which are the eigenstates of the electronic Hamiltonian within the Born-Oppenheimer approximation, *diabatic* states are *not* eigenstates of the elec-

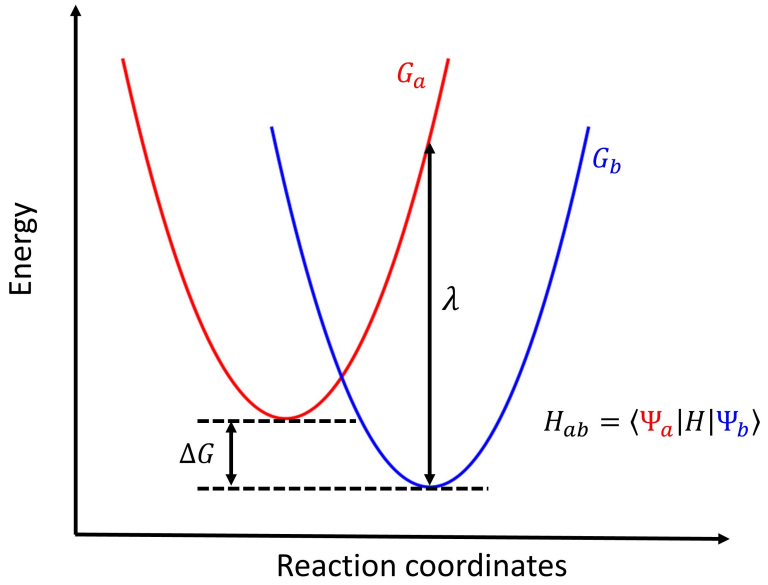

Figure B.1: Free energy curves for two diabatic states Ψ_a and Ψ_b with free energy G_a and G_b associated to a reaction where a charge (electron or hole) is transferred from site A to site B. The charge is localized on site A for Ψ_a and site B for Ψ_b, and the charge localization characters of Ψ_a and Ψ_b do not change as the reaction occurs. The charge transfer rate can be written as a function of the free energy difference ΔG, reorganization energy λ, and electronic coupling H_{ab}.

tronic Hamiltonian of the whole system, and therefore are not directly accessible from standard electronic structure calculations. Constrained density functional theory (CDFT) provides a powerful and robust framework for constructing diabatic states from first principles and predicting their electronic coupling [172, 110], including instances where hybrid functionals may fail to produce a localized state [246] and where time-dependent DFT may fail to produce the correct spatial decay of the electronic coupling [80]. In CDFT, additional constraint potentials are added to the Kohn-Sham Hamiltonian, and their strengths are optimized so as to obtain a desired localized charge on a given site. To obtain the electronic coupling H_{ab}, one first performs two separate CDFT calculations in which one localizes the charge on the initial and final sites. Then, one constructs the electronic Hamiltonian matrix on the basis composed of the two diabatic states, and finally the H_{ab} is given by the off-diagonal elements of the Hamiltonian matrix.

A CDFT formulation was originally proposed by Dederichs in 1984 [70] to study excita-

tions of Ce impurities in metals. Wu, van Voorhis and co-workers established the modern formulation of CDFT in the mid-2000s [405, 404]. Since then it has been implemented in several DFT codes using localized basis sets, such as SIESTA [354], NWChem [404], Q-CHEM [402] and ADF [367].

Implementations of CDFT using plane-wave basis sets appeared more recently, for instance in CPMD [262, 263], VASP [221] and CP2K (dual basis) [155]. These plane-wave implementations enabled CDFT calculations for condensed systems, and facilitated the study of important problems such as redox couples in aqueous solution [38, 262, 262], charge transfer in biological molecules and proteins [264], in quantum dots [44] and doped nanoparticles [383], electron tunneling between defects [37] and polaron transport [336, 388] in oxides, molecular solids [264], and organic photovoltaic polymers [111] (see Ref. 172 and Ref. 36 for extensive reviews). In existing implementations, DFT and CDFT are developed and maintained in the same code, thus requiring direct modifications of core DFT routines to support CDFT functionalities.

In recent years, an emerging trend in scientific simulation software is the development of light-weight code, with focus on specific tasks, which can be interfaced with other codes to perform complex tasks. This strategy is well aligned with the modular programming coding practice, which enables maintainability, re-usability, and simplicity of codes. Compared to conventional strategies integrating a wide range of functionalities into one single code, this design strategy decouples the development cycle of different functionalities and leads to interoperable codes that are easier to modify and maintain, facilitating rapid developments and release of new features. Some notable codes for chemical and materials simulations that have adopted this strategy include Qbox [124], WEST [117, 220], and SSAGES [342, 337].

In this work we present `PyCDFT`, a Python package that performs single-point self-consistent-field (SCF) and geometry optimization calculations using CDFT. `PyCDFT` can be interfaced with existing DFT codes to perform DFT calculations with constraint potentials. Compared to existing implementations of CDFT, the novelty of the `PyCDFT` code is twofold:

- `PyCDFT` is a light-weight, interoperable code. The operations specific to CDFT calculations are decoupled from those carried out by existing DFT codes (DFT engines). Communications between `PyCDFT` and the DFT engine are handled by client-server interfaces (see Sec. B.2.3). Hence, the development of `PyCDFT` and of the DFT engine may occur independently. This is advantageous for maintainability and reusability, and `PyCDFT` may be interfaced with multiple DFT engines.

- `PyCDFT` features an object-oriented design that is user-friendly and extensible. Extra functionalities can be easily added to `PyCDFT` thanks to the extensive use of abstract classes. Furthermore, `PyCDFT` supports being used within Jupyter notebooks or Python terminals, thus allowing users to perform and analyze CDFT calculations in a flexible and interactive manner.

We note that Python has become increasingly popular as a high-level programming language for scientific computing due to its ease of use and wide applicability. The development of `PyCDFT` echos this trend and contributes to the rapidly expanding open-source Python ecosystem for the molecular and materials science fields, where some widely-used packages include Atomic Simulation Environment (`ASE`) [145], `pymatgen` [270], and `PySCF` [360].

To demonstrate the use of `PyCDFT`, we coupled it with the massively parallel first-principles molecular dynamics code `Qbox` [124], which features efficient DFT calculations using plane-wave basis sets and pseudopotentials. We computed diabatic electronic coupling for a set of organic molecules in the HAB18 data set [199, 198] and compared our results with those of existing implementations. The results obtained with `PyCDFT`(Qbox) are in good agreement with those of other plane-wave implementations of CDFT, thus verifying the correctness and robustness of `PyCDFT`.

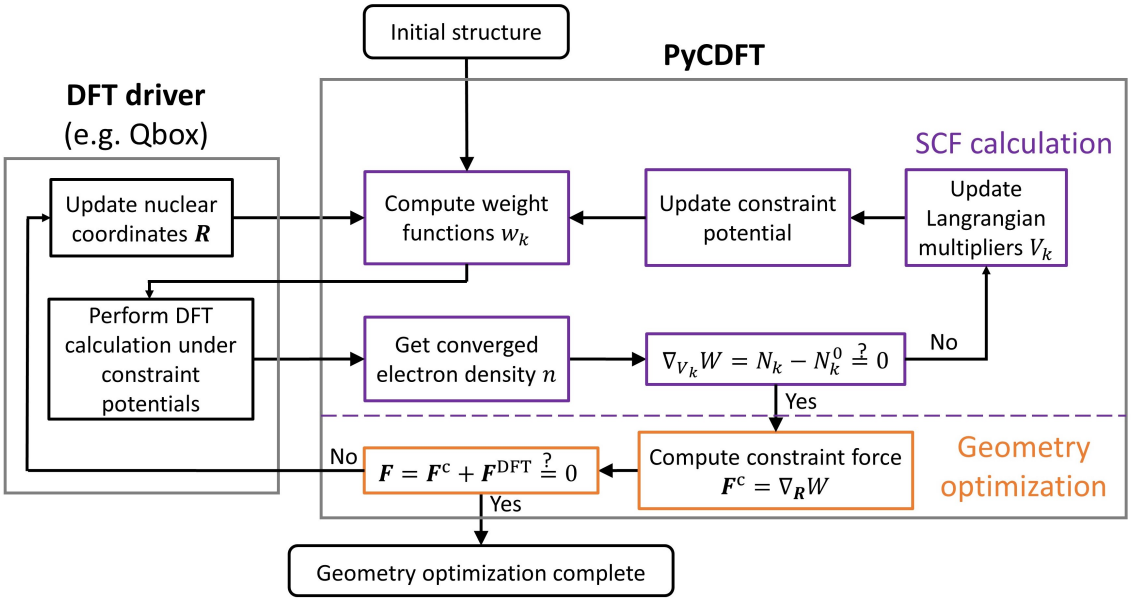

Figure B.2: Workflow for self-consistent-field (SCF) and geometry optimization calculations performed by `PyCDFT`. In SCF calculations, the free energy functional W is minimized with respect to the electron density n (equivalent to a standard DFT calculation under constraint potentials) and maximized with respect to Lagrange multipliers V_k. For geometry optimization calculations, W is further minimized with respect to nuclear coordinates $\mathbf{R}$. `PyCDFT` is designed to implement CDFT-specific algorithms and to be interfaced with external DFT codes (drivers).

B.2.2 Computational methodology

Constrained Density Functional Theory

We briefly outline the CDFT methodology adopted here and we refer the reader to Refs. 172, 263, 403, 404, 246 for further details. The core of the CDFT method is the iterative calculation of the stationary point of a free energy functional W defined as

$$W[n, V_k] = E[n] + \sum_k V_k \left(\int w_k(\mathbf{r}) n(\mathbf{r}) d\mathbf{r} - N_k^0 \right), \tag{B.4}$$

where n is the electron density; $E[n]$ is the DFT total energy functional; the second term on the right-hand side of Eq. B.4 represents the sum of constraint potentials applied to the system to ensure that the desired number of electrons N_k^0 is localized on given parts of the

system (e.g., chosen atomic site, molecule, or structural fragment). More than one constraint can be applied to the system, if needed. The strength of the k^{th} constraint potential is controlled by the scalar Lagrange multiplier V_k, and its shape is determined by a weight function $w_k(\mathbf{r})$. CDFT calculations are performed by self-consistently minimizing W with respect to n and maximizing W with respect to V_k. The minimization of W with respect to n is equivalent to performing a DFT calculation with additional constraint potentials $\sum_k V_k w_k(\mathbf{r})$ added to the Kohn-Sham Hamiltonian. Upon convergence of the SCF cycle, the number of electrons localized on a given site $N_k = \int d\mathbf{r}\, w_k(\mathbf{r}) n(\mathbf{r})$ is equal to the desired value N_k^0. In geometry optimization calculations, the free energy W is further minimized with respect to nuclear coordinates, as shown in the outermost cycle in Fig. B.2.

Calculation of weight functions

The weight function allows one to partition the total electron density into contributions from different fragments of the whole system. Several different partitioning schemes have been proposed, such as Mulliken [253], Becke [27], and Hirshfeld partitioning [144]. In `PyCDFT` we implemented the Hirshfeld partitioning, which is widely used in plane-wave implementations of CDFT [199, 198, 110]. The Hirshfeld weight function w is defined as the ratio between the pseudoatomic densities belonging to a given site and the total pseudoatomic density

$$w(\boldsymbol{r}) = \frac{\sum_{I \in F} \rho_I(\mathbf{r} - \mathbf{R}_I)}{\sum_I \rho_I(\mathbf{r} - \mathbf{R}_I)}, \tag{B.5}$$

where I denotes atoms and $I \in F$ denotes atoms belonging to a fragment F to which the constraint is applied; $\mathbf{R}_I$ is the coordinate of atom I; ρ_I denotes the electron density of the *isolated* I-th atom and should not be confused with the electron density n of the whole system.

Alternatively, to enforce constraints on the electron number difference between a donor

site D and an acceptor site A, one can define the weight function as:

$$w(\mathbf{r}) = \frac{\sum_{I \in D} \rho_I(\mathbf{r} - \mathbf{R}_I) - \sum_{I \in A} \rho_I(\mathbf{r} - \mathbf{R}_I)}{\sum_I \rho_I(\mathbf{r} - \mathbf{R}_I)}. \tag{B.6}$$

Both definitions of Hirshfeld weights are implemented in `PyCDFT`. For charge transfer processes where the whole system consists of only two fragments (donor and acceptor), the above two definitions of Hirshfeld weights are equivalent. For more complex processes where multiple parts of the system are involved, one can use a combination of the two definitions to enforce complex charge constraints.

In Eqs. B.5 and Eq. B.6, the real-space electron density of an atom located at R_I is computed as:

$$\rho_I(\mathbf{r} - \mathbf{R}_I) = 4\pi \mathcal{F}^{-1} \left[e^{-i\mathbf{G}\cdot\mathbf{R}_I} \int_0^\infty \rho_I(r) \frac{r \sin(Gr)}{G} dr \right], \tag{B.7}$$

where $\mathcal{F}^{-1}$ denotes an inverse Fourier transform; $\mathbf{G}$ is a reciprocal lattice vector with norm G; $\rho_I(r)$ is the radial electron density of atom I. For a given atomic species, $\rho_I(r)$ can be easily obtained by performing DFT calculations for isolated atoms. `PyCDFT` is distributed with pre-computed spherically-averaged electron densities obtained with the SG15 pseudopotentials [129, 324] for all species in the periodic table before bismuth (excluding the lanthanides).

Calculation of Forces

In order to perform geometry optimizations or molecular dynamics simulations on a diabatic potential energy surface, the force on each nucleus due to the applied constraints must be evaluated. Forces on the diabatic potential energy surface are the sum of the DFT forces F^{DFT} and the constraint force F^{c} arising from the derivative of the constraint potential with respect to nuclear coordinates.

For a system subject to constraints, the α component ($\alpha \in \{x, y, z\}$) of the constraint force F^{c} on the I^{th} atom is given by:

$$
\begin{aligned}
F^{\mathrm{c}}_{I\alpha} &= -\sum_k V_k \int d\mathbf{r}\, \rho(\mathbf{r}) \frac{\partial w_k(\mathbf{r})}{\partial R_{I\alpha}} \\
&= -\sum_k V_k \int d\mathbf{r}\, \rho(\mathbf{r}) \frac{\delta - w_k(\mathbf{r})}{\sum_J \rho_J(\mathbf{r}-\mathbf{R}_J)} \frac{\partial \rho_I(\mathbf{r}-\mathbf{R}_I)}{\partial R_{I\alpha}},
\end{aligned}
\tag{B.8}
$$

where $\delta = \delta_{I\in F}$ for constraints on absolute electron numbers (Eq. B.5) and $\delta = \delta_{I\in D} - \delta_{I\in A}$ for constraints on electron number differences (Eq. B.6). The term $\frac{\partial \rho_I(\mathbf{r}-\mathbf{R}_I)}{\partial R_{I\alpha}}$ is evaluated as:

$$
\frac{\partial \rho_I(\mathbf{r}-\mathbf{R}_I)}{\partial R_{I\alpha}} = \mathcal{F}^{-1}\left\{-iG_\alpha e^{-i\mathbf{G}\cdot\mathbf{R}_I}\mathcal{F}\left[\rho_I(\mathbf{r})\right]\right\}, \tag{B.9}
$$

where $\mathcal{F}$ and $\mathcal{F}^{-1}$ denote forward and backward Fourier transforms, respectively.

Diabatic electronic coupling

To compute the electronic coupling H_{ab}[405], we consider the Hamiltonian matrix on the diabatic basis composed of two diabatic states Ψ_a and Ψ_b, each obtained from a converged CDFT calculation with `PyCDFT`. Here we consider the case of a single constraint. Denoting the value of the Lagrange multiplier for the two CDFT calculations as V_a and V_b, respectively, the Hamiltonian on the diabatic basis is:

$$
\mathbf{H} = \begin{pmatrix} H_{aa} & H_{ab} \\ H_{ba} & H_{bb} \end{pmatrix}, \tag{B.10}
$$

where the diagonal elements H_{aa} and H_{bb} correspond to the DFT total energies of diabatic states Ψ_a and Ψ_b, respectively. Then, denoting the overlap matrix $\mathbf{S}$ between the two diabatic states as

$$
\mathbf{S} = \begin{pmatrix} 1 & S_{ab} \\ S_{ba} & 1 \end{pmatrix}, \tag{B.11}
$$

where $S_{ab} = \langle \Psi_a | \Psi_b \rangle$ and $S_{ab} = S_{ba}^*$, the off-diagonal Hamiltonian elements can be written as [263]:

$$H_{ab} = F_b S_{ab} - V_b W_{ab} \tag{B.12}$$

$$H_{ba} = F_a S_{ba} - V_a W_{ba} \tag{B.13}$$

where F_a and F_b are the CDFT total energies including the contribution of constraint potentials; the weight function matrix elements $W_{ab} = W_{ba}^*$ are given by $W_{ab} = \langle \Psi_a | w(\mathbf{r}) | \Psi_b \rangle$.

After $\mathbf{H}$ is evaluated in the diabatic basis, we follow Ref. 263 and average the off-diagonal elements of $\mathbf{H}$ to ensure its Hermiticity. Finally, we perform a Löwdin orthogonalization [217] for $\mathbf{H}$ using the overlap matrix $\mathbf{S}$

$$\tilde{\mathbf{H}} = \mathbf{S}^{-1/2} \mathbf{H} \mathbf{S}^{-1/2} \tag{B.14}$$

and the off-diagonal matrix element of $\tilde{\mathbf{H}}$ corresponds to the electronic coupling H_{ab}.

B.2.3 Software

Implementation

`PyCDFT` features an object-oriented design and extensive use of abstract classes and abstract methods to facilitate future extensions of functionalities. Here we list the major classes defined in the `PyCDFT` package.

- `Sample`: a container class to organize relevant information about the physical system. A `Sample` instance is constructed by specifying the positions of the atoms within the periodic cell. The `Sample` class utilizes the `ASE` [145] package to parse atomic structures from geometry files (e.g., `cif` files).

- `Fragment`: a container class to represent a part of the whole system to which constraints are applied. A `Fragment` instance is constructed by specifying a list of atoms belonging

to the fragment.

- `Constraint`: an abstract class representing a constraint applied to the system. A `Constraint` instance keeps track of physical quantities relevant to the constraint, such as N_k^0, N_k, V_k, and $w_k(\mathbf{r})$ (see Eq. B.4). Except for the parameter N_k^0, which is defined upon the construction of the instance, other quantities are updated self-consistently as the CDFT calculation proceeds. Currently, two types of constraints based on Hirshfeld partitioning are implemented: `ChargeConstraint` (Eq. B.5) and `ChargeTransferConstraint` (Eq. B.6).

- `DFTDriver`: an abstract class that controls how `PyCDFT` interacts with an external DFT code. It specifies how `PyCDFT` communicates the constraint potentials and constraint forces to the DFT code and how to fetch the charge densities and other relevant quantities from the DFT code. Currently, a subclass `QboxDriver` is implemented, which allows `PyCDFT` to interact with the `Qbox` code. The implementation of the `QboxDriver` class leverages the client-server interface of `Qbox`, which allows `Qbox` to interactively respond to commands provided by a user or an external code [220, 261] (`PyCDFT` in this case).

- `CDFTSolver`: the core class of `PyCDFT` that executes a CDFT calculations. `CDFTSolver` provides a `solve` method, which is used to perform a CDFT self-consistent or geometry optimization calculation. Optimization of the Lagrange multipliers is performed within the `solve` method, which utilizes the `scipy` package.

In addition to the above classes, `PyCDFT` contains a `compute_elcoupling` function, which takes two `CDFTSolver` instances as input and computes the electronic coupling H_{ab} between two diabatic states (see Sec. B.2.2). To enable the calculation of electronic coupling, `PyCDFT` implements an auxiliary `Wavefunction` class that stores and manipulates the Kohn-Sham orbitals from CDFT calculations.

Extensibility

Thanks to the use of abstract classes, `PyCDFT` can be easily extended to provide new functionalities. For instance, support for additional weight functions (such as spin-dependent weight functions) can be easily implemented by defining subclasses of `Constraint` and overriding its abstract methods. Similarly, one can extend `PyCDFT` to support other DFT codes by overriding the abstract methods in the `DFTDriver` class. In addition to the C++ code `Qbox` used here, several Python implementations of DFT (e.g., `PySCF`) may be called as a DFT driver in an interactive manner; therefore they may be used as DFT drivers of `PyCDFT` once the corresponding `DFTDriver` subclass is implemented. Currently, the calculation of electronic coupling in PyCDFT is compatible with DFT drivers that use a plane-wave basis set. PyCDFT may be extended to be compatible with other types of basis sets.

`PyCDFT` may also be readily integrated with existing Python-based interfaces for generating, executing, and analyzing electronic structure calculations using software such as `ASE` [145] and `Atomate` [240].

Installation and usage

Installation of `PyCDFT` follows the standard procedure using the `setup.py` file included in the distribution. Currently, it depends on a few readily available Python packages including `ASE`, `scipy`, `pyFFTW`, and `lxml`.

In Fig. B.3 we present an example script that utilizes `PyCDFT` to compute the diabatic electronic coupling for the helium dimer He_2^+. This and other examples are included in the distribution of `PyCDFT`.

B.2.4 Verification

We now turn to the verification of our implementation of CDFT in `PyCDFT`, focusing on the calculation of electronic couplings. We compare results obtained with `PyCDFT`(Qbox),

```python
# An example input for computing electronic coupling of He2+ dimer

from pycdft import *
from ase.io import read

# Read atomic structure
cell = read("./He2.cif")

# Construct sample class, set FFT grid
sample = Sample(ase_cell=cell, n1=112, n2=112, n3=112)

# Set up the DFT driver, provide necessary commands to initialize
# the external DFT code (Qbox in this case)
qboxdriver = QboxDriver(
    sample=sample,
    init_cmd="load gs.xml\nset xc PBE\n"
    scf_cmd="run 0 50 5",
)

# Set up two CDFT solvers for two diabatic states
solver1 = CDFTSolver(
    job="scf",  # Indicate the calculation is an SCF calculation
    optimizer="brenth",  # Specify the optimizer used for the Lagrangian multiplier
    sample=sample,
    dft_driver=qboxdriver
)
solver2 = solver1.copy()

# Initialize two constraints that localize the extra +1 charge on each site
# Here we use ChargeTransferConstraint, which constrains the relative electron number
# between two Fragments that represent donor and acceptor
ChargeTransferConstraint(
    sample=solver1.sample,
    donor=Fragment(solver1.sample, solver1.sample.atoms[0:1]),  # Donor fragment
    acceptor=Fragment(solver1.sample, solver1.sample.atoms[1:2]),  # Acceptor fragment
    V_brak=(-1, 1),  # Search region for the brenth optimizer
    N0=1,  # Desired charge to be localized
)
ChargeTransferConstraint(
    sample=solver2.sample,
    donor=Fragment(solver2.sample, solver2.sample.atoms[0:1]),
    acceptor=Fragment(solver2.sample, solver2.sample.atoms[1:2]),
    V_brak=(-1, 1),
    N0=-1,
)

# Perform CDFT calculations
solver1.solve()
solver2.solve()

# Compute the electronic coupling between the two diabatic states obtained
compute_elcoupling(solver1, solver2)
```

Figure B.3: An example Python script to perform CDFT calculations for He_2^+. Two `CDFTSolver` instances are created for the calculation of two diabatic states with different charge localization, then the `compute_elcoupling` function is called to compute the electronic coupling H_{ab} between the two diabatic states.

CPMD [199, 198, 263]), CP2K, and the implementation of CDFT in Quantum Espresso [106] originally contributed by Goldey et al. [110]. We note that all codes utilized for this comparison use plane-wave basis sets, with the exception of CP2K, which uses a mixed

Gaussian and plane-wave basis set. As the values obtained for the electronic coupling have been shown to be sensitive to the choice of weight partitioning schemes [263], we compare with only results obtained with the Hirshfeld partitioning scheme.

Our results, `PyCDFT`(Qbox), are obtained by performing DFT calculations with the `Qbox` [124] code. We used optimized norm-conserving Vanderbilt pseudopotentials (ONCV) [129, 324], and an energy cutoff of 40 Ry for all molecules; we tested up to a 90 Ry energy cutoff and found changes of 1-2% in the electronic coupling compared to calculations using a 40 Ry cutoff. We used a convergence threshold of 5×10^{-5} for $|N - N_0|$. The electronic couplings were converged to within less than 0.5% with respect to cell size, in order to minimize interactions with periodic images. When using CP2K, we adopted the TZV2P basis set with GTH pseudopotentials [109]. Results obtained with Quantum Espresso (QE) and CPMD have been previously reported in Ref. 110 and Refs. 199, 198, respectively. In all cases the DFT electronic structure problem was solved using the generalized gradient approximation of Perdew, Burke, and Ernzerhof (PBE) [279].

We first discuss results for the electronic coupling of the He_2^+ dimer. Fig. B.4 compares the decay in H_{ab} with distance for hole transfer in the He-He^+ dimer obtained with `PyCDFT`(Qbox) and other codes. We find excellent agreement between our computed electronic couplings and those from Oberhofer and Blumberger [263] obtained using CPMD and the results of Goldey et al. [110] obtained using QE. As wavefunctions decay exponentially, the variation of the electronic coupling with separation may be expressed as $H \propto \exp(-\beta R/2)$, and we can compare the decay behaviors obtained here and in the literature by using the decay rate β, which is found to be 4.64, 4.98, 4.13 1/Å with `PyCDFT`(Qbox), CPMD, and Quantum Espresso (QE), respectively.

We now turn to bench-marking results for molecular dimers in the HAB18 dataset, which combines the HAB11 [199] and HAB7 [198] data sets, and consists of π-stacked organic homodimers. The molecules in the HAB11 data set contain members with different number of π-bonds and atomic species; the HAB7 dataset contains larger molecules. The combined

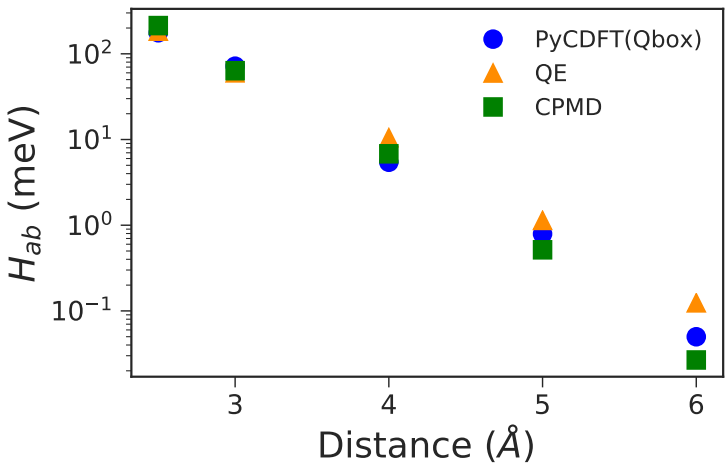

Figure B.4: Comparison of diabatic electronic coupling H_{ab} of the He-He+ dimer as a function of distance R, calculated with constrained density functional theory, and using PyCDFT interfaced with the Qbox code (`PyCDFT`(Qbox)), the implementation of CDFT in CPMD from Oberhofer and Blumberger [263], and the implementation in Quantum Espresso (QE) from Goldey et al [110]. In all implementations, the Hirshfeld partitioning [144] scheme is used. The calculated β decay rates are 4.64, 4.98, and 4.13 1/Å respectively.

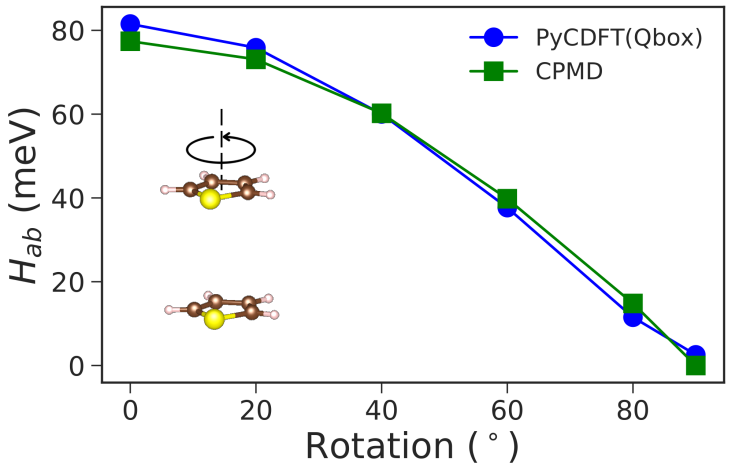

Figure B.5: Diabatic electronic coupling H_{ab} of the stacked thiophene dimer at a separation of 5 Å as a function of the relative rotation of the two units, calculated with constrained density functional theory as implemented in this work (`PyCDFT`(Qbox)) and in Kubas et al in CPMD [199]. Carbon atoms are shown in brown, sulfur in yellow, and hydrogen in beige.

HAB18 data set has been previously used for other implementations of CDFT [110]. The first molecule we consider here is one where imperfect π-stacking is present, due to one of the monomers being rotated relative to the other. Fig. B.5 compares our calculated electron

coupling for this configuration of the thiophene dimer with that of Kubas et al as implemented in CPMD [199]. We find excellent agreement between the two results, thus demonstrating the accuracy and robustness of `PyCDFT`(Qbox) for off-symmetry configurations.

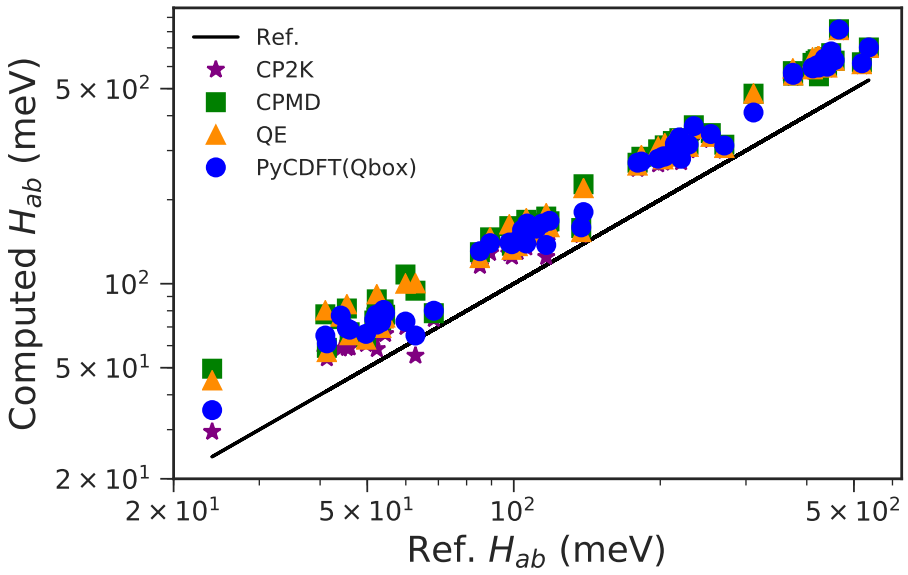

Figure B.6: Log-log plot of computed diabatic electronic couplings for molecular dimers in the HAB18 data set [199, 198] at various inter-molecular distances using `PyCDFT`(Qbox) (blue circles), CP2K (purple stars), CPMD (green squares), and Quantum Espresso (QE, yellow triangles). Reference values (black line) are based on multi-reference configuration interaction (MRCI+Q)[199] and single-determinant spin-component-scaled coupled cluster (SCS-CC2)[198] level of theory.

We compare our computed electronic couplings of molecular dimers in the HAB18 data set at varying intermolecular distances using `PyCDFT`(Qbox) with those obtained with CP2K, CPMD, and QE. These are plotted in Fig. B.6 on a log-log scale. In general, there is good agreement among the various codes. There is a systematic deviation of all DFT results from those based on multi-reference configuration interaction (MRCI+Q)[199] and single-determinant spin-component-scaled coupled cluster (SCS-CC2)[198] calculations. This systematic deviation arises from the well-known delocalization error of the semi-local functional used here (PBE) and from its shortcoming to properly describe long-range dispersion interactions. Using more accurate functionals would improve the accuracy of CDFT, as

previously reported in the literature [198]. Nevertheless, inspection of Fig. B.6 shows that PyCDFT(Qbox) generally yields electronic couplings and decay constants within the range of values obtained from previous implementations. Finally, we emphasize that PyCDFT(Qbox) captures the physically relevant exponential decay of the electronic coupling with intermolecular distance.

B.2.5 Conclusions

In this work we presented PyCDFT, a Python module for performing calculations based on constrained density function theory (CDFT). PyCDFT allows for SCF and geometry optimization calculations of diabatic states, as well as calculations of diabatic electronic couplings. The implementation of CDFT in PyCDFT is flexible and modular, and enables ease of use, maintenance, and effective dissemination of the code. Using molecules from the HAB18 data set [199, 198] as benchmarks, we demonstrated that PyCDFT(Qbox) yields results in good agreement with those of existing CDFT implementations using plane-wave basis sets and pseudopotentials. As a robust implementation for CDFT calculations, PyCDFT is well-suited for first-principles studies of charge transfer processes.

REFERENCES

[1] A. Abragam and B. Bleaney. *Electron Paramagnetic Resonance of Transition Ions*. Oxford University Press, 2013.

[2] H. Abraham, I. Y. Akhalwaya, G. Aleksandrowicz, T. Alexander, G. Alexandrowics, E. Arbel, A. Asfaw, C. Azaustre, P. Barkoutsos, G. Barron, L. Bello, Y. Ben-Haim, D. Bevenius, L. S. Bishop, S. Bosch, D. Bucher, CZ, F. Cabrera, P. Calpin, L. Capelluto, J. Carballo, G. Carrascal, A. Chen, C.-F. Chen, R. Chen, J. M. Chow, C. Claus, C. Clauss, A. J. Cross, A. W. Cross, J. Cruz-Benito, Cryoris, C. Culver, A. D. Córcoles-Gonzales, S. Dague, M. Dartiailh, A. R. Davila, D. Ding, E. Dumitrescu, K. Dumon, I. Duran, P. Eendebak, D. Egger, M. Everitt, P. M. Fernández, A. Frisch, A. Fuhrer, I. GOULD, J. Gacon, Gadi, B. G. Gago, J. M. Gambetta, L. Garcia, S. Garion, Gawel-Kus, J. Gomez-Mosquera, S. de la Puente González, D. Greenberg, J. A. Gunnels, I. Haide, I. Hamamura, V. Havlicek, J. Hellmers, Ł. Herok, H. Horii, C. Howington, S. Hu, W. Hu, H. Imai, T. Imamichi, R. Iten, T. Itoko, A. Javadi-Abhari, Jessica, K. Johns, N. Kanazawa, A. Karazeev, P. Kassebaum, A. Kovyrshin, V. Krishnan, K. Krsulich, G. Kus, R. LaRose, R. Lambert, J. Latone, S. Lawrence, D. Liu, P. Liu, P. B. Z. Mac, Y. Maeng, A. Malyshev, J. Marecek, M. Marques, D. Mathews, A. Matsuo, D. T. McClure, C. McGarry, D. McKay, S. Meesala, A. Mezzacapo, R. Midha, Z. Minev, M. D. Mooring, R. Morales, N. Moran, P. Murali, J. Müggenburg, D. Nadlinger, G. Nannicini, P. Nation, Y. Naveh, Nick-Singstock, P. Niroula, H. Norlen, L. J. O'Riordan, P. Ollitrault, S. Oud, D. Padilha, H. Paik, S. Perriello, A. Phan, M. Pistoia, A. Pozas-iKerstjens, V. Prutyanov, J. Pérez, Quintiii, R. Raymond, R. M.-C. Redondo, M. Reuter, D. M. Rodríguez, M. Ryu, M. Sandberg, N. Sathaye, B. Schmitt, C. Schnabel, T. L. Scholten, E. Schoute, I. F. Sertage, N. Shammah, Y. Shi, A. Silva, Y. Siraichi, S. Sivarajah, J. A. Smolin, M. Soeken, D. Steenken, M. Stypulkoski, H. Takahashi, C. Taylor, P. Taylour, S. Thomas, M. Tillet, M. Tod, E. de la Torre, K. Trabing, M. Treinish, TrishaPe, W. Turner, Y. Vaknin, C. R. Valcarce, F. Varchon, D. Vogt-Lee, C. Vuillot, J. Weaver, R. Wieczorek, J. A. Wildstrom, R. Wille, E. Winston, J. J. Woehr, S. Woerner, R. Woo, C. J. Wood, R. Wood, S. Wood, J. Wootton, D. Yeralin, J. Yu, L. Zdanski, Zoufalc, anedumla, azulehner, bcamorrison, brandhsn, dennis-liu 1, drholmie, elfrocampeador, fanizzamarco, gruu, kanejess, klinvill, lerongil, ma5x, merav aharoni, mrossinek, ordmoj, strickroman, tigerjack, yang.luh, and yotamvakninibm. Qiskit: An open-source framework for quantum computing, 2019.

[3] D. S. Abrams and S. Lloyd. Simulation of many-body fermi systems on a universal quantum computer. *Phys. Rev. Lett.*, 79(13):2586, 1997.

[4] C. Adamo and V. Barone. Toward reliable density functional methods without adjustable parameters: The pbe0 model. *The Journal of chemical physics*, 110(13):6158–6170, 1999.

[5] S. Albrecht, L. Reining, R. Del Sole, and G. Onida. Ab initio calculation of excitonic effects in the optical spectra of semiconductors. *Phys. Rev. Lett.*, 80:4510–4513, 1998.

[6] C. P. Anderson, A. Bourassa, K. C. Miao, G. Wolfowicz, P. J. Mintun, A. L. Crook, H. Abe, J. Ul Hassan, N. T. Son, T. Ohshima, and D. D. Awschalom. Electrical and optical control of single spins integrated in scalable semiconductor devices. *Science*, 366(6470):1225–1230, 2019.

[7] D. G. Anderson. Iterative procedures for nonlinear integral equations. *J. Assoc. Comput. Mach.*, 12(4):547–560, 1965.

[8] V. I. Anisimov, F. Aryasetiawan, and A. Lichtenstein. First-principles calculations of the electronic structure and spectra of strongly correlated systems: the lda+u method. *J. Phys.: Condens. Matter*, 9(4):767, 1997.

[9] F. Aryasetiawan, M. Imada, A. Georges, G. Kotliar, S. Biermann, and A. I. Lichtenstein. Frequency-dependent local interactions and low-energy effective models from electronic structure calculations. *Phys. Rev. B*, 70:195104, 2004.

[10] F. Aryasetiawan, J. M. Tomczak, T. Miyake, and R. Sakuma. Downfolded self-energy of many-electron systems. *Phys. Rev. Lett.*, 102(17):176402, 2009.

[11] A. Aspuru-Guzik. Simulated quantum computation of molecular energies. *Science*, 309(5741):1704–1707, 2005.

[12] D. D. Awschalom, L. C. Bassett, A. S. Dzurak, E. L. Hu, and J. R. Petta. Quantum spintronics: engineering and manipulating atom-like spins in semiconductors. *Science*, 339(6124):1174–1179, 2013.

[13] D. D. Awschalom, R. Hanson, J. Wrachtrup, and B. B. Zhou. Quantum technologies with optically interfaced solid-state spins. *Nature Photonics*, 12(9):516–527, 2018.

[14] R. Babbush, N. Wiebe, J. McClean, J. McClain, H. Neven, and G. K.-L. Chan. Low-depth quantum simulation of materials. *Phys. Rev. X*, 8(1):011044, 2018.

[15] V. Babin, C. Leforestier, and F. Paesani. Development of a "first principles" water potential with flexible monomers: Dimer potential energy surface, vrt spectrum, and second virial coefficient. *J. Chem. Theory Comput.*, 9(12):5395–5403, 2013.

[16] M. S. Bahramy, M. H. Sluiter, and Y. Kawazoe. Pseudopotential hyperfine calculations through perturbative core-level polarization. *Phys. Rev. B*, 76(3):035124, 2007.

[17] G. Balasubramanian, P. Neumann, D. Twitchen, M. Markham, R. Kolesov, N. Mizuochi, J. Isoya, J. Achard, J. Beck, J. Tissler, et al. Ultralong spin coherence time in isotopically engineered diamond. *Nat. Mater.*, 8(5):383–387, 2009.

[18] P. G. Baranov, I. Il'in, E. Mokhov, M. Muzafarova, S. B. Orlinskii, and J. Schmidt. Epr identification of the triplet ground state and photoinduced population inversion for a si-c divacancy in silicon carbide. *Journal of Experimental and Theoretical Physics Letters*, 82(7):441–443, 2005.

[19] A. Barfuss, J. Kölbl, L. Thiel, J. Teissier, M. Kasperczyk, and P. Maletinsky. Phase-controlled coherent dynamics of a single spin under closed-contour interaction. *Nature Physics*, 14(11):1087–1091, 2018.

[20] A. Barfuss, J. Teissier, E. Neu, A. Nunnenkamp, and P. Maletinsky. Strong mechanical driving of a single electron spin. *Nature Physics*, 11(10):820–824, 2015.

[21] S. Baroni, S. de Gironcoli, A. D. Corso, and P. Giannozzi. Phonons and related crystal properties from density-functional perturbation theory. *Rev. Mod. Phys.*, 73(2):515–562, 2001.

[22] S. Baroni, P. Giannozzi, and A. Testa. Green's-function approach to linear response in solids. *Phys. Rev. Lett.*, 58(18):1861–1864, 1987.

[23] M. S. J. Barson, P. Peddibhotla, P. Ovartchaiyapong, K. Ganesan, R. L. Taylor, M. Gebert, Z. Mielens, B. Koslowski, D. A. Simpson, L. P. McGuinness, J. McCallum, S. Prawer, S. Onoda, T. Ohshima, A. C. Bleszynski Jayich, F. Jelezko, N. B. Manson, and M. W. Doherty. Nanomechanical sensing using spins in diamond. *Nano Letters*, 17(3):1496–1503, 2017. PMID: 28146361.

[24] H. Bässler and A. Köhler. Charge transport in organic semiconductors. In R. M. Metzger, editor, *Unimolecular and Supramolecular Electronics I: Chemistry and Physics Meet at Metal-Molecule Interfaces*, pages 1–65. Springer Berlin Heidelberg, Berlin, Heidelberg, 2012.

[25] B. Bauer, S. Bravyi, M. Motta, and G. K.-L. Chan. Quantum algorithms for quantum chemistry and quantum materials science. *Preprint at arXiv:2001.03685*, 2020.

[26] B. Bauer, D. Wecker, A. J. Millis, M. B. Hastings, and M. Troyer. Hybrid quantum-classical approach to correlated materials. *Phys. Rev. X*, 6:031045, 2016.

[27] A. D. Becke. A multicenter numerical integration scheme for polyatomic molecules. *The Journal of Chemical Physics*, 88(4):2547–2553, 1988.

[28] A. D. Becke. Perspective: Fifty years of density-functional theory in chemical physics. *J. Chem. Phys.*, 140(18):18A301, 2014.

[29] L. X. Benedict, E. L. Shirley, and R. B. Bohn. Optical absorption of insulators and the electron-hole interaction: An ab initio calculation. *Phys. Rev. Lett.*, 80:4514–4517, 1998.

[30] S. D. Bennett, N. Y. Yao, J. Otterbach, P. Zoller, P. Rabl, and M. D. Lukin. Phonon-induced spin-spin interactions in diamond nanostructures: application to spin squeezing. *Physical Review Letters*, 110:156402, 2013.

[31] T. Biktagirov, W. G. Schmidt, and U. Gerstmann. Calculation of spin-spin zero-field splitting within periodic boundary conditions: Towards all-electron accuracy. *Phys. Rev. B*, 97(11):115135, 2018.

[32] X. Blase and C. Attaccalite. Charge-transfer excitations in molecular donor-acceptor complexes within the many-body bethe-salpeter approach. *Appl. Phys. Lett.*, 99(17):171909, 2011.

[33] X. Blase, I. Duchemin, and D. Jacquemin. The bethe-salpeter equation in chemistry: relations with td-dft, applications and challenges. *Chem. Soc. Rev.*, 47:1022–1043, 2018.

[34] P. E. Blöchl. Projector augmented-wave method. *Phys. Rev. B*, 50:17953–17979, 1994.

[35] S. Blügel, H. Akai, R. Zeller, and P. H. Dederichs. Hyperfine fields of 3d and 4d impurities in nickel. *Phys. Rev. B*, 35:3271–3283, 1987.

[36] J. Blumberger. Recent Advances in the Theory and Molecular Simulation of Biological Electron Transfer Reactions. *Chemical Reviews*, 115(20):11191–11238, 2015.

[37] J. Blumberger and K. P. McKenna. Constrained density functional theory applied to electron tunnelling between defects in MgO. *Physical Chemistry Chemical Physics*, 15(6):2184, 2013.

[38] J. Blumberger, I. Tavernelli, M. L. Klein, and M. Sprik. Diabatic free energy curves and coordination fluctuations for the aqueous Ag+/Ag2+ redox couple: A biased Born-Oppenheimer molecular dynamics investigation. *The Journal of Chemical Physics*, 124(6):064507, 2006.

[39] M. Bockstedte, F. Schütz, T. Garratt, V. Ivády, and A. Gali. Ab initio description of highly correlated states in defects for realizing quantum bits. *npj Quantum Mater.*, 3(1):31, 2018.

[40] Z. Bodrog and A. Gali. The spin–spin zero-field splitting tensor in the projector-augmented-wave method. *J. Phys.: Condens. Matter*, 26(1):015305, 2013.

[41] S. Botti, F. Sottile, N. Vast, V. Olevano, L. Reining, H.-C. Weissker, A. Rubio, G. Onida, R. D. Sole, and R. W. Godby. Long-range contribution to the exchange-correlation kernel of time-dependent density functional theory. *Phys. Rev. B*, 69(15):155112, 2004.

[42] A. Bourassa, C. P. Anderson, K. C. Miao, M. Onizhuk, H. Ma, A. L. Crook, H. Abe, J. Ul-Hassan, T. Ohshima, N. T. Son, et al. Entanglement and control of single nuclear spins in isotopically engineered silicon carbide. *Nature Materials*, pages 1–7, 2020.

[43] S. Bravyi, J. M. Gambetta, A. Mezzacapo, and K. Temme. Tapering off qubits to simulate fermionic hamiltonians. *Preprint at arXiv:1701.08213*, 2017.

[44] N. P. Brawand, M. B. Goldey, M. Vörös, and G. Galli. Defect States and Charge Transport in Quantum Dot Solids. *Chemistry of Materials*, 29(3):1255–1262, 2017.

[45] N. P. Brawand, M. Vörös, M. Govoni, and G. Galli. Generalization of dielectric-dependent hybrid functionals to finite systems. *Phys. Rev. X*, 6:041002, 2016.

[46] S. C. Brenner and R. Scott. *The mathematical theory of finite element methods*. Springer-Verlag, New York, 2009.

[47] F. Bruneval, S. M. Hamed, and J. B. Neaton. A systematic benchmark of the ab initio bethe-salpeter equation approach for low-lying optical excitations of small organic molecules. *J. Chem. Phys.*, 142(24):244101, 2015.

[48] F. Bruneval, F. Sottile, V. Olevano, R. D. Sole, and L. Reining. Many-body perturbation theory using the density-functional concept: Beyond the gw approximation. *Phys. Rev. Lett.*, 94(18):186402, 2005.

[49] M. E. Casida. Time-dependent density functional response theory for molecules. In D. P. Chong, editor, *Recent Advances in Density Functional Methods*, pages 155–192. World Scientific, 1995.

[50] M. E. Casida. *Time-Dependent Density Functional Response Theory for Molecules*. World Scientific, 2011.

[51] M. E. Casida and M. Huix-Rotllant. Progress in time-dependent density-functional theory. *Annu. Rev. Phys. Chem.*, 63(1):287–323, 2012.

[52] I. E. Castelli, F. Hüser, M. Pandey, H. Li, K. S. Thygesen, B. Seger, A. Jain, K. A. Persson, G. Ceder, and K. W. Jacobsen. New light-harvesting materials using accurate and efficient bandgap calculations. *Adv. Energy Mater.*, 5(2):1400915, 2015.

[53] D. Ceperley and B. Alder. Quantum monte carlo. *Science*, 231(4738):555–560, 1986.

[54] H. Y. Chen, E. R. MacQuarrie, and G. D. Fuchs. Orbital state manipulation of a diamond nitrogen-vacancy center using a mechanical resonator. *Physical Review Letters*, 120:167401, 2018.

[55] W. Chen, F. Ambrosio, G. Miceli, and A. Pasquarello. Ab initio electronic structure of liquid water. *Phys. Rev. Lett.*, 117:186401, 2016.

[56] W. Chen and A. Pasquarello. Accurate band gaps of extended systems via efficient vertex corrections in gw. *Phys. Rev. B*, 92(4):041115, 2015.

[57] L. Childress, R. Walsworth, and M. Lukin. Atom-like crystal defects. *Physics Today*, 67(10):38, 2014.

[58] S. Choi, M. Jain, and S. G. Louie. Mechanism for optical initialization of spin in NV-center in diamond. *Phys. Rev. B*, 86(4):041202, 2012.

[59] D. J. Christle, A. L. Falk, P. Andrich, P. V. Klimov, J. U. Hassan, N. T. Son, E. Janzén, T. Ohshima, and D. D. Awschalom. Isolated electron spins in silicon carbide with millisecond coherence times. *Nat. Mater.*, 14(2):160–163, 2015.

[60] D. J. Christle, P. V. Klimov, C. F. de las Casas, K. Szász, V. Ivády, V. Jokubavicius, J. U. Hassan, M. Syväjärvi, W. F. Koehl, T. Ohshima, N. T. Son, E. Janzén, A. Gali, and D. D. Awschalom. Isolated spin qubits in sic with a high-fidelity infrared spin-to-photon interface. *Phys. Rev. X*, 7:021046, 2017.

[61] A. J. Cohen, P. Mori-Sánchez, and W. Yang. Insights into current limitations of density functional theory. *Science*, 321(5890):792–794, 2008.

[62] Z.-H. Cui, T. Zhu, and G. K.-L. Chan. Efficient implementation of ab initio quantum embedding in periodic systems: Density matrix embedding theory. *J. Chem. Theory Comput.*, 2019.

[63] G. H. O. Daalderop, P. J. Kelly, and M. F. H. Schuurmans. Magnetocrystalline anisotropy of yco_5 and related $reco_5$ compounds. *Phys. Rev. B*, 53:14415–14433, 1996.

[64] A. Dal Corso. Pseudopotentials periodic table: From h to pu. *Computational Materials Science*, 95:337–350, 2014.

[65] S. M. Dancoff. Non-adiabatic meson theory of nuclear forces. *Phys. Rev.*, 78:382–385, 1950.

[66] E. R. Davidson. The iterative calculation of a few of the lowest eigenvalues and corresponding eigenvectors of large real-symmetric matrices. *J. Comput. Phys.*, 17(1):87–94, 1975.

[67] G. Davies and M. F. Hamer. Optical studies of the 1.945 eV vibronic band in diamond. *Proc. R. Soc. A*, 348(1653):285–298, 1976.

[68] W. Dawson and F. Gygi. Performance and accuracy of recursive subspace bisection for hybrid DFT calculations in inhomogeneous systems. *J. Chem. Theory Comput.*, 11(10):4655–4663, 2015.

[69] W. Dawson and F. Gygi. Equilibration and analysis of first-principles molecular dynamics simulations of water. *J. Chem. Phys.*, 148(12):124501, 2018.

[70] P. H. Dederichs, S. Blügel, R. Zeller, and H. Akai. Ground States of Constrained Systems: Application to Cerium Impurities. *Physical Review Letters*, 53(26):2512–2515, 1984.

[71] C. L. Degen, F. Reinhard, and P. Cappellaro. Quantum sensing. *Reviews of modern physics*, 89(3):035002, 2017.

[72] B. Diler, S. J. Whiteley, C. P. Anderson, G. Wolfowicz, M. E. Wesson, E. S. Bielejec, F. J. Heremans, and D. Awschalom. Coherent control and high-fidelity readout of chromium ions in commercial silicon carbide. *Preprint at arXiv:1909.08778*, 2019.

[73] R. Dixon. The 0–0 and 1–0 bands of the a (3π i)–x (3σ-) system of nh. *Can. J. Phys.*, 37(10):1171–1186, 1959.

[74] M. W. Doherty, F. Dolde, H. Fedder, F. Jelezko, J. Wrachtrup, N. B. Manson, and L. C. L. Hollenberg. Theory of the ground-state spin of the nv$^-$ center in diamond. *Phys. Rev. B*, 85:205203, 2012.

[75] M. W. Doherty, N. B. Manson, P. Delaney, and L. C. L. Hollenberg. The negatively charged nitrogen-vacancy centre in diamond: the electronic solution. *New J. Phys.*, 13(2):025019, 2011.

[76] M. W. Doherty, N. B. Manson, P. Delaney, F. Jelezko, J. Wrachtrup, and L. C. Hollenberg. The nitrogen-vacancy colour centre in diamond. *Phys. Rep.*, 528(1):1–45, 2013.

[77] M. W. Doherty, V. V. Struzhkin, D. A. Simpson, L. P. McGuinness, Y. Meng, A. Stacey, T. J. Karle, R. J. Hemley, N. B. Manson, L. C. Hollenberg, et al. Electronic properties and metrology applications of the diamond nv- center under pressure. *Physical review letters*, 112(4):047601, 2014.

[78] R. Dovesi, A. Erba, R. Orlando, C. M. Zicovich-Wilson, B. Civalleri, L. Maschio, M. Rérat, S. Casassa, J. Baima, S. Salustro, and B. Kirtman. Quantum-mechanical condensed matter simulations with crystal. *Wiley Interdiscip. Rev.: Comput. Mol. Sci.*, page e1360, 2018.

[79] U. F. S. D′Haenens-Johansson, A. M. Edmonds, B. L. Green, M. E. Newton, G. Davies, P. M. Martineau, R. U. A. Khan, and D. J. Twitchen. Optical properties of the neutral silicon split-vacancy center in diamond. *Phys. Rev. B*, 84:245208, 2011.

[80] A. Dreuw and M. Head-Gordon. Failure of Time-Dependent Density Functional Theory for Long-Range Charge-Transfer Excited States: The Zincbacteriochlorin-Bacteriochlorin and Bacteriochlorophyll-Spheroidene Complexes. *Journal of the American Chemical Society*, 126(12):4007–4016, 2004.

[81] C. E. Dreyer, A. Alkauskas, J. L. Lyons, A. Janotti, and C. G. Van de Walle. First-principles calculations of point defects for quantum technologies. *Annu. Rev. Mater. Res.*, 48(1):1–26, 2018.

[82] T. H. Dunning Jr. Gaussian basis sets for use in correlated molecular calculations. i. the atoms boron through neon and hydrogen. *J. Chem. Phys.*, 90(2):1007–1023, 1989.

[83] M. Dvorak and P. Rinke. Dynamical configuration interaction: Quantum embedding that combines wave functions and green's functions. *Phys. Rev. B*, 99:115134, 2019.

[84] W. C. Easley and W. Weltner Jr. Esr of the cn radical in inert matrices. *J. Chem. Phys.*, 52(1):197–205, 1970.

[85] A. L. Falk, B. B. Buckley, G. Calusine, W. F. Koehl, V. V. Dobrovitski, A. Politi, C. A. Zorman, P. X.-L. Feng, and D. D. Awschalom. Polytype control of spin qubits in silicon carbide. *Nature Communications*, 4:1819, 2013. Article.

[86] A. L. Falk, P. V. Klimov, B. B. Buckley, V. Ivády, I. A. Abrikosov, G. Calusine, W. F. Koehl, Á. Gali, and D. D. Awschalom. Electrically and mechanically tunable electron spins in silicon carbide color centers. *Phys. Rev. Lett.*, 112(18):187601, 2014.

[87] S. Felton, A. Edmonds, M. Newton, P. Martineau, D. Fisher, D. Twitchen, and J. Baker. Hyperfine interaction in the ground state of the negatively charged nitrogen vacancy center in diamond. *Phys. Rev. B*, 79(7):075203, 2009.

[88] A. L. Fetter and J. D. Walecka. *Quantum Theory of Many-Particle Systems*. McGraw-Hill, Boston, 1971.

[89] A. Fleszar and W. Hanke. Spectral properties of quasiparticles in a semiconductor. *Phys. Rev. B*, 56(16):10228–10232, 1997.

[90] C. Freysoldt, B. Grabowski, T. Hickel, J. Neugebauer, G. Kresse, A. Janotti, and C. G. Van de Walle. First-principles calculations for point defects in solids. *Reviews of modern physics*, 86(1):253, 2014.

[91] C. Freysoldt, J. Neugebauer, and C. G. Van de Walle. Fully ab initio finite-size corrections for charged-defect supercell calculations. *Physical review letters*, 102(1):016402, 2009.

[92] M. Fukami, C. Yale, P. Andrich, X. Liu, F. Heremans, P. Nealey, and D. Awschalom. All-optical cryogenic thermometry based on nitrogen-vacancy centers in nanodiamonds. *Phys. Rev. Applied*, 12:014042, 2019.

[93] A. P. Gaiduk, M. Govoni, R. Seidel, J. H. Skone, B. Winter, and G. Galli. Photoelectron spectra of aqueous solutions from first principles. *J. Am. Chem. Soc.*, 138(22):6912–6915, 2016.

[94] A. P. Gaiduk, F. Gygi, and G. Galli. Density and compressibility of liquid water and ice from first-principles simulations with hybrid functionals. *J. Phys. Chem. Lett.*, 6(15):2902–2908, 2015.

[95] A. P. Gaiduk, T. A. Pham, M. Govoni, F. Paesani, and G. Galli. Electron affinity of liquid water. *Nat. Commun.*, 9(1):247, 2018.

[96] A. Gali. Time-dependent density functional study on the excitation spectrum of point defects in semiconductors. *physica status solidi (b)*, 248(6):1337–1346, 2011.

[97] A. Gali, E. Janzén, P. Deák, G. Kresse, and E. Kaxiras. Theory of spin-conserving excitation of the n- v- center in diamond. *Physical review letters*, 103(18):186404, 2009.

[98] A. Gali and J. R. Maze. Ab initio study of the split silicon-vacancy defect in diamond: Electronic structure and related properties. *Phys. Rev. B*, 88:235205, 2013.

[99] W. Gao, A. Imamoglu, H. Bernien, and R. Hanson. Coherent manipulation, measurement and entanglement of individual solid-state spins using optical fields. *Nature Photonics*, 9(6):363, 2015.

[100] V. Garbuio, M. Cascella, I. Kupchak, O. Pulci, and A. P. Seitsonen. Proton disorder in cubic ice: Effect on the electronic and optical properties. *J. Chem. Phys.*, 143(8):084507, 2015.

[101] V. Garbuio, M. Cascella, L. Reining, R. D. Sole, and O. Pulci. Ab initio calculation of optical spectra of liquids: Many-body effects in the electronic excitations of water. *Phys. Rev. Lett.*, 97:137402, 2006.

[102] A. Genova, D. Ceresoli, and M. Pavanello. Periodic subsystem density-functional theory. *J. Chem. Phys.*, 141(17):174101, 2014.

[103] A. Georges, G. Kotliar, W. Krauth, and M. J. Rozenberg. Dynamical mean-field theory of strongly correlated fermion systems and the limit of infinite dimensions. *Rev. Mod. Phys.*, 68:13–125, 1996.

[104] M. Gerosa, F. Gygi, M. Govoni, and G. Galli. The role of defects and excess surface charges at finite temperature for optimizing oxide photoabsorbers. *Nat. Mater.*, 17:1122–1127, 2018.

[105] K. Ghosh, H. Ma, V. Gavini, and G. Galli. All-electron density functional calculations for electron and nuclear spin interactions in molecules and solids. *Phys. Rev. Mater.*, 3(4):043801, 2019.

[106] P. Giannozzi, S. Baroni, N. Bonini, M. Calandra, R. Car, C. Cavazzoni, D. Ceresoli, G. L. Chiarotti, M. Cococcioni, I. Dabo, A. D. Corso, S. de Gironcoli, S. Fabris, G. Fratesi, R. Gebauer, U. Gerstmann, C. Gougoussis, A. Kokalj, M. Lazzeri, L. Martin-Samos, N. Marzari, F. Mauri, R. Mazzarello, S. Paolini, A. Pasquarello, L. Paulatto, C. Sbraccia, S. Scandolo, G. Sclauzero, A. P. Seitsonen, A. Smogunov, P. Umari, and R. M. Wentzcovitch. QUANTUM ESPRESSO: a modular and open-source software project for quantum simulations of materials. *J. Phys.: Condens. Matter*, 21(39):395502, 2009.

[107] N. Gillet, L. Berstis, X. Wu, F. Gajdos, A. Heck, A. de la Lande, J. Blumberger, and M. Elstner. Electronic Coupling Calculations for Bridge-Mediated Charge Transfer Using Constrained Density Functional Theory (CDFT) and Effective Hamiltonian Approaches at the Density Functional Theory (DFT) and Fragment-Orbital Density Functional Tight Binding (FODFTB) Level. *Journal of Chemical Theory and Computation*, 12(10):4793–4805, 2016.

[108] F. Giustino. Electron-phonon interactions from first principles. *Rev. Mod. Phys.*, 89(1):015003, 2017.

[109] S. Goedecker, M. Teter, and J. Hutter. Separable dual-space gaussian pseudopotentials. *Physical Review B*, 54(3):1703, 1996.

[110] M. B. Goldey, N. P. Brawand, M. Vörös, and G. Galli. Charge Transport in Nanostructured Materials: Implementation and Verification of Constrained Density Functional Theory. *Journal of Chemical Theory and Computation*, 13(6):2581–2590, 2017.

[111] M. B. Goldey, D. Reid, J. de Pablo, and G. Galli. Planarity and multiple components promote organic photovoltaic efficiency by improving electronic transport. *Physical Chemistry Chemical Physics*, 18(46):31388–31399, 2016.

[112] M. L. Goldman, M. W. Doherty, A. Sipahigil, N. Y. Yao, S. D. Bennett, N. B. Manson, A. Kubanek, and M. D. Lukin. State-selective intersystem crossing in nitrogen-vacancy centers. *Phys. Rev. B*, 91:165201, 2015.

[113] D. A. Golter, T. Oo, M. Amezcua, I. Lekavicius, K. A. Stewart, and H. Wang. Coupling a surface acoustic wave to an electron spin in diamond via a dark state. *Physical Review X*, 6:041060, 2016.

[114] D. A. Golter, T. Oo, M. Amezcua, K. A. Stewart, and H. Wang. Optomechanical quantum control of a nitrogen-vacancy center in diamond. *Physical Review Letters*, 116:143602, 2016.

[115] J. D. Goodpaster, T. A. Barnes, F. R. Manby, and T. F. Miller. Accurate and systematically improvable density functional theory embedding for correlated wavefunctions. *J. Chem. Phys.*, 140(18):18A507, 2014.

[116] L. Gordon, A. Janotti, and C. G. Van de Walle. Defects as qubits in 3 c- and 4 h- sic. *Physical Review B*, 92(4):045208, 2015.

[117] M. Govoni and G. Galli. Large scale gw calculations. *J. Chem. Theory Comput.*, 11(6):2680–2696, 2015.

[118] M. Govoni and G. Galli. GW100: Comparison of methods and accuracy of results obtained with the west code. *J. Chem. Theory Comput.*, 14(4):1895–1909, 2018.

[119] B. L. Green, M. W. Doherty, E. Nako, N. B. Manson, U. F. S. D′Haenens-Johansson, S. D. Williams, D. J. Twitchen, and M. E. Newton. Electronic structure of the neutral silicon-vacancy center in diamond. *Phys. Rev. B*, 99:161112, 2019.

[120] B. L. Green, S. Mottishaw, B. G. Breeze, A. M. Edmonds, U. F. S. D'Haenens-Johansson, M. W. Doherty, S. D. Williams, D. J. Twitchen, and M. E. Newton. Neutral silicon-vacancy center in diamond: Spin polarization and lifetimes. *Phys. Rev. Lett.*, 119:096402, 2017.

[121] A. Grüneis, G. Kresse, Y. Hinuma, and F. Oba. Ionization potentials of solids: The importance of vertex corrections. *Phys. Rev. Lett.*, 112(9):096401, 2014.

[122] F.-S. Guo, B. M. Day, Y.-C. Chen, M.-L. Tong, A. Mansikkamäki, and R. A. Layfield. Magnetic hysteresis up to 80 kelvin in a dysprosium metallocene single-molecule magnet. *Science*, 362(6421):1400–1403, 2018.

[123] P. Guyot-Sionnest. Electrical Transport in Colloidal Quantum Dot Films. *The Journal of Physical Chemistry Letters*, 3(9):1169–1175, 2012.

[124] F. Gygi. Architecture of qbox: A scalable first-principles molecular dynamics code. *IBM J. Res. Dev.*, 52(1.2):137–144, 2008.

[125] F. Gygi. Compact representations of kohn-sham invariant subspaces. *Phys. Rev. Lett.*, 102(16):166406, 2009.

[126] F. Gygi and A. Baldereschi. Self-consistent hartree-fock and screened-exchange calculations in solids: Application to silicon. *Phys. Rev. B*, 34:4405–4408, 1986.

[127] F. Gygi and I. Duchemin. Efficient computation of hartree-fock exchange using recursive subspace bisection. *J. Chem. Theory Comput.*, 9(1):582–587, 2012.

[128] P. H. Hahn, W. G. Schmidt, K. Seino, M. Preuss, F. Bechstedt, and J. Bernholc. Optical absorption of water: Coulomb effects versus hydrogen bonding. *Phys. Rev. Lett.*, 94:037404, 2005.

[129] D. Hamann. Optimized norm-conserving vanderbilt pseudopotentials. *Physical Review B*, 88(8):085117, 2013.

[130] W. Hanke and L. J. Sham. Many-particle effects in the optical excitations of a semiconductor. *Phys. Rev. Lett.*, 43:387–390, 1979.

[131] J. E. Harriman. *Theoretical Foundations of Electron Spin Resonance*. Academic press, 2013.

[132] X.-F. He, N. B. Manson, and P. T. Fisk. Paramagnetic resonance of photoexcited n-v defects in diamond. i. level anticrossing in the 3 a ground state. *Phys. Rev. B*, 47(14):8809, 1993.

[133] L. Hedin. New method for calculating the one-particle green's function with application to the electron-gas problem. *Phys. Rev.*, 139(3A):A796–A823, 1965.

[134] R. Heitz, P. Thurian, I. Loa, L. Eckey, A. Hoffmann, I. Broser, K. Pressel, B. K. Meyer, and E. N. Mokhov. Identification of the 1.19-eV luminescence in hexagonal GaN. *Phys. Rev. B*, 52(23):16508–16515, 1995.

[135] T. Helgaker, P. Jorgensen, and J. Olsen. *Molecular electronic-structure theory*. John Wiley & Sons, 2014.

[136] J. M. Heller Jr., R. N. Hamm, R. D. Birkhoff, and L. R. Painter. Collective oscillation in liquid water. *J. Chem. Phys.*, 60(9):3483–3486, 1974.

[137] B. Hensen, H. Bernien, A. E. Dréau, A. Reiserer, N. Kalb, M. S. Blok, J. Ruitenberg, R. F. Vermeulen, R. N. Schouten, C. Abellán, et al. Loophole-free bell inequality violation using electron spins separated by 1.3 kilometres. *Nature*, 526(7575):682–686, 2015.

[138] F. J. Heremans, C. G. Yale, and D. D. Awschalom. Control of Spin Defects in Wide-Bandgap Semiconductors for Quantum Technologies. *Proceedings of the IEEE*, 104(10):2009–2023, 2016.

[139] A. Hermann, W. G. Schmidt, and P. Schwerdtfeger. Resolving the optical spectrum of water: Coordination and electrostatic effects. *Phys. Rev. Lett.*, 100:207403, 2008.

[140] A. Hermann and P. Schwerdtfeger. Blueshifting the onset of optical uv absorption for water under pressure. *Phys. Rev. Lett.*, 106:187403, 2011.

[141] J. Heyd, G. E. Scuseria, and M. Ernzerhof. Hybrid functionals based on a screened coulomb potential. *J. Chem. Phys.*, 118(18):8207–8215, 2003.

[142] M. Hirayama, T. Miyake, and M. Imada. Derivation of static low-energy effective models by an ab initio downfolding method without double counting of coulomb correlations: Application to srvo$_3$, fese, and fete. *Phys. Rev. B*, 87:195144, 2013.

[143] M. Hirayama, T. Miyake, M. Imada, and S. Biermann. Low-energy effective hamiltonians for correlated electron systems beyond density functional theory. *Phys. Rev. B*, 96:075102, 2017.

[144] F. L. Hirshfeld. Bonded-atom fragments for describing molecular charge densities. *Theoretica Chimica Acta*, 44(2):129–138, 1977.

[145] A. Hjorth Larsen, J. Jørgen Mortensen, J. Blomqvist, I. E. Castelli, R. Christensen, M. Dułak, J. Friis, M. N. Groves, B. Hammer, C. Hargus, E. D. Hermes, P. C. Jennings, P. Bjerre Jensen, J. Kermode, J. R. Kitchin, E. Leonhard Kolsbjerg, J. Kubal, K. Kaasbjerg, S. Lysgaard, J. Bergmann Maronsson, T. Maxson, T. Olsen, L. Pastewka, A. Peterson, C. Rostgaard, J. Schiøtz, O. Schütt, M. Strange, K. S. Thygesen, T. Vegge, L. Vilhelmsen, M. Walter, Z. Zeng, and K. W. Jacobsen. The atomic simulation environment—a Python library for working with atoms. *Journal of Physics: Condensed Matter*, 29(27):273002, 2017.

[146] P. Hohenberg and W. Kohn. Inhomogeneous electron gas. *Phys. Rev.*, 136(3B):B864–B871, 1964.

[147] M. Holt, R. Harder, R. Winarski, and V. Rose. Nanoscale hard x-ray microscopy methods for materials studies. *Annual Review of Materials Research*, 43:183–211, 2013.

[148] S. Hong, M. S. Grinolds, P. Maletinsky, R. L. Walsworth, M. D. Lukin, and A. Yacoby. Coherent, mechanical control of a single electronic spin. *Nano Letters*, 12(8):3920–3924, 2012.

[149] J. J. Hopfield. Electron Transfer Between Biological Molecules by Thermally Activated Tunneling. *Proceedings of the National Academy of Sciences*, 71(9):3640–3644, 1974.

[150] S. O. Hruszkewycz, M. Allain, M. V. Holt, C. E. Murray, J. R. Holt, P. H. Fuoss, and V. Chamard. High-resolution three-dimensional structural microscopy by single-angle Bragg ptychography. *Nature Materials*, 16:244–251, 2017.

[151] S. Hsieh, P. Bhattacharyya, C. Zu, T. Mittiga, T. Smart, F. Machado, B. Kobrin, T. Höhn, N. Rui, M. Kamrani, et al. Imaging stress and magnetism at high pressures using a nanoscale quantum sensor. *Science*, 366(6471):1349–1354, 2019.

[152] C. Huang, M. Pavone, and E. A. Carter. Quantum mechanical embedding theory based on a unique embedding potential. *J. Chem. Phys.*, 134(15):154110, 2011.

[153] P. Huang and E. A. Carter. Self-consistent embedding theory for locally correlated configuration interaction wave functions in condensed matter. *J. Chem. Phys.*, 125(8):084102, 2006.

[154] K. Huber. *Molecular Spectra and Molecular Structure, Constants of Diatomic Molecules*. Springer, 1979.

[155] J. Hutter, M. Iannuzzi, F. Schiffman, and J. VandeVondele. CP2K: Atomistic simulations of condensed matter systems. *WIREs Computational Molecular Science*, 4:15–25, 2014.

[156] M. S. Hybertsen and S. G. Louie. First-principles theory of quasiparticles: calculation of band gaps in semiconductors and insulators. *Physical review letters*, 55(13):1418, 1985.

[157] M. S. Hybertsen and S. G. Louie. Electron correlation in semiconductors and insulators: Band gaps and quasiparticle energies. *Phys. Rev. B*, 34(8):5390–5413, 1986.

[158] I. Žutić, J. Fabian, and S. Das Sarma. Spintronics: Fundamentals and applications. *Rev. Mod. Phys.*, 76:323–410, 2004.

[159] M. Imada and T. Miyake. Electronic structure calculation by first principles for strongly correlated electron systems. *J. Phys. Soc. Jpn.*, 79(11):112001, 2010.

[160] V. Ivády, I. A. Abrikosov, and A. Gali. First principles calculation of spin-related quantities for point defect qubit research. *npj Comput. Mater.*, 4(1), 2018.

[161] V. Ivady, A. Gällström, N. T. Son, E. Janzén, and A. Gali. Asymmetric split-vacancy defects in sic polytypes: A combined theoretical and electron spin resonance study. *Physical review letters*, 107(19):195501, 2011.

[162] V. Ivády, T. Simon, J. R. Maze, I. A. Abrikosov, and A. Gali. Pressure and temperature dependence of the zero-field splitting in the ground state of nv centers in diamond: A first-principles study. *Phys. Rev. B*, 90:235205, 2014.

[163] V. Ivády, K. Szász, A. L. Falk, P. V. Klimov, D. J. Christle, E. Janzén, I. A. Abrikosov, D. D. Awschalom, and A. Gali. Theoretical model of dynamic spin polarization of nuclei coupled to paramagnetic point defects in diamond and silicon carbide. *Physical Review B*, 92(11):115206, 2015.

[164] C. R. Jacob and J. Neugebauer. Subsystem density-functional theory. *Wiley Interdiscip. Rev.: Comput. Mol. Sci.*, 4(4):325–362, 2014.

[165] D. Jacquemin, I. Duchemin, and X. Blase. Benchmarking the bethe–salpeter formalism on a standard organic molecular set. *J. Chem. Theory Comput.*, 11(7):3290–3304, 2015.

[166] F. Jelezko, T. Gaebel, I. Popa, A. Gruber, and J. Wrachtrup. Observation of coherent oscillations in a single electron spin. *Physical Review Letters*, 92:076401, 2004.

[167] Y. Jiang, H. Geng, W. Li, and Z. Shuai. Understanding carrier transport in organic semiconductors: computation of charge mobility considering quantum nuclear tunneling and delocalization effects. *Journal of chemical theory and computation*, 15(3):1477–1491, 2019.

[168] Y. Jiang, Q. Peng, H. Geng, H. Ma, and Z. Shuai. Negative isotope effect for charge transport in acenes and derivatives–a theoretical conclusion. *Physical Chemistry Chemical Physics*, 17(5):3273–3280, 2015.

[169] M. L. Jones, I. V. Kurnikov, and D. N. Beratan. The Nature of Tunneling Pathway and Average Packing Density Models for Protein-Mediated Electron Transfer †. *The Journal of Physical Chemistry A*, 106(10):2002–2006, 2002.

[170] P. Jordan and E. P. Wigner. About the pauli exclusion principle. *Z. Phys.*, 47:631–651, 1928.

[171] E. S. Kadantsev and T. Ziegler. Implementation of a density functional theory-based method for the calculation of the hyperfine a-tensor in periodic systems with the use of numerical and slater type atomic orbitals: Application to paramagnetic defects. *J. Phys. Chem. A*, 112(19):4521–4526, 2008.

[172] B. Kaduk, T. Kowalczyk, and T. Van Voorhis. Constrained Density Functional Theory. *Chemical Reviews*, 112(1):321–370, 2012.

[173] A. Kandala, A. Mezzacapo, K. Temme, M. Takita, M. Brink, J. M. Chow, and J. M. Gambetta. Hardware-efficient variational quantum eigensolver for small molecules and quantum magnets. *Nature*, 549(7671):242–246, 2017.

[174] A. Kandala, K. Temme, A. D. Córcoles, A. Mezzacapo, J. M. Chow, and J. M. Gambetta. Error mitigation extends the computational reach of a noisy quantum processor. *Nature*, 567(7749):491, 2019.

[175] B. Kanungo and V. Gavini. Large-scale all-electron density functional theory calculations using an enriched finite-element basis. *Phys. Rev. B*, 95:035112, 2017.

[176] H. Kataura, N. Irie, N. Kobayashi, Y. Achiba, K. Kikuchi, T. Hanyu, and S. Yamaguchi. Optical absorption of gas phase c 60 and c 70. *Jpn. J. Appl. Phys.*, 32(11B):L1667, 1993.

[177] E. Kaxiras. *Atomic and Electronic Structure of Solids*. Cambridge University Press, 2003.

[178] K. V. Kepesidis, S. D. Bennett, S. Portolan, M. D. Lukin, and P. Rabl. Phonon cooling and lasing with nitrogen-vacancy centers in diamond. *Physical Review B*, 88:064105, 2013.

[179] G. D. Kerr, R. N. Hamm, M. W. Williams, R. D. Birkhoff, and L. R. Painter. Optical and dielectric properties of water in the vacuum ultraviolet. *Phys. Rev. A*, 5:2523–2527, 1972.

[180] C. Kittel, P. McEuen, and P. McEuen. *Introduction to solid state physics*, volume 8. Wiley New York, 1996.

[181] I. D. Kivlichan, J. McClean, N. Wiebe, C. Gidney, A. Aspuru-Guzik, G. K.-L. Chan, and R. Babbush. Quantum simulation of electronic structure with linear depth and connectivity. *Phys. Rev. Lett.*, 120:110501, 2018.

[182] P. V. Klimov, A. L. Falk, B. B. Buckley, and D. D. Awschalom. Electrically driven spin resonance in silicon carbide color centers. *Physical Review Letters*, 112:087601, 2014.

[183] P. V. Klimov, A. L. Falk, D. J. Christle, V. V. Dobrovitski, and D. D. Awschalom. Quantum entanglement at ambient conditions in a macroscopic solid-state spin ensemble. *Science Advances*, 1(10):e1501015, 2015.

[184] L. Knight Jr and W. Weltner Jr. Esr and optical spectroscopy of the alo molecule at 4 k; observation of an al complex and its interaction with krypton. *J. Chem. Phys.*, 55(10):5066–5077, 1971.

[185] G. Knizia and G. K.-L. Chan. Density matrix embedding: A simple alternative to dynamical mean-field theory. *Phys. Rev. Lett.*, 109(18):186404, 2012.

[186] P. Knowles and N. Handy. A new determinant-based full configuration interaction method. *Chem. Phys. Lett.*, 111(4-5):315–321, 1984.

[187] K. Kobayashi. Optical spectra and electronic structure of ice. *J. Chem. Phys.*, 87(21):4317–4321, 1983.

[188] W. F. Koehl, B. B. Buckley, F. J. Heremans, G. Calusine, and D. D. Awschalom. Room temperature coherent control of defect spin qubits in silicon carbide. *Nature*, 479(7371):84–87, 2011.

[189] W. F. Koehl, B. Diler, S. J. Whiteley, A. Bourassa, N. T. Son, E. Janzén, and D. D. Awschalom. Resonant optical spectroscopy and coherent control of Cr^{4+} spin ensembles in sic and gan. *Phys. Rev. B*, 95:035207, 2017.

[190] W. F. Koehl, H. Seo, G. Galli, and D. D. Awschalom. Designing defect spins for wafer-scale quantum technologies. *MRS Bull.*, 40(12):1146–1153, 2015.

[191] W. Kohn and L. J. Sham. Self-consistent equations including exchange and correlation effects. *Phys. Rev.*, 140(4A):A1133–A1138, 1965.

[192] S. Kolkowitz, A. C. Bleszynski Jayich, Q. P. Unterreithmeier, S. D. Bennett, P. Rabl, J. G. E. Harris, and M. D. Lukin. Coherent sensing of a mechanical resonator with a single-spin qubit. *Science*, 335(6076):1603–1606, 2012.

[193] S. Kossmann, B. Kirchner, and F. Neese. Performance of modern density functional theory for the prediction of hyperfine structure: meta-gga and double hybrid functionals. *Mol. Phys.*, 105(15-16):2049–2071, 2007.

[194] G. Kotliar, S. Y. Savrasov, K. Haule, V. S. Oudovenko, O. Parcollet, and C. A. Marianetti. Electronic structure calculations with dynamical mean-field theory. *Rev. Mod. Phys.*, 78(3):865–951, 2006.

[195] K. Krause, M. E. Harding, and W. Klopper. Coupled-cluster reference values for the gw27 and gw100 test sets for the assessment of gw methods. *Mol. Phys.*, 113(13-14):1952–1960, 2015.

[196] J. M. Kreula, L. García-Álvarez, L. Lamata, S. R. Clark, E. Solano, and D. Jaksch. Few-qubit quantum-classical simulation of strongly correlated lattice fermions. *EPJ Quantum Technol.*, 3(1):1–19, 2016.

[197] A. V. Krukau, O. A. Vydrov, A. F. Izmaylov, and G. E. Scuseria. Influence of the exchange screening parameter on the performance of screened hybrid functionals. *J. Chem. Phys.*, 125(22):224106, 2006.

[198] A. Kubas, F. Gajdos, A. Heck, H. Oberhofer, M. Elstner, and J. Blumberger. Electronic couplings for molecular charge transfer: Benchmarking CDFT, FODFT and FODFTB against high-level ab initio calculations. II. *Physical Chemistry Chemical Physics*, 17(22):14342–14354, 2015.

[199] A. Kubas, F. Hoffmann, A. Heck, H. Oberhofer, M. Elstner, and J. Blumberger. Electronic couplings for molecular charge transfer: Benchmarking CDFT, FODFT, and FODFTB against high-level *ab initio* calculations. *The Journal of Chemical Physics*, 140(10):104105, 2014.

[200] S. Kümmel and L. Kronik. Orbital-dependent density functionals: Theory and applications. *Rev. Mod. Phys.*, 80(1):3–60, 2008.

[201] G. Kurizki, P. Bertet, Y. Kubo, K. Mølmer, D. Petrosyan, and P. Rabl. Quantum technologies with hybrid systems. *Proceedings of the National Academy of Sciences of the United States of America*, 112(13):3866–3873, 2015.

[202] A. L. Kutepov. Electronic structure of na, k, si, and lif from self-consistent solution of hedin's equations including vertex corrections. *Phys. Rev. B*, 94(15), 2016.

[203] A. L. Kutepov. Self-consistent solution of hedin's equations: Semiconductors and insulators. *Phys. Rev. B*, 95(19):195120, 2017.

[204] W. Kutzelnigg, U. Fleischer, and M. Schindler. The iglo-method: ab-initio calculation and interpretation of nmr chemical shifts and magnetic susceptibilities. In *Deuterium and shift calculation*, pages 165–262. Springer, 1990.

[205] T. N. Lan, A. A. Kananenka, and D. Zgid. Rigorous ab initio quantum embedding for quantum chemistry using green's function theory: Screened interaction, nonlocal self-energy relaxation, orbital basis, and chemical accuracy. *J. Chem. Theory Comput.*, 12(10):4856–4870, 2016.

[206] X. Lan, M. Chen, M. H. Hudson, V. Kamysbayev, Y. Wang, P. Guyot-Sionnest, and D. V. Talapin. Quantum dot solids showing state-resolved band-like transport. *Nature Materials*, 19(3):323–329, 2020.

[207] L. Landau. On the theory of transfer of energy at collisions. *Phys. Z. Sowjetunion*, 1:88, 1932.

[208] J. Latosińska. Nqr parameters: Electric field gradient tensor and asymmetry parameter studied in terms of density functional theory. *Int. J. Quantum Chem.*, 91(3):284–296, 2003.

[209] D. Lee, K. W. Lee, J. V. Cady, P. Ovartchaiyapong, and A. C. Bleszynski Jayich. Topical review: spins and mechanics in diamond. *Journal of Optics*, 19(3):033001, 2017.

[210] K. W. Lee, D. Lee, P. Ovartchaiyapong, J. Minguzzi, J. R. Maze, and A. C. Bleszynski Jayich. Strain coupling of a mechanical resonator to a single quantum emitter in diamond. *Physical Review Applied*, 6:034005, 2016.

[211] X. Leng, F. Jin, M. Wei, and Y. Ma. Gw method and bethe-salpeter equation for calculating electronic excitations. *Wiley Interdiscip. Rev.: Comput. Mol. Sci.*, 6(5):532–550, 2016.

[212] M. E. Levinshtein, S. L. Rumyantsev, and M. S. Shur, editors. *Properties of Advanced Semiconductor Materials: GaN, AlN, InN, BN, SiC, SiGe.* John Wiley & Sons, 2001.

[213] S. Lin, C. Chang, K. Liang, R. Chang, J. Zhang, T. Yang, M. Hayashi, Y. Shiu, and F. Hsu. Ultrafast dynamics and spectroscopy of bacterial photosynthetic reaction centers. *Advances in chemical physics*, 121:1–88, 2002.

[214] P. Liu, M. Kaltak, J. Klimeš, and G. Kresse. Cubic scaling gw: Towards fast quasiparticle calculations. *Phys. Rev. B*, 94(16):165109, 2016.

[215] M. P. Ljungberg, P. Koval, F. Ferrari, D. Foerster, and D. Sánchez-Portal. Cubic-scaling iterative solution of the bethe-salpeter equation for finite systems. *Phys. Rev. B*, 92:075422, 2015.

[216] J. Loubser and J. van Wyk. Electron spin resonance in the study of diamond. *Rep. Prog. Phys.*, 41(8):1201, 1978.

[217] P.-O. Löwdin. On the Non-Orthogonality Problem Connected with the Use of Atomic Wave Functions in the Theory of Molecules and Crystals. *The Journal of Chemical Physics*, 18(3):365–375, 1950.

[218] H. Ma, M. Govoni, and G. Galli. Pyzfs: A python package for first-principles calculations of zero-field splitting tensors. *Journal of Open Source Software*, 5(47):2160, 2020.

[219] H. Ma, M. Govoni, and G. Galli. Quantum simulations of materials on near-term quantum computers. *npj Comput. Mater.*, 6:85, 2020.

[220] H. Ma, M. Govoni, F. Gygi, and G. Galli. A finite-field approach forGWCalculations beyond the random phase approximation. *J. Chem. Theory Comput.*, 15(1):154–164, 2018.

[221] P.-W. Ma and S. L. Dudarev. Constrained density functional for noncollinear magnetism. *Physical Review B*, 91(5), 2015.

[222] E. MacQuarrie, M. Otten, S. Gray, and G. Fuchs. Cooling a mechanical resonator with nitrogen-vacancy centres using a room temperature excited state spin–strain interaction. *Nature communications*, 8(1):1–10, 2017.

[223] E. R. Macquarrie, T. A. Gosavi, S. A. Bhave, and G. D. Fuchs. Continuous dynamical decoupling of a single diamond nitrogen-vacancy center spin with a mechanical resonator. *Physical Review B*, 92:224419, 2015.

[224] E. R. MacQuarrie, T. A. Gosavi, A. M. Moehle, N. R. Jungwirth, S. A. Bhave, and G. D. Fuchs. Coherent control of a nitrogen-vacancy center spin ensemble with a diamond mechanical resonator. *Optica*, 2(3):233–238, 2015.

[225] E. R. MacQuarrie, M. Otten, S. K. Gray, and G. D. Fuchs. Cooling a mechanical resonator with nitrogen-vacancy centres using a room temperature excited state spin-strain interaction. *Nature Communications*, 8:14358, 2017. Article.

[226] E. Maggio and G. Kresse. GW vertex corrected calculations for molecular systems. *J. Chem. Theory Comput.*, 13(10):4765–4778, 2017.

[227] G. Makov and M. C. Payne. Periodic boundary conditions in ab initio calculations. *Phys. Rev. B*, 51(7):4014–4022, 1995.

[228] R. Manenti, A. F. Kockum, A. Patterson, T. Behrle, J. Rahamim, G. Tancredi, F. Nori, and P. J. Leek. Circuit quantum acoustodynamics with surface acoustic waves. *Nature Communications*, 8(1):975, 2017.

[229] R. A. Marcus. On the Theory of Oxidation-Reduction Reactions Involving Electron Transfer. I. *The Journal of Chemical Physics*, 24(5):966–978, 1956.

[230] R. A. Marcus. Electron transfer reactions in chemistry. Theory and experiment. *Reviews of Modern Physics*, 65(3):599–610, 1993.

[231] A. Marini, R. Del Sole, and A. Rubio. Bound excitons in time-dependent density-functional theory: Optical and energy-loss spectra. *Phys. Rev. Lett.*, 91:256402, 2003.

[232] A. Marini, C. Hogan, M. Grüning, and D. Varsano. yambo: An ab initio tool for excited state calculations. *Comput. Phys. Commun.*, 180(8):1392 – 1403, 2009.

[233] A. Marini and A. Rubio. Electron linewidths of wide-gap insulators: Excitonic effects in lif. *Phys. Rev. B*, 70(8):081103, 2004.

[234] A. Marini, R. D. Sole, and A. Rubio. Bound excitons in time-dependent density-functional theory: Optical and energy-loss spectra. *Phys. Rev. Lett.*, 91(25):256402, 2003.

[235] M. A. L. Marques and E. K. U. Gross. *Time-Dependent Density Functional Theory*. Springer Berlin Heidelberg, Berlin, Heidelberg, 2003.

[236] M. Marsili, E. Mosconi, F. De Angelis, and P. Umari. Large-scale *gw*-bse calculations with N^3 scaling: Excitonic effects in dye-sensitized solar cells. *Phys. Rev. B*, 95:075415, 2017.

[237] R. M. Martin, L. Reining, and D. M. Ceperley. *Interacting Electrons*. Cambridge University Press, 2016.

[238] L. Martin-Samos and G. Bussi. Sax: An open source package for electronic-structure and optical-properties calculations in the gw approximation. *Comput. Phys. Commun.*, 180(8):1416 – 1425, 2009.

[239] N. Marzari, A. A. Mostofi, J. R. Yates, I. Souza, and D. Vanderbilt. Maximally localized wannier functions: Theory and applications. *Rev. Mod. Phys.*, 84:1419–1475, 2012.

[240] K. Mathew, J. H. Montoya, A. Faghaninia, S. Dwarakanath, M. Aykol, H. Tang, I.-h. Chu, T. Smidt, B. Bocklund, M. Horton, J. Dagdelen, B. Wood, Z.-K. Liu, J. Neaton, S. P. Ong, K. Persson, and A. Jain. Atomate: A high-level interface to generate, execute, and analyze computational materials science workflows. *Compuational Materials Science*, 139:140–152, 2017.

[241] V. May and O. Kühn. *Charge and energy transfer dynamics in molecular systems*, volume 2. Wiley Online Library, 2011.

[242] J. R. Maze, A. Gali, E. Togan, Y. Chu, A. Trifonov, E. Kaxiras, and M. D. Lukin. Properties of nitrogen-vacancy centers in diamond: the group theoretic approach. *New J. Phys.*, 13(2):025025, 2011.

[243] R. L. McAvoy, M. Govoni, and G. Galli. Coupling first-principles calculations of electron–electron and electron–phonon scattering, and applications to carbon-based nanostructures. *J. Chem. Theory Comput.*, 14(12):6269–6275, 2018.

[244] J. R. McClean, J. Romero, R. Babbush, and A. Aspuru-Guzik. The theory of variational hybrid quantum-classical algorithms. *New J. Phys.*, 18(2):023023, 2016.

[245] R. McWeeny. R. mcweeny and y. mizuno, proc. r. soc. london, ser. a 259, 554 (1961). *Proc. R. Soc. London, Ser. A*, 259:554, 1961.

[246] M. Melander, E. Ö. Jónsson, J. J. Mortensen, T. Vegge, and J. M. García Lastra. Implementation of Constrained DFT for Computing Charge Transfer Rates within the Projector Augmented Wave Method. *Journal of Chemical Theory and Computation*, 12(11):5367–5378, 2016.

[247] T. Miyake, F. Aryasetiawan, and M. Imada. Ab initio procedure for constructing effective models of correlated materials with entangled band structure. *Phys. Rev. B*, 80:155134, 2009.

[248] B. A. Moores, L. R. Sletten, J. J. Viennot, and K. W. Lehnert. Cavity quantum acoustic device in the multimode strong coupling regime. *Physical Review Letters*, 120:227701, 2018.

[249] A. J. Morris, M. Stankovski, K. T. Delaney, P. Rinke, P. García-González, and R. W. Godby. Vertex corrections in localized and extended systems. *Phys. Rev. B*, 76(15):155106, 2007.

[250] K. J. Morse, R. J. Abraham, A. DeAbreu, C. Bowness, T. S. Richards, H. Riemann, N. V. Abrosimov, P. Becker, H.-J. Pohl, M. L. Thewalt, et al. A photonic platform for donor spin qubits in silicon. *Sci. Adv.*, 3(7):e1700930, 2017.

[251] P. Motamarri, M. R. Nowak, K. Leiter, J. Knap, and V. Gavini. Higher-order adaptive finite-element methods for kohn-sham density functional theory. *J. Comput. Phys.*, 253:308–343, 2013.

[252] M. Motta, C. Sun, A. T. Tan, M. J. O'Rourke, E. Ye, A. J. Minnich, F. G. Brandão, and G. K.-L. Chan. Determining eigenstates and thermal states on a quantum computer using quantum imaginary time evolution. *Nat. Phys.*, pages 1–6, 2019.

[253] R. S. Mulliken. Electronic Population Analysis on LCAO–MO Molecular Wave Functions. I. *The Journal of Chemical Physics*, 23(10):1833–1840, 1955.

[254] G. Nan, X. Yang, L. Wang, Z. Shuai, and Y. Zhao. Nuclear tunneling effects of charge transport in rubrene, tetracene, and pentacene. *Physical Review B*, 79(11):115203, 2009.

[255] F. Neese. Efficient and accurate approximations to the molecular spin-orbit coupling operator and their use in molecular g-tensor calculations. *J. Chem. Phys.*, 122(3):034107, 2005.

[256] F. Neese. Calculation of the zero-field splitting tensor on the basis of hybrid density functional and hartree-fock theory. *J. Chem. Phys.*, 127(16):164112, 2007.

[257] F. Neese. The orca program system. *Wiley Interdiscip. Rev.: Comput. Mol. Sci.*, 2(1):73–78, 2012.

[258] D. Neuhauser, Y. Gao, C. Arntsen, C. Karshenas, E. Rabani, and R. Baer. Breaking the theoretical scaling limit for predicting quasiparticle energies: The stochastic gw approach. *Phys. Rev. Lett.*, 113(7):076402, 2014.

[259] M. D. Newton and N. Sutin. Electron Transfer Reactions in Condensed Phases. *Annual Review of Physical Chemistry*, 35:437–480, 1984.

[260] H.-V. Nguyen, T. A. Pham, D. Rocca, and G. Galli. Improving accuracy and efficiency of calculations of photoemission spectra within the many-body perturbation theory. *Phys. Rev. B*, 85(8):081101, 2012.

[261] N. L. Nguyen, H. Ma, M. Govoni, F. Gygi, and G. Galli. Finite-field approach to solving the bethe-salpeter equation. *Phys. Rev. Lett.*, 122:237402, 2019.

[262] H. Oberhofer and J. Blumberger. Charge constrained density functional molecular dynamics for simulation of condensed phase electron transfer reactions. *The Journal of Chemical Physics*, 131(6):064101, 2009.

[263] H. Oberhofer and J. Blumberger. Electronic coupling matrix elements from charge constrained density functional theory calculations using a plane wave basis set. *The Journal of Chemical Physics*, 133(24):244105, 2010.

[264] H. Oberhofer and J. Blumberger. Revisiting electronic couplings and incoherent hopping models for electron transport in crystalline C60 at ambient temperatures. *Physical Chemistry Chemical Physics*, 14(40):13846, 2012.

[265] H. Oberhofer, K. Reuter, and J. Blumberger. Charge Transport in Molecular Materials: An Assessment of Computational Methods. *Chemical Reviews*, 117(15):10319–10357, 2017.

[266] P. J. Ollitrault, A. Kandala, C.-F. Chen, P. K. Barkoutsos, A. Mezzacapo, M. Pistoia, S. Sheldon, S. Woerner, J. Gambetta, and I. Tavernelli. Quantum equation of motion for computing molecular excitation energies on a noisy quantum processor. *Preprint at arXiv:1910.12890*, 2019.

[267] L. Olsen, O. Christiansen, L. Hemmingsen, S. P. Sauer, and K. V. Mikkelsen. Electric field gradients of water: A systematic investigation of basis set, electron correlation, and rovibrational effects. *J. Chem. Phys.*, 116(4):1424–1434, 2002.

[268] T. Olsen and K. S. Thygesen. Extending the random-phase approximation for electronic correlation energies: The renormalized adiabatic local density approximation. *Phys. Rev. B*, 86(8):081103, 2012.

[269] T. Olsen and K. S. Thygesen. Beyond the random phase approximation: Improved description of short-range correlation by a renormalized adiabatic local density approximation. *Phys. Rev. B*, 88(11):115131, 2013.

[270] S. P. Ong, W. D. Richards, A. Jain, G. Hautier, M. Kocher, S. Cholia, D. Gunter, V. L. Chevrier, K. A. Persson, and G. Ceder. Python Materials Genomics (pymatgen): A robust, open-source python library for materials analysis. *Computational Materials Science*, 68:314–319, 2013.

[271] G. Onida, L. Reining, and A. Rubio. Electronic excitations: density-functional versus many-body green's-function approaches. *Rev. Mod. Phys.*, 74(2):601–659, 2002.

[272] M. Onizhuk, K. C. Miao, J. P. Blanton, H. Ma, C. P. Anderson, A. Bourassa, D. D. Awschalom, and G. Galli. Probing the coherence of solid-state qubits at avoided crossings. *arXiv:2010.11077*, 2020.

[273] P. Ovartchaiyapong, K. W. Lee, B. A. Myers, and A. C. Bleszynski Jayich. Dynamic strain-mediated coupling of a single diamond spin to a mechanical resonator. *Nature Communications*, 5:4429, 2014.

[274] H. Overhof and U. Gerstmann. Ab initio calculation of hyperfine and superhyperfine interactions for shallow donors in semiconductors. *Phys. Rev. Lett.*, 92:087602, 2004.

[275] J. Paier, M. Marsman, and G. Kresse. Dielectric properties and excitons for extended systems from hybrid functionals. *Phys. Rev. B*, 78(12):121201, 2008.

[276] A. Pateras, J. Park, Y. Ahn, J. A. Tilka, M. V. Holt, C. Reichl, W. Wegscheider, T. A. Baart, J. P. Dehollain, U. Mukhopadhyay, L. M. K. Vandersypen, and P. G. Evans. Mesoscopic elastic distortions in gaas quantum dot heterostructures. *Nano Letters*, 18(5):2780–2786, 2018. PMID: 29664645.

[277] C. E. Patrick and K. S. Thygesen. Adiabatic-connection fluctuation-dissipation DFT for the structural properties of solids—the renormalized ALDA and electron gas kernels. *J. Chem. Phys.*, 143(10):102802, 2015.

[278] L. Patrick and W. J. Choyke. Static dielectric constant of sic. *Physical Review B*, 2(6):2255, 1970.

[279] J. P. Perdew, K. Burke, and M. Ernzerhof. Generalized gradient approximation made simple. *Phys. Rev. Lett.*, 77:3865–3868, 1996.

[280] J. P. Perdew, M. Ernzerhof, and K. Burke. Rationale for mixing exact exchange with density functional approximations. *J. Chem. Phys.*, 105(22):9982–9985, 1996.

[281] J. P. Perdew and A. Zunger. Self-interaction correction to density-functional approximations for many-electron systems. *Phys. Rev. B*, 23(10):5048–5079, 1981.

[282] A. Peruzzo, J. McClean, P. Shadbolt, M.-H. Yung, X.-Q. Zhou, P. J. Love, A. Aspuru-Guzik, and J. L. O'Brien. A variational eigenvalue solver on a photonic quantum processor. *Nat. Commun.*, 5(1):4213, 2014.

[283] I. Petousis, D. Mrdjenovich, E. Ballouz, M. Liu, D. Winston, W. Chen, T. Graf, T. D. Schladt, K. A. Persson, and F. B. Prinz. High-throughput screening of inorganic compounds for the discovery of novel dielectric and optical materials. *Sci. Data*, 4:160134, 2017.

[284] H. Q. Pham, M. R. Hermes, and L. Gagliardi. Periodic electronic structure calculations with density matrix embedding theory. *Preprint at arXiv:1909.08783*, 2019.

[285] T. A. Pham, M. Govoni, R. Seidel, S. E. Bradforth, E. Schwegler, and G. Galli. Electronic structure of aqueous solutions: Bridging the gap between theory and experiments. *Sci. Adv.*, 3(6):e1603210, 2017.

[286] T. A. Pham, H.-V. Nguyen, D. Rocca, and G. Galli. Gw calculations using the spectral decomposition of the dielectric matrix: Verification, validation, and comparison of methods. *Phys. Rev. B*, 87(15):155148, 2013.

[287] T. A. Pham, Y. Ping, and G. Galli. Modelling Heterogeneous Interfaces for Solar Water Splitting. *Nat. Mater.*, 16(4):401, 2017.

[288] T. A. Pham, C. Zhang, E. Schwegler, and G. Galli. Probing the electronic structure of liquid water with many-body perturbation theory. *Phys. Rev. B*, 89:060202, 2014.

[289] C. J. Pickard and F. Mauri. All-electron magnetic response with pseudopotentials: Nmr chemical shifts. *Phys. Rev. B*, 63(24):245101, 2001.

[290] C. J. Pickard and F. Mauri. First-principles theory of the epr g tensor in solids: Defects in quartz. *Phys. Rev. Lett.*, 88(8):086403, 2002.

[291] Y. Ping, D. Rocca, and G. Galli. Electronic excitations in light absorbers for photoelectrochemical energy conversion: first principles calculations based on many body perturbation theory. *Chem. Soc. Rev.*, 42(6):2437, 2013.

[292] Y. Ping, D. Rocca, and G. Galli. Optical properties of tungsten trioxide from first-principles calculations. *Phys. Rev. B*, 87:165203, 2013.

[293] Y. Ping, D. Rocca, D. Lu, and G. Galli. Ab initio calculations of absorption spectra of semiconducting nanowires within many-body perturbation theory. *Phys. Rev. B*, 85:035316, 2012.

[294] M. J. Powell. A direct search optimization method that models the objective and constraint functions by linear interpolation. In *Advances in optimization and numerical analysis*, pages 51–67. Springer, 1994.

[295] J. Preskill. Quantum Computing in the NISQ era and beyond. *Quantum*, 2:79, 2018.

[296] X. Qian, P. Umari, and N. Marzari. First-principles investigation of organic photovoltaic materials c_{60}, c_{70}, [c_{60}]PCBM, and bis-[c_{60}]PCBM using a many-body G_0W_0-lanczos approach. *Phys. Rev. B*, 91:245105, 2015.

[297] T. Rangel, S. M. Hamed, F. Bruneval, and J. B. Neaton. An assessment of low-lying excitation energies and triplet instabilities of organic molecules with an ab initio bethe-salpeter equation approach and the tamm-dancoff approximation. *J. Chem. Phys.*, 146(19):194108, 2017.

[298] M. Rayson and P. Briddon. First principles method for the calculation of zero-field splitting tensors in periodic systems. *Phys. Rev. B*, 77(3):035119, 2008.

[299] N. Rega, M. Cossi, and V. Barone. Development and validation of reliable quantum mechanical approaches for the study of free radicals in solution. *J. Chem. Phys.*, 105(24):11060–11067, 1996.

[300] L. Reining, V. Olevano, A. Rubio, and G. Onida. Excitonic effects in solids described by time-dependent density-functional theory. *Phys. Rev. Lett.*, 88(6):066404, 2002.

[301] R. Reviakine, A. V. Arbuznikov, J.-C. Tremblay, C. Remenyi, O. L. Malkina, V. G. Malkin, and M. Kaupp. Calculation of zero-field splitting parameters: Comparison of a two-component noncolinear spin-density-functional method and a one-component perturbational approach. *J. Chem. Phys.*, 125(5):054110, 2006.

[302] P. Rinke, M. Winkelnkemper, A. Qteish, D. Bimberg, J. Neugebauer, and M. Scheffler. Consistent set of band parameters for the group-iii nitrides aln, gan, and inn. *Physical Review B*, 77(7):075202, 2008.

[303] D. Rocca, R. Gebauer, Y. Saad, and S. Baroni. Turbo charging time-dependent density-functional theory with lanczos chains. *J. Chem. Phys.*, 128(15):154105, 2008.

[304] D. Rocca, D. Lu, and G. Galli. Ab initio calculations of optical absorption spectra: Solution of the bethe–salpeter equation within density matrix perturbation theory. *J. Chem. Phys.*, 133(16):164109, 2010.

[305] D. Rocca, Y. Ping, R. Gebauer, and G. Galli. Solution of the bethe-salpeter equation without empty electronic states: Application to the absorption spectra of bulk systems. *Phys. Rev. B*, 85:045116, 2012.

[306] D. Rocca, M. Vörös, A. Gali, and G. Galli. Ab initio optoelectronic properties of silicon nanoparticles: Excitation energies, sum rules, and tamm–dancoff approximation. *J. Chem. Theory Comput.*, 10(8):3290, 2014.

[307] D. M. Roessler and W. C. Walker. Optical constants of magnesium oxide and lithium fluoride in the far ultraviolet∗. *J. Opt. Soc. Am.*, 57(6):835–836, 1967.

[308] L. J. Rogers, S. Armstrong, M. J. Sellars, and N. B. Manson. Infrared emission of the NV centre in diamond: Zeeman and uniaxial stress studies. *New J. Phys.*, 10(10):103024, 2008.

[309] M. Rohlfing and S. G. Louie. Excitonic effects and the optical absorption spectrum of hydrogenated si clusters. *Phys. Rev. Lett.*, 80:3320–3323, 1998.

[310] M. Rohlfing and S. G. Louie. Electron-hole excitations and optical spectra from first principles. *Phys. Rev. B*, 62:4927–4944, 2000.

[311] P. Romaniello, S. Guyot, and L. Reining. The self-energy beyond gw: Local and nonlocal vertex corrections. *J. Chem. Phys.*, 131(15):154111, 2009.

[312] B. C. Rose, D. Huang, Z.-H. Zhang, P. Stevenson, A. M. Tyryshkin, S. Sangtawesin, S. Srinivasan, L. Loudin, M. L. Markham, A. M. Edmonds, et al. Observation of an environmentally insensitive solid-state spin defect in diamond. *Science*, 361(6397):60–63, 2018.

[313] N. C. Rubin. A hybrid classical/quantum approach for large-scale studies of quantum systems with density matrix embedding theory. *Preprint at arXiv:1610.06910*, 2016.

[314] E. Runge and E. K. U. Gross. Density-functional theory for time-dependent systems. *Phys. Rev. Lett.*, 52(12):997–1000, 1984.

[315] I. Rungger, N. Fitzpatrick, H. Chen, C. Alderete, H. Apel, A. Cowtan, A. Patterson, D. M. Ramo, Y. Zhu, N. Nguyen, et al. Dynamical mean field theory algorithm and experiment on quantum computers. *Preprint at arXiv:1910.04735*, 2019.

[316] S. Sagmeister. *Excitonic Effects in Solids: Time-Dependent Density Functional Theory versus the Bethe-Salpeter Equation*. PhD thesis, 2009.

[317] E. E. Salpeter and H. A. Bethe. A relativistic equation for bound-state problems. *Phys. Rev.*, 84:1232–1242, 1951.

[318] T. Sander, E. Maggio, and G. Kresse. Beyond the tamm-dancoff approximation for extended systems using exact diagonalization. *Phys. Rev. B*, 92:045209, 2015.

[319] K. J. Satzinger, Y. P. Zhong, H.-S. Chang, G. A. Peairs, A. Bienfait, M.-H. Chou, A. Y. Cleland, C. R. Conner, É. Dumur, J. Grebel, I. Gutierrez, B. H. November, R. G. Povey, S. J. Whiteley, D. D. Awschalom, D. I. Schuster, and A. N. Cleland. Quantum control of surface acoustic-wave phonons. *Nature*, 563(7733):661–665, 2018.

[320] M. Saunders, R. Berger, A. Jaffe, J. M. McBride, J. O'Neill, R. Breslow, J. M. Hoffmann, C. Perchonock, E. Wasserman, R. S. Hutton, and V. Kuck. Unsubstituted cyclopentadienyl cation, a ground-state triplet. *J. Am. Chem. Soc.*, 95(9):3017–3018, 1973.

[321] E. R. Sayfutyarova and G. K.-L. Chan. Electron paramagnetic resonance g-tensors from state interaction spin-orbit coupling density matrix renormalization group. *J. Chem. Phys.*, 148(18):184103, 2018.

[322] P. Scherpelz, M. Govoni, I. Hamada, and G. Galli. Implementation and validation of fully relativistic gw calculations: Spin–orbit coupling in molecules, nanocrystals, and solids. *J. Chem. Theory Comput.*, 12(8):3523–3544, 2016.

[323] A. Schindlmayr and R. W. Godby. Systematic vertex corrections through iterative solution of hedin's equations beyond the gw approximation. *Phys. Rev. Lett.*, 80(8):1702–1705, 1998.

[324] M. Schlipf and F. Gygi. Optimization algorithm for the generation of oncv pseudopotentials. *Comput. Phys. Commun.*, 196:36–44, 2015.

[325] P. S. Schmidt, C. E. Patrick, and K. S. Thygesen. Simple vertex correction improves gw band energies of bulk and two-dimensional crystals. *Phys. Rev. B*, 96(20):205206, 2017.

[326] C. Schober, K. Reuter, and H. Oberhofer. Critical analysis of fragment-orbital DFT schemes for the calculation of electronic coupling values. *The Journal of Chemical Physics*, 144(5):054103, 2016.

[327] M. Schreiber, M. R. Silva-Junior, S. P. A. Sauer, and W. Thiel. Benchmarks for electronically excited states: Caspt2, cc2, ccsd, and cc3. *J. Chem. Phys.*, 128(13):134110, 2008.

[328] M. J. A. Schuetz, E. M. Kessler, G. Giedke, L. M. K. Vandersypen, M. D. Lukin, and J. I. Cirac. Universal Quantum Transducers Based on Surface Acoustic Waves. *Physical Review X*, 031031:1–30, 2015.

[329] M. J. Schütz. Universal quantum transducers based on surface acoustic waves. In *Quantum Dots for Quantum Information Processing: Controlling and Exploiting the Quantum Dot Environment*, pages 143–196. Springer, 2017.

[330] K. Schwarz and P. Blaha. Solid state calculations using wien2k. *Comput. Mater. Sci.*, 28(2):259 – 273, 2003.

[331] A. Schweiger and G. Jeschke. *Principles of pulse electron paramagnetic resonance*. Oxford University Press, 2001.

[332] U. N. Science and T. Council. Advancing quantum information science: National challenges and opportunities, 2016.

[333] H. Seo, A. L. Falk, P. V. Klimov, K. C. Miao, G. Galli, and D. D. Awschalom. Quantum decoherence dynamics of divacancy spins in silicon carbide. *Nature communications*, 7(1):1–9, 2016.

[334] H. Seo, M. Govoni, and G. Galli. Design of defect spins in piezoelectric aluminum nitride for solid-state hybrid quantum technologies. *Sci. Rep.*, 6(1):20803, 2016.

[335] H. Seo, H. Ma, M. Govoni, and G. Galli. Designing defect-based qubit candidates in wide-gap binary semiconductors for solid-state quantum technologies. *Phys. Rev. Mater.*, 1(7):075002, 2017.

[336] H. Seo, Y. Ping, and G. Galli. Role of Point Defects in Enhancing Conductivity of $BiVO_4$. *Chemistry of Materials*, 30(21):7793–7802, 2018.

[337] E. Sevgen, F. Giberti, H. Sidky, J. K. Whitmer, G. Galli, F. Gygi, and J. J. de Pablo. Hierarchical Coupling of First-Principles Molecular Dynamics with Advanced Sampling Methods. *Journal of Chemical Theory and Computation*, 14(6):2881–2888, 2018.

[338] R. Shaltaf, G.-M. Rignanese, X. Gonze, F. Giustino, and A. Pasquarello. Band offsets at the si/sio2 interface from many-body perturbation theory. *Phys. Rev. Lett.*, 100(18):186401, 2008.

[339] R. D. Shannon. Revised effective ionic radii and systematic studies of interatomic distances in halides and chalcogenides. *Acta crystallographica section A: crystal physics, diffraction, theoretical and general crystallography*, 32(5):751–767, 1976.

[340] M. Shishkin, M. Marsman, and G. Kresse. Accurate quasiparticle spectra from self-consistent gw calculations with vertex corrections. *Phys. Rev. Lett.*, 99(24):246403, 2007.

[341] Z. Shuai, L. Wang, and C. Song. *Theory of charge transport in carbon electronic materials*. Springer Science & Business Media, 2012.

[342] H. Sidky, Y. J. Colón, J. Helfferich, B. J. Sikora, C. Bezik, W. Chu, F. Giberti, A. Z. Guo, X. Jiang, J. Lequieu, et al. Ssages: software suite for advanced general ensemble simulations. *The Journal of chemical physics*, 148(4):044104, 2018.

[343] M. R. Silva-Junior, S. P. Sauer, M. Schreiber, and W. Thiel. Basis set effects on coupled cluster benchmarks of electronically excited states: Cc3, ccsdr(3) and cc2. *Mol. Phys.*, 108(3-4):453–465, 2010.

[344] M. R. Silva-Junior, M. Schreiber, S. P. A. Sauer, and W. Thiel. Benchmarks of electronically excited states: Basis set effects on caspt2 results. *J. Chem. Phys.*, 133(17):174318, 2010.

[345] S. Sinnecker and F. Neese. Spin- spin contributions to the zero-field splitting tensor in organic triplets, carbenes and biradicals a density functional and ab initio study. *J. Phys. Chem. A*, 110(44):12267–12275, 2006.

[346] J. H. Skone, M. Govoni, and G. Galli. Self-consistent hybrid functional for condensed systems. *Phys. Rev. B*, 89(19):195112, 2014.

[347] S. E. Smart and D. A. Mazziotti. Quantum-classical hybrid algorithm using an error-mitigating n-representability condition to compute the mott metal-insulator transition. *Phys. Rev. A*, 100:022517, 2019.

[348] S. E. Smart, D. I. Schuster, and D. A. Mazziotti. Experimental data from a quantum computer verifies the generalized pauli exclusion principle. *Commun. Phys.*, 2(1):1–6, 2019.

[349] T. J. Smart, F. Wu, M. Govoni, and Y. Ping. Fundamental principles for calculating charged defect ionization energies in ultrathin two-dimensional materials. *Phys. Rev. Materials*, 2:124002, 2018.

[350] R. D. Sole, L. Reining, and R. W. Godby. Gwγ approximation for electron self-energies in semiconductors and insulators. *Phys. Rev. B*, 49(12):8024–8028, 1994.

[351] V. A. Soltamov, A. A. Soltamova, P. G. Baranov, and I. I. Proskuryakov. Room temperature coherent spin alignment of silicon vacancies in 4 h-and 6 h-sic. *Physical review letters*, 108(22):226402, 2012.

[352] N. T. Son, A. Ellison, B. Magnusson, M. F. MacMillan, W. M. Chen, B. Monemar, and E. Janzén. Photoluminescence and zeeman effect in chromium-doped 4h and 6h SiC. *J. Appl. Phys.*, 86(8):4348–4353, 1999.

[353] F. Sottile, V. Olevano, and L. Reining. Parameter-free calculation of response functions in time-dependent density-functional theory. *Phys. Rev. Lett.*, 91(5):056402, 2003.

[354] A. M. Souza, I. Rungger, C. D. Pemmaraju, U. Schwingenschloegl, and S. Sanvito. Constrained-DFT method for accurate energy-level alignment of metal/molecule interfaces. *Physical Review B*, 88(16), 2013.

[355] Ö. Soykal, P. Dev, and S. E. Economou. Silicon vacancy center in 4 h-sic: Electronic structure and spin-photon interfaces. *Physical Review B*, 93(8):081207, 2016.

[356] M. Steiner, P. Neumann, J. Beck, F. Jelezko, and J. Wrachtrup. Universal enhancement of the optical readout fidelity of single electron spins at nitrogen-vacancy centers in diamond. *Physical Review B*, 81(3):035205, 2010.

[357] G. Strinati. Dynamical shift and broadening of core excitons in semiconductors. *Phys. Rev. Lett.*, 49:1519–1522, 1982.

[358] N. Q. Su, C. Li, and W. Yang. Describing strong correlation with fractional-spin correction in density functional theory. *Proc. Natl. Acad. Sci. U. S. A.*, 115(39):9678–9683, 2018.

[359] K. Sugisaki, K. Toyota, K. Sato, D. Shiomi, M. Kitagawa, and T. Takui. Ab initio calculations of spin-orbit contribution to the zero-field splitting tensors of nπ excited states by the casscf method with mrmp2 energy correction. *Chem. Phys. Lett.*, 477(4-6):369–373, 2009.

[360] Q. Sun, T. C. Berkelbach, N. S. Blunt, G. H. Booth, S. Guo, Z. Li, J. Liu, J. D. McClain, E. R. Sayfutyarova, S. Sharma, S. Wouters, and G. K.-L. Chan. Py SCF: the python-based simulations of chemistry framework. *Wiley Interdiscip. Rev.: Comput. Mol. Sci.*, 8(1):e1340, 2017.

[361] Q. Sun and G. K.-L. Chan. Quantum embedding theories. *Acc. Chem. Res.*, 49(12):2705–2712, 2016.

[362] K. Szász, V. Ivády, I. A. Abrikosov, E. Janzén, M. Bockstedte, and A. Gali. Spin and photophysics of carbon-antisite vacancy defect in 4 h silicon carbide: A potential quantum bit. *Physical Review B*, 91(12):121201, 2015.

[363] Y. Takagaki, P. V. Santos, E. Wiebicke, O. Brandt, H.-P. Schönherr, and K. H. Ploog. Guided propagation of surface acoustic waves in aln and gan films grown on 4h-sic (0001) substrates. *Physical Review B*, 66:155439, 2002.

[364] D. V. Talapin, J.-S. Lee, M. V. Kovalenko, and E. V. Shevchenko. Prospects of Colloidal Nanocrystals for Electronic and Optoelectronic Applications. *Chemical Reviews*, 110(1):389–458, 2010.

[365] I. Tamm. *Relativistic Interaction of Elementary Particles*. Springer Berlin Heidelberg, Berlin, Heidelberg, 1991.

[366] M. Tanimoto, S. Saito, and E. Hirota. Microwave spectrum of the boron monoxide radical, bo. *J. Chem. Phys.*, 84(3):1210–1214, 1986.

[367] G. te Velde, F. M. Bickelhaupt, E. J. Baerends, C. Fonseca Guerra, S. J. A. van Gisbergen, J. G. Snijders, and T. Ziegler. Chemistry with adf. *J. Comput. Chem.*, 22(9):931–967, 2001.

[368] J. Teissier, A. Barfuss, P. Appel, E. Neu, and P. Maletinsky. Strain coupling of a nitrogen-vacancy center spin to a diamond mechanical oscillator. *Phys. Rev. Lett.*, 113:020503, 2014.

[369] G. Thiering and A. Gali. Ab initio magneto-optical spectrum of group-iv vacancy color centers in diamond. *Phys. Rev. X*, 8:021063, 2018.

[370] G. Thiering and A. Gali. The (eg $\otimes$ eu) $\otimes$ eg product jahn–teller effect in the neutral group-IV vacancy quantum bits in diamond. *npj Comput. Mater.*, 5(1):18, 2019.

[371] M. L. Tiago and J. R. Chelikowsky. Optical excitations in organic molecules, clusters, and defects studied by first-principles green's function methods. *Phys. Rev. B*, 73(20):205334, 2006.

[372] D. M. Toyli, C. D. Weis, G. D. Fuchs, T. Schenkel, and D. D. Awschalom. Chip-scale nanofabrication of single spins and spin arrays in diamond. *Nano Letters*, 10(8):3168–3172, 2010. PMID: 20698632.

[373] Y. Tu, Z. Tang, X. Zhao, Y. Chen, Z. Zhu, J. Chu, and J. Fang. A paramagnetic neutral valon center in wurtzite aln for spin qubit application. *Applied Physics Letters*, 103(7):072103, 2013.

[374] P. Udvarhelyi and A. Gali. *Ab initio* spin-strain coupling parameters of divacancy qubits in silicon carbide. *Physical Review Applied*, 10:054010, 2018.

[375] P. Udvarhelyi, V. O. Shkolnikov, A. Gali, G. Burkard, and A. Pályi. Spin-strain interaction in nitrogen-vacancy centers in diamond. *Physical Review B*, 98:075201, 2018.

[376] P. Umari, G. Stenuit, and S. Baroni. Optimal representation of the polarization propagator for large-scale gw calculations. *Phys. Rev. B*, 79(20):201104, 2009.

[377] C. G. Van de Walle and P. E. Blöchl. First-principles calculations of hyperfine parameters. *Phys. Rev. B*, 47:4244–4255, 1993.

[378] M. J. van Setten, F. Caruso, S. Sharifzadeh, X. Ren, M. Scheffler, F. Liu, J. Lischner, L. Lin, J. R. Deslippe, S. G. Louie, C. Yang, F. Weigend, J. B. Neaton, F. Evers, and P. Rinke. Gw100: Benchmarking g0w0 for molecular systems. *J. Chem. Theory Comput.*, 11(12):5665–5687, 2015.

[379] J. Varley, A. Janotti, and C. Van de Walle. Defects in aln as candidates for solid-state qubits. *Physical Review B*, 93(16):161201, 2016.

[380] J. Verhoeven, A. Dymanus, and H. Bluyssen. Hyperfine structure of hd17o by beam-maser spectroscopy. *J. Chem. Phys.*, 50(8):3330–3338, 1969.

[381] H. Von Bardeleben, J. Cantin, A. Csóré, A. Gali, E. Rauls, and U. Gerstmann. Nv centers in 3 c, 4 h, and 6 h silicon carbide: A variable platform for solid-state qubits and nanosensors. *Physical Review B*, 94(12):121202, 2016.

[382] H. Von Bardeleben, J. Cantin, E. Rauls, and U. Gerstmann. Identification and magneto-optical properties of the nv center in 4 h- sic. *Physical Review B*, 92(6):064104, 2015.

[383] M. Vörös, N. P. Brawand, and G. Galli. Hydrogen Treatment as a Detergent of Electronic Trap States in Lead Chalcogenide Nanoparticles. *Chemistry of Materials*, 29(6):2485–2493, 2017.

[384] L. K. Wagner and D. M. Ceperley. Discovering correlated fermions using quantum monte carlo. *Rep. Prog. Phys.*, 79(9):094501, 2016.

[385] G. Waldherr, Y. Wang, S. Zaiser, M. Jamali, T. Schulte-Herbrüggen, H. Abe, T. Ohshima, J. Isoya, J. Du, P. Neumann, et al. Quantum error correction in a solid-state hybrid spin register. *Nature*, 506(7487):204–207, 2014.

[386] B. Walker, A. M. Saitta, R. Gebauer, and S. Baroni. Efficient approach to time-dependent density-functional perturbation theory for optical spectroscopy. *Phys. Rev. Lett.*, 96:113001, 2006.

[387] J. L. Walsh. A closed set of normal orthogonal functions. *Am. J. Math.*, 45(1):5, 1923.

[388] W. Wang, P. Strohbeen, D. Lee, C. Zhou, J. Kawasaki, K.-S. Choi, M. Liu, and G. Galli. The role of surface oxygen vacancies in $BiVO_4$. *Chemistry of Materials*, Just accepted., 2020.

[389] X.-B. Wang, C.-F. Ding, and L.-S. Wang. High resolution photoelectron spectroscopy of c60. *J. Chem. Phys.*, 110(17):8217–8220, 1999.

[390] E. Wasserman, R. Hutton, V. Kuck, and W. Yager. Zero-field parameters of"free"ch 2: Spin—orbit contributions in xenon. *J. Chem. Phys.*, 55(5):2593–2594, 1971.

[391] J. Weber, W. Koehl, J. Varley, A. Janotti, B. Buckley, C. Van de Walle, and D. Awschalom. Defects in sic for quantum computing. *J. Appl. Phys.*, 109(10):102417, 2011.

[392] J. R. Weber, W. F. Koehl, J. B. Varley, A. Janotti, B. B. Buckley, C. G. V. de Walle, and D. D. Awschalom. Quantum computing with defects. *Proc. Natl. Acad. Sci. U. S. A.*, 107(19):8513–8518, 2010.

[393] J. A. Weil and J. R. Bolton. *Electron paramagnetic resonance: elementary theory and practical applications*. John Wiley & Sons, 2007.

[394] W. Weltner. *Magnetic Atoms and Molecules*. Dover Publications, 1989.

[395] X. Wen, D. S. Graham, D. V. Chulhai, and J. D. Goodpaster. Absolutely localized projection-based embedding for excited states. *Preprint at arXiv:1909.12423*, 2019.

[396] S. J. Whiteley, G. Wolfowicz, C. P. Anderson, A. Bourassa, H. Ma, M. Ye, G. Koolstra, K. J. Satzinger, M. V. Holt, F. J. Heremans, et al. Spin–phonon interactions in silicon carbide addressed by gaussian acoustics. *Nat. Phys.*, 15(5):490–495, 2019.

[397] M. Widmann, S.-Y. Lee, T. Rendler, N. T. Son, H. Fedder, S. Paik, L.-P. Yang, N. Zhao, S. Yang, I. Booker, et al. Coherent control of single spins in silicon carbide at room temperature. *Nature materials*, 14(2):164–168, 2015.

[398] M. Widmann, S.-Y., T. Rendler, N. T. Son, H. Fedder, S. Paik, L.-P. Yang, N. Zhao, S. Yang, I. Booker, A. Denisenko, M. Jamali, S. A. Momenzadeh, I. Gerhardt, T. Ohshima, A. Gali, E. Janzén, and J. Wrachtrup. Coherent control of single spins in silicon carbide at room temperature. *Nature Materials*, 14(2):164–168, 2015.

[399] H. F. Wilson, F. Gygi, and G. Galli. Efficient iterative method for calculations of dielectric matrices. *Phys. Rev. B*, 78:113303, 2008.

[400] H. F. Wilson, D. Lu, F. Gygi, and G. Galli. Iterative calculations of dielectric eigenvalue spectra. *Phys. Rev. B*, 79:245106, 2009.

[401] S. Wouters, C. A. Jiménez-Hoyos, Q. Sun, and G. K.-L. Chan. A practical guide to density matrix embedding theory in quantum chemistry. *J. Chem. Theory Comput.*, 12(6):2706–2719, 2016.

[402] Q. Wu, B. Kaduk, and T. Van Voorhis. Constrained density functional theory based configuration interaction improves the prediction of reaction barrier heights. *The Journal of Chemical Physics*, 130(3):034109, 2009.

[403] Q. Wu and T. Van Voorhis. Direct optimization method to study constrained systems within density-functional theory. *Physical Review A*, 72(2):024502, 2005.

[404] Q. Wu and T. Van Voorhis. Direct Calculation of Electron Transfer Parameters through Constrained Density Functional Theory. *The Journal of Physical Chemistry A*, 110(29):9212–9218, 2006.

[405] Q. Wu and T. Van Voorhis. Extracting electron transfer coupling elements from constrained density functional theory. *The Journal of Chemical Physics*, 125(16):164105, 2006.

[406] Y. Wu, F. Jelezko, M. B. Plenio, and T. Weil. Diamant-quantensensoren in der biologie. *Angewandte Chemie*, 128(23):6696–6709, 2016.

[407] C. G. Yale, F. J. Heremans, B. B. Zhou, A. Auer, G. Burkard, and D. D. Awschalom. Optical manipulation of the berry phase in a solid-state spin qubit. *Nat. Photonics*, 10(3):184–189, 2016.

[408] H. Yamada and K. Iguchi. Some Effective Tight-Binding Models for Electrons in DNA Conduction: A Review. *Advances in Condensed Matter Physics*, 2010:1–28, 2010.

[409] T. Yamazaki, S. Matsuura, A. Narimani, A. Saidmuradov, and A. Zaribafiyan. Towards the practical application of near-term quantum computers in quantum chemistry simulations: A problem decomposition approach. *Preprint at arXiv:1806.01305*, 2018.

[410] L.-P. Yang, C. Burk, M. Widmann, S.-Y. Lee, J. Wrachtrup, and N. Zhao. Electron spin decoherence in silicon carbide nuclear spin bath. *Physical Review B*, 90(24):241203, 2014.

[411] W. Yang and R.-B. Liu. Quantum many-body theory of qubit decoherence in a finite-size spin bath. *Physical Review B*, 78(8):085315, 2008.

[412] B. Yavkin, G. Mamin, and S. Orlinskii. High-frequency pulsed endor spectroscopy of the nv centre in the commercial hpht diamond. *J. Magn. Reson.*, 262:15 – 19, 2016.

[413] M. Ye, H. Seo, and G. Galli. Spin coherence in two-dimensional materials. *NPJ Computational Materials*, 5(1):1–6, 2019.

[414] M. Yoshida, A. Onodera, M. Ueno, K. Takemura, and O. Shimomura. Pressure-induced phase transition in sic. *Physical Review B*, 48(14):10587, 1993.

[415] D. Yu, C. Wang, B. L. Wehrenberg, and P. Guyot-Sionnest. Variable Range Hopping Conduction in Semiconductor Nanocrystal Solids. *Physical Review Letters*, 92(21), 2004.

[416] S. Zargaleh, B. Eble, S. Hameau, J.-L. Cantin, L. Legrand, M. Bernard, F. Margaillan, J.-S. Lauret, J.-F. Roch, H. Von Bardeleben, et al. Evidence for near-infrared photoluminescence of nitrogen vacancy centers in 4 h-sic. *Physical Review B*, 94(6):060102, 2016.

[417] C. Zener. Non-Adiabatic Crossing of Energy Levels. *Proceedings of the Royal Society A: Mathematical, Physical and Engineering Sciences*, 137(833):696–702, 1932.

[418] X. Zeng, X. Hu, and W. Yang. Fragment-Based Quantum Mechanical/Molecular Mechanical Simulations of Thermodynamic and Kinetic Process of the Ru $^{2+}$ –Ru $^{3+}$ Self-Exchange Electron Transfer. *Journal of Chemical Theory and Computation*, 8(12):4960–4967, 2012.

[419] Z.-H. Zhang, P. Stevenson, G. Thiering, B. C. Rose, D. Huang, A. M. Edmonds, M. L. Markham, S. A. Lyon, A. Gali, and N. P. de Leon. Optically detected magnetic resonance in the neutral silicon vacancy center in diamond via bound exciton states. *arXiv:2004.12544*, 2020.

[420] T. Zhu, Z.-H. Cui, and G. K.-L. Chan. Efficient formulation of ab initio quantum embedding in periodic systems: Dynamical mean-field theory. *J. Chem. Theory Comput.*, 2019.

[421] J. A. Zimmerman, J. R. Eyler, S. B. H. Bach, and S. W. McElvany. "magic number" carbon clusters: Ionization potentials and selective reactivity. *J. Chem. Phys.*, 94(5):3556–3562, 1991.